

University of Southampton Research Repository ePrints Soton

Copyright © and Moral Rights for this thesis are retained by the author and/or other copyright owners. A copy can be downloaded for personal non-commercial research or study, without prior permission or charge. This thesis cannot be reproduced or quoted extensively from without first obtaining permission in writing from the copyright holder/s. The content must not be changed in any way or sold commercially in any format or medium without the formal permission of the copyright holders.

When referring to this work, full bibliographic details including the author, title, awarding institution and date of the thesis must be given e.g.

AUTHOR (year of submission) "Full thesis title", University of Southampton, name of the University School or Department, PhD Thesis, pagination

UNIVERSITY OF SOUTHAMPTON

FACULTY OF ENGINEERING, SCIENCE & MATHEMATICS

School of Civil Engineering and the Environment

Wave Energy Resource Assessment

by

Edward B. L. Mackay

Thesis for the degree of Doctor of Philosophy

June 2009

UNIVERSITY OF SOUTHAMPTON

ABSTRACT

FACULTY OF ENGINEERING, SCIENCE & MATHEMATICS
SCHOOL OF CIVIL ENGINEERING & THE ENVIRONMENT

Doctor of Philosophy

WAVE ENERGY RESOURCE ASSESSMENT

By Edward B. L. Mackay

The use of satellite altimeter data for spatial mapping of the wave resource is examined. A new algorithm for estimating wave period from altimeter data is developed and validated, which enables estimates of wave energy converter (WEC) power to be derived. Maps of the long-term mean WEC power from altimeter data are of a higher spatial resolution than is available from global wave model data. They can be used for identifying promising wave energy locations along particular stretches of coastline, before a detailed study using nearshore models is undertaken.

The accuracy of estimates of WEC power from wave model data is considered. Without calibration estimates of the mean WEC power from model data can be biased of the order of 10-20%. The calibration of wave model data is complicated by non-linear dependence of model parameters on multiple factors, and seasonal and interannual changes in biases. After calibration the accuracy in the estimate of the historic power production at a site is of the order of 5%, but the changing biases make it difficult to specify the accuracy more precisely.

The accuracy of predictions of the future energy yield from a WEC is limited by the accuracy of the historic data and the variability in the resource. The variability in 5, 10 and 20 year mean power levels is studied for an area in the north of Scotland, and shown to be greater than if annual power anomalies were uncorrelated noise. The sensitivity of WEC power production to climate change is also examined, and it is shown that the change in wave climate over the life time of a wave farm is likely to be small in comparison to the natural level of variability. It is shown that despite the uncertainty related to variability in the wave climate, improvements in the accuracy of historic data will improve the accuracy of predictions of future WEC yield.

The topic of extreme wave analysis is also considered. A comparison of estimators for the generalised Pareto distribution (GPD) is presented. It is recommended that the Likelihood-Moment estimator should be used in preference to other estimators for the GPD. The use of seasonal models for extremes is also considered. In contrast to assertions made in previous studies, it is demonstrated that non-seasonal models have a lower bias and variance than models which analyse the data in separate seasons.

Contents

List of abbreviations	vi
List of tables	vii
List of figures	viii
1. Introduction	1
1.1 The need for wave energy resource assessment	1
1.2 Research aims	2
1.3 The nature of the resource	4
1.3.1 The wave spectrum	4
1.3.2 Wave parameters	7
1.3.3 Uncertainty and variability	9
1.4 Estimating WEC power	10
1.5 Research overview and relation to previous studies	12
1.6 Research limitations	15
2. Wave Data Sources	17
2.1 Wave measurements from moored buoys	20
2.1.1 Instrumental characteristics	21
2.1.2 Quality checks	24
2.1.3 Sampling variability for temporal averages	25
2.1.4 Short-term temporal variability of wave height	34
2.2 Wave measurements from satellite altimeters	38
2.2.1 Instrumental characteristics	40
2.2.2 Quality checks	48
2.2.3 Sampling variability for spatial averages	57
2.2.4 Short-scale spatial variability of wave height	60
2.3 Numerical wave models	62
2.3.1 Brief introduction to numerical wind-wave models	63
2.3.2 Sources of error in wave models	64
2.3.3 Qualitative description of model errors	66
3. Intercomparison of Altimeter and Buoy Measurements	69
3.1 Significant wave height	69
3.1.1 Statistical techniques for calibration and validation	69
3.1.2 Example calibration / validation for H_s	71
3.2 Wave period	77
3.2.1 Previous work on altimeter wave period	77
3.2.2 Development of a new period algorithm	79
3.2.3 Results	83
3.2.4 Discussion	89
3.2.5 Conclusions	94
4. Large Scale Resource Mapping Using Altimeter Data	96
4.1 Introduction	96
4.2 Comparison of individual power estimates	97
4.3 Mean values over $2^\circ \times 2^\circ$ squares	102

4.4 Along-track averages	107
4.5 Example and discussion	112
4.6 Conclusions	114
5. Resource Estimation from Model Data	115
5.1 Calibration and confidence bounds	115
5.1.1 Techniques for estimating model errors	116
5.1.2 Assessment of EMEC hindcast errors	120
5.1.3 Estimating uncertainty in WEC yield	130
5.1.4 Comparison of calibrated hindcasts	137
5.1.5 Discussion and conclusions	141
5.2 The limiting accuracy due to sampling variability	143
5.3 Comparison of altimeter and model accuracy	145
5.3.1 Altimeter sampling patterns	146
5.3.2 Uncertainty from sparse temporal sampling	148
5.3.3 Discussion and conclusions	154
6. Variability and Predictability of Wave Energy Resource	156
6.1 Introduction	156
6.2 Data and validation	161
6.2.1 Wave data	161
6.2.2 NAO index	164
6.3 A stochastic model for long-term variability in WEC yield	165
6.3.1 Observed variability in WEC power levels	165
6.3.2 The relationship between the NAO and power anomalies	167
6.3.3 Temporal variability of the NAO	170
6.4 Predictability of WEC yield	173
6.4.1 Distribution of multi-year mean values	173
6.4.2 The effect of uncertainty in historic data	176
6.4.3 Sensitivity to climate change	177
6.5 Discussion and conclusions	179
7. Extreme Wave Analysis	181
7.1 Introduction	181
7.2 Overview of methods for estimating extreme H_s	183
7.3 The generalised Pareto distribution	186
7.3.1 CDF and PDF	186
7.3.2 Return values	188
7.3.3 Threshold choice	189
7.3.4 Model diagnostics	191
7.4 Estimation of GPD parameters	193
7.4.1 Methods	193
7.4.2 Simulation study	203
7.5 Seasonality, directionality and other covariates	210
7.6 Examples using buoy data	215
7.6.1 Buoy data	215
7.6.2 Declustering	217
7.6.3 Model fitting and checking	222
7.6.4 Results	226
7.6.5 Simulation study	231

7.7 Conclusions	240
8. Conclusions and further work	243
8.1 Conclusions	243
8.1.1 Spatial mapping of wave energy resource	243
8.1.2 Detailed information at selected site	244
8.2 Further work	246
8.2.1 Spatial mapping of wave energy resource	247
8.2.2 Detailed information at selected site	247
Appendix A: Quality controls for EMEC Waverider data	250
Appendix B: Altimeter missions to date	258
Appendix C: Notes on linear regression	263
Appendix D: A Parametric Model for Ocean Wave Period from Ku-band Altimeter Data	268
Appendix E: Wave Energy Resource Assessment Using Satellite Altimeter Data	284
Appendix F: Notes on time series models	294
Appendix G: Results of extreme value analysis of NDBC buoy data	300
References	305

List of abbreviations

AD	Anderson-Darling statistic
ADCP	Acoustic Doppler Current Profiler
AOGCM	Coupled atmosphere-ocean global circulation models
ARMA	Auto-regressive moving-average
CDF	Cumulative distribution function
CM	Cramer-von Mises statistic
COV	Coefficient of variation
DWR	Directional Waverider
ECMWF	European Centre for Medium Range Weather Forecasts
EMEC	European Marine Energy Centre
EOF	Empirical Orthogonal Function
EPM	Empirical percentile method
FAR(1)	First-order fractionally-differenced autoregressive model
G03	Altimeter wave period algorithm of Gommenginger et al (2003)
GCM	Global circulation models
GDR	Geophysical Data Records
GEV	Generalised Extreme Value
GHG	Green house gas
GPD	Generalised Pareto Distribution
HM	Hybrid-moment
IPCC	Intergovernmental Panel on Climate Change
LM	Likelihood-moment
LS	Least squares
MCP	Measure-Correlate-Predict
MGF	Maximum goodness of fit
ML	Maximum likelihood
MOM	Method of moments
NAO	North Atlantic Oscillation
NDBC	National Data Buoy Centre
NOAA	National Oceanographic and Atmospheric Administration
ODR	Orthogonal distance regression

PDF	Probability density function
PM	Pierson-Moskowitz
POT	Peaks Over Threshold
PWM	Probability weighted moment
Q04	Altimeter wave period algorithm of Quilfen et al (2004)
RAO	Response Amplitude Operator
RMS	Root-mean-square
RMSE	Root-mean-square-error
SAR	Synthetic aperture radar
SLP	Sea level pressure
T/P	TOPEX/Poseidon
VOS	Voluntary observing ship
WEC	Wave energy converter

List of tables

Table 1.1. Power matrix for the Pelamis.

Table 3.1. Linear calibrations of altimeter H_s against NDBC buoy data. N is the number of data points used in the regression.

Table 3.2. Slope and intercept of fitted line for various T_z .

Table 3.3. RMS errors for the look-up table method.

Table 4.1. Bias and RMS error of altimeter estimates of Pelamis power with 95% confidence intervals in brackets.

Table 4.2. Bias and RMS error in along-track annual mean Pelamis power compared to buoy measurements, 95% confidence limits given in brackets.

Table 4.4. Attainable accuracy, given the length of data available, for along-track averages of Pelamis power.

Table 7.1. Details of the NDBC buoys used in this section.

Table 7.2. Bias and RMS errors in estimated return values for case study 1.

Table 7.3. Bias and RMS errors in estimated return values for case study 2.

Table 7.4. Bias and RMS errors in estimated return values for case study 3.

Table 7.5. Bias and RMS errors in estimated return values for case study 4.

Table 7.6. Bias and RMS errors in estimated return values for case study 2, with 30% missing data in winter.

List of figures

Figure 2.1. Locations of EMEC buoys.

Figure 2.2. Autocorrelation of normalised differences in H_s (left) and T_e (right).

Figure 2.3. Standard deviation of differences in H_s and T_e against H_s and T_e .

Figure 2.4. Standard deviation of differences in H_s and T_e , binned by H_s and T_e .

Figure 2.5. Correlation of differences in H_s and T_e , binned by H_s and T_e .

Figure 2.6. Standard deviation of differences in Pelamis power against mean power (left) and binned by H_s and T_e (right).

Figure 2.7. (a) Bar plot: distribution of differences for $2\text{m} < H_{ave} < 3\text{m}$ at separation of 6 hours. Line: fitted normal distribution. (b) Standard deviation of δ against H_{ave} at separation of 6 hours, bin width 0.5m.

Figure 2.8. (a) Observed and true values of $a(\tau)$ from numerical simulation. (b) Raw and corrected values of $a(\tau)$ from the data.

Figure 2.9. Standard deviation of difference in power (uncorrected) against P_{ave} for $\tau = 1, 2, \dots, 12$ hours, lowest line is $\tau = 1$.

Figure 2.10. 3D view of TOPEX phase A orbit. Left: first 5 passes of a cycle. Right: A full cycle of 254 passes.

Figure. 2.11. Altimeter passes in the vicinity of United Kingdom (TOPEX/Poseidon/Jason in Black, ERS-1&2/ENVISAT in Red)

Figure 2.12. (a) The transmitted pulse of radar energy from an altimeter at vertical incidence (b) The illumination of a flat sea surface by the radar pulse shown in (a). (c) The evolution of returned power received at the altimeter for a single pulse. (From Challenor, 2006).

Figure 2.13. As Figure 2.12, but with waves on the sea surface. (From Challenor, 2006).

Figure 2.14. Returned power for Gaussian sea surface height distributions for various H_s . (From Challenor, 2006).

Figure 2.15. Footprint diameter against H_s for two orbital altitudes.

Figure 2.16. (a) A single returned waveform. (b) Averages of 50 and 1000 waveforms. (From Challenor, 2006).

- Figure 2.17. The effect of mispointing angle on the returned waveform. (From Challenor, 2006).
- Figure 2.18. Scatter plots of standard deviation in 20 Hz measurements of H_s and range against H_s . Data from ERS-2 over the North Atlantic. Circles and dashed lines are the median and 95% bounds of data in 0.5m bins. Solid line is upper bound for the quality check.
- Figure 2.19. H_s against latitude for TOPEX phase A, pass 222, cycles 54, 69, 210 and 268. Data failing the quality checks is highlighted in red.
- Figure 2.20. Scatter plots of collocated 1Hz measurements, left: T/P with Jason, right: ERS-2 with ENVISAT.
- Figure 2.21. Standard deviation in difference of collocation measurements against mean H_s , in bins of width 1m. Diamonds are ERS-2 and ENVISAT, circles are T/P and Jason.
- Figure 2.22. Standard deviation of differences against average H_s in bins of width 1m, at separations of 1, 5, 10, 15 and 20 samples.
- Figure 3.1. Locations of the 28 deep-water NDBC buoys used in the collocated data set.
- Figure 3.2. Orthogonal regression of altimeter on buoy data. Left: TOPEX; right: ERS-2.
- Figure 3.3. Circles: Standard deviation of differences between buoy and altimeter. Solid line: Standard deviation of differences altimeter measurements at 50km.
- Figure 3.4. Mean T_z (left) and T_e (right) against H_s and σ_0 for combined collocated data.
- Figure 3.5. (a) Mean significant steepness against H_s and σ_0 for combined collocated data. (b) Scatter plot of significant steepness against σ_0 , with contours showing distribution of data.
- Figure 3.6. Linear fits to TOPEX data for T_z between 3 and 12s. The correlation, ρ , and number of points, n , are given at the top of each plot.
- Figure 3.7. Scatter plot of slope of fitted line against T_z .
- Figure 3.8. Scatter plots of altimeter T_z against buoy T_z for the Q04, G03 and two-piece algorithms using TOPEX data, with contours showing distribution of data.
- Figure 3.9. Scatter plot of altimeter T_e (two-piece algorithm) against T_e (buoy) for TOPEX data, with contours showing distribution of data.
- Figure 3.10. Coloured squares indicate mean buoy T_z binned by H_s and σ_0 for TOPEX data with contours of T_z for the two-piece, Q04 and G03 models overlaid. Contours are at 1s intervals, from 4 to 12s.

Figure 3.11. Residual errors for the two-piece model (top row), Q04 model (middle row) and G03 model (bottom row) for TOPEX data, with buoy T_z , buoy H_s , buoy significant steepness and altimeter σ_0 . Contours show distribution of data.

Figure 3.12. Histograms of buoy and altimeter T_z and significant steepness for TOPEX (data is $\sigma_0 < 16\text{dB}$ for comparison with Q04)

Figure 3.13. Joint distribution of H_s and T_z from buoy and altimeter data (TOPEX, $\sigma_0 \leq \delta$), with contours showing distribution of data.

Figure 3.14. The joint distribution of H_s and T_z from buoy data when TOPEX $\sigma_0 > \delta$. The dashed line shows the value of T_z for two-piece algorithm.

Figure 3.15. Standard deviation and skewness of T_z for data binned by H_s and σ_0 , for combined collocated data.

Figure 3.16. Standard error of T_z and T_e (defined as the standard deviation divided by the mean) for data binned by H_s and σ_0 , for combined collocated data.

Figure 3.17. Scatter plots of T_z against T_e for buoy measurements and the two-piece altimeter model (TOPEX data).

Figure 4.1. Locations of NDBC buoys used in the collocated dataset. Solid diamonds denote buoys in depths $>100\text{m}$, hollow diamonds denote depths $<100\text{m}$.

Figure 4.2. Scatter plots of altimeter Pelamis power against buoy Pelamis power, with contours showing density of occurrence, for $\sigma_0 \leq \delta$ (left) and $\sigma_0 > \delta$ (right).

Figure 4.3. Quantile-quantile plot of Pelamis power measured by altimeter and buoys.

Figure 4.4. Mean difference in power against difference in H_s and T_e .

Figure 4.5. Scatter plots of collocated altimeter estimates of Pelamis power from tandem orbits. Left: T/P phase A and Jason-1. Right: ENVISAT and ERS-2.

Figure 4.6. Scatter plot of collocated altimeter estimates of Pelamis power from Jason-1 and TOPEX phase B orbit.

Figure 4.7. Scatter plots of altimeter against buoy monthly and annual mean Pelamis power.

Figure 4.8. Correlation of altimeter monthly mean Pelamis power with buoy monthly mean Pelamis power against number of transects, with 95% confidence limits.

Figure 4.9. Annual mean Pelamis power in $2^\circ \times 2^\circ$ squares for the period 1996-2005 from the combined altimeter dataset.

Figure 4.10. Mean Pelamis power in $2^\circ \times 2^\circ$ squares over December-February (top) and June-August (bottom) for the period 1996-2005 from the combined altimeter dataset.

Figure 4.11. Mean along-track Pelamis power for T/P and Jason data for the period Jan 1992 – Dec 2007

Figure 4.12. Difference in annual mean Pelamis power against separation between ground tracks and buoys for deep water buoys (left) and shallow water buoys (right).

Figure 4.13. Annual mean Pelamis power from altimeter along-track averages against buoy measurements. Values for the shallow water buoys are marked with circles.

Figure 4.14. Scatter plots of intra-monthly standard deviation against monthly mean Pelamis power. Values have been normalised by the annual average Pelamis power.

Figure 4.15. Variation in monthly mean Pelamis power: crosses are individual months, line is climatological monthly mean. Values have been normalised by the annual average Pelamis power.

Figure 4.16. Percentage uncertainty from limited sampling for various sites

Figure 4.17. Annual mean Pelamis power around New Caledonia for combined altimeter tracks.

Figure 5.1. Summer and winter distributions of H_s at EMEC.

Figure 5.2. Solid line: mean model H_s binned by buoy H_s ; dashed line: mean buoy H_s binned by model H_s ; dotted line: q-q plot. For distributions of H_s shown in Figure 5.1, left – summer; right – winter.

Figure 5.3. Time series plots of H_s from buoy and models.

Figure 5.4. Scatter plots of buoy and model H_s (left) and T_e (right), colour denoting buoy T_e (left) and buoy H_s (right).

Figure 5.5. Bias in H_s and T_e for OCEANOR model, binned by buoy H_s and T_e .

Figure 5.6. Bias in H_s and T_e for ARGOSS model, binned by buoy H_s and T_e .

Figure 5.7. Left: bias in ARGOSS T_e , binned by model H_s and T_e . Right: bias in ARGOSS T_e against model steepness, black crosses – individual points, red circles – bin average, cyan line – fitted exponential curve.

Figure 5.8. Bias in model H_s in binned by month and buoy H_s . Left: OCEANOR, right: ARGOSS.

Figure 5.9. Correlation in errors in model H_s and T_e , binned by buoy H_s and T_e .

Figure 5.10. (a) Error in model H_s against buoy H_s ; black crosses: individual points, red circles: bin average, cyan line: fitted quadratic curve. (b) Standard deviation of error in model H_s ; circles: bin average, line: fitted linear relationship. (c) Error in model T_e against buoy T_e , for buoy $H_s > 1\text{m}$; black crosses: individual points, red circles: bin average, cyan line: fitted linear relationship. (d) Standard deviation of error in model T_e ; circles: bin average, line: average over dataset. All plots for OCEANOR data.

Figure 5.11. As previous figure, but for ARGOSS data.

Figure 5.12. Quantile plots of model against buoy Pelamis power. Crosses: uncalibrated models; diamonds: calibrated.

Figure 5.13. Scatter plots of monthly mean Pelamis power for calibrated models against buoy values.

Figure 5.14. Monthly mean Pelamis power from the calibrated models.

Figure 5.15. Distribution of normalised errors in model H_s and T_e (histograms) with fitted normal distribution (lines).

Figure 5.16. Standard deviation of the error in model power for OCEANOR (top) and ARGOSS (bottom). Left: from equation 5.1.7. Right: from equation 5.1.8.

Figure 5.17. Auto-correlation series of normalised errors. Circles and solid line: values for OCEANOR and fitted ARMA(2,3) model. Diamonds and dashed line: values for ARGOSS and fitted ARMA(3,2) model.

Figure 5.18. Standard deviation of the error in monthly mean power from the ARMA simulations against estimated monthly mean power from the hindcasts.

Figure 5.19. Scatter plots of H_s coloured by T_e (left) and T_e coloured by H_s (right) for the calibrated hindcasts.

Figure 5.20. Mean and standard deviation of differences in T_e between calibrated models, for average $H_s > 1\text{m}$.

Figure 5.21. Mean and standard deviation of differences in H_s between calibrated models.

Figure 5.22. (a) Mean difference in H_s , binned by H_s and T_e . (b) Mean difference in H_s , binned by H_s and month.

Figure 5.23. Mean T_e (left) and steepness (right) binned by H_s and month, from 5 years of EMEC buoy data.

Figure 5.24. Seasonal mean difference in H_s between the calibrated models, binned by H_s and T_e .

Figure 5.25. Solid line with circles: differences between hindcasts after seasonal re-calibration. Dashed lines: 95% bounds from combined ARMA models.

Figure 5.26. Histogram: Distribution of normalised differences in Pelamis power estimated from concurrent buoy data. Line: Fitted Student's t -distribution.

Figure 5.27. Standard deviation in monthly mean Pelamis power from sampling variability against monthly mean power.

Figure 5.28. Altimeter sampling patterns. Colour denotes day of the cycle on which the track is sampled. (a) TOPEX/Poseidon and Jason (b) GEOSAT/GFO (c) ERS-2/ENVISAT days 1-17, (b) ERS-2/ENVISAT days 18-35.

Figure 5.29. Zoom of ERS-2/ENVISAT sampling pattern, showing alternating sampling of crossover points. Colour denotes day of the cycle on which the track is sampled.

Figure 5.30. Altimeter tracks near Orkney. Red lines: TOPEX/Poseidon and Jason (Phase A). Blue lines: GFO. Green lines: ERS-2 and ENVISAT. Black circles show locations of data considered. Black cross marks target location.

Figure 5.31. Days between altimeter samples from altimeter indicated in Figure 5.30. Dashed lines indicate the dates of the launch of ERS-2 and GFO.

Figure 5.32. Standard deviation in the monthly mean Pelamis power, calculated from altimeter sampling patterns shown in Figure 5.31, against the monthly mean power from hindcast.

Figure 5.33. Altimeter tracks over South West England. Red lines: TOPEX/Poseidon and Jason (Phase A). Blue lines: GFO. Green lines: ERS-2 and ENVISAT. Black circles show locations of data considered. Black cross marks target location.

Figure 5.34. Days between altimeter samples from tracks indicated in Figure 5.33. Dashed lines indicate the dates of the launch of ERS-2 and GFO.

Figure 5.35. Standard deviation in the monthly mean Pelamis power, calculated from altimeter sampling patterns shown in Figure 5.34, against the monthly mean power from hindcast.

Figure 5.36. Altimeter tracks over Northern Portugal. Red lines: TOPEX/Poseidon and Jason (Phase A). Blue lines: GFO. Green lines: ERS-2 and ENVISAT. Black circles show locations of data considered. Black cross marks target location.

Figure 5.37. Days between altimeter samples from tracks indicated in Figure 5.36. Dashed line indicates the date of the launch of GFO.

Figure 5.38. Standard deviation in the monthly mean Pelamis power, calculated from altimeter sampling patterns shown in Figure 5.37, against the monthly mean power from hindcast.

Figure 6.1. Contour map of the correlation of winter mean wave height with NAO index (from Woolf et al, 2002).

Figure 6.2. Altimeter tracks near the hindcast point. Top left: TOPEX/Poseidon/Jason phase A. Top right: TOPEX phase B. Bottom left: GFO. Bottom right: ERS-2/ENVISAT. Concentric circles at 25, 50, 75 and 100km from hindcast point.

Figure 6.3. Scatter plot of collocated altimeter and model H_s .

Figure 6.4. (a) Difference in model and altimeter H_s against altimeter H_s . Black crosses: individual values; red circles: bin average. (b) Standard deviation of difference in H_s against altimeter H_s and fitted linear relationship.

Figure 6.5. (a) Circles: Individual monthly mean power; Line: Climatological monthly power. (b) Histogram of anomalies in monthly mean power and fitted normal distribution.

Figure 6.6. Annual mean Pelamis power and running 5, 10 and 20 year mean values.

Figure 6.7. Correlation of monthly mean power level with NAO index and 95% error bars.

Figure 6.8. Linear regression over various periods of monthly power anomalies on NAO anomalies.

Figure 6.9. Linear regression of annual power anomalies against annual NAO anomalies.

Figure 6.10. Linear predictor for annual mean Pelamis power from NAO anomaly.

Figure 6.11. Annual NAO anomaly with 5, 10 and 20 year moving average.

Figure 6.12. 5 and 20 year moving averages of simulated anomalies in annual mean Pelamis power from FAR(1) model.

Figure 7.1. Probability density function of the generalised Pareto distribution for scale parameter $\sigma = 1$ and various values of shape parameter ζ .

Figure 7.2. Probability that the N -year return value is not exceeded in N years.

Figure 7.3. Percentage of samples with no ML solution against ζ for $n = 25$ (left) and $n = 50$ (right).

Figure 7.4. Scatter plot of $\tilde{\xi}$ against $\hat{\xi}$ for 1000 samples of size $n = 25$ for $\xi = -0.5$ and $\sigma = 1$.

Figure 7.5. Critical value $\tilde{\xi}_c$ against sample size n .

Figure 7.6. Normalised bias and RMS error in quantile estimates at probabilities of 0.99 (top) and 0.999 (bottom) for $n = 25$.

Figure 7.7. As previous figure, but for $n = 50$.

Figure 7.8. As previous figure, but for $n = 100$.

Figure 7.9. As previous figure, but for $n = 200$.

Figure 7.10. As previous figure, but for $n = 500$.

Figure 7.11. Scatter plots of HM estimators against LM estimators for various values of ξ (increasing left to right) and $n = 25$ (top row), 50 (second row), 100 (third row) and 200 (bottom row).

Figure 7.12. Locations of the 14 buoys used in this section.

Figure 7.13. (a) 3-hour average H_s (black crosses), daily mean value (red circles), Fourier expansion of daily mean (cyan line). (b) Daily standard deviation in H_s (red circles), Fourier expansion of daily standard deviation (black line).

Figure 7.14. (a) Storm peaks identified using declustering criteria $p = 0.75$ and $\tau = 1.5$ days. (b) Normalised values of storm peaks from (a).

Figure 7.15. (a) Correlation between declustered peaks exceeding the variable threshold for various values of declustering criteria p and τ . (b) Average number of peaks for various values of declustering criteria p and τ .

Figure 7.16. Threshold plots using the PWM and LM estimators, for annual data from buoy 46002.

Figure 7.17. Threshold plots for data from buoy 46002. Thin solid line: estimates without resampling. Bold line: mean of modified bootstrap estimates. Dotted line: 95% confidence bounds from modified bootstrap trials.

Figure 7.18. Diagnostic plots for model fitted using LM estimators with a threshold of 6.2m. Left: Probability plot; right: quantile plot.

Figure 7.19. Storm peak H_s against day of year for buoy 46005. Dashed lines indicate seasonal boundaries.

Figure 7.20. Threshold plots for data from buoy 46005, September-October. Solid lines: mean bootstrap value; dotted lines: 95% confidence bounds. Dashed line on upper right plot is the maximum observed H_s between September-October.

Figure 7.21. Probability and quantile plots for data from buoy 46005, Sep-Oct, using a threshold of 4.5m.

Figure 7.22. Probability and quantile plots for data from buoy 46005, Sep-Oct, using a threshold of 7.3m.

Figure 7.23. Threshold plots for annual data from buoy 46005. Solid lines: mean bootstrap value; dotted lines: 95% confidence bounds. Dashed line on upper right plot is the maximum observed H_s .

Figure 7.24. Probability and quantile plots for annual data from buoy 46005, using a threshold of 5.3m.

Figure 7.25. Percentage of data in each season relative to the season with the most data, for buoys 46028 (left) and 46041 (right).

Figure 7.26. (a) Mean number of storms exceeding threshold per month; (b) threshold; (c) estimated shape parameter; (d) estimated scale parameter. For all plots circles indicate estimates for a specific buoy and lines indicate the mean value over all buoys.

Figure 7.27. Distribution of storm peaks in the four case studies. Black circles: storm peaks from 50 year realisations. Dashed red lines: theoretical 0.9, 0.99 and 0.999 quantiles for each day. Solid red line: upper limit of distribution.

1. Introduction

One of the most important problems faced by society at present is the provision of low-carbon technology for energy production. In the United Kingdom, electricity supply accounts for around 20 per cent of green house gas emissions. Various studies have shown that wave energy has the potential to meet a significant proportion of UK electricity demand (e.g. Thorpe, 1992; Thorpe 1999; DTI, 2004). At present the wave energy industry is in its infancy, with a small number of devices at the commercial demonstration stage and many more at earlier stages of development.

Designs for wave energy converters (WECs) vary widely. There are shore-mounted oscillating water columns such as LIMPET (Wavegen, UK) and the Pico Wave Power Plant (Wave Energy Centre, Portugal) which have been operational for several years. A number of buoy-type point absorber devices are at advanced stages of pre-commercial development, such as Power Buoy (Ocean Power Technologies, USA), Aqua Buoy (Finevera, Canada), Archimedes Wave Swing (AWS Ocean Energy, UK) and Wavebob (Wavebob Ltd, Ireland). Wave Dragon (Wave Dragon ApS, Denmark), an over-topping device is also at the demonstration stage. Recently the world's first commercial wave farm has been commissioned in Aguçadoura, Portugal, consisting of three Pelamis P1A machines, manufactured by Pelamis Wave Power Ltd, each rated at 750 kW.

As the industry grows, an important factor for the development of wave energy farms will be the accurate quantification of the power production. This research addresses the topic of assessing the available wave energy at both regional and site-specific levels.

1.1 The need for wave energy resource assessment

The process of wave energy resource assessment can be split into two stages. The first stage is comparative: to select the best sites for development. There are many factors other than the wave resource which influence site selection, such as availability of a grid

connection, proximity to ports or appropriate sea bed conditions. These factors can often be limiting, but without an adequate wave resource a project is not viable.

The second stage is quantitative: to accurately determine the resource at a given site. A detailed understanding of the wave energy resource is necessary to assess the economic viability of a wave energy project. Since waves are a free resource, the cost of a wave energy project is determined by the capital and operating costs. The revenue from a wave farm is determined by the electrical power produced, which is in turn dependent on the wave conditions. The profitability of the project and the cost to produce energy are set by the difference between the revenue and the capital plus operating costs.

Like other sources of renewable energy, ocean waves are a variable resource, impossible to predict precisely. This increases the risk associated with the development of a wave energy farm, since the upfront cost is large and the return is variable and imprecisely known. It is therefore necessary to calculate the average power produced, the variability in power production and confidence bounds on these estimates.

Another important issue for wave energy developers is survivability. Wave energy converters must be designed to withstand the most severe conditions expected in their lifetime. Since it is not possible to predict the severity of a storm at a certain location, more than a few days in advance, a probabilistic approach must be taken to determine design conditions which represent an acceptable level of risk.

1.2 Research aims

The primary aim of the work presented in this thesis is to provide the information on the wave resource necessary for the economic assessment of a wave energy project. The stand point of a developer is taken, who wishes to choose the best site for a wave energy project in terms of energy yield and to know the accuracy of the predicted yield estimate. It is assumed that the response of a WEC in a given sea state has been specified by the manufacturer. Since this is a relatively new field, with the first wave farms in planning at the moment, this research sets out to answer some basic questions:

What wave data is available, how accurate is it and how should the various types of data be used to maximise their usefulness? What is the accuracy of estimated historic WEC yield over monthly, annual and multi-year periods? How variable is the resource and how does variability affect the prediction of future WEC yield?

Wave energy developers also need an estimate of the extreme wave conditions which can be expected at a site. Extreme wave prediction is a well established subject and remains an active area of research. The topic is broad in scope and it is not the intention of this research to cover all aspects. Instead two problems are focused on. It is common practice for extreme wave conditions to be modelled using the generalised Pareto distribution. Numerous methods have been proposed to estimate the parameters of this distribution, but no consensus exists on which is the most appropriate for extreme wave analysis. The second topic considered is the effect of seasonal variability on annual extremes. Some authors have suggested that models which account for seasonal variability should be used in preference to non-seasonal models. However, it has not been conclusively demonstrated that these model are more accurate in practice. This research will compare the use of seasonal and non-seasonal models in practical situations.

The specific objectives of the research are:

- (A) To develop procedures for using satellite altimeter wave measurements to produce spatial maps of WEC yield, for first stage site selection, and to establish the accuracy of the derived estimates.
- (B) To quantify the accuracy of estimates of the historic WEC yield at a specific site which can be achieved using the data that is currently available.
- (C) To determine the limitations on the accuracy of predictions of future WEC yield which are imposed by the variable nature of the resource and potential effects of climate change.
- (D) To compare the performance of different estimators of the generalised Pareto distribution, and determine which is most appropriate for use in extreme wave predictions.
- (E) To determine whether it is preferable to use seasonal or non-seasonal models for extreme wave predictions.

In the remainder of this introductory chapter the fundamental concepts necessary for this research are presented. We start by discussing the characteristics of the wave resource and how the sea surface is described. We go on to discuss how the power produced by a WEC in a given sea state is estimated. This is followed by a brief review of the previous work on wave energy resource assessment and a discussion of how the research presented here develops on this work. We finish by giving an overview of work presented in subsequent chapters in order to fulfil objectives listed above.

1.3 The nature of the resource

Understanding the nature of the wave resource is essential when discussing the yield from a wave energy converter. The important areas to us are the measurement of waves and the analysis and interpretation of the data. This section presents the standard concepts and definitions used to describe waves, which are fundamental to the work in subsequent chapters. For a more detailed introduction to waves in an engineering context the reader is referred to Tucker and Pitt (2001). Introductions to the generation of waves by the action of the wind on the sea surface are given by Young (1999a) and Janssen (2004). A thorough overview of the mathematical description of wave dynamics and modelling is given by Komen et al (1994).

The aspects of the wave resource which are most important to emphasise here are the random nature of the sea surface and the variability of sea states on multiple scales. These factors dictate the accuracy to which wave parameters can be measured and how to best combine various sources of wave data in order to estimate energy yield.

1.3.1 The wave spectrum

For many purposes the sea surface elevation, η , at location (x, y) and time t , can be considered as a linear superposition of a large number of sine wave components:

$$\eta(x, y, t) = \sum_{n=1}^{\infty} A_n \sin[k_n(x \cos \theta_n + y \sin \theta_n) - \omega_n t + \phi_n] \quad [1.1]$$

where

A_n is the amplitude of the sine wave component

$k_n = 2\pi / \lambda_n$ is the wave number and λ_n is the wavelength

$\omega_n = 2\pi f_n$ is the angular frequency and f_n is the frequency

θ_n is the direction

ϕ_n is the phase

It is normally assumed that phases are distributed randomly over $[0, 2\pi]$ with uniform probability density, and that frequency and wavelength are related by the linear dispersion relationship

$$\omega_n^2 = gk_n \tanh(k_n d) \quad [1.2]$$

where g is acceleration due to gravity and d is the water depth.

The directional variance spectrum $S(f, \theta)$ describes how the energy in the wave field is distributed with frequency and direction. For small δf and $\delta \theta$ we have

$$\sum_f^{f+\delta f} \sum_\theta^{\theta+\delta \theta} \frac{1}{2} A_n^2 = S(f, \theta) \delta f \delta \theta \quad [1.3]$$

That is, the spectral density is the sum of the variances of the individual sinusoidal components over a given frequency and directional range.

The directional spectrum can be decomposed into two functions, one representing the total energy at each frequency, and the other describing how the energy at each frequency is distributed with direction:

$$S(f, \theta) = S(f)D(f, \theta) \quad [1.4]$$

$S(f)$ is called the omnidirectional spectrum (or sometimes the frequency spectrum) and is related to the directional spectrum by

$$S(f) = \int_{-\pi}^{\pi} S(f, \theta) d\theta \quad [1.5]$$

$D(f, \theta)$ is the directional spreading function and satisfies two properties:

$$1. \int_{-\pi}^{\pi} D(f, \theta) d\theta = 1 \quad [1.6]$$

$$2. D(f, \theta) \geq 0 \text{ over } [-\pi, \pi] \quad [1.7]$$

It is a slight abuse of notation to use S to denote both directional and omnidirectional spectral density, but it is usually clear from the context which function S denotes.

In assuming linearity in the above, it is implicitly assumed that ocean surface waves have low amplitude compared to their wavelength. This is a surprisingly good model for ocean waves and forms the basis for most stochastic wave analysis in ocean engineering. Nevertheless, linear wave theory assumes that the ocean waves are solutions of linear equations which they are not. It is possible to give a rigorous derivation of the wave spectrum by assuming that the ocean surface is a solution to the full nonlinear equations for surface waves. Linear wave theory is then recovered as the leading order term of the full solution (Kahma et al, 2005). Nonlinear effects become significant in steep seas and in shallow water, and are essential for understanding the evolution of the wave spectrum (Hasselmann, 1962), but for the majority of the following work linear theory is sufficient.

The technique used to estimate the directional or omnidirectional spectrum depends on the type of measuring device. The simplest case is that of an instrument recording a time series of the vertical displacements of the sea surface, such as a buoy or wave-staff. In this situation a Fast Fourier Transform is used to estimate the energy of wave components at each frequency. The procedure is described by Tucker and Pitt (2001).

The case for the directional spectrum is more complicated. None of the instruments used today can provide all the information needed to make a robust estimate of the complete directional spectrum (Kahma et al, 2005). It is necessary to make some assumptions

about properties of the directional spectrum in order to estimate it from measured data. Moreover, these assumptions differ depending on the instrument and method used. An introduction to the various analysis methods available is given by Benoit et al (1997) and more detail can be found in Kahma et al (2005).

It is sometimes useful to assume standard shapes for the wave spectrum and directional distribution. Various forms have been proposed over the years, mostly derived empirically but with some theoretical guidance. The most commonly used are the Pierson-Moskowitz spectrum, (which in its generalised form is also known as the Bretschneider spectrum) and the JONSWAP spectrum. Details of these and others can be found in Tucker and Pitt (2001).

1.3.2 Wave parameters

The wave spectrum can be summarised to a reasonable accuracy using a small number of parameters. The most important are a measure of average wave height and period, followed by descriptors of directional properties. Wave height and period parameters are defined in terms of moments of the omnidirectional spectrum. The n^{th} moment of the spectrum is defined as

$$m_n = \int_0^{\infty} f^n S(f) df \quad [1.8]$$

Wave height and period parameters are defined as follows:

$$\text{Significant wave height} \quad H_s = 4\sqrt{m_0} \quad [1.9]$$

$$\text{Energy period} \quad T_e = m_{-1} / m_0 \quad [1.10]$$

$$\text{Mean period} \quad T_m = m_0 / m_1 \quad [1.11]$$

$$\text{Zero-crossing period} \quad T_z = \sqrt{m_0 / m_2} \quad [1.12]$$

$$\text{Peak period} \quad T_p = 1 / f_p \quad [1.13]$$

where f_p is the frequency at which $S(f)$ takes its maximum value.

These definitions have a natural interpretation: m_0 is the variance of the sea surface elevation and hence H_s as defined in equation 1.9 is 4 times the RMS displacement of the sea surface. The factor 4 arises for historical reasons. When significant wave height was estimated by eye it was common practice to use the symbol H_s to denote the average height of the highest 1/3 zero up- or down-cross waves. In narrow-band seas this definition is approximately equivalent to the spectral definition. Some authors use the symbols $H_{1/3}$ and H_{m0} to distinguish between the two definitions of significant wave height. In this work H_s always denotes the spectral definition given in equation 1.9.

The definition of the energy period stems from the formula for the power transported per meter of crest length by waves in deep water (Tucker and Pitt, 2001):

$$P = \rho g^2 H_s^2 T_e / 64\pi \quad [1.14]$$

The mean period is simply the reciprocal of the mean frequency of the spectrum. The zero-crossing period is the approximately equal to the average time between waves crossing the mean sea level in an upward direction. This was first shown by Rice (1944-45) for the case of a random Gaussian signal, which is a good approximation for ocean waves.

The mean direction, $\theta_m(f)$, and directional spread, $\sigma(f)$, at each frequency are given by:

$$\theta_m(f) = \text{ATAN2} \left[\int_{-\pi}^{\pi} D(f, \theta) \sin(\theta) d\theta, \int_{-\pi}^{\pi} D(f, \theta) \cos(\theta) d\theta \right] \quad [1.15]$$

$$\sigma(f) = \left[\int_{-\pi}^{\pi} D(f, \theta) (\theta - \theta_m)^2 d\theta \right]^{1/2} \quad [1.16]$$

where $\text{ATAN2}(y, x)$ is the four-quadrant inverse tangent function, which uses logic on the signs of x and y to resolve the 180° ambiguity in direction. The directional spread can be interpreted as the standard deviation of the directional distribution.

An average direction and spread over the whole spectrum can be defined as follows

$$\text{MDIR} = \text{ATAN2} \left[\int_0^{\infty} S(f) \sin(\theta_m(f)) df, \int_0^{\infty} S(f) \cos(\theta_m(f)) df \right] \quad [1.17]$$

$$\text{SDIR} = \frac{\int_0^{\infty} S(f) \sigma(f) df}{\int_0^{\infty} S(f) df} \quad [1.18]$$

1.3.3 Uncertainty and variability

Waves on the sea surface can be considered as a random process in space and time, the properties of which vary at multiple scales. Any measurement of the sea surface is finite in extent, both in the area and duration of measurement and therefore only records a finite number of waves from a theoretically infinite population. This means that derived wave statistics have an associated uncertainty, known as sampling variability. The longer the duration of a record or the larger the area it covers, the closer the measured value will be to the true value. However, wave conditions are non-stationary so averaging periods or areas are a compromise between the statistical stability of an estimate and adequate sampling of the changes in wave conditions.

This raises the question: Over what periods does it make sense to estimate average conditions and hence WEC yield. At a fixed location, the temporal scales at which wave conditions vary can be split into the following categories: sampling variability, synoptic, seasonal, interannual and climatic. Synoptic variability refers to variability in wave conditions caused by passing weather systems, typically on the scale of a few hours to a few days. Weather is a chaotic process and is unpredictable more than a few days in advance, but we may expect the mean wave conditions to be stable over the period of month, say. It therefore makes sense to examine the variations in monthly mean WEC power throughout the year.

The mean wave conditions over a given month will vary from year to year. Similarly, the annual mean will vary from year to year. It is therefore sensible to examine

interannual variations in the wave climate. Finally, long-term multi-year mean values may vary with changes in climate, both natural and anthropogenic, so this must be taken into account as well. It is therefore necessary to examine both long and densely sampled records of wave conditions in order to make projections of the yield from a wave farm at a specific site.

Wave conditions are also variable on multiple spatial scales. In the open ocean wave conditions can be considered stationary over large distances, whereas close to the coast spatial variability increases due to sheltering and bathymetric effects. Therefore, when comparing sites it is necessary to have an adequate sampling of the spatial variability of wave conditions.

No one source of wave data has the accuracy, spatial and temporal coverage and sampling that we require to choose the best sites and accurately estimate the energy yield for a specific site. Understanding the variability in the wave conditions is necessary in order to assess the accuracy of each type of data and to combine various sources of wave data to maximise their value. Chapter 2 describes the most important sources of data for wave energy resource assessment, along with methods to quality check the data, sampling properties and the short scale spatial and temporal variability of the wave field.

1.4 Estimating WEC power

The response of a wave energy converter to a given sea state is dependent on the full directional spectrum. However, for the purposes of estimating the yield it is useful to describe the response in terms of a small number of parameters. Currently, few manufacturers of WECs publish details on the response of their device, partly due to commercial reasons and partly because many devices are still at the developmental stage. For those manufacturers that have published details of the power produced by their machine, it has been common practice to specify it in terms H_s and T_e , in a ‘power matrix’. Wave height and period parameters are natural choices for the initial parameterisation of the device response. The energy period is used in preference to

other period parameters since it is less sensitive than T_m and T_z to the high frequency end of the spectrum at which there is little useful energy. And whilst T_p is a useful parameter to describe theoretical spectra, it is less stable than integral parameters when estimated from measured data.

The power matrix for the Pelamis P1A machine is given in Table 1.1. The power response is calculated from a numerical model of the Pelamis using Bretschneider spectra. It has been validated using a combination of scale-model tank tests and sea trials with a full scale prototype.

		T_e [s]																	
		5.0	5.5	6.0	6.5	7.0	7.5	8.0	8.5	9.0	9.5	10.0	10.5	11.0	11.5	12.0	12.5	13.0	
H_s [m]	0.5	Idle	Idle	Idle	Idle	Idle	Idle	Idle	Idle	Idle	Idle	Idle	Idle	Idle	Idle	Idle	Idle	Idle	
	1.0	Idle	22	29	34	37	38	38	37	35	32	29	26	23	21	Idle	Idle	Idle	
	1.5	32	50	65	76	83	86	86	83	78	72	65	59	53	47	42	37	33	
	2.0	57	88	115	136	148	153	152	147	138	127	116	104	93	83	74	66	59	
	2.5	89	138	180	212	231	238	238	230	216	199	181	163	146	130	116	103	92	
	3.0	129	198	260	305	332	340	332	315	292	266	240	219	210	188	167	149	132	
	3.5		270	354	415	438	440	424	404	377	362	326	292	260	230	215	202	180	
	4.0			462	502	540	546	530	499	475	429	384	366	339	301	267	237	213	
	4.5			554	635	642	648	628	590	562	528	473	432	382	356	338	300	266	
	5.0				739	726	731	707	687	670	607	557	521	472	417	369	348	328	
	5.5					750	750	750	750	750	737	667	658	586	520	496	446	395	355
	6.0						750	750	750	750	750	750	711	633	619	558	512	470	415
	6.5							750	750	750	750	750	750	743	658	621	579	512	481
	7.0								750	750	750	750	750	750	750	676	613	584	525
	7.5									750	750	750	750	750	750	750	686	622	593
	8.0										750	750	750	750	750	750	750	690	625

Table 1.1 Power matrix for the Pelamis, values in kW.

For real wave spectra there will be some deviation in spectral shape and directional spreading from theoretical forms. This will result in differences in power produced from the values specified in the power matrix. A point absorber type device may be relatively insensitive to directional effects, since it is axisymmetric, but the shape of the frequency spectrum may still have some effect. In contrast the Pelamis has both a pitch and sway response to incoming waves and is therefore more sensitive to directional effects.

The assumption that WEC response can be parameterised solely in terms of H_s and T_e may be unrealistic, but at this stage of the industry, where experimental or hard data does not exist, it is a necessary approximation. Kerbiriou et al (2007) have shown that partitioning directional spectra into separate sea states improves accuracy when estimating the performance of the SEAREV device, compared to using a simple parametric representation of the whole spectrum. Initial modelling for the Pelamis has

shown that the effect of parameterisation is less important for higher H_s , since spectra tend toward standard shapes in larger seas. Modelling has also shown that Pelamis generates more power in spread seas, so not factoring this into the power matrix may result in conservative values.

Once further data has been gathered on the effects of changes in spectral shape and directional spreading, this could be factored in to the power table in a probabilistic manner. For each H_s and T_e , a weighted mean power could be given, based on the occurrence of different spectral shapes (see discussion in Section 5.1)

1.5 Research overview and relation to previous studies

Numerous studies on the wave resource have been published since the 1970s when interest began in ocean waves as a source of energy. Most studies have focused on assessing the wave power climate rather than the yield from a specific device.

A number of atlases have been created showing the geographic distribution of wave energy on various scales. Recent examples include the European Wave Energy Resource Atlas (Pontes et al, 1997), the Atlas of UK Marine Renewable Energy Resources (DTI, 2004), the Sea Power South West Review (Metoc Plc, 2004), and the Accessible Wave Energy Resource Atlas, Ireland (ESBI, 2005). These give annual and seasonal mean values of wave power (equation 1.14) for offshore locations, based on a few years of data from numerical wind-wave models. Validation is limited for these atlases and they do not give confidence bounds on estimates of mean power. They are intended primarily for use in strategic level considerations, i.e. identifying areas suitable for wave energy development, rather than predicting the potential energy yield at a specific site. The ability to produce strategic level maps showing the estimated yield for a specific device, quickly and cost effectively for any location in the world, would aid the development of the wave energy industry.

The first objective of this research addresses this need. The choice for spatial wave data is between wave model data and satellite altimeter data. Model data is normally

purchased on a point-by-point basis and spatial mapping of the wave resource can be costly using model data. Altimeter data is well suited to spatial mapping of oceanographic properties and its use for mapping wave climate has been demonstrated by numerous authors. Previous studies of wave climate using altimeter data have considered H_s only. To estimate the power produced by a WEC an estimate of wave period is required as well. Existing algorithms for estimating wave period from altimeter data are not suitable for estimating WEC power, since they do not correctly reproduce the joint distribution of wave height and period. This research will develop on previous studies in the following ways:

- In Chapter 3 a new algorithm is developed for estimating wave period from satellite altimeter data, which is capable of reproducing the joint distribution of wave height and period.
- In Chapter 4 it is demonstrated that the power produced by a WEC can be reliably estimated from altimeter measurements of H_s and the new algorithm for altimeter T_e . The accuracy of long-term mean values of WEC power from altimeter measurements is calculated. The limitations imposed by the variability in wave conditions and the sampling patterns of satellite altimeters are investigated.

The result is a tool which can be used to create spatial maps of not just wave conditions, but also of the estimated yield of a WEC with quantified accuracy, at any location in the world. These altimeter maps provide a cost-effective alternative to using model data for strategic level planning.

The second stage of wave energy resource assessment is to provide detailed information on the wave conditions at a chosen site. The method used to estimate the long-term resource at a particular site is similar to that used by the wind energy industry to predict the yield of a wind farm, known as Measure-Correlate-Predict (MCP). It is rare that at a site of a proposed wave energy development there will be an existing long term dataset. In the MCP procedure short-term measurements recorded at the site of a proposed development (the predictor site) are correlated with concurrent measurements taken at a nearby reference site for which long-term data exists. This calibration is then applied to the historic data at the reference site to estimate the historic climate at the predictor site.

In anticipation that the MCP procedure could be used for site assessment in the wave energy industry, Halliday and Douglas (2008) have presented a survey of the long-term wave data available in UK waters. They note that there is relatively little in-situ data available for the most energetic locations and that it would aid wave energy development if coverage was increased in these areas.

Due to the lack of long-term measurements as a reference dataset, some authors have proposed the use of data from numerical wind-wave models as a long-term reference (e.g. Mollison, 1994; Barstow et al, 1998; Pitt, 2006a). Mollison (1994) proposed that offshore data from ocean-scale models could be used as the boundary conditions of a smaller scale shallow-water wave model, which is used to estimate the wave conditions at the site of interest. Since wave model data are estimates rather than measurements, Mollison (1994) suggests that the model data should be calibrated against nearby buoy measurements before use. Barstow et al (1998) take a similar approach, but use satellite altimeter measurements to calibrate the offshore wave model data, before using it to drive a nearshore model. Pitt (2006a) compares estimates of wave power from model data to estimates from buoy measurements at the site of the proposed Wave Hub site in south west Britain. He finds that the mean values are generally quite close, but that sometimes the model fails to reproduce long-period swell energy measured by the buoy.

Crucially though, the issue of uncertainty of wave energy yield predictions necessary for the economic assessment of a wave energy project has not been addressed. This is in part because until recently the industry has not required such detailed calculations. With the first full scale devices being deployed and rapid expansion of the wave energy industry foreseen over the next decade, the problem of making accurate yield predictions with quantified uncertainty needs to be considered. Objective B of this research addresses this point. In Chapter 5 the calibration of wave model data is discussed and a method is proposed to calculate confidence bounds for estimates of WEC yield from calibrated model data. This is compared to the accuracy it is possible to achieve using in-situ and satellite altimeter measurements.

An assumption central to the MCP procedure is that weather patterns will not change significantly in the future, and the historic data provides a good estimate of the available resource at a site. Objective C of this research addresses the validity of this assumption.

Chapter 6 reviews studies of the long-term variability in wave climate and potential effects of anthropogenic climate change. A model is proposed to account for both historic variability in the resource and the potential effects of climate change at a site in Northern Scotland. This is used to examine the accuracy of predictions of WEC yield.

Chapter 7 discusses the estimation of extreme wave conditions at a site. A review of the methods proposed to estimate extreme values of H_s is presented, and the motivation for the Peaks Over Threshold (POT) / Generalised Pareto Distribution (GPD) model is described. Numerous methods have been proposed to estimate the parameters of this distribution, but no consensus exists on which is the most appropriate for extreme wave analysis. This research attempts to answer this question. In Chapter 7 the performance of different estimators of the generalised Pareto distribution is compared in order to determine which is most appropriate for use in extreme wave predictions (Objective D).

An assumption made in classical extreme value modelling is that the data being modelled are stationary. This assumption is not strictly true for wave data because of seasonal and climatic variability. It has been suggested by some authors that extreme value models which account for seasonal variability should be used in preference to non-seasonal models. However, it has not been conclusively demonstrated that these model are more accurate in practice. In Chapter 7 a simulation study is conducted to compare the use of seasonal and non-seasonal models in realistic situations (Objective E).

1.6 Research limitations

Throughout this work we will use the power matrix of the Pelamis, given in Table 1.1, as an example. The results should be directly transferable to other WECs in deep water and intermediate depths, by substituting the power matrix. The case for shoreline devices may be slightly more complicated due to the increased non-linearities in shallow water. This may necessitate a more detailed analysis of the nearshore model data than presented in Chapter 5, but the main results on uncertainty, variability and predictability of WEC yield should hold.

The uncertainty that arises due to the parameterisation of the Pelamis response in terms of H_s and T_e will not be considered in depth, since this has not been quantified by the manufacturer. A brief discussion is given in Section 5.1.3 of a method to factor this uncertainty into the estimated error bounds for the estimated energy yield.

The effects of interactions between WECs within a wave farm are also not considered in this work. The results can be considered to apply to a single WEC and can be generalised to apply to a whole array when information on interaction effects becomes available.

It is possible that through improved wave modelling techniques, the confidence bounds on estimates of both energy yield and extremes could be improved. Ocean-scale and nearshore wave modelling are both large and active areas of research, which it is not practical to consider here. This research considers the accuracy which is achievable with the data which is currently available from meteorological agencies and commercial companies.

2. Wave Data Sources

There are three main types of wave data which are commonly used at present. These are: in-situ measurements, satellite remote sensing and numerical wave models. Each type of data has different characteristics and is subject to certain limitations. The best picture of the wave resource is obtained from an integrated use of the three types of data.

In the introduction it was mentioned that the wave resource is spatially and temporally varying on multiple scales. In-situ, satellite and model data all provide wave information about different scales of the resource. In-situ measurements typically provide a temporal average of waves at a point or over a small area. Satellite measurements provide a near-instantaneous average of waves over an area of several square kilometres. Wave models provide an estimate of the wave spectrum which can be interpreted as an average over both space and time.

To make sense of comparisons between different types of wave data it is important to account for the natural variability in the wave field as well as the characteristics of the data source itself. Moreover, these uncertainties and variabilities influence the choice of statistical techniques used to compare and combine different types of data. In this chapter we provide details of the main characteristics of each data source, necessary for comparisons with other data.

Of the many types of in-situ instruments capable of measuring waves, we focus on wave-buoys here. An overview of the different types of in-situ instruments is given by Tucker and Pitt (2001). Although fixed instruments can provide high quality wave data, they are less likely to be deployed at a wave energy site, due to the cost of installing a suitable platform to mount the device. Details of a recent intercomparison study of fixed platform instruments are given by Forristall et al (2004).

The use of an Acoustic Doppler Current Profiler (ADCP) has also been proposed for wave monitoring at wave energy sites. The ADCP is designed to measure current speed

and direction through the water column, but is capable of making accurate directional wave measurements as well. Details of a validation study of wave measurements from an ADCP are given by Strong et al (2000). The use of ADCPs at wave energy sites may be limited by water depth. If the range of the sensor to the sea surface is too great then the strength of the returned acoustic pulse may be too weak to measure waves. Mounting an ADCP on a sub-surface buoy has been suggested as a solution, but this method is experimental at present (Pedersen and Siegel, 2008). There are also concerns about the quality of measurement when the water column becomes aerated due to wave breaking (Tucker and Pitt, 2001).

Various types of radar systems can also be used for wave measurements (such as marine X-band radar and high-frequency (HF) radar). An overview of these is given by Kahma et al (2005). These can provide high resolution directional measurements over a wide area, although the accuracy of measurements is dependent of the ratio between the wave frequency and radar frequency. Radar systems are also typically much more expensive than a wave buoy, with a land-based high-frequency radar costing upwards of £100k to install compared to around £20k for a small wave buoy.

Pitt (2006b) makes a comparison of buoys, ADCP and HF radar for making wave measurements at the Wave Hub site. He recommends the use of wave buoys as the most appropriate, since they are accurate, well-proven and relatively easy to deploy.

There are two types of satellite borne instruments used to measure waves: the radar altimeter and synthetic aperture radar (SAR). Of the two types of remote sensing data, SAR provides the only direct source of spectral and directional information. Several inversion schemes exist to extract wave spectra and parameters from SAR data (e.g. Collard et al, 2005; Schulz-Stellenfleth et al, 2005 & 2007) and SAR spectra are routinely assimilated into operational wave models (e.g. Abdalla et al., 2006). However, SAR can only measure the low frequency part of wave spectrum. Violante-Carvalho et al (2005) note that the high-frequency cut-off is sea state dependent, but in general, waves shorter than 150–200 m (around 0.1Hz for deep water linear waves) propagating parallel to the satellite track are not mapped directly by SAR. Moreover, SAR data are sparse both temporally and spatially, with data acquired at intervals of 200 km along

track for ERS-1, ERS-2 and ENVISAT. Therefore SAR data will not be considered further in this study.

In contrast to SAR, altimeter data is collected continuously as the satellite orbits, giving higher spatial resolution. Altimeters are capable of making accurate measurements of H_s and a reasonable estimate of wave period, but they do not provide any information on spectral shape or directional properties of the wave field and they cannot measure close to the coast (although future missions may not have this restriction). However, the global coverage and long-record of measurements make altimeter data a valuable source of wave information.

Data from numerical wave models are estimates rather than measurements. Nonetheless, modern models are of sufficient accuracy that modelled wave data can be used to calculate accurate wave energy statistics. Global hindcasts over long periods at high spatial and temporal resolution are available from several meteorological institutions and commercial companies. Such hindcast data is likely to be used as the long-term dataset for many wave MCP studies. However, quantifying the errors and uncertainties in model data is an important and non-trivial problem, with model biases and random errors non-stationary in both space and time (see Section 5.1). In Section 2.3 we give a very brief introduction to the current generation of wave models and qualitatively describe the form of model errors.

Finally, a source of wave data that is not considered here, but deserves mentioning, is voluntary observing ship (VOS) data. Officers aboard voluntary observing ships provided visual estimates of wave parameters worldwide starting from 1856. These data are useful for long-term climatological studies (e.g. Gulev and Grigorieva, 2004 & 2006) but are much less appropriate for calculating wave energy statistics. The data are reasonably dense along major shipping routes but the coverage is poor outside these areas and particularly in the Southern Ocean. Moreover, they are subject to larger uncertainties and biases than other sources of wave data. Comparisons with altimeter data show that even for well-sampled regions, the occurrence of high waves is underestimated in the VOS data, since ships intentionally avoid rough seas (Gulev et al, 2003).

2.1 Wave measurements from moored buoys

Measurements from buoys are often taken as a ‘truth’ to which other measurements are compared. Buoys are capable of making accurate measurements of waves, but are subject to certain limitations which it is important to be aware of. The sea surface displacement is inferred from the motions of the buoy, measured by accelerometers, tilt sensors and compasses. The accuracy of the inferred wave motions is dependent upon the buoy response, the accuracy of the transfer function (from buoy motion to wave motion) and the sensor accuracy. One advantage to using buoys to measure waves is that the sea surface is usually well defined – it is the point at which the buoy floats (although in high seas it is possible for the buoy can be dragged through wave crests). In rough conditions spray in the air or bubbles in the water can cause problems with devices that measure the waves from below or above the surface, such as ADCP or lasers.

There are also some innate differences in the measurements of waves made by buoys compared to a fixed instrument. Small wave buoys essentially follow the particle motions of the water surface whereas fixed instruments such as a laser sensors or capacitance wire gauges measure the spatial profile of the waves. Particle-following and fixed measurements are known as Lagrangian and Eulerian measurements respectively, referring to the frame of reference in which measurements are made. For low amplitude waves the differences between Lagrangian and Eulerian measurements are small, but in steep waves the differences can be significant (James, 1986; Longuet-Higgins, 1986). There are pros and cons to both types of measurements. A Lagrangian device measuring the orbital motions of a water particle at a particular frequency will attribute all the wave energy to this frequency whereas an Eulerian device will distribute some of the energy among the harmonics of the orbital frequency (Rademakers, 1993; Joosten, 2006a). On the other hand Lagrangian devices are not capable of measuring some non-linear aspects of the wave profile (James, 1986; Longuet-Higgins, 1986; Forristall, 2000, Prevosto et al 2000). The results of an intercomparison study of Eulerian measuring devices are presented by Forristall et al (2004).

This section discusses topics relevant to most types of wave buoys, but focuses on NDBC buoys and Datawell Waveriders since the majority of buoy data used in this study comes from these sources. Also the focus will be on non-directional parameters since we are only using H_s and T_e for the estimation of Pelamis power.

2.1.1. Instrumental characteristics

2.1.1.1. Buoy response

The buoy response is governed by the size and shape of the buoy and its mooring. Designs of buoys vary, with dimensions ranging from small spherical buoys less than one meter in diameter, to large rectangular hulled buoys around 12m in length. Small buoys have the best surface following properties, with a spherical buoy 2m or less in diameter having effectively unity response for waves up to about 0.5Hz (Tucker and Pitt, 2001). For larger buoys the response to shorter wavelengths is damped and the wave motions must be indirectly estimated through the Response Amplitude Operator (RAO) of the buoy (see e.g. Steele et al, 1995; Barrick et al 1989). Meteorological institutions implementing wave measurement programs often require simultaneous measurements of winds (and other parameters) with waves, therefore the buoy size will be a compromise between a compact shape for good surface following properties and stability required for mounting an anemometer.

2.1.1.2. Moorings

Moorings can affect the response of the buoy, by restricting its range of motion. If the mooring does not have sufficient flexibility it is possible for the buoy to be dragged through or around wave crests (Allender et al, 1989). Joosten (2006a, 2006b) discusses the need for elastic moorings for wave buoys. He shows that for waves above the mass-spring resonance frequency, f_0 , of the rubber cord and buoy combined the buoy motions are not restricted by mooring forces, but for frequencies lower than f_0 the buoy does not perfectly follow the wave and heave energy is spread over a wide range of frequencies. For a Waverider buoy with the manufacturer's specified elastic mooring f_0 is around 0.05Hz where there is very little energy in most wave spectra.

Nicalsen and Simonsen (2008) discuss a case where a non-elastic mooring used on a Waverider buoy caused an apparent semi-tidal variation in the measured wave-height time-series. They concluded that this was a result of not using a length of compliant

rubber cord in the moorings, as recommended by the manufacturer. Steele (1996) discusses Doppler effects on buoy measurements in the presence of currents. He notes that significant wave height is not affected, but there can be shifts in spectral energy at high frequencies and changes in mean wave direction, relative to that which would be observed in a frame of reference relative to the current.

2.1.1.3. Sensors

Several types of sensor are commonly used in wave buoys to measure heave, tilt, and direction. These range from vertically stabilised accelerometers such as Datawell's HIPPY sensor, solid state accelerometers such as the Motion Reference Unit (MRU) manufactured by Seatex, to accelerometers which infer their motion from Doppler shifts in Global Positioning Satellites' (GPS) signals. Until recently the industry standard for offshore recording has been Datawell's HIPPY sensor (Tucker and Pitt, 2001). The sensor contains a sphere of water in which a horizontal disc is suspended. An accelerometer is mounted on the disc and the compound pendulum formed by the water and the disc is adjusted to have a natural period of either 40 s or 120 s. The accelerometer is approximately critically damped and thus does not tilt significantly at wave frequencies so that its axis stays effectively vertical (Tucker and Pitt, 2001). Krogstad et al (1999a) note that the MRU has several advantages over Datawell's HIPPY sensor: it has no moving parts, small size, low weight and is not sensitive to rapid rotation under transport or to low temperatures. They compare measurements made by an MRU and a HIPPY sensor in the same buoy and show that the recorded heave and slope time series are indistinguishable. De Vries et al (2003) compare measurements from a HIPPY and a GPS sensor in the same buoy. They note that the sensors give close to identical heave measurements, with a correlation of 0.99994 in H_s .

2.1.1.4. Performance of Datawell's Waverider:

An evaluation of directional wave instrumentation available at the time was carried out in the Wave Direction Measurement Calibration Project (WADIC) (Allender et al, 1989). Measurements were conducted in the North Sea over a 3 month period covering diverse conditions, with H_s exceeding 5m in 9 separate storms and exceeding 10m in one storm. There were also 5 separate swell events where T_p exceeded 15s. Many cases where bi-modal or tri-modal spectra were identified, leading to very steep waves, which in one storm caused two of the buoys to capsize. Overall the measurements from

different devices agreed well, with systems utilizing widely different measurement principles returning consistent results. However, some small variation in system accuracy with H_s and frequency were noted, indicating a non-linear response for some devices.

It was found that the Waverider underestimates H_s , with biases increasing from about 5cm for low wave height, 20cm for H_s around 4m and 25cm for records with H_s over 6m. This tendency for slight underestimation of wave height was also noticed for the Directional Waverider by Barstow and Kollstad (1991), which was not available at the time of the WADIC project. The accuracy of estimates of non-directional spectra varied with frequency, with high frequency ($>0.3\text{Hz}$) components being underestimated and very low-frequency ($<0.05\text{Hz}$) components being noisy overestimates. Rademakers (1993) shows that the underestimation at high frequencies observed in the WADIC project is likely to be due to the differences between buoys (Lagrangian) and the fixed (Eulerian) measuring devices, used as the 'best estimate dataset'. He concludes that it is more likely that the high frequencies components were overestimated by the fixed instruments. The noise in the spectrum at low frequencies could be a result of mooring constraints (Joosten, 2006a). De Vries et al (2003) note that a GPS sensor can give much more accurate measurements of low frequency components of the spectra than the HIPPIY accelerometer, although it is not clear whether mooring forces would still limit accuracy.

In high sea states there are a number of problems which can affect buoy measurements. Allender et al (1989) noted that some of the smaller buoys appeared to miss a number of the very highest waves, either due to being submerged or traversing around the large short-crested waves. Slamming or shock loads from breaking waves can cause spikes in the acceleration time series which appear as realistically shaped but unrealistically large waves in the displacement time series. The acceleration signals recorded by the buoy are double integrated using a digital filter and the displacement values are the convolution of the acceleration and the filter. So a spike in the acceleration signal will amplify the filter pattern in the displacement signal. Faults of this kind can be identified by testing for cross-correlation of the displacement signal with the filter pattern (see Appendix A).

A second problem occurs if the buoy is tilted through angles greater than or equal to 90 degrees. At such angles the axis transformation that rotates the buoy coordinate system (xyz) to the earth-fixed coordinate system (North West Up) is indeterminate and the motions of the buoy cannot be calculated (H. Noteborn, Datawell, personal communication).

2.1.1.5. Performance of NDBC buoys:

Details of NDBC wave measurements are well documented in the literature and instead of repeating these here references to the relevant documents are given. An overview of the types of buoys and wave measurement systems operated by the NDBC is given by Steele and Mettlach (1993). Calibration techniques for NDBC buoys are given in Steele et al (1985) and Barrick et al (1989). The analysis procedures and quality controls are detailed in NDBC (1996) and NDBC (2003).

O'Reilly et al (1996) compares wave measurements of Pacific swell (0.06-0.14 Hz) from a Directional Waverider, a NDBC 3m discus buoy and measurements from an array of 6 pressure transducers mounted on fixed platform. They find that measurements of total swell energy from both buoys are in excellent agreement with the platform measurements, but the DWR provides significantly better estimates of spread and skewness than the NDBC 3m discus buoy.

2.1.2. Quality controls for buoy data

A useful summary of real time and post processing quality control tests for wave data can be found in NDBC (2003) and NOAA (2005). These can be summarised as follows:

The time series of sea surface elevation can be checked for irregularities such as:

- Flat episode – data rejected if N consecutive values are unchanged
- Equal peaks – data rejected when N consecutive peaks or troughs exhibit the same values
- Spikes – points greater than N standard deviations from the mean are considered spikes
- Acceleration – data rejected where accelerations exceed N times gravitational acceleration.

- Mean crossing– if more than $N\%$ of a time series does not cross the mean the data are rejected

Values of N are left to user discretion.

Post processing:

Processed data can be compared to preceding values for consistency, or to climatological values or other meteorological measurements such as wind. Tests include:

- Continuity with previous values
- Swell direction consistent with buoy location
- Wind speed consistent with high frequency wave energy
- Wind direction consistent with high frequency wave direction
- Wave height consistent with period

Since the tests described above have already been applied to the NDBC buoy data used in this thesis the reader is referred to the relevant documents for details. Data provided by the European Marine Energy Centre (EMEC) from the DWR buoys on site were not quality checked and contained significant numbers of corruptions. The quality control procedures developed for the EMEC buoy data (which should be applicable to any DWR) are given in Appendix A.

2.1.3 Sampling variability for temporal averages

Understanding the sampling properties of wave parameters is important for several reasons:

- Intercomparison of wave measurements – what level of difference is from sampling only?
- Verification of WEC performance – if we know the wave conditions at a buoy how well can we know wave conditions and hence power a nearby WEC?
- How accurately can we determine monthly or annual mean values, e.g. if we know the monthly mean at one location, how accurately can we know it nearby?

This section considers only uncertainty that arises from the statistical variability of the sea surface. There are other factors which affect the stability of spectral parameters such as the high frequency cut-off of the spectrum, frequency resolution (degrees of

freedom), and method of spectral estimation. The high frequency cut-off is important for T_z , but less so for T_1 and T_e . For example, in the case of a Pierson-Moskowitz spectrum with a cut-off of 0.4 Hz (typical of NDBC buoys) T_z will be overestimated 16% for a peak frequency of 0.2 Hz, 4% for a peak frequency of 0.1 Hz, and 1% for a peak frequency of 0.05 Hz. For T_e the overestimate is 4% for a peak frequency of 0.2 Hz and 0.3% overestimate for a peak frequency of 0.1 Hz. Numerical factors are much less important than sampling variability for integral parameters but can have significant effect on T_p , see Rodriguez et al (1999) and references therein for details.

2.1.3.1. Theoretical results

Sampling variance for spectral parameters of theoretical spectra can be calculated from the covariance of spectral moments. This is given by: (Krogstad et al, 1999b)

$$\text{cov}(\hat{m}_r, \hat{m}_s) = \frac{1}{\tau} \int_0^{\infty} f^{r+s} S^2(f) df + O(N^{-2}) \quad [2.1.1]$$

where τ is the record length, N is the number of points in the time series and the *caret* “^” is used to denote an estimator \hat{a} of parameter a . Using a Taylor expansion, variance for estimates of spectral parameters are given by

$$\text{var}(\hat{H}_s) = \text{var}(4\sqrt{m_0}) = \frac{4}{\tau} \frac{m_{00}}{m_0} \quad [2.1.2]$$

$$\text{var}(\hat{T}_e) = \text{var}\left(\frac{m_{-1}}{m_0}\right) = \frac{1}{\tau} \left(\frac{m_{-1}}{m_0}\right)^2 \left(\frac{m_{-1-1}}{m_{-1}^2} - 2\frac{m_{-10}}{m_{-1}m_0} + \frac{m_{00}}{m_0^2}\right) \quad [2.1.3]$$

$$\text{var}(\hat{T}_m) = \text{var}\left(\frac{m_0}{m_1}\right) = \frac{1}{\tau} \left(\frac{m_0}{m_1}\right)^2 \left(\frac{m_{00}}{m_0^2} - 2\frac{m_{01}}{m_0m_1} + \frac{m_{11}}{m_1^2}\right) \quad [2.1.4]$$

$$\text{var}(\hat{T}_z) = \text{var}\left(\sqrt{\frac{m_0}{m_2}}\right) = \frac{1}{4\tau} \left(\frac{m_0}{m_2}\right) \left(\frac{m_{00}}{m_0^2} - 2\frac{m_{02}}{m_0m_2} + \frac{m_{22}}{m_2^2}\right) \quad [2.1.5]$$

where $m_{rs} = \text{cov}(\hat{m}_r, \hat{m}_s)$. Note that m_0 is the variance of the sea surface elevation, whereas m_{00} is the variance of the estimate of m_0 .

For commonly used theoretical spectra, the coefficients of variation (defined as the standard deviation divided by the mean) for spectral parameters can be calculated using the equations above. The generalised Pierson-Moskowitz spectrum is defined as

$$S(f) = Af^{-5} \exp(-Bf^{-4}) \quad [2.1.6]$$

where $A = \frac{1}{4}H_s^2 B$, $B = (\Gamma(5/4)/T_e)^4$. So using equations 2.1.1-2.1.5 above the coefficients of variation are

$$\text{C.O.V.}(\hat{H}_s) = 0.513\sqrt{T_e/\tau} \quad [2.1.7]$$

$$\text{C.O.V.}(\hat{T}_e) = 0.217\sqrt{T_e/\tau} \quad [2.1.8]$$

$$\text{C.O.V.}(\hat{T}_m) = 0.231\sqrt{T_e/\tau} \quad [2.1.9]$$

$$\text{C.O.V.}(\hat{T}_z) = 0.238\sqrt{T_e/\tau} \quad [2.1.9]$$

For a JONSWAP spectrum it is not possible to calculate a formula analytically, but the results can be calculated numerically. The spectrum is defined by

$$S(f) = G(f)\alpha g^2 (2\pi)^{-4} f^{-5} \exp[-(5/4)(f/f_p)^{-4}] \quad [2.1.10]$$

where

$$G(f) = \gamma \exp\left\{-\frac{(f-f_p)^2}{2\sigma^2 f_p^2}\right\}$$

and

$$\sigma = \sigma_a \text{ for } f < f_p$$

$$\sigma = \sigma_b \text{ for } f > f_p$$

The value of α is not important for the C.O.V. of H_s and T_e , T_m or T_z since it divides out. If the mean values of γ , σ_a and σ_b found in the JONSWAP experiment are used, that is, $\gamma = 3.3$, $\sigma_a = 0.07$, $\sigma_b = 0.09$, then we can parameterise the spectrum in terms of T_e , T_m or T_z using relationships derived from numerical integration of the spectrum:

$$f_p = \frac{0.90}{T_e} = \frac{0.83}{T_m} = \frac{0.78}{T_z} \quad [2.1.11]$$

Again using equations 2.1.1-2.1.5, the coefficients of variation are

$$\text{C.O.V.}(\hat{H}_s) = 0.649\sqrt{T_e/\tau} \quad [2.1.12]$$

$$\text{C.O.V.}(\hat{T}_e) = 0.178\sqrt{T_e/\tau} \quad [2.1.13]$$

$$\text{C.O.V.}(\hat{T}_m) = 0.226\sqrt{T_e/\tau} \quad [2.1.14]$$

$$\text{C.O.V.}(\hat{T}_z) = 0.257\sqrt{T_e/\tau} \quad [2.1.15]$$

The variability of H_s is greater for JONSWAP than PM spectra because narrower-banded spectra give longer wave groups and thus larger variation in results over a given sample duration. In contrast, variability of period parameters increases with bandwidth. In the limiting case, if the bandwidth is infinitely narrow then fluctuations in various moments are 100% correlated, giving zero variation in period. The physical interpretation of this is that the surface elevation is a sum of waves with the same frequency and therefore can be expressed as a single sinusoidal wave.

The distribution function of H_s has been discussed by Donelan and Pierson (1983), Carter and Tucker (1986) and Young (1986). Forristall et al (1996) note that for practical purposes the distribution can be approximated with a Gaussian.

2.1.3.2. Empirical results

When comparing empirical estimates of sampling variability to theoretical results it is important to take into account the difference between the variance of a parameter and the RMS difference between two measurements. Suppose we have two buoys making simultaneous measurements, located close to each other, so that they are experiencing the same wave field. We denote the measurement of H_s made by each buoy as $\hat{H}(A)$ and $\hat{H}(B)$. If for simplicity, we assume that sampling error is not dependent on period, so that $\hat{H}(A) = H_s + k\varepsilon_A H_s$ and $\hat{H}(B) = H_s + k\varepsilon_B H_s$ where the errors, ε_A and ε_B , are assumed to be distributed $N(0,1)$, and k is the coefficient of variation. We denote the

difference between the measurements as $d = \hat{H}(A) - \hat{H}(B)$, and an estimate of the true H_s as the average between the measurements: $\hat{H}_s = \frac{1}{2}(\hat{H}(A) + \hat{H}(B))$. Then the normalised differences between the measurements are given by

$$\frac{d}{\hat{H}_s} = \frac{\hat{H}(A) - \hat{H}(B)}{\frac{1}{2}(\hat{H}(A) + \hat{H}(B))} = \frac{k(\varepsilon_A - \varepsilon_B)}{1 + k(\varepsilon_A + \varepsilon_B)/2} \quad [2.1.16]$$

Numerical simulation shows that for small k

$$\text{std}(d / \hat{H}_s) \approx 1.4k, \quad [2.1.17]$$

In other words the normalised RMS difference between the buoys is about 1.4 times the coefficient of variation.

Steele and Earle (1979) compare estimates made by two buoys moored approximately 100m apart. Over 198 pairs of 20 minute measurements of H_s , the RMS difference was 7%. Their experiment corresponds to the situation described above, so using equation 2.1.17 we deduce that the coefficient of variation was 5%.

Tournadre (1993) takes a different approach which does not involve comparing measurements from two buoys. An iterative procedure is used to determine durations of stationarity for H_s and the coefficient of variation of a 20 minute record is found to be around 4%.

Tucker and Pitt (2001) give a note of caution for the use of equation 2.1.1 for the calculation of variability from measured spectra. Since the estimator $\hat{S}(f_j)$ has a negative exponential distribution the expected value of $\hat{S}^2(f_j)$ is

$$E[\hat{S}^2(f_j)] = 2[\hat{S}(f_j)]^2 \quad [2.1.18]$$

Therefore use of equation 2.1.1 on measured spectra gives a bias of a factor of 2. However, if estimates of $S(f_j)$ smoothed over 10 or more harmonics then the bias factor is reduced to 1.1 or less.

We examine measurements from two buoys at the EMEC test site. The buoys are moored approximately 1.5 km apart, in 50m and 52m depths, with similar exposure to oncoming waves. The buoy locations are shown in Figure 2.1. The situation is similar to that described by Steele and Earle (1979), with both buoys experiencing roughly the same synoptic wave field. Due to the proximity of the buoys to the coastline (about 1km), there may be some systematic differences from reflections, different currents or sheltering. In this location there are strong tidal currents both into and out of Scapa Flow (the sound between the two main islands), but local bathymetric effects produce a current mostly in a northerly direction at the buoy locations. The average difference in H_s and T_e between the buoys is low (0.04m and 0.03s) which gives confidence that any differences are small. Plots of differences against time show no trend, indicating that calibration of both buoys remains consistent. The period of concurrent measurements spans 5 years, but with some gaps, and consists of about 40,000 concurrent 30 minute records.

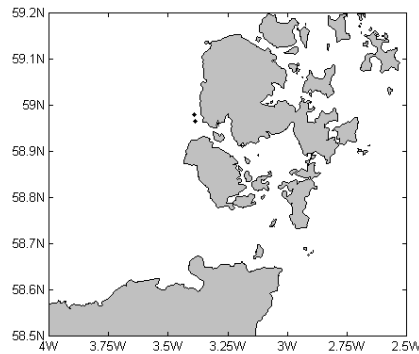


Figure 2.1 Locations of EMEC buoys marked with black diamonds.

If differences between the buoys arise from sampling variability only (i.e. recording only a finite number of waves from a theoretically infinite distribution), then differences for consecutive half hour periods will be independent and hence uncorrelated. However, examining the autocorrelation series of the differences shows that they are in fact periodically correlated, with period of 12.4 hr, equal to the tidal period. Figure 2.2

shows the autocorrelation series for the normalised differences in H_s and T_e , as defined equation 2.1.16.

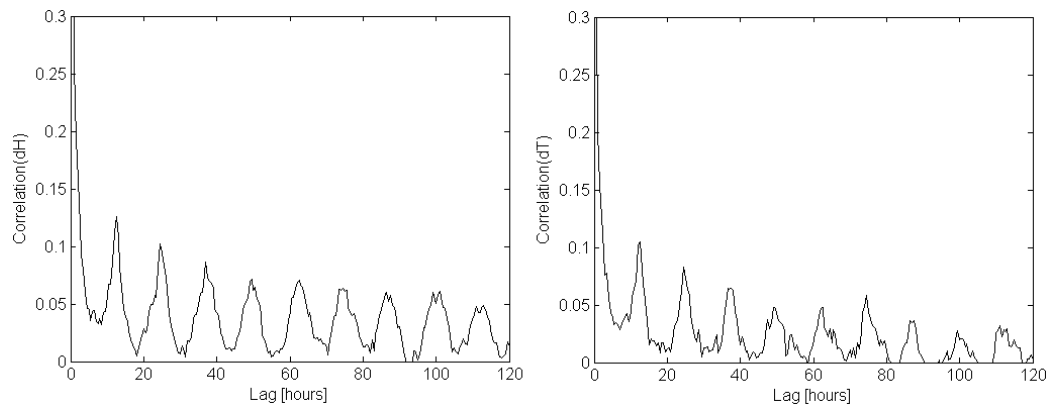


Figure 2.2. Autocorrelation of normalised differences in H_s (left) and T_e (right).

The correlation of the residuals implies that the tidal current effects differ between the buoy locations, causing differences in the wave field. The magnitude of this effect will depend on the wave and current conditions which are non-stationary. From inspection of the power spectrum, peaks at multiples of the tidal period are visible but it is difficult to estimate the magnitude of tidal effects. Since the correlation is small, we can use the buoy EMEC buoy results as upper bounds for sampling variability.

Figure 2.3 shows plots of the standard deviation of the percentage difference in H_s and T_e against H_s and T_e . We see that in contrast to the theoretical results there is a slight dependency of the variability on H_s but less so with T_e . A possible explanation for this is that for low H_s there are large differences in the shape of measured spectra from PM or JONSWAP forms. For large H_s , spectral shapes tend toward standard PM or JONSWAP forms. Moreover, any tidal effects causing differences between the buoys will be greater for low H_s . Using equation 2.1.17 we get an average C.O.V. for H_s , T_e , T_m and T_z over a half hour period as 6.2%, 3.2%, 4.3% and 4.5% respectively. These are higher than the theoretical results and slightly higher than the values for H_s found by Steele and Earle (1979) and Tournadre (1993). This is possibly a result of the increased separation compared to the experiment of Steele and Earle and the different tidal effects at each buoy.

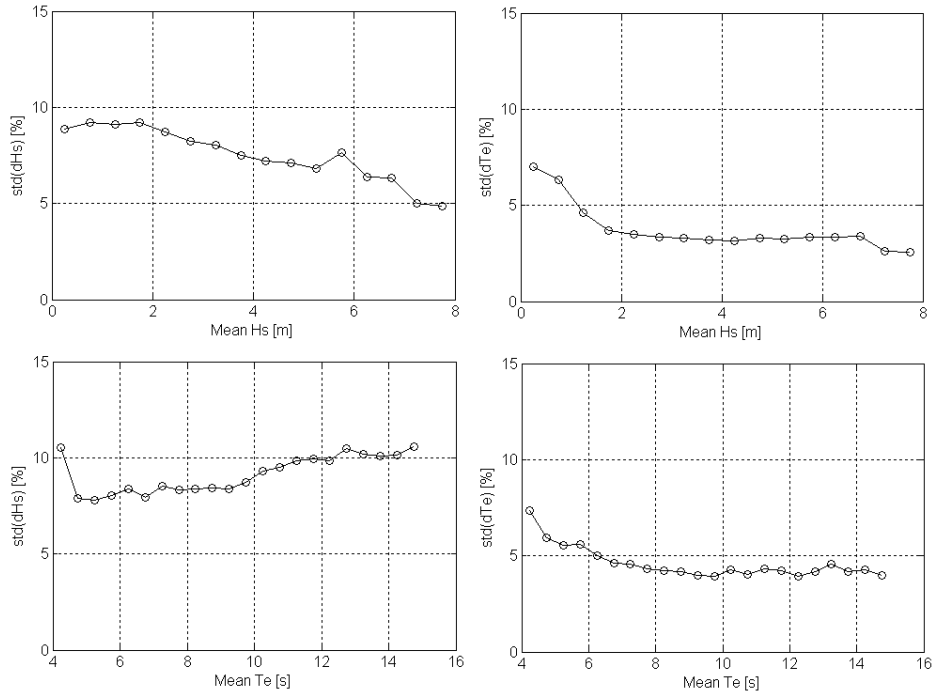


Figure 2.3. Standard deviation of differences in H_s and T_e against H_s and T_e .

We can examine the results sampling effects in a slightly different manner, by plotting the standard deviation of the differences in H_s and T_e , binned by H_s and T_e (see Figure 2.4). The pattern is quite different for H_s and T_e . For H_s the largest percentage differences between the buoys occur for long period swell events, presumably because there is increased groupiness for longer periods and therefore higher sampling uncertainty. For T_e the differences are smallest for steep seas, where spectra tend toward standard PM or JONSWAP type shapes, and highest for low H_s where there can be a large range of spectral shapes.

Figure 2.5 shows the correlation of differences in H_s and T_e between the buoys, binned by H_s and T_e . There is a strong positive correlation in steep seas and in swell events and a negative correlation in small, short period seas. Correlation in the sampling errors will affect the sampling uncertainty of WEC power, which is dependent on both H_s and T_e .

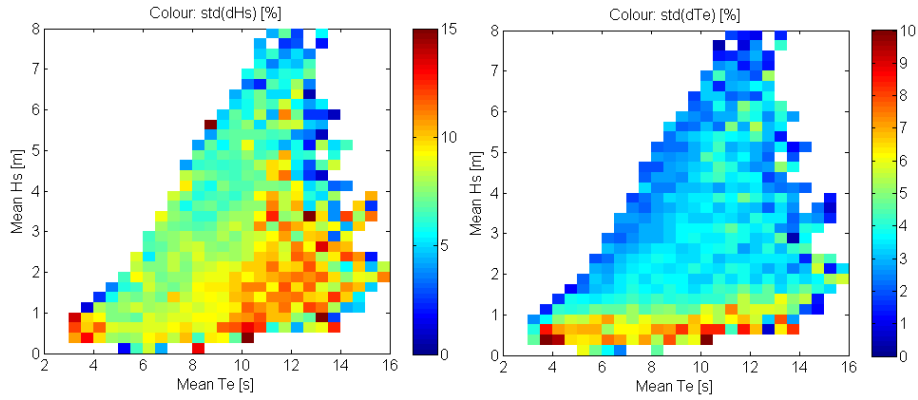


Figure 2.4. Standard deviation of differences in H_s and T_e , binned by H_s and T_e .

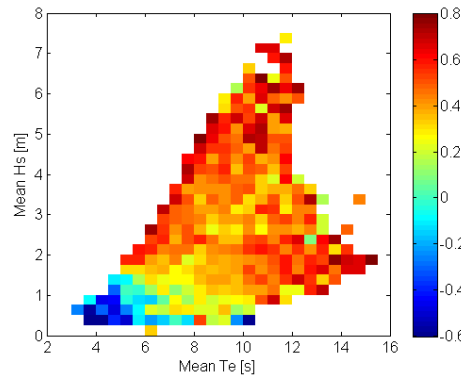


Figure 2.5. Correlation of differences in H_s and T_e , binned by H_s and T_e .

Figure 2.6 shows the standard deviation of differences in Pelamis power from each buoy as functions of both mean power and binned by H_s and T_e . The sampling uncertainty decreases at high powers, since the power is limited at 750kW. This can also be seen, when the differences are binned by H_s and T_e , but it is clear that for high H_s there is a larger difference for long T_e , since the Pelamis power decreases with T_e above about 8 seconds.

For very low powers the differences can be large if one buoy measures a sea state below the cut-in threshold for the Pelamis to produce power. Ignoring values for the mean power less than 50kW, the average RMS difference in Pelamis power between the buoys is 16%. Using equation 2.1.17 this gives the coefficient of variation to be 11% for a half hour record.

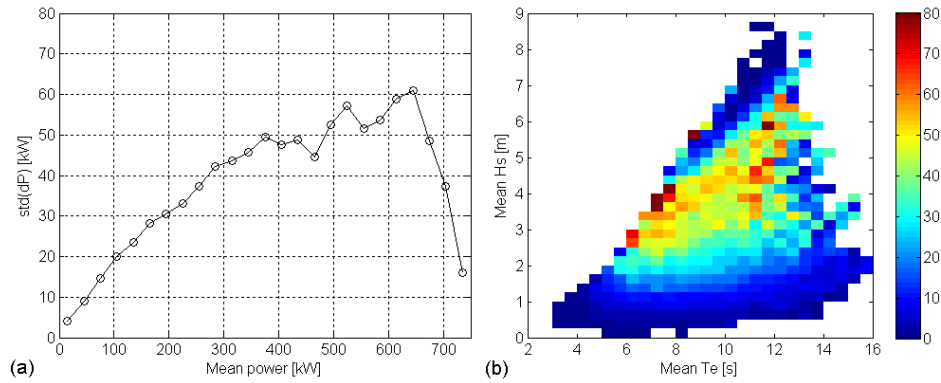


Figure 2.6. Standard deviation of differences in Pelamis power against mean power (left) and binned by H_s and T_e (right).

Rainey (2007) discusses the power generated by the Pelamis full scale prototype during sea trials at EMEC. During the trial a buoy was moored about 300m from the Pelamis. The mean power absorbed in each 30 minute period was compared to the value calculated from the PELS computer model for the spectra measured at the buoy. The mean H_s over the 6 hour period was 2.5m and the mean T_e was 6.3 s, the standard deviation of the difference in the absorbed power was 14.7 kW. This is a remarkably good agreement, compared to our results using two buoys where the standard deviation of the differences for these conditions is around 30 kW, especially considering that the difference between the prototype and the simulation will include a component due to the uncertainty from the computer model. The reason for the good agreement maybe due to the decreased separation, making tidal effects less significant. Also, if the buoy is directly ahead of the machine, in the direction of oncoming waves, then sampling effects maybe significantly reduced as the machine will experience essentially the same waves as the buoy. Since there are only 12 samples, a 90% confidence interval for the RMS difference in this experiment is (9.7%, 18.9%) and we can conclude that the uncertainty in the PELS numerical simulation is low.

2.1.4 Short-term temporal variability of wave height

The purpose of this section is to provide some information of the short-term variability in wave height for the purposes of assessing the effect of a temporal separation when comparing wave measurements. Monaldo (1988) calculates the expected difference in wave height for a given separation time from the autocorrelation series of buoy measurements. However this estimate includes a noise component, mainly from

sampling variability. Moreover the expected difference at a given separation time will also depend on wave height, for instance if $H_s = 10\text{m}$ we would expect a larger difference after 6 hours than if $H_s = 1\text{m}$. Tournadre (1993) uses a method to detect stationary states in stochastic processes which removes the noise component. He shows that the mean value of the difference in H_s between consecutive sea states is approximately linear with H_s and notes that durations of stationarity in sea state are dependent on location. In the North Sea which is mainly dominated by wind waves, time scales are much shorter than in the equatorial Atlantic which is mainly swell dominated. For both locations the durations of stationarity have large dispersion and are approximately exponentially distributed. Thus no scale can be considered predominant.

We will calculate an estimate of the effect of temporal separation from the EMEC buoy data as an example. Suppose that $H_s(t + \tau) = H_s(t) + \delta$, where the difference, δ , has mean μ and standard deviation σ . If we model the difference as a function of $H_s(t)$ and τ , then for high $H_s(t)$ and large τ , μ will be negative, because for a high sea state we would expect H_s to decrease after some time. Therefore we model δ as a function of the average, $H_{ave} = (H_s(t) + H_s(t + \tau))/2$, so that we can assume $\mu = 0$. We note that the distribution of δ may not be symmetric about zero. For instance if H_s increases rapidly and falls off slowly then $H_s(t + \tau) - H_s(t)$ will be positive for a greater proportion of time than it is negative. However, from the data we see that the effect is not too pronounced (see Figure 2.7 a) and we will approximate δ with a normal variable with zero mean. Figure 2.7 (b) shows the standard deviation of the differences, σ , against H_{ave} for $\tau = 6$ hours. It is evident that σ increases approximately linearly with H_{ave} . This linear relationship was observed for all $\tau < 12$ hours, so we model the differences as $\delta = a(\tau)H_{ave}\varepsilon$, where ε is a standard normal variable.

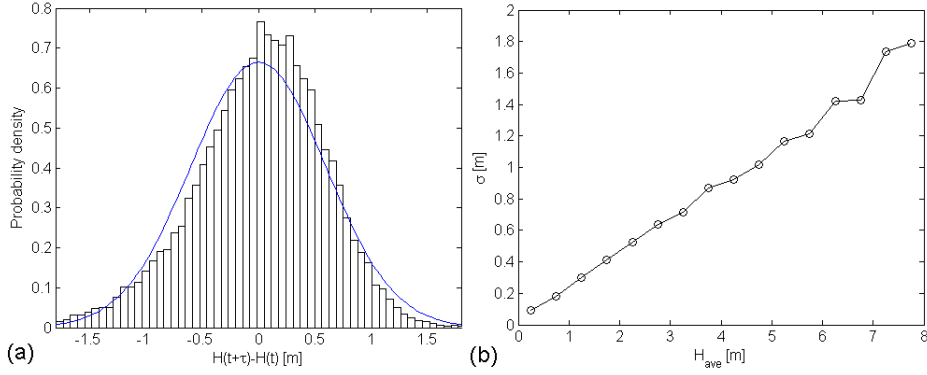


Figure 2.7. (a) Bar plot: distribution of differences for $2m < H_{ave} < 3m$ at separation of 6 hours. Line: fitted normal distribution. (b) Standard deviation of δ against H_{ave} at separation of 6 hours, bin width 0.5m.

If we estimate $a(\tau)$ from the data it will be overestimated due to sampling variability. We can calculate the difference between the estimate $\hat{a}(\tau)$ and the true value $a(\tau)$ as follows. For brevity we will denote $H_s(t)$ as H_t , and denote the C.O.V. for sampling variability as k (as in section 2.1.3). Then the normalised difference at separation τ is

$$\begin{aligned}
 \frac{d(\tau)}{\hat{H}_{ave}} &= \frac{\hat{H}_{t+\tau} - \hat{H}_t}{\frac{1}{2}[\hat{H}_{t+\tau} + \hat{H}_t]} \\
 &= \frac{H_{t+\tau}(1+k\varepsilon_1) - H_t(1+k\varepsilon_2)}{\frac{1}{2}[H_{t+\tau}(1+k\varepsilon_1) + H_t(1+k\varepsilon_2)]} \\
 &= \frac{(H_{ave} + \delta/2)(1+k\varepsilon_1) - (H_{ave} - \delta/2)(1+k\varepsilon_2)}{\frac{1}{2}[(H_{ave} + \delta/2)(1+k\varepsilon_1) + (H_{ave} - \delta/2)(1+k\varepsilon_2)]} \\
 &= \frac{(1+a(\tau)\varepsilon_3/2)(1+k\varepsilon_1) - (1-a(\tau)\varepsilon_3/2)(1+k\varepsilon_2)}{\frac{1}{2}[(1+a(\tau)\varepsilon_3/2)(1+k\varepsilon_1) + (1-a(\tau)\varepsilon_3/2)(1+k\varepsilon_2)]}
 \end{aligned} \tag{2.1.19}$$

where ε_1 , ε_2 and ε_3 are independent standard normal variables. From numerical simulation we can calculate $\hat{a}(\tau) = \text{std}(d(\tau)/\hat{H}_{ave})$ for various values of a and k (see Figure 2.8 a). This can then be used to adjust the values of $\hat{a}(\tau)$ estimated from the buoy data. Figure 2.8 (b) shows the raw and corrected values for $k = 4\%$. The function $a(\tau)$ is well fit by a quadratic law, giving

$$a(\tau) = -0.00218\tau^2 + 0.0516\tau \quad \text{for } \tau < 12 \text{ hours} \tag{2.1.20}$$

with τ in hours.

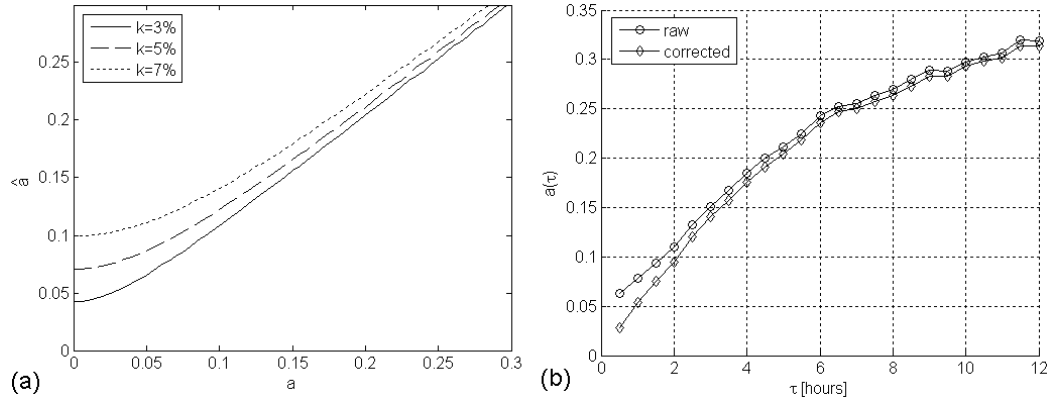


Figure 2.8. (a) Observed and true values of $a(\tau)$ from numerical simulation. (b) Raw and corrected values of $a(\tau)$ from the data.

Pitt (2008) recommends the use of wave records averaged over one hour as a reasonable compromise between statistical stability of the measurements and adequate sampling of the underlying variation of the sea state. From the results of the present and previous sections the expected change in H_s over a half hour period is 2% and the sampling variability is 4%. Over one hour the expected change in H_s and the sampling variability are both about 3%. So we can conclude that a one hour averaging period is indeed a reasonable compromise.

The case for Pelamis power is complicated by the fact that the power is limited at 750 kW. This means that the standard deviation of the differences, $\sigma = \text{std}(P(t + \tau) - P(t))$, will increase with the average power, P_{ave} , to a certain point and then decrease again as P_{ave} approaches the limiting value of 750 kW. Moreover, the value of P_{ave} at which σ reaches its maxima varies with τ . Therefore we do not attempt to model σ as a function of P_{ave} and τ , or correct for the effects of sampling variability. Figure 2.9 shows plots of σ against P_{ave} for various τ . Here half hour average values of power have been used, however the instantaneous power produced by the Pelamis will be greater than this due to wave groupiness. This variation is smoothed to a certain extent by the hydraulic accumulators used in the power take off system. The distribution of power for a given sea state is a dependent on the size of the accumulators, the power absorbed by the Pelamis and the control system used. Since the accumulator size is constant, the

variance in power output will increase with H_s . At present the control system for the Pelamis has not been finalised so the variability in output power for a given average power level cannot be specified precisely. The standard deviation is estimated to be around 20-30%.

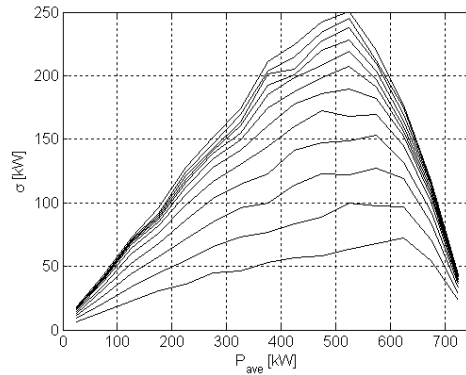


Figure 2.9. Standard deviation of difference in power (uncorrected) against P_{ave} for $\tau = 1, 2, \dots, 12$ hours, lowest line is $\tau = 1$.

2.2 Wave measurements from satellite altimeters

Measurements of waves from satellite radar altimeters provide an important complement to in-situ measurements. While in-situ measurements provide a time series of measurements at one location, satellite altimeters provide measurements over the entire globe, with a continuous record dating back to 1991.

The precision and accuracy of satellite altimeter measurements of H_s is well established and there have been many published studies on this subject in the last two decades (e.g. Dobson et al, 1987; Monaldo, 1988; Carter et al, 1992; Callahan et al, 1994; Cotton and Carter 1994; Gower, 1996; Krogstad and Barstow, 1999; Young, 1999b; Challenor and Cotton, 2002; Caires and Sterl, 2003; Queffeuou, 2004; Janssen et al, 2007). Less has been written on the subject of deriving wave period information from altimeter measurements. This is an important topic for wave energy since estimation of WEC power requires both wave height and period. In this section we give a brief introduction to altimetry and the principles of altimeter measurements. In order to establish the

accuracy of altimeter measurements it is necessary to discuss the sampling properties of altimeter measurements and the spatial variability of the wave field. The accuracy of altimeter measurements of both wave height and period is then discussed in Chapter 3.

The nature of altimeter measurements

In general, in-situ instruments measure the displacement of the water surface at a fixed point with respect to time. Altimeters are not able to measure in this way. Instead they provide measurements whilst the satellite orbits the earth. They interrogate an area or footprint of about 5 km diameter and report a measure of the average wave conditions over the whole area. Data is reported at 1 Hz, in which time the footprint of the altimeter footprint will have moved about 6.5 km.

Satellite altimeters orbit the earth following a fixed path relative to the ground. The orbits are divided in passes, cycles and phases. A pass spans half an orbital revolution and is either ascending (South-North) or descending (North-South). A cycle is completed once the satellite returns to the same location above the earth. The time taken to complete one cycle is known as the repeat period. If a satellite is moved into a new orbit, this is denoted by a new phase, e.g. A, B, etc. Figure 2.10 shows a 3 dimensional view of the first 5 passes of a cycle, and a full cycle of 254 passes for the TOPEX phase A orbit. Details of the orbits of the satellite altimeter missions to date are given in Appendix B.

There is an inherent compromise in the choice of orbit between the regularity of measurements at a point on the ocean surface and the spatial resolution of the satellite's coverage. For example, although the TOPEX/Poseidon (T/P) mission returns to a cross-over point of the ground tracks every 5 days on average, there is a relatively large distance between adjacent cross-over points. In contrast the ERS and ENVISAT missions have a much smaller distance between cross-over points of the ground tracks but a longer repeat period of 35 days. Ground tracks of the T/P and ERS missions are shown in Figure 2.11.

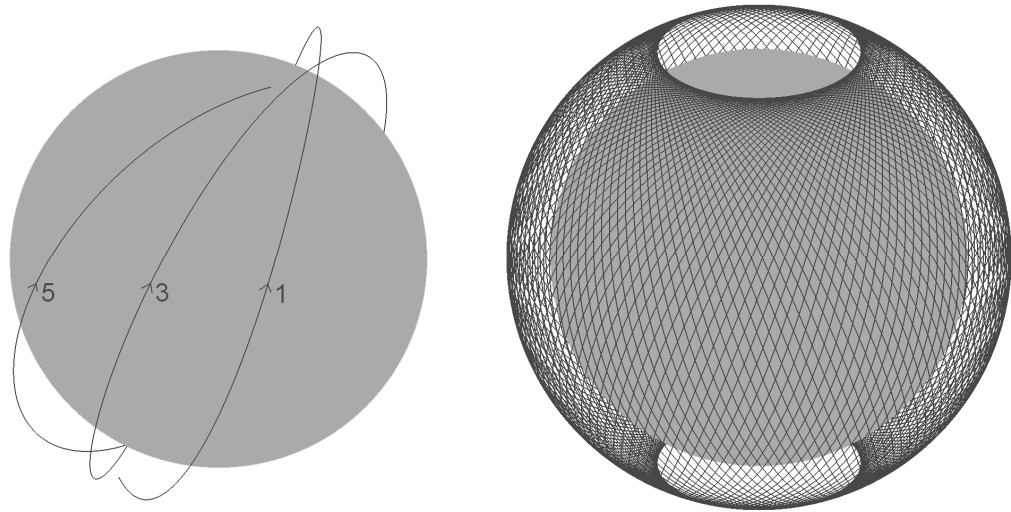


Figure 2.10. 3D view of TOPEX phase A orbit. Left: first 5 passes of a cycle. Right: A full cycle of 254 passes.

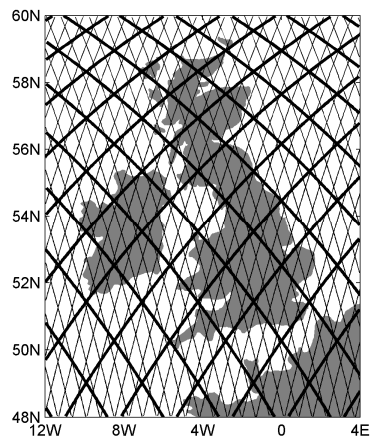


Figure. 2.11. Altimeter passes in the vicinity of United Kingdom (Bold lines: TOPEX/Poseidon/Jason, thin lines: ERS-1&2/ENVISAT)

2.2.1. Instrumental characteristics

The satellite altimeter is a radar oriented at near vertical incidence to the sea surface. It measures the return signal from specular (mirror-like) reflection from the sea surface. A brief overview of the principles of radar altimetry is given in this section. For a more detailed description and extensive references, the reader is referred to Fu and Cazenave (2001).

Altimeters operate within the microwave frequency range where graybody emission of electromagnetic radiation from the sea surface is very weak and the reflectivity of water is high, thus allowing easy distinction of radar return and natural emission. All altimeters flown to date have carried a Ku-band (10.9 – 22.0 GHz) altimeter, but the TOPEX, Jason and ENVISAT altimeters also made simultaneous measurements at a lower frequency. TOPEX and Jason both have a dual-frequency altimeter which operates simultaneously at 13.6 GHz (Ku-band) and 5.3 GHz (C-band), and ENVISAT had a dual frequency 13.6 GHz (Ku-band) and 3.2 GHz (S-band) altimeter. In this study we will mainly consider Ku-band wave measurements, since they have been extensively studied and validated.

Measurements of the ocean surface are made as follows: The altimeter sends a pulse of radar energy to the ocean surface and records the return pulse. Wave height, wave period and wind speed are inferred from the form of the return pulse. The technique used to transmit the pulse of radar energy and interpret the return signal is known as pulse-compression, whereby an altimeter transmits a relatively long pulse with a short frequency modulation called a chirp. The return signal is processed in a way that is equivalent to transmitting a short pulse and measuring the time history of the returned power. The equivalent pulse length is equal to the reciprocal of the chirp bandwidth. A detailed account of the use of pulse compression in satellite altimetry is given by Chelton et al (1989). Since it is more intuitive to understand how waves affect the time history of a short pulse of radar energy, we will use this interpretation in the following sections.

2.2.1.1. The effect of waves on the return pulse

The power in the radar return pulse is proportional to the area illuminated by the radar energy on the sea surface. At the first instant a pulse reaches the surface, it illuminates a small circular region nadir to the altimeter. At successive times, the same narrow pulse illuminates annular regions with ever increasing diameters. Despite the increasing diameters, the area illuminated remains constant. This is due to the Earth's surface being curved rather than flat (see Appendix A1 of Chelton et al, 1989). Figure 2.12 illustrates this for the case of a flat sea surface.

Waves on the sea surface change the shape of the waveform that the altimeter receives (see Figure 2.13). The leading edge of the returned waveform is stretched as a result of the earlier returns from wave crests and later returns from wave troughs. The higher the waves, the greater the time between the arrivals of returns from the crests and from the troughs of the waves, and the more spread out is the return pulse. This stretching of the shape of the return pulse can be related quantitatively to the variance of the sea surface, and hence to the significant wave height H_s . A detailed description of how the presence of waves on the sea surface alters the shape of the returned wave form is given by Fu and Cazenave (2001), Chapter 1, Section 2.4.2.

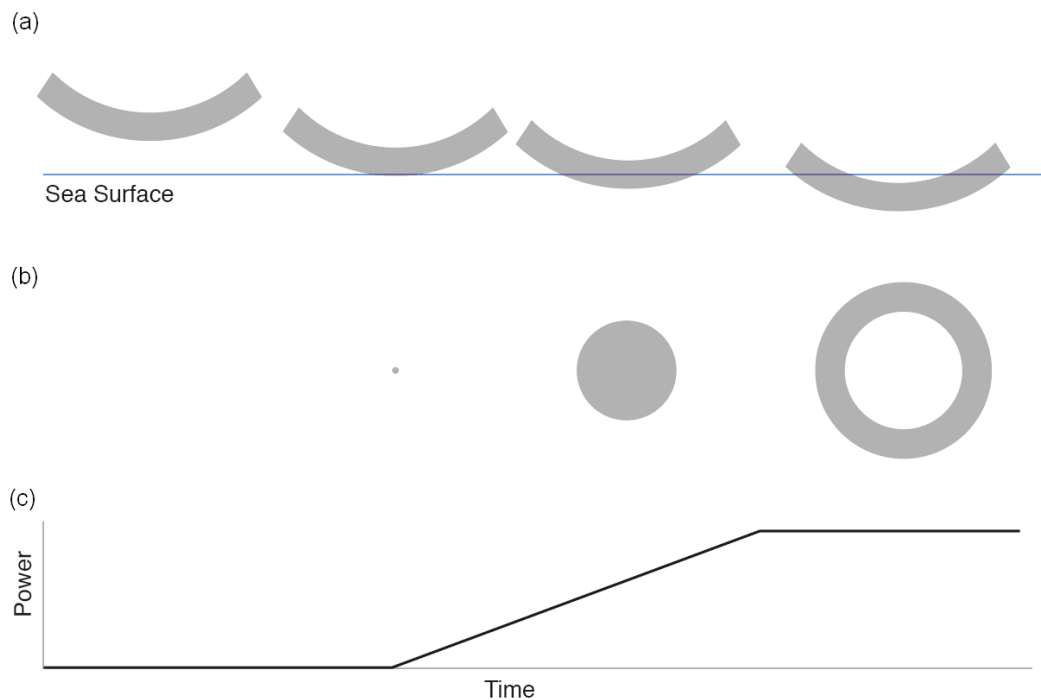


Figure 2.12. (a) The transmitted pulse of radar energy from an altimeter at vertical incidence (b) The illumination of a flat sea surface by the radar pulse shown in (a). (c) The evolution of returned power received at the altimeter for a single pulse. (From Challenor, 2006).

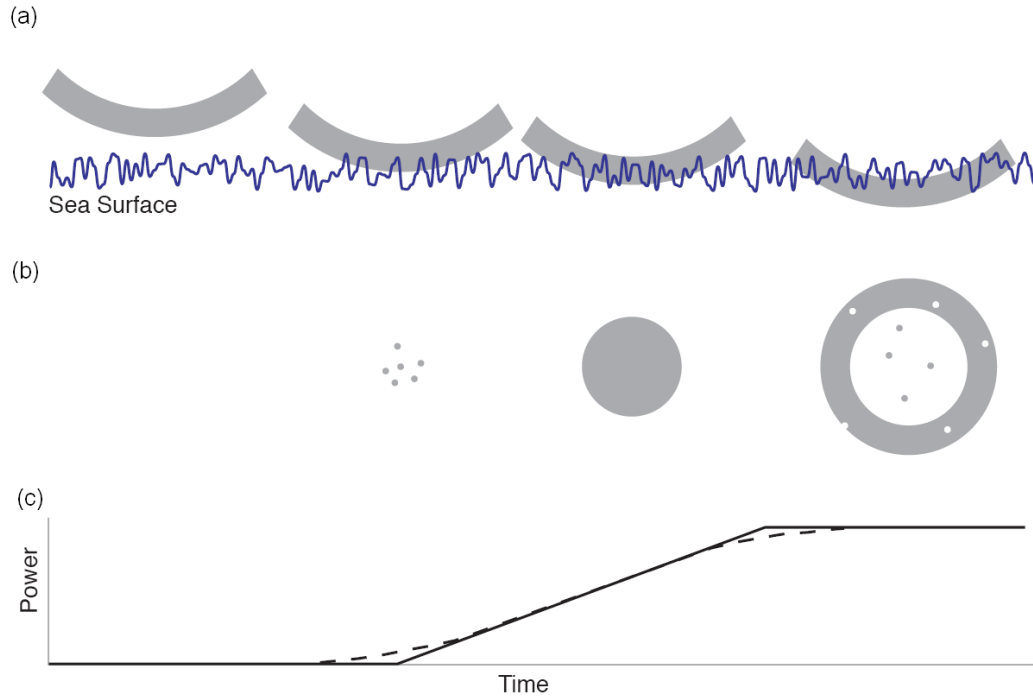


Figure 2.13. As Figure 2.12, but with waves on the sea surface. (From Challenor, 2006).

2.2.1.2 The normalised radar cross section

Another key parameter of the reflected waveform received by the altimeter is σ_0 , a dimensionless quantity referred to as the normalised radar cross section or backscatter coefficient. It is a measure of the ratio between transmitted power and the power of the return pulse received by the altimeter. It can be shown that the returned power and hence σ_0 depends only on the radar scattering characteristics or "roughness" of the target area. The sea surface roughness increases with wind speed. At small incidence angles relevant to satellite altimetry, returned power and therefore σ_0 decrease monotonically with increasing roughness. The backscatter coefficient σ_0 can therefore be used together with the measurement of H_s to estimate wind speed and wave period (see Section 3.2).

The backscatter coefficient is given by (Fu and Cazenave, 2001):

$$\sigma_0 = \frac{(4\pi)^3 R^4}{t_\lambda^2 \lambda^2 G_0^2 A_i} \cdot \frac{P_r}{P_t} \quad [2.2.1]$$

where P_t is the transmitted power in watts, P_r is the returned power, G_0 is the boresight antenna gain, A_i is the illuminated area on the sea surface, and $t_\lambda(R, \theta)$ is the atmospheric transmittance, defined to be the fraction of electromagnetic radiation at wavelength λ that is transmitted through the atmosphere from an altitude R at off-nadir angle θ . The two-way transmittance is $t_\lambda^2(R, \theta)$.

The illuminated area is the area on the sea surface contributing to the radar return. This is not the same as the total oceanographic footprint, discussed in section 2.2.1.4, which is the area over which sea surface statistics are measured by the altimeter. The illuminated area is given by

$$A_i = \frac{\pi R_0 c \tau}{1 + R_0 / R_E} \quad [2.2.2]$$

where c is the speed of light, τ is the pulse duration, R_0 is the altitude of the satellite and R_E is the radius of the Earth.

The backscatter coefficient is actually corrected for the effects of atmospheric attenuation so that the transmittance, t_λ , is equal to one. At the Ku-band frequency of 13.6GHz, the clear sky one-way transmittance of at normal incidence angles is rarely less than 0.96 even in a moist tropical atmosphere. The corresponding two-way attenuation ($1 - t_\lambda^2$) is therefore generally less than 8%. At C-band and S-band frequencies the attenuation is much less. The clear-sky attenuation of σ_0 can be accurately corrected for using transmittance values derived from meteorological models. Cloud attenuation can also be accurately corrected for and is estimated using a multi-frequency microwave radiometer onboard the satellite.

Rain has a much greater effect on radar signal than clouds, water vapour or dry gases. Because of the difficulties in obtaining rain-rate profiles from satellite data, no attempt is made to correct for rain attenuation of σ_0 . Rather, rain-contaminated altimeter observations are flagged and excluded, this is discussed in Section 2.2.2.1. However measurements at lower frequencies are less effected by rain and can be used to maintain data coverage through severe storms (see Quartly, 1997).

2.2.1.3 The returned power

Brown (1977) showed that the returned power P_r is given by a three fold convolution:

$$P_r(t) = P_{FS}(t) \otimes P_{PT}(t) \otimes P_H(-z) \quad [2.2.3]$$

where convolution is defined in the standard sense:

$$g(t) \otimes h(t) = \int_{-\infty}^{\infty} g(\tau)h(t - \tau)d\tau$$

$P_{FS}(t)$ is the flat surface response function. It is the response you would get from the radar pulse being reflected from a flat surface and is dependent on the antenna gain pattern. $P_{PT}(t)$ is the point target response function is the shape of the transmitted pulse. $P_H(-z)$ is the probability density function of specular points on the sea surface. Brown (1977) used the pdf for a linear, Gaussian-distributed sea, but Challenor and Srokosz (1989) showed that a slightly non-linear sea gives essentially the same answer. However, the method does not account for highly non-linear behaviour such as wave breaking.

Some example waveforms for Gaussian wave height distributions are shown in Figure 2.14. The slope of the leading edge varies approximately linearly with H_s . Note that after the initial sharp rise in energy as the return pulse reaches the altimeter, unlike the illuminated area which remains constant, the returned power slowly decreases with time because of the roll off in the antenna beam pattern. This is sometimes referred to as the “plateau droop” of the waveform. Algorithms for calculating H_s and σ_0 from the return wave form are described in Fu and Cazenave (2001) pages 92 and 95 respectively.

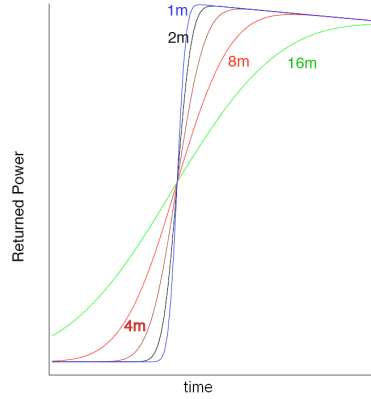


Figure 2.14. Returned power for Gaussian sea surface height distributions for various H_s . (From Challenor, 2006).

2.2.1.4. The total oceanographic footprint

The total oceanographic footprint, often just referred to as the footprint, is the area over which sea surface statistics are measured by the altimeter. For the case of a Gaussian-distributed sea with significant wave height H_s , Chelton et al (1989) show that the maximum footprint area contributing to the radar return when the expanding circle becomes an annulus is given by

$$A_{\max} = \frac{\pi R_0 (c\tau + 2H_s)}{1 + R_0/R_E} \quad [2.2.4]$$

where c is the speed of light, τ is the pulse duration, R_0 is the altitude of the satellite and R_E is the radius of the Earth. TOPEX/Poseidon and Jason have nominal orbital altitudes of 1335km, ERS-1, ERS-2 and ENVISAT have altitudes of 800km and GEOSAT and GFO have an altitude of 785km. The effective pulse duration for GEOSAT and T/P is 3.125ns, and 3.03ns for ERS-1&2. Figure 2.15 shows the effective footprint diameter against H_s for two orbital altitudes.

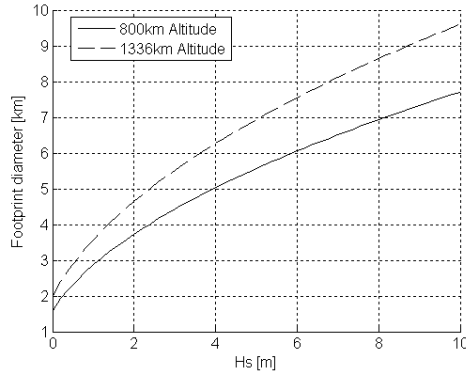


Figure 2.15. Footprint diameter against H_s for two orbital altitudes.

2.2.1.5. Noise on the return signal

The time series of returned power shown in Figure 2.14 actually represent the time evolution of illuminated area averaged over a hypothetical infinite ensemble of realisations. Any particular realisation will be very noisy owing to the random nature of the phases of the various components of the wave field over the antenna footprint that contribute to the radar return at any particular two-way travel time.

As the altimeter moves along the satellite orbit, the path lengths to the specular reflectors on the various wave facets change, resulting in pulse-to-pulse fluctuations in the illuminated area time series. The noisiness of each individual pulse time series can be reduced by averaging. If the individual time series in the average are statistically independent (which depends on the pulse repetition rate and the satellite ground-track velocity), the noise decreases as the square root of the number of time series in the average. Walsh (1982) has shown that the maximum pulse repetition rate for independent samples is proportional to the square root of H_s , increasing from about 1000 Hz for $H_s = 2$ m to about 3000Hz for $H_s = 10$ m. The SEASAT and GEOSAT altimeters operated at 1000 Hz and T/P operated at 4000 Hz, meaning that successive pulses were somewhat correlated for T/P.

As well as noise from the random nature of the wave field, if the altimeter is simply used as a detector it will receive a signal from thermal noise, also known as Rayleigh fading noise (Ulaby et al, 1986). It is sometimes assumed to be constant and sometimes its mean is measured. For most altimeters the noise on the signal is independent in each gate and has a negative exponential distribution. For a negative exponential distribution

the variance is equal to the mean. Thus the individual pulses are very noisy (see Figure 2.16).

To reduce the effect of this, the pulses, which are transmitted at repetition rates of 1000 to 4000 per second, are averaged to give one estimate of H_s every 0.1 s, and ten of these 10 Hz values are averaged again to give the 1 Hz values which are distributed as the Geophysical Data Records (GDR). The standard deviation of the ten 10 Hz values comprising each 1 Hz value is also given in the GDR, and provides a useful check on the validity of the H_s value (see Section 2.2.2).

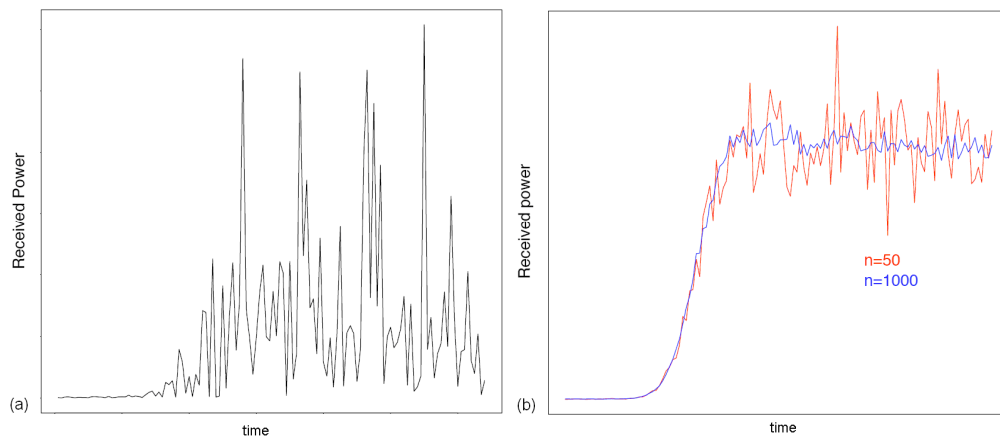


Figure 2.16. (a) A single returned waveform. (b) Averages of 50 and 1000 waveforms. (From Challenor, 2006).

2.2.2. Quality checks for altimeter data

Errors can occur in the measured data for a number of reasons. These errors can be identified by a visual inspection of plots of the raw data, but this is not practical for large data sets. There is no simple solution to the problem of quality checking altimeter geophysical data. Criteria can be set based on various statistical parameters, but the limiting values are subjective. In this section we start by discussing factors which can affect the quality of altimeter measurements, then go on to review some of the methods proposed by previous authors and use these to derive a new set of quality checks.

2.2.2.1. Factors affecting quality of measurement

Rain attenuation

Radar signals are attenuated by raindrops from both absorption and scattering. In addition to reducing the measured value of σ_0 , rain cells that are smaller than the illuminated area of the antenna footprint distort the shape of the radar signal that is returned from the sea surface, which can corrupt measurements of H_s . The effects of rain contamination are often apparent from erratic variation of H_s and σ_0 . In some cases, however, the effects of rain contamination can lead to more subtle but significant errors in these quantities. It is therefore important to identify records for which rain contamination is highly probable.

Rain flags are distributed by the space agencies as part of the GDR, based on the integrated columnar liquid water content. However, selecting such a threshold is problematic and subsequent studies have shown that this criterion alone is insufficient.

Since rain attenuation is an order of magnitude greater at Ku-band than C-band, rain contaminated observations from the T/P dual frequency altimeter can usually be identified as an abrupt decrease in Ku-band σ_0 relative to C-band σ_0 . Cailliau and Zlotnicki (2000) suggest using a formula based on both the columnar liquid water content and a statistically derived relation between Ku-band and C-band σ_0 .

Mispointing effects

The tail of the returned waveform is sensitive to the pointing accuracy of the altimeter since the returned power decreases with increased two-way travel time. The effect of mispointing on the received power is illustrated in Figure 2.17. Carter et al (1992) note that mispointing was a serious problem for GEOSAT. Moreover, estimation of the mispointing angle (also called the off-nadir or attitude angle) for GEOSAT was not good and not measured directly. Hayne and Hancock (1990) developed an improved waveform fitting procedure for GEOSAT data (compared to the on board procedure). They derive an empirical correction factor, which is a third order expression in H_s and mispointing angle.

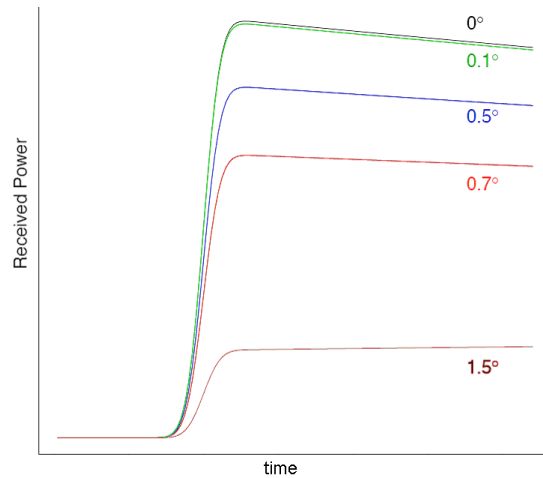


Figure 2.17. The effect of mispointing angle on the returned waveform. (From Challenor, 2006).

Loss of tracking

In order to calculate H_s , σ_0 and two-way travel time correctly, the altimeter return signal has to be centred in the tracking loop window. Strong returns from ships, sea ice and other objects and non-uniform attenuation from patchy rain cells can cause leading edge of the waveform to become distorted and lead to errors in the tracking algorithm. After a period of bad returns the wave measurements may continue to be faulty until the altimeter return signal has been reacquired correctly and centred in the tracking loop window.

There is a similar delay when the altimeter starts making measurements again after crossing the coastline. The waveform is distorted if there is land within the footprint (of about 7 km diameter, depending on wave height, as explained in section 2.2.1.4). When the satellite is moving from land to sea it can travel about 30 km before regaining lock on the sea surface. Often no data are obtained, but sometimes spurious measurements are recorded, which require careful quality checking of the individual measurements. GEOSAT had a particular problem in locking on to the sea surface as it came off the land (Carter, 1993), but subsequent satellites have provided more data in coastal regions.

2.2.2.2. Review of published quality checking procedures

Land and ocean flags

Most methods mentioned in the literature include checking a flag indicating if data is recorded over land. Data used in this study have been extracted from the RADS database (Scharroo, 2005) and come with land / water and ocean / non-ocean flags based on a 2 minute (~3.5km) mask.

Absolute limits on values

Some authors have imposed upper limits on the values which H_s and σ_0 can take and reject zero values as the default value used when it is not possible to estimate the parameter (e.g. Challenor et al, 1990; Carter et al, 1992; Young and Holland, 1996, Cotton, 2001). Limiting values for H_s range between 20m and 30m and 20dB to 30dB for σ_0 .

Number of averaged values

The number of 10Hz or 20Hz (depending on satellite) values averaged to the 1Hz mean is a good indication of quality. Pitt (1997) rejects TOPEX data if the number of 10Hz measurements averaged is less than 8 and Cotton et al (2004) reject ENVISAT data if the number of 20Hz measurements averaged is less than 18.

Attitude angle

The attitude angle has a much greater effect on σ_0 than H_s so the limiting values proposed in the literature depend on the use of the data. Carter et al (1992) and Young and Holland (1996) both use $\theta < 1^\circ$, whereas Cotton (2001) uses $\theta < 0.1^\circ$.

Standard deviation of the range

If standard deviation of the 10 or 20Hz range values about the 1Hz value is unusually high, this can indicate that the return waveform is not properly centred in the tracking loop (e.g. caused by rain cells or passage over land). Cotton and Carter (1996) reject ERS-2 data if the standard deviation in the range is greater than 0.2m and Cotton (2001) uses a limit of 0.1m for GFO data.

Standard deviation of H_s and σ_0

Similarly to the range, high standard deviations of the 10 or 20Hz values of H_s and σ_0 can indicate problems. Young and Holland (1996) and Cotton and Carter (1996) propose criteria GEOSAT and ERS-2 respectively, and Pitt (1997) proposes a criteria for TOPEX based on a weighted combination of the standard deviations of the Ku and C band values. Note that using a test such as $std(H_s) > AH_s + B$ may not pick up points where H_s is anomalously high.

Difference between measurements at two frequencies

Three of the altimeters flown to date operate simultaneously at two frequencies. TOPEX and Jason take measurements at Ku-band and C-band frequencies and ENVISAT takes measurements at Ku-band and S-band frequencies. Differences between H_s at each frequency can indicate corruption of the measurement by rain, as the higher frequency Ku-band measurement will suffer greater attenuation.

Quality flags

In addition to the above criteria the space agencies who provide the data also give a number of quality flags for each measurement. For the purpose of quality checking H_s and σ_0 the most important of these are: corruption of altimeter measurement by rain / ice, H_s quality flag, σ_0 quality flag, attitude status. For definitions how these flags are defined the reader is referred to the user manuals of the individual altimeters.

Methods involving more than one data point

Several authors have proposed quality checks based on various statistical relationships of data points to their neighbours. Challenor et al (1990) use a method to screen GEOSAT data based on a linear fit to the five previous 1Hz values. Young and Holland (1996) use a procedure to check GEOSAT data based on the standard deviation of blocks of 50 consecutive 1 Hz values. In the presence of outliers the mean and standard deviation can be poor descriptors of the location and spread of the data. In this case these tests can discard entire blocks where one large outlier biases the standard deviation. It may therefore be more appropriate to use the median and interquartile range.

2.2.2.3 Construction and testing of quality checking procedures

Quality checks for altimeter measurements of H_s and σ_0 have been constructed as follows. Firstly raw data is retrieved for a large area of open ocean so that corruption by land is not a problem. Absolute limits are imposed on the data of $0 < H_s < 25$ m and $0 < \sigma_0 < 30$ dB. The distribution of various parameters with H_s and σ_0 is established from scatter plots.

Examples for ERS-2 data are shown in Figure 2.18, using data from cycles 1-10 for the area $40^\circ\text{N} - 60^\circ\text{N}$ by $15^\circ\text{W} - 30^\circ\text{W}$ in the North Atlantic. The blue crosses are the standard deviations of the 20 Hz values averaged to obtain the 1 Hz value. The black circles are the median values of the 20 Hz standard deviation in bins of width 0.5m and the dashed lines are 95% bounds. The solid line indicated the upper bound on the 20 Hz standard deviation that is imposed for the quality check. These values have been chosen using an iterative procedure, whereby an upper bound is imposed on one parameter and then the distribution of the other parameter is checked. A bound is then established for the second parameter and then the distribution of the first parameter is rechecked. The idea is to iteratively remove bad data in order to determine the distribution of the uncorrupted data. Ultimately the limits imposed are somewhat subjective, but they should agree approximately with the observed distributions.

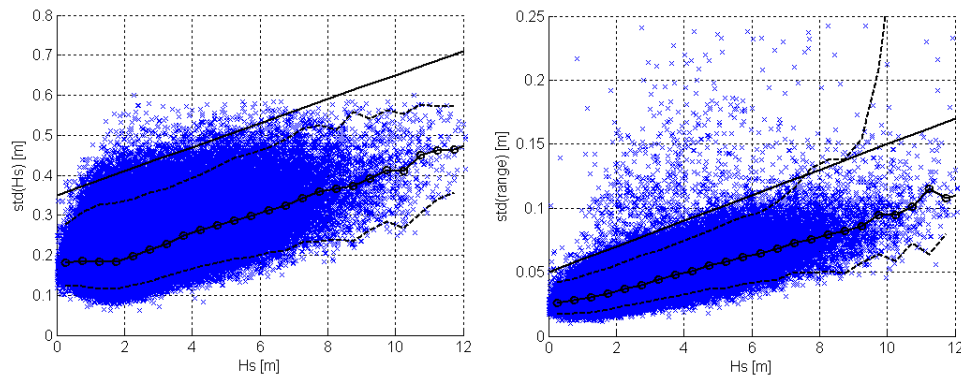


Figure 2.18. Scatter plots of standard deviation in 20 Hz measurements of H_s and range against H_s . Data from ERS-2 over the North Atlantic. Circles and dashed lines are the median and 95% bounds of data in 0.5m bins. Solid line is upper bound for the quality check.

The efficacy of the quality flags supplied by the space agencies is assessed by producing a scatter plot of H_s against σ_0 and highlighting the points with flags. Quality flags are used if they are judged to remove outlying points. Some flags supplied by the space agencies simply impose fixed limits on the parameters. For example the sea-state bias flag for GEOSAT removes all data with $H_s > 11\text{m}$ and σ_0 outside the range $7.3 < \sigma_0 < 14.05\text{ dB}$.

To ensure the quality control produces reliable data without unnecessarily discarding good data, plots of along-track values H_s and σ_0 for individual passes are visually examined, and the effect of varying the severity of the quality checks is tested. Using the procedure described above a set of quality checking criteria have been established for each altimeter. The following notation is used to describe the quality checks: N is the number of averaged 10 Hz or 20 Hz values, R is the range and θ is the off-nadir angle. Unless otherwise indicated, the notations H_s and σ_0 refer to the Ku-band values. The tests developed for each altimeter depend on the parameters provided by the space agencies, for example the standard deviation of the 10-Hz H_s measurement is not available for GEOSAT.

GEOSAT:

$$N = 10$$

$$0 < \text{std}(R) < 0.05 + 0.0075H_s$$

$$\theta < 1$$

$$H_s < 15\text{ m}$$

$$\sigma_0 > 7\text{ dB}$$

θ quality flag

GFO:

$$N \geq 9$$

$$0 < \text{std}(R) < 0.075 + 0.01H_s$$

$$\text{std}(H_s) < 0.15 + 0.033H_s$$

$$0 < \theta < 0.5$$

H_s quality flag

σ_0 quality flag

θ quality flag

ERS-1:

$$N \geq 17$$

$$0 < std(R) < 0.2 + 0.035H_s$$

$$0 < std(H_s) < 1.5 + 0.1H_s$$

$$0 < std(\sigma_0) < 0.6$$

H_s quality flag

σ_0 quality flag

ERS-2:

$$N \geq 18$$

$$0 < std(R) < 0.05 + 0.1H_s$$

$$0 < std(H_s) < 0.35 + 0.03H_s$$

$$0 < std(\sigma_0) < 0.15$$

H_s quality flag

TOPEX:

$$N \geq 8$$

$$0 < std(R) < 0.07 + 0.007H_s$$

$$0 < std(H_s) < 0.1 \text{ or } 0.1H_s$$

$$0 < std(\sigma_0) < 0.3$$

$$|H_s(Ku) - H_s(C)| < 0.5$$

θ quality flag

Poseidon:

$$N \geq 18$$

$$0 < std(R) < 0.1 + 0.02H_s$$

$$\theta < 0.2$$

θ quality flag

Ice flag

ENVISAT:

$$N \geq 18$$

$$0 < std(R) < 0.10 + 0.018H_s$$

$$0 < std(H_s) < 0.067 + 0.086H_s$$

$$0 < std(\sigma_0) < 0.3$$

$$0 < \theta < 0.3$$

$$1.5 < peakiness(Ku) < 1.8$$

If $1.5 < peakiness(S) < 1.8$ then

$$0.13H_s(Ku) - 2 < H_s(Ku) - H_s(S) < \\ < 0.2H_s(Ku) + 0.8$$

JASON:

$$N \geq 18$$

$$0 < std(R) < 0.08 + 0.014H_s$$

$$0 < std(H_s) < 0.65 + 0.05H_s$$

$$0 < \theta < 0.3$$

$$|H_s(Ku) - H_s(C)| < 1$$

H_s quality flag

σ_0 quality flag

θ quality flag

Ice flag

To illustrate the performance of the quality checks described above we will look at H_s data from a section of TOPEX phase a, pass 222 over the North Atlantic. From visual inspection of data from individual passes the quality checks performed very well on the

whole, picking up the majority obvious data spikes. Figure 2.19 shows four examples of raw and quality checked data.

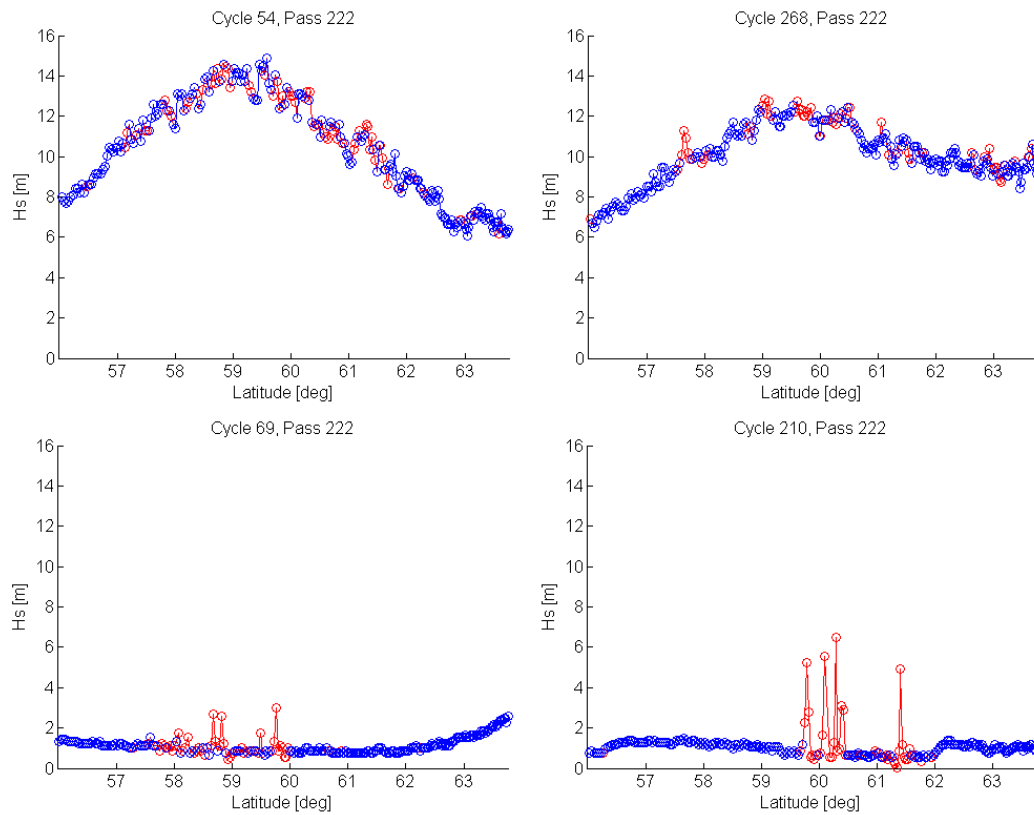


Figure 2.19. H_s against latitude for TOPEX phase A, pass 222, cycles 54, 69, 210 and 268. Data failing the quality checks is highlighted in red.

The quality checks have the tendency to exclude data preferentially in higher seas. This is normally due to greater variability and hence an increase in the standard deviation of H_s . Limiting values for the quality checking criteria are necessarily a compromise between picking up bad data and excluding good data. Despite the exclusion of some data for high values of H_s , there is sufficient data remaining that the mean or median over a distance of 30-40km should be reasonably accurate.

Close to the coast, the quality controls may fail in some instances because of along-track smoothing. In some cases when the altimeter is moving from land to sea, a good measurement may be smoothed in with a preceding corrupt measurement. However quality control parameters such as 10 and 20 Hz standard deviations are not smoothed,

so they will not catch these smoothed in points. More sophisticated statistical methods using multiple 1Hz values, similar to those described by Challenor et al (1990) and Young and Holland (1996) were tested. They picked up some bad points when the altimeter comes off land that the test on individual 1-Hz points missed. However, it was found that they did not pick up smaller data spikes and unnecessarily discard a greater quantity of good data. They are also considerably more computationally intensive when checking large quantities of data. When looking at data close to land it is recommended that a cut-off point is set by visual inspection of the data.

2.2.3 Sampling variability for spatial averages

The sampling variability for spatial averages of waves has been examined by Krogstad et al (1999b). They compare the sampling variability of estimates of H_s calculated over an area to those from time series by considering the coefficient of variation of H_s . For a JONSWAP frequency spectrum and a $\cos(2s)$ directional spectrum they derive the following approximate lower bounds for deep water:

$$C.O.V_{time} \approx 0.52(T_p / T)^{1/2} \quad [2.2.5]$$

$$C.O.V_{space} \approx 0.33(\lambda_p / d) \quad [2.2.6]$$

where T is the recording interval, T_p the spectral peak period, d the diameter of the region, and λ_p is wavelength corresponding to T_p . It should be noted that the above equations refer to theoretical lower bounds for an ideal instrument.

We can examine the sampling variability of 1Hz altimeter measurements of H_s using data from the periods where T/P was flying in tandem with Jason, and ERS-2 in tandem with ENVISAT. From its launch, ENVISAT has been flying along the same ground tracks as ERS-2, leading by 28 minutes. Similarly, Jason flew in the same orbit as T/P, leading by 1 minute, until T/P was manoeuvred into its phase B orbit.

Data from the tandem missions have been extracted and collocated for 20W to 40W by 45N to 55N in the North Atlantic. The maximum separation between 1Hz measurements allowed for the collocation is 5km. This means that the temporal separation is 1 minute for TOPEX and Jason and 28 minutes for ERS-2 and ENVISAT.

The data have been quality checked using the criteria listed in Section 2.2.2. A linear calibration has also been applied to the data (see Section 3.1 for details). Although this may seem slightly circular to use calibrated data when assessing the precision, the linear calibration only affects the bias component of the altimeter error and not the random component.

Scatter plots of the collocated 1Hz measurements are shown in Figure 2.20. The good agreement and low number of outliers gives confidence in quality checks, and indicates that altimeter measurements of H_s have a high precision, even at very high values.

Figure 2.21 shows the standard deviation in the difference between the collocated measurements against mean H_s . Unlike the case for buoy measurements, the standard deviation of the differences is roughly quadratic in H_s and does not approach zero for zero H_s . The pattern shown in Figure 2.21 is similar to the standard deviation of the 20 Hz values shown in Figure 2.18. The non-zero intercept occurs because the difference between the two measurements is a combination of the random nature of the sea surface and noise on the returned radar signal, discussed in Section 2.2.1.5. For simplicity we will refer to this combined measurement uncertainty as sampling variability.

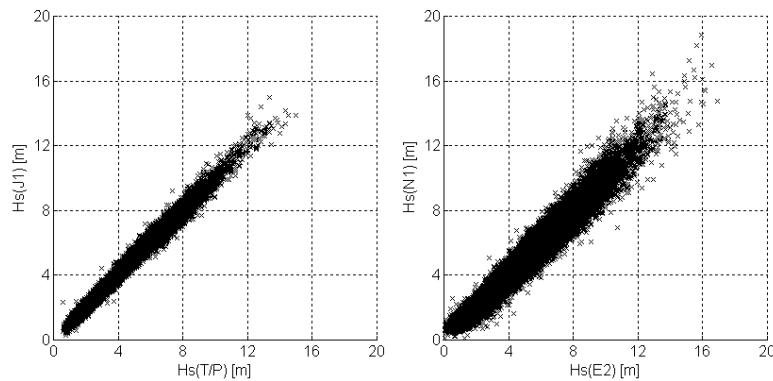


Figure 2.20. Scatter plots of collocated 1Hz measurements, left: T/P with Jason, right: ERS-2 with ENVISAT.

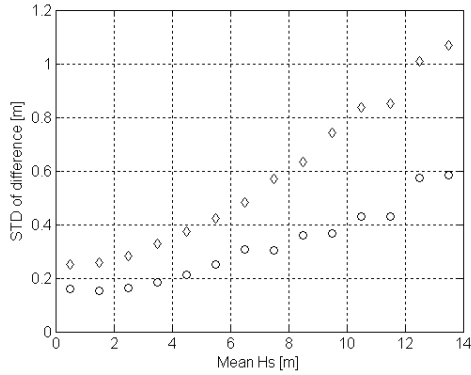


Figure 2.21. Standard deviation in difference of collocation measurements against mean H_s , in bins of width 1m. Diamonds are ERS-2 and ENVISAT, circles are T/P and Jason.

We will not attempt to quantify the sampling variability precisely here since it will be shown in the following section that the sampling variability differs for each altimeter. Also measurements of H_s from TOPEX were only reported to the nearest 0.1m (all other altimeters reported H_s to the nearest centimetre), which introduces a component to the uncertainty from rounding errors. Moreover, the comparison for ERS-2 and ENVISAT includes the effects of temporal separation as well as sampling variability, which adds a further complication. Even without the temporal separation we would expect the sampling variability to be slightly higher for ERS-2 and ENVISAT than for T/P and Jason since they have a slightly lower orbital altitude (785km compared to 1336km). The altimeter footprint diameter increases with both orbital altitude and H_s (see Section 2.2.1.4). So from equations 2.2.4 and 2.2.6 we would expect ERS-2 and ENVISAT to have about 25% higher standard deviation for a given H_s .

Another reason for the difference in sampling variability is the algorithms used to derive H_s from the return wave form. Fu and Cazenave (2001) note that an improved method of wave height estimation was implemented for TOPEX compared to GEOSAT, giving better resolution, so it is likely that the different algorithms used in different altimeters will effect sampling variability.

Finally, the smoothing algorithms used on board the satellite also has an effect on the sampling variability. Measurements from TOPEX and Jason are smoothed over 5 consecutive 1 Hz samples and ERS-2 and ENVISAT are smoothed over 10 samples (Janssen et al, 2007). One would assume that the greater number of samples used in the

smoothing algorithm for ERS-2 and ENVISAT would reduce the sampling uncertainty. However, the form of the algorithm is not known, so one cannot draw firm conclusions without knowing the weights for each sample.

The level of sampling variability shown in Figure 2.21 for T/P and Jason-1 is similar to that given by Tournadre (1993) for GEOSAT data, who found that the standard deviation of 1Hz measurements was $0.06+0.03H_s$. We can conclude that the sampling variability from altimeter measurements is a similar level to that from buoy measurements, except at low H_s . In Section 3.1.2, we will go on to make direct comparisons of buoy and altimeter measurements of H_s and assess the accuracy of each. First we need to discuss the effects of short-scale spatial variability of wave height. A discussion of sampling effects on period parameters from altimeter measurements is given in Section 3.2.

2.2.4 Short-scale spatial variability of wave height

It is important to quantify the effects of spatial variability in the wave field when comparing measurements from two instruments. Spatial variability of the wave field is difficult to quantify with in-situ instrumentation since it would require instrument deployment in a dense grid over a large area. Because of high speed of satellites we can assume that a transect across an ocean basin is synoptic, i.e. data is obtained simultaneously over a large area.

Spatial wave height spectra have been presented by Monaldo (1988, 1990) and Challenor (1993). However, these include a component from sampling variability and therefore may overestimate the variability. Moreover, as with temporal variability we would expect greater variability at higher wave heights. Tournadre (1993) presents spatial spectra of GEOSAT data with the noise component removed and finds that the shapes of the spatial and temporal spectra very similar, both spectra being linear in log-log space up to 300km or 3 days.

It is not a simple problem to determine the spatial variability as we did for temporal variability in Section 2.1.4, since we do not know the sampling variability precisely. Moreover, the effects of the along-track smoothing will affect the observed spatial

variability as well. This problem was noted by Challenor (1993) when comparing along-track spectra of H_s from GEOSAT and ERS-1.

Figure 2.22 shows the standard deviation in the difference between measurements at separations of 1, 5, 10, 15 and 20 samples, against the mean H_s . It is clear that there are differences in the level of variability for each altimeter at a given separation and mean H_s . TOPEX has the lowest variability at low H_s and also the lowest variability for low separations. This may be a result of the along-track smoothing of measurements on board the satellite. For larger separations, the differences between each altimeter decrease as the component of the difference from sampling variability becomes proportionally smaller. Also at greater separations the effect of along-track smoothing will also be much weaker.

The plots for Jason-1 and ENVISAT are similar, indicating that the sampling variability and smoothing level is similar for each. The sampling variability for ERS-2 is the highest of the four altimeters, especially at low H_s . From this we can conclude that the higher standard deviation for the differences between ERS-2 and ENVISAT shown in Figure 2.21 is not only due to temporal separation, but from the higher sampling variability of ERS-2 compared to TOPEX.

From the result of Tournadre (1993) that spatial and temporal spectra are the same shape, we would expect that in the absence of sampling variability and smoothing effects, the plots shown in Figure 2.22 would be linear in H_s , similar to those shown in Section 2.1.4. We should note that even with no sampling variability on the measurements, we would not expect the line to pass exactly through zero. In the hypothetical case of zero wave height, we would not expect these conditions to persist spatially for an indefinite distance. However, a linear relationship with zero intercept was a reasonable approximation for temporal separation so may be appropriate here as well.

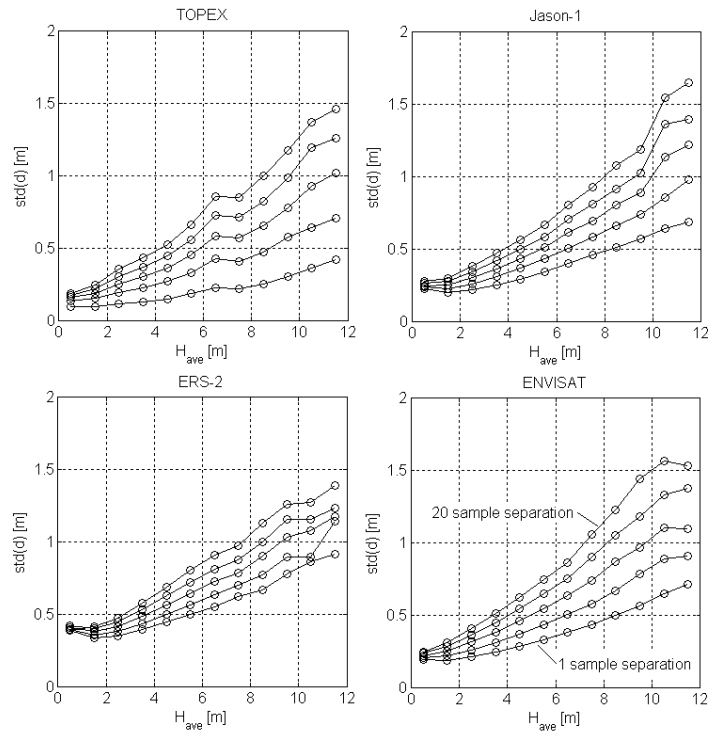


Figure 2.22. Standard deviation of differences against average H_s in bins of width 1m, at separations of 1, 5, 10, 15 and 20 samples.

As noted in Section 2.1.4, Tournadre (1993) found that spatial and temporal scales of H_s are dependent on location, with areas with a swell dominated wave climate having larger scales than areas with a wind wave climate. It is therefore possible that part differences between the altimeters may be due to climatic variations in wave conditions, between the periods covered by each altimeter. This has been tested by comparing ten individual years of data from TOPEX. It was found that the differences were most pronounced at high H_s , where there is typically little data. At low H_s where there is plenty of data, spatial variability is fairly constant from year to year and any differences between years are far less than differences between altimeters. Interannual and climatic variability in wave conditions are discussed further in Section 6.

2.3 Numerical Wind-Wave Models

Estimates of wave conditions produced from numerical wind-wave models are an important complement to in-situ and remotely sensed observations. The usefulness of

in-situ observations is limited by the sparseness of their deployment, whilst altimeter observations are limited by spatial and temporal sampling issues, lack of spectral and directional information and problems measuring close to the coast. Model data can be produced with dense resolution in space and time and can provide long histories for assessing inter-annual and climatic variability.

Understanding the errors in model data is vital for the calculation of uncertainty of derived wave energy statistics. In this section we start by giving an introduction to numerical wind-wave models and briefly discuss the factors which can affect the accuracy of their predictions. We then give a qualitative description of the error structure of model data.

2.3.1. Brief introduction to numerical wind-wave models

Wave models attempt to replicate the growth, propagation and decay of ocean waves based on the winds over the area in question. The fundamental concept underpinning wind-wave modelling is the energy balance equation. This states that the evolution of the wave spectrum is the sum of three source terms describing the input of energy from the wind, non-linear transfer of energy within the spectrum and the dissipation of energy from breaking or shallow water processes. It can be written as (e.g. Tolman et al, 2002)

$$\frac{dE(f, \theta)}{dt} = S_{in} + S_{nl} + S_{ds} \quad [2.3.1]$$

where $E(f, \theta)$ is the wave variance spectrum, S_{in} is the wind input, S_{nl} are non-linear interactions and S_{ds} is the dissipation source term. In slowly varying conditions such as non-steady currents or water depth, wave action density (defined as the variance spectrum divided by the intrinsic angular frequency - the frequency measured in a frame of reference moving with the current) is conserved rather than wave energy. When equation 2.3.1 is rewritten in terms of wave action it is known as the action balance equation. A detailed derivation of the energy and action balance equations is given by Komen et al (1994).

In the first generation of wave models non-linear interactions were not computed. The second generation of wave models resulted from a better understanding of energy

transfer processes, but due to limitations in computer power at the time, nonlinear interactions were computed in a simple parameterised form. The third generation of wave models, used at present, compute an explicit representation of the all three source terms and the step-by-step evolution of the wave spectrum, without *a priori* assumptions about the spectral shape. There are currently two third generation wave models run operationally at meteorological agencies: the WAM model (WAMDI Group, 1988; Komen *et al.*, 1994) and the WaveWatch III model (Tolman et al, 2002).

As well as using information on the wind field, wave observations from in-situ measurements, satellite altimeters and SAR can be routinely assimilated into both analysed and hindcast wave fields (see e.g. Lionello et al, 1992; Hasselmann et al, 1997; Voorrips, 1999; Abdalla et al, 2006). Model runs with assimilated data have been shown to significantly reduce the errors in modelled wave parameters.

2.3.2 Sources of error in wave models

The error sources in the estimates produced by wave models can be viewed as either internal or external to the model. The internal sources of error are the formulation of sources terms or ‘model physics’ and the numerical scheme, while external errors refer to errors in the input data, primarily the wind field. An in-depth review of the present state of the art and limiting factors in the physics and numerics of wave modelling is given by Cavaleri et al (2007). In the following we give a brief overview of the error sources.

2.3.2.1 Input data

In validation studies it is common practice to assess quality of wind input at the same time as the wave estimates, in order to estimate the relative importance of internal and external errors. It is not straightforward to separate internal from external errors. Janssen (1998) has presented a simple model for the error in H_s resulting from wind speed errors and shows that they are proportional to the square of the error in wind speed. Rogers et al (2005) have shown that, in contrast to previous studies, the errors in the wind fields used at Fleet Numerical Meteorology and Oceanography Center (FNMOC) are no longer the dominant source of errors in wave estimates from WaveWatch III. However, this is not to say that the quality of the wind forcing is no longer important to accuracy. Recently, Feng et al (2006) have tested the sensitivity of WaveWatch III to four

different wind input fields and shown that the accuracy is critically sensitive to choice of the wind field product. Other input fields such as currents, bathymetry, or bottom conditions are less important in the open ocean but become significant in shallower coastal waters.

2.3.2.2 Numerical resolution

Describing a continuous physical process such as wave growth, propagation and dissipation with a discrete model can lead to significant errors. The resolution of the geographic grid, the time step for integration and the spectral resolution (number of frequency and direction bins) all affect accuracy. The propagation of swell on a grid with discrete directional resolution can lead to the disintegration of a continuous swell field into discrete packets. This process is known as the Garden Sprinkler Effect and is discussed by Tolman (2002b). The accuracy of swell propagation is also affected by blockage by small islands and ice which are not resolved in the spatial grid (Tolman, 2003; Ponce de Leon and Guedes Soares, 2005). Coarse geographic and temporal resolution can also lead to small intense systems being subject to some smoothing, resulting in systematic underestimation of peak wind speeds and hence peak wave heights (Tolman 2002a).

2.3.2.3 Model physics

There remain many open questions about the formulation of source terms in spectral wave models. Amongst the most important ones are the method used to estimate non-linear interactions, spectral dissipation in deep water, and air–sea momentum transfer at high wind speeds. At high wind speeds many of the assumptions about the processes involved are stretched to their limit. Moreover observation of wave growth in extreme conditions are, by their nature, limited. Rogers et al (2005) stress that “*given the necessary reliance on approximations in today's state-of-the-art wave models, it may be especially difficult for these models to have ‘universal’ tuning. In particular, tuning for applications at one scale may inevitably degrade performance at another scale. For example, tuning to short-fetch empirical growth curves probably will not produce a skilful global model.*”

There is also some growing concern in the wave modelling community that there may be an intrinsic limit to the accuracy achievable from the spectral approach (Liu et al,

2002; Cavaleri, 2006). Liu et al (2002) show that even when working with accurate, carefully evaluated wind fields, the wave model results show a scatter not justified by the known uncertainties in the input information. Nevertheless, some improvements can be expected to be made by improving the physics and numerics in wave models.

2.3.3. Qualitative description of model errors

The performance of models in terms of integral parameters such as H_s and T_e is, on the whole, fairly good. However, Cavaleri (2006) notes that the comparison between modelled and measured spectra is often unsatisfactory, not only in the details, but sometimes also in the general structure. In this study we will only consider the accuracy of integral parameters.

As noted before, modelled wave spectra can be considered an estimate of the average conditions over the grid spacing and time step used in the model. Typically, global or oceanic scale wave models will be run with a grid spacing somewhere between 0.5° and 3° (about 50-300km) with a time step of 3 or 6 hours. Measured data is usually obtained over a smaller scale, with buoys representing a point average over time (between 20 minutes and 1 hour) and altimeter data representing an instantaneous spatial average over an area of 5-10km in diameter. The spatial and temporal variability of wave conditions will therefore result in differences between measurements and modelled data. These differences are sometimes referred to as ‘representativeness errors’ and the error is assigned to the measured data (Janssen et al, 2007).

The errors in modelled parameters exhibit short term temporal correlation. That is, an over- or under-estimate in H_s or other parameters will typically persist for a number of hours. For instance models will tend to over or under predict the intensity of an entire storm, which leads to correlation of errors for up to a few days.

Additionally errors in different parameters can be correlated. At high sea states, since wave spectra tend toward standard Bretschneider or JONSWAP type forms, an overestimate in model H_s will result in an overestimate of period as well. This correlation of errors in different parameters means that one needs to be careful when calibrating model data, since adjusting model parameters independently may lead to changes in the shape of the joint distribution.

Errors in modelled parameters can be thought of as having a mean or bias and also a random component. Both the mean and bias component will have a complex dependence on the actual wave conditions. For instance the bias of a model estimate of H_s may have a dependence on the actual H_s , period, spectral shape, swell age, etc. Moreover, it has been shown by numerous authors that biases change both with location and with time. This is due to the way that errors occur in models and their propagation through the model domain.

Janssen (2008) presents a particularly clear illustration of the non-stationary biases in ECMWF WAM model spectra. A plot of the bias in spectral energy binned by frequency shows that the model tends to over-predict energy at lower frequencies in the (Northern Hemisphere) summer and much less in the winter time. Moreover, the magnitude of this bias and its dependence on both frequency and time of year changes from year to year. He notes that the main reasons for the changing biases are that large swells generated in the Southern Ocean in the Southern Hemisphere winter time are not well modelled due to unresolved islands and atolls (mainly in the Pacific) and the formulation of the dissipation source term.

This goes to show that it is difficult to define and adjust for a ‘mean error component’ since varying conditions lead to varying amounts of internal and external errors occurring and aggregating over the model domain. Therefore errors in wind seas and young swells can be expected to have different characteristics to older swells that have propagated further, increasing uncertainties.

A further reason for non-stationary biases in model data is changes made to the models themselves. This is more of an issue for archived data from operational models than for hindcasts. However, despite the fact that hindcasts are run with a constant model setup, the quality of the input wind fields and assimilated wave data may be varying.

Finally, we note that modelled data may be subject to temporal offsets, with the model predicting that a storm arrives slightly earlier or later than it actually does. This type of error is sometimes referred to as a ‘jitter error’. Jitter errors are not so important when calculating long-term mean statistics from modelled data, but are important for validation purposes where concurrent modelled and measured data are compared.

To summarise, the main features of the errors in model data are:

- The bias and variance of modelled parameters may depend on multiple factors such as H_s , T_e , swell age, etc.
- Errors in parameters will exhibit short-term autocorrelation.
- There may also be correlation of errors between parameters, e.g. errors in H_s and T_e may be correlated.
- The bias and variance of the modelled parameters may be non-stationary in both time and space.
- There may be temporal offsets or ‘jitter errors’ in modelled parameters.

3. Intercomparison of Altimeter and Buoy Measurements

In the last chapter we discussed the precision of altimeter and buoy measurements. Precision is a measure of repeatability of the instrument, limited by instrumental noise and by the random nature of the sea surface, and is not the same as absolute accuracy. In this chapter we discuss the intercomparison of altimeter and buoy measurements to assess their accuracy. We also develop a new method of estimating wave period from altimeter data, which is vital for the estimation of the power produced by a WEC.

Due to the innate differences between altimeter and buoy measurement principles it is possible for both a buoy and altimeter to be making perfectly accurate estimates and for those estimates to differ. Moreover, measurements are often separated both spatially and temporally. Therefore we compare the observed differences between buoy and altimeter measurements to the differences we would expect from sampling variability and separation, based on the results established in Chapter 2.

3.1 Significant wave height

The accuracy of significant wave height from satellite altimeters has been well documented over the years, with numerous techniques used to establish calibrations. We make a brief review of the theory, then go on to perform an example calibration/validation exercise to demonstrate the accuracy of altimeter measurements and confirm the results from Chapter 2 on spatial, temporal and sampling variability.

3.1.1. Statistical techniques for calibration and validation

There are a number of ways in which altimeter and buoy datasets can be analysed. The most appropriate technique will depend on the kind of information one is looking to extract. Unlike the usual calibration problem, we cannot assume that our standard, buoy measurements, have such small errors that they can be neglected. As we have seen in Chapter 2, the sampling variability of buoy and altimeter measurements is of a similar level. Therefore it is not appropriate to use standard least squares regression which

assumes that all the random errors occur in the dependent variable. Preferably a weighted orthogonal distance regression (ODR – see Cheng and van Ness, 1999) should be used, however in practice standard ODR is normally used because of the difficulty of estimating the errors in each dataset. Some notes on the use of different types of linear regression are presented in Appendix C.

3.1.1.1. Collocated datasets

The most popular approach is to make a direct comparison of near-coincident altimeter and buoy measurements. Since it is unlikely that an altimeter ground track will pass directly over a buoy the two measurements will be separated spatially. Buoys commonly only report wave conditions averaged over 20-40 minutes once per hour, therefore altimeter and buoy measurements are likely to be separated temporally as well. This spatial and temporal separation introduces a random error to the comparison in addition to the sampling variability of each instrument. Some studies use the mean or median value of the altimeter measurement within a certain radius of the buoy to reduce the effect of sampling uncertainty, whereas others use the nearest 1Hz value from the altimeter.

The collocation criteria used in a study are a compromise between assumption that wave conditions are stationary and the number of points included. Criteria are normally in the range of 50-100km and 30-60 minutes. As we have seen in Chapter 2, in the open ocean it is a fair assumption that conditions are stationary over these intervals, although in shallow water or close to the coast there can be considerable variability on these scales.

The relation between the collocated measurements is found using ODR. Some earlier studies used ordinary least squares regression, but this can underestimate the slope of the regression line (see Tolman, 1998). The use of orthogonal distance regression requires knowledge of the ratio of the variances of the random errors (see Appendix B). However, often it is simply assumed that the variances of the errors are equal, which as we have seen in Chapter 2 is a reasonable approximation. The presence of three data sets makes it possible to estimate both systematic errors between the data sets and the variance of the random errors of each data set. Caires and Sterl (2003) and Cotton et al (2004) describe similar methods for computing functional relationship estimates between three or more datasets and estimating their random error variances. This

method can be applied whenever there are three simultaneous measurements of the same parameter, such as buoy, altimeter and wave model data, or buoy data together with two altimeter measurements (e.g. from a dual frequency altimeter such as TOPEX, ENVISAT or JASON).

3.1.1.2. Comparison of climatological means

Cotton and Carter (1994) compare monthly mean values of altimeter H_s averaged over $2^\circ \times 2^\circ$ squares with buoy measurements. The method greatly increases the available data as collocation in time is not required. Also, taking means of the data reduces the effect of sampling variability. Their results are in good agreement with results from collocation studies. However, comparisons of high H_s are obscured by taking means, so differences at high values cannot be revealed by this method.

3.1.1.3. Comparison of distribution functions

Occurrence statistics, or probability density functions, are a useful way of examining how well an instrument can recreate an accurate, physically representative distribution. In considering density functions one is looking for a smooth shape, which matches with previous data or a physical understanding of the parameter involved. If the function is not smooth, then there is an indication that the instrument may preferentially measure some values and not others. This sort of fault may not be observed by regression.

When implementing this technique it is important to restrict the two datasets to the same area and period so that locational and seasonal effects are not confused with instrumental effects. Freilich and Challenor (1994) describe a method of constructing a fully empirical model function relating the backscatter coefficient, σ_0 , to the near surface wind speed, U_{10} , using only the individual (rather than joint) distributions of σ_0 and U_{10} .

3.1.2. Example calibration / validation for H_s

3.1.2.1. The collocated data set

The NDBC buoy network is the largest source of open ocean buoy data calibrated to a consistent standard. It has been noted by previous authors (e.g., Challenor and Cotton, 2002) that buoy networks operated by other agencies (e.g., UK Met Office, Meteorological Services of Canada, Japan Meteorological Agency) have different

calibrations relative to the altimeter H_s . Therefore only NDBC buoy data has been used in this analysis. Buoys located in deep water in open-ocean, at least 200 km from land have been used, so that there are no shallow water effects and spatial variability is low. The locations of the buoys are shown in Figure 3.1. Further details of the buoys used in this analysis can be found in Mackay et al (2008a), which is included as Appendix D to this report.

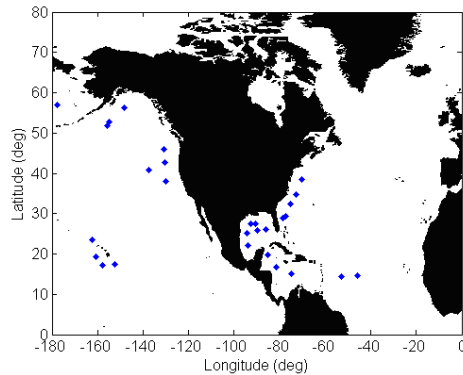


Figure 3.1. Locations of the 28 deep-water NDBC buoys used in the collocated data set.

Spectral moments are usually defined as integrals over frequencies from zero to infinity. In practice no instrument can measure infinitely high frequencies so either a theoretical high frequency tail must be added to the spectrum or an appropriate cut-off frequency chosen. In this chapter, moments are calculated as the integral over the frequency range reported by the buoys, detailed in Table A2 of Mackay et al (2008a) [Appendix D].

Altimeter data has been retrieved from the RADS database (Scharroo, 2005) held at the National Oceanography Centre (Southampton, UK) for TOPEX, Poseidon, Jason, ERS-2, Envisat, and Geosat Follow-On (GFO). Data for ERS-1 and GEOSAT have not been used because the NDBC buoy data is only available in an easily useable format from 1996 onwards. Note that all data are for Ku-band and offline (as opposed to fast delivery) products. TOPEX values of H_s have been corrected for the drift at the end of the life of the TOPEX Side A circuitry using a quadratic function based on ERS2-TOPEX crossovers (see Queffeuilou, 2004). TOPEX Side B values have been offset slightly to conform to side A levels (Scharroo, 2005). We therefore consider data from the TOPEX A and B-side circuits as one data set. Other than this, no calibrations have been applied to the data.

The altimeter data have been quality checked using the procedures described in Section 2.2.2 and the buoy data is quality controlled by the suppliers (see National Data Buoy Centre, 2003). A small number of additional outliers, not picked up by the quality control procedures, were visible from scatter plots of altimeter against buoy H_s . These have been removed as follows: First the altimeter H_s is calibrated against the buoy H_s using orthogonal regression. If the calibrated altimeter measurement differs from the buoy measurement by more than 3 standard deviations, then the pair is removed. The standard deviation is estimated as $0.15 + 0.05H_s$.

A maximum separation of 100 km and 30 minutes has been chosen to define a coincident measurement. The nearest 1 Hz value from the altimeter is used in preference to a mean or median value within a certain value of the buoy so that the results of Chapter 2 can be verified.

3.1.2.2. Results

Figure 3.2 shows examples of scatter plots of altimeter against buoy measurements with orthogonal regression lines overlaid, for TOPEX and ERS-2 data. There is no evidence of non-linearity in the relationship. Some authors have noted that the Fast Delivery data from some altimeters has a non-linear calibration for low wave heights (e.g. Tolman 2002, Janssen et al 2007). However, this does not appear to be the case for the offline products, with the regression line passing through the centre of the data at all wave heights. The calculated calibrations for each altimeter are given in Table 3.1 in the form $H_s(buoy) = a + bH_s(alt)$.

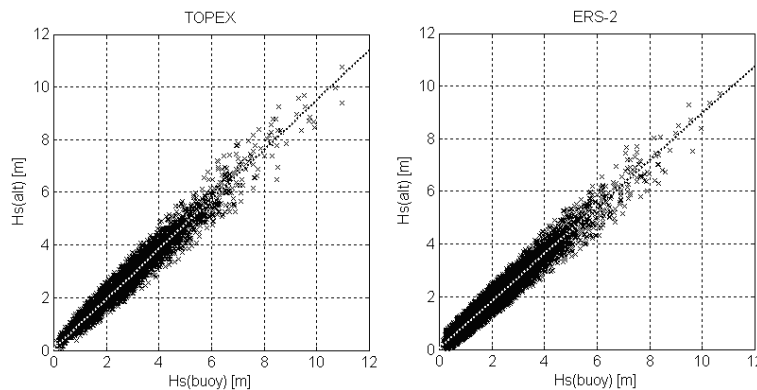


Figure 3.2. Orthogonal regression of altimeter H_s on buoy H_s . Left: TOPEX data; right: ERS-2 data.

	N	a	b
TOPEX	9332	-0.07	1.06
Poseidon	502	-0.19	1.07
Jason-1	3962	-0.08	1.08
ERS-2	8306	-0.08	1.12
ENVISAT	2974	-0.23	1.08
GFO	6247	0.06	1.09

Table 3.1. Linear calibrations of altimeter H_s against NDBC buoy data. N is the number of data points used in the regression.

Monaldo (1988) estimated the level of scatter expected when comparing buoy and altimeter measurements by considering the effects of sampling variability and spatial and temporal separation. As we have noted in Chapter 2 the estimates of spatial and temporal variability of Monaldo (1988) included a component from sampling variability and did not account for the increasing variability with H_s . As a result, Monaldo's estimate of the expected RMS difference slightly exceeded the observed RMS difference.

We can make a slightly different check on the level of scatter observed between the collocated measurements. Figure 3.3 shows the standard deviation of the differences between the buoy and altimeter H_s and the standard deviation of the differences altimeter measurements at a separation of 50km (the average separation in the collocated dataset) for TOPEX and ERS-2 data. The agreement is good for TOPEX, indicating that the sampling variability of the buoy data and 1Hz altimeter measurements are similar. For ERS-2 the difference between two altimeter measurements is greater than the difference between the buoy and altimeter, especially at low wave heights. This is consistent with the results from Section 2.2.3 and 2.2.4 which showed higher sampling variability for ERS-2 than for TOPEX, in particular at low H_s . As noted in the previous chapter, it is difficult to separate the altimeter sampling variability from the spatial variability of the wave field due to the effects of along-track smoothing. This makes it difficult when quantifying the expected differences between altimeter and buoy measurements to be more precise than to say that the scatter is broadly in agreement with our understanding of the sampling properties of each instrument. The comparison made here has neglected the contribution to the scatter, from the temporal separation between the buoy and altimeter measurements. From equation 2.1.20 we estimate that this is approximately $0.013H_s$ for an average separation

of 15 minutes, which is small in comparison to the sampling variability and spatial variability. It should therefore not effect our calculations greatly.

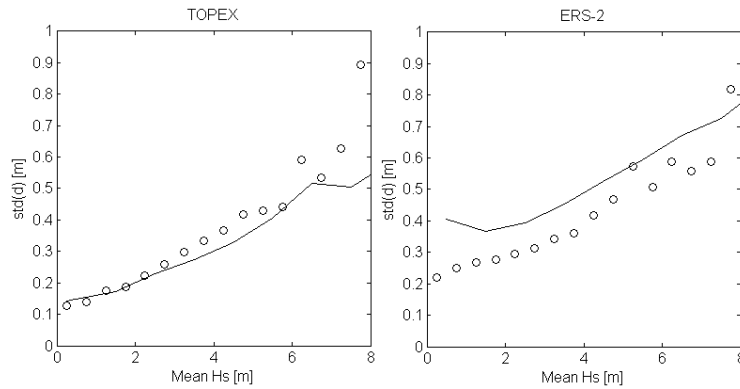


Figure 3.3. Circles: Standard deviation of differences between buoy and altimeter. Solid line: Standard deviation of differences altimeter measurements at 50km.

A similar investigation into the level of scatter was made by Krogstad et al (1999b). They compare TOPEX data averaged over 3 consecutive points with NDBC buoy data. They show that the level of scatter for H_s over 2m is equivalent to the simulated scatter between two 20 minute buoy measurements, with no spatial separation (they do not state what the actual spatial separation in their collocated dataset was). For H_s below 2m the observed scatter is slightly higher than the simulated level, and they suggest that this is because of the effects of spatial separation.

3.1.2.3. Discussion

Cotton et al (1997) note that there remain problems with providing calibrations and accuracy estimates at high H_s where there are few collocated measurements. Inaccurate calibrations at high values have a significant effect on climatological means and predicted extreme values. Krogstad & Barstow (1999) note that all calibration relations for TOPEX give more or less the same correction for the most frequent medium sea states. However, there is a 0.5m difference in the range of calibration functions at $H_s = 10m$. This highlights the necessity of validating altimeter data against as large a set of buoy data as possible before using the data for extreme wave analysis.

Challenor & Cotton (2002) note a further problem is the lack of calibration data in the southern hemisphere. Wave conditions can be expected to be different here with larger

fetches and more swell. It would therefore be useful confirm the calibrations and the altimeter algorithms in these regions.

It has been noted by several authors that buoy networks operated by different countries have different calibrations. Challenor and Cotton (2002) calibrate altimeter H_s measurements from GEOSAT, ERS-1, ERS-2, TOPEX, and POSEIDON against the NDBC buoy network, so that they have a dataset which is internally consistent and consistent with the NDBC buoy network. They use this merged altimeter dataset to check the calibrations of three other buoy networks operated by the UK Met Office (UKMO), the Japan Meteorological Agency (JMA) and the Meteorological Services of Canada (MSC). They note significant differences between the buoy networks in terms of their slopes (UKMO, MSC) or intercept (JMA), with the UKMO buoys reading about 4 per cent high compared to NDBC, MSC to be 5 per cent low and the JMA buoys to have a bias of about 30 cm. These are relative measures and they note that they cannot say which calibration is correct.

Challenor and Cotton (2002) have tested for a possible dependency of the altimeter/buoy H_s relationship on buoy size, using calibrated altimeter-NDBC buoy collocated data (about 5500 data pairs from TOPEX, GEOSAT, ERS-1 and ERS-2). Although the buoy platforms range from 3-12 m in diameter, they found no significant change in the regression line with buoys of different size. This indicates that despite large differences in size (and therefore response) the NDBC buoys appear to be consistently calibrated in terms of H_s .

3.1.2.4. Conclusions

We can conclude that with the application of linear calibrations, altimeter data provide an accurate measurement of H_s . The precision of altimeter measurements compares well to that of buoy data, even at high H_s , but varies between altimeters. The scatter between altimeter and buoy measurements agrees with the expected differences from sampling variability and separation, calculated in Chapter 2 without comparing the instruments directly.

3.2 Wave period

In order to estimate the energy produced by a WEC an estimate of both wave height and period is required. Several models have been proposed to derive wave period estimates from satellite altimeter data, but each has its drawbacks. In this section a new algorithm is developed to provide wave period estimates from altimeter data. The new algorithm is compared to existing algorithms and shown to perform better in terms of bias and RMS error, ability to replicate the joint distribution of wave height and period, and residual trends with various parameters. In Chapter 4 we go on to show that an accurate estimate of WEC power can be obtained using estimates of T_e from the new algorithm together with the calibrated H_s measurements described in the previous section.

The following work (Section 3.2) has been published as: Mackay EBL, Retzler CH, Challenor PG, Gommenginger CP, 2008. “A parametric model for ocean wave period from Ku-band altimeter data”. *J. Geophys. Res.*, 113, C03029, doi:10.1029/2007JC004438. The paper is included as Appendix D. The co-authors listed above provided advice on the manuscript, but the work presented here is my own.

3.2.1 Previous studies on altimeter wave period

In addition to significant wave height and range, satellite altimeters measure the backscattered power σ_0 , returned from the sea surface. The backscatter coefficient is routinely used to estimate near-surface wind speed (U_{10}), but there is evidence that altimeter wind speed are affected by the degree of sea state development, and can be biased low by as much as 1.5 m/s in developing wind sea conditions (Gommenginger et al, 2002).

Several models have been proposed relating altimeter H_s and σ_0 to wave period (Davies et al, 1997; Hwang et al, 1998; Sarkar et al, 1998; Gommenginger et al, 2003; Quilfen et al 2004; Kshatriya et al, 2005). To date the most accurate model proposed is that of Quilfen et al (2004) [hereafter referred to as Q04]. They use a neural network to establish a relationship between altimeter H_s and σ_0 with buoy T_z , based on a collocated dataset of TOPEX/Poseidon and National Data Buoy Centre (NDBC) buoy

measurements. They exclude data where $\sigma_0 > 16$ dB from their analysis, suggesting that these are due to surface slicks for which there are no waves. Their algorithm is:

$$T_z = \exp(-17.1642a + 13.5844), \quad [3.1]$$

where

$$a = \frac{1}{1 + \exp(0.6573H_s^{0.1084} \sigma_0^{0.2962} - 2.2377)} \quad [3.2]$$

Although the Q04 algorithm is quite accurate, there are some disadvantages with this approach. Firstly, the accuracy of the algorithm attainable from a neural network is limited by the architecture of the network. Secondly, the underlying relationship between the variables is often not clear from the output of a neural network. So, in order to apply the Q04 algorithm to data from other altimeters, the measurements must be cross-calibrated to the same levels. Quilfen et al (2004) also create a second algorithm, which makes use of C-band data as well. We will only consider their Ku-band algorithm in this paper. A brief discussion of dual-frequency period algorithms is given in Section 3.2.4.

An earlier semi-empirical model was proposed by Gommenginger et al (2003) [hereafter referred to as G03]. They use heuristic arguments to show that $T \sim \sigma_{0_L}^{0.25} H_s^{0.5}$, where σ_{0_L} denotes the backscatter in its linear, non-dB form, (elsewhere the symbol σ_0 without the subscript L , denotes the backscatter coefficient in decibels). Empirical models for T_z , T_m and T_p (the inverse of the peak spectral frequency) are created using linear regressions of wave period against $X = \sigma_{0_L}^{0.25} H_s^{0.5}$ in both linear and log-log space, using collocated NDBC buoy and TOPEX Ku-band measurements. The models created by performing the log-log regression proved to be more accurate and only these will be considered from now on. Although not as accurate as the Q04 algorithm, the G03 algorithm is still widely used, so it is included here for comparison.

Previous comparisons of buoy, altimeter and model period data have shown that the models in question performed worse than the existing altimeter wave period algorithms. Caires et al (2005) perform a triple collocation of T_z measurements from NDBC buoys, TOPEX G03 algorithm and the ECMWF ERA-40 wave re-analysis. They show that the

standard deviation in the ERA-40 T_z data is higher than both the buoy data and TOPEX G03 estimate. Quilfen et al (2004) compared one month of global data from WaveWatch III to NDBC data and T_z estimates from TOPEX using the Q04 algorithm. They showed that in all locations the WaveWatch III data had a larger bias than the altimeter data when compared to the buoy measurements. However, since these comparisons were performed improvements have been made in numerical wave modelling. For example, Bidlot et al (2007) show that using a reformulated dissipation source term reduces the rms error in T_z for the ECMWF WAM model, compared to the version of WAM used for the ERA-40 re-analysis.

3.2.2 Development of a new period algorithm

The same collocated dataset, described in Section 3.1.2.1, is used to develop a new period algorithm. To start with trends are observed using the combined collocated data from the six altimeters, a total of 30,733 data points. Differences in calibration between altimeters are small, of the order of tenths of meters for H_s and tenths of decibels for σ_0 (comparisons of the calibrations of σ_0 for different altimeters can be found in e.g. Callahan et al, 1994, Tran et al, 2005), and the greater number of data points makes trends in the data easier to observe. Since different period parameters are useful for different applications (T_z is often used for ocean engineering, whilst T_e is used for wave energy applications), the relationship of altimeter measurements with both T_z and T_e is discussed.

Figures 3.4 (a) and (b) show the mean T_z and T_e for bins of H_s and σ_0 . It is apparent that there is a threshold level around 13dB above which σ_0 is no longer related to the wave period. Figure 3.5 (a) shows a similar plot of mean significant steepness (defined as $2\pi H_s/gT_z^2$) for bins of H_s and σ_0 . It can be seen that times when σ_0 is above the threshold level correspond to times of low significant steepness. Figure 3.5 (b) shows a density plot of σ_0 against significant steepness. The step-change in the response of σ_0 to significant steepness at around 13dB is clearly visible.

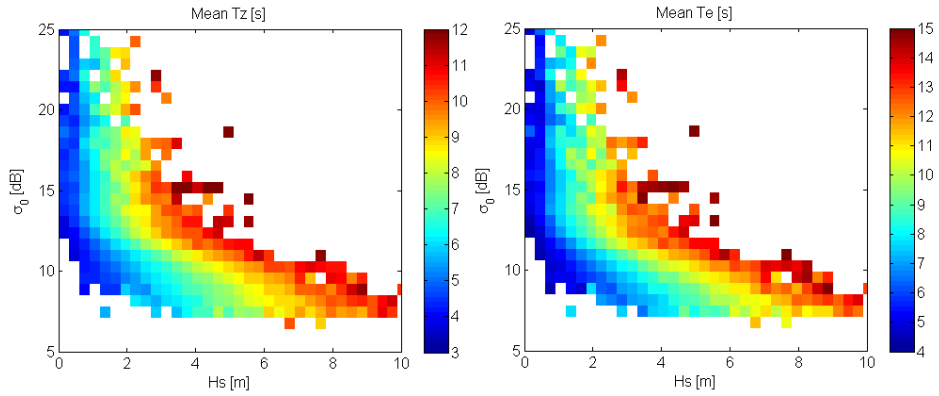


Figure 3.4. Mean T_z (left) and T_e (right) against H_s and σ_0 for combined collocated data.

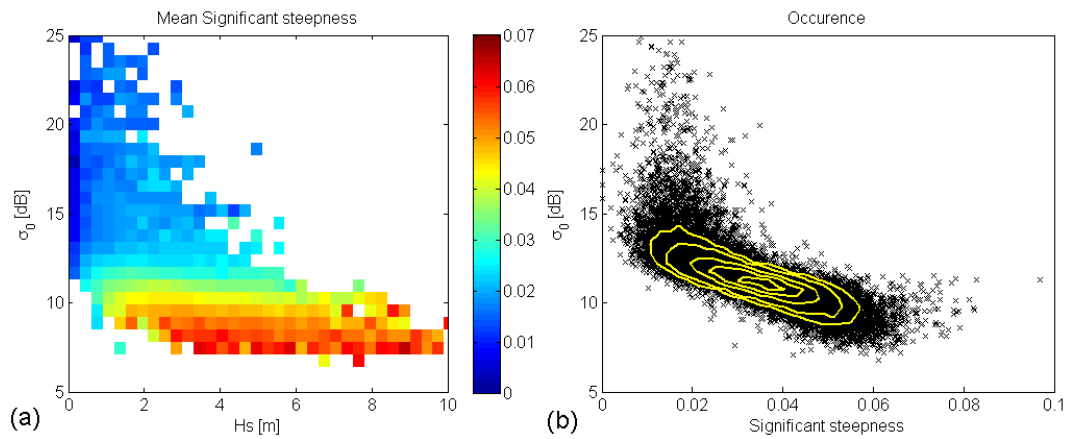


Figure 3.5. (a) Mean significant steepness against H_s and σ_0 for combined collocated data. (b) Scatter plot of significant steepness against σ_0 , with contours showing distribution of data.

From Figure 3.4 it appears that when σ_0 is below the threshold level, for constant T_e or T_z the relationship between H_s and σ_0 is linear. To test this hypothesis data from individual altimeters is used, so as not to introduce any bias from calibration differences. The data is binned by buoy T_z or T_e in bins of size 1s and orthogonal regression (Cheng & Van Ness, 1999) is used to fit lines of the form $\sigma_0 = A + BH_s$. Figure 3.6 shows the results for TOPEX and T_z , but the same trends were observed for all the altimeters. A strong correlation is observed for all values of T_z , with no evidence of non-linearity. The same relationship was also observed for T_e . Lines of the form $\sigma_0 = A \exp(BH_s)$ and $\sigma_0 = AH_s^B$ were also tried, but the best fit was obtained for the

linear relationship. The G03 algorithm makes the implicit assumption that for constant T_z the relationship between H_s and σ_0 is of the form $\sigma_0 = AH_s^B$, since

$$T_z = 10^\alpha (\sigma_0^{0.25} H_s^{0.5})^\beta \Rightarrow \sigma_0 = \left(\frac{T_z}{10^\alpha} \right)^{4/\beta} H_s^{-2} \quad [3.3]$$

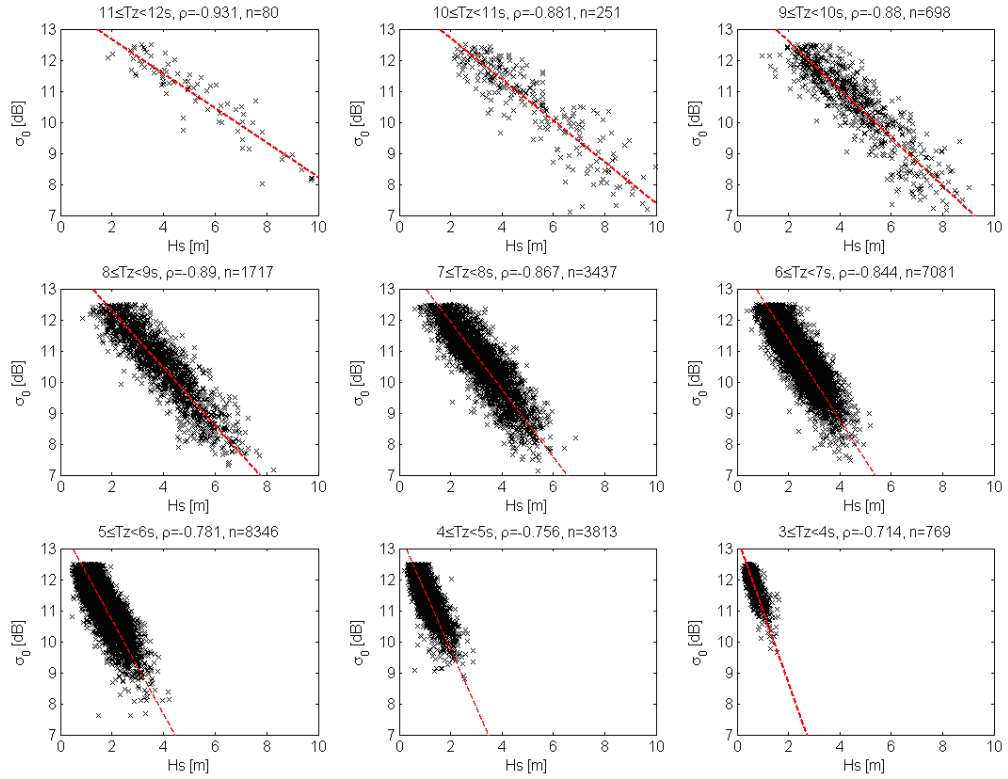


Figure 3.6. Linear fits to TOPEX data for T_z between 3 and 12s. The correlation, ρ , and number of points, n , are given at the top of each plot.

The slopes and intercepts of the fitted lines are shown in figure 3.7 and Table 3.2. The slope of the line, B , varies smoothly with T_z . Lines of the following forms were fitted:

- (a) $B = \alpha T^2 + \beta T + \gamma$
- (b) $B = \alpha T^\beta$
- (c) $B = \alpha \exp(\beta T)$
- (d) $B = \alpha + \beta \ln(T)$

The best results were obtained for $B = \alpha \exp(\beta T)$.

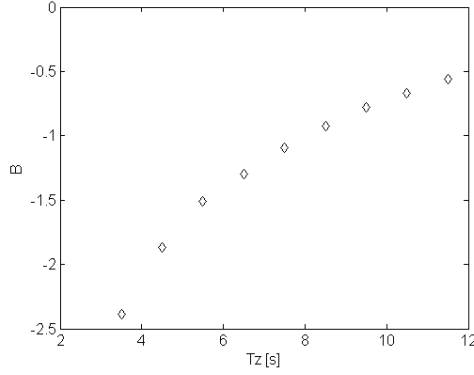


Figure 3.7. Scatter plot of slope of fitted line against T_z .

	A	B
$3 \leq T_z < 4s$	13.61	-2.103
$4 \leq T_z < 5s$	13.48	-1.593
$5 \leq T_z < 6s$	13.81	-1.409
$6 \leq T_z < 7s$	13.97	-1.195
$7 \leq T_z < 8s$	14.15	-1.028
$8 \leq T_z < 9s$	14.24	-0.887
$9 \leq T_z < 10s$	14.17	-0.725
$10 \leq T_z < 11s$	14.25	-0.652
$11 \leq T_z < 12s$	13.94	-0.563

Table 3.2. Slope and intercept of fitted line for various T_z .

It was found that if the values of H_s were offset by a constant γ , then the intercept A remains roughly constant with T . For σ_0 above the threshold no dependence of T on σ_0 was observed. It is therefore impossible to define an altimeter wave period model of the form $T = f(H_s, \sigma_0)$. Therefore, a model for T is define in two sections, above and below the threshold δ :

$$T = \begin{cases} \frac{1}{\beta} \ln \left[\frac{1}{\alpha} \left(\frac{\sigma_0 - A}{H_s + \gamma} \right) \right] & \text{if } \sigma_0 \leq \delta \\ \frac{1}{\beta} \ln \left[\frac{1}{\alpha} \left(\frac{\delta - A}{H_s + \gamma} \right) \right] & \text{if } \sigma_0 > \delta \end{cases} \quad [3.4]$$

To fit the model described by equation 3.4 the collocated dataset is divided into a development dataset (50%) for the determination of the fitted coefficients, and a validation dataset (50%) for the calculation of bias and rms error. The data forming the development and validation datasets are sampled at random without replacement from the original dataset. The model is fitted using a simplex search method (Lagarias et al,

1998) to find the five parameters A , α , β , γ , and δ , which minimise the sum of squared residuals $(T(alt) - T(buoy))^2$.

It was found that if the fitting process was repeated, there were small variations in the fitted parameters and also in the bias and rms error in the validation dataset. This is due to the random nature of separating the collocated data into development and validation datasets. To account for this the fitting process was carried out 1000 times to establish confidence bounds on all the parameters. All parameters were observed to vary normally about their mean values, and the 95% confidence intervals quoted have been calculated as 1.96 times the standard deviation of the parameter.

3.2.3 Results

The model was fitted for both T_z and T_e . The fitted parameters and confidence intervals are shown in Tables 2 and 3 of Appendix D. The bias is calculated as the mean of $T(alt) - T(buoy)$ and the RMS error is calculated as the square root of the mean of $(T(alt) - T(buoy))^2$. Values of bias and RMS error are given for each section of the two-piece model, and an overall value. The differences in the fitted model parameters between altimeters are most likely due to calibration differences in both H_s and σ_0 .

For comparison the G03 and Q04 models were also fitted. The Q04 model is defined only for TOPEX data for $\sigma_0 \leq 16$ dB, comprising 8866 data points. The bias in T_z is -0.067 s, with an RMS error of 0.69s. The G03 model was fitted for each altimeter, following the authors' method. That is, σ_0 was kept in its linear, non-decibel form and orthogonal regression was used to find A and B such that $\log_{10}(T_z) = A + B \log_{10}(X)$ where $X = \sigma_0^{0.25} H_s^{0.5}$. Again, the collocated dataset was divided into development and validation datasets and the fit was repeated 1000 times to establish confidence bounds for the parameters. The results are given in table 4 of Appendix D. It can be seen that, the two-piece algorithm has negligible bias and performs better than both the Q04 and G03 algorithms in terms of rms error, with 15% reduction in rms error from Q04 and 25% reduction from G03.

Figure 3.8 shows scatter plots of the three algorithms against the buoy measurements for TOPEX data, with the contours showing the distribution of the data (contours are

omitted from the top right plot as there are an insufficient number of data points). Similar trends were observed for other altimeters. Below 12.5dB the plot for the two-piece algorithm shows a tighter distribution about the line $T_z(\text{altimeter}) = T_z(\text{buoy})$ than both the Q04 and G03 algorithms. The same plot for T_e (Figure 3.9) has considerably more scatter. The slight discretisation of the two-piece T_z and T_e values, for $\sigma_0 > \delta$, visible in Figures 3.8 and 3.9 is due to the fact that the period algorithm only depends on H_s in this region and TOPEX H_s measurements were reported to the nearest 0.1m (the small number of intermediate values are due to the drift correction at the end of the side A circuit). The effect on the derived values of T_z is small, for $H_s = 1.0$ m, the discretisation is 0.3 s and at $H_s = 3.0$ m the discretisation is 0.14 s.

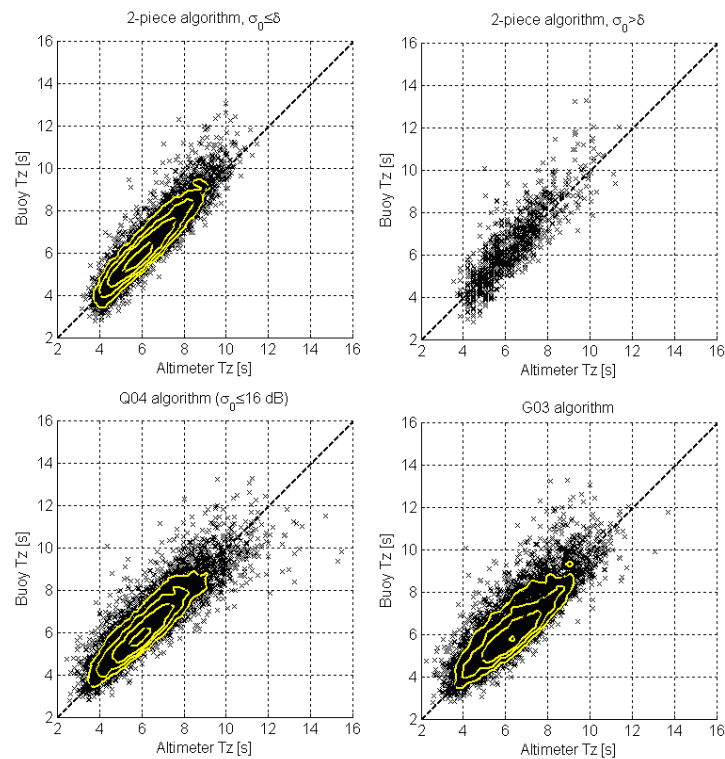


Figure 3.8. Scatter plots of altimeter T_z against buoy T_z for the Q04, G03 and two-piece algorithms using TOPEX data, with contours showing distribution of data.

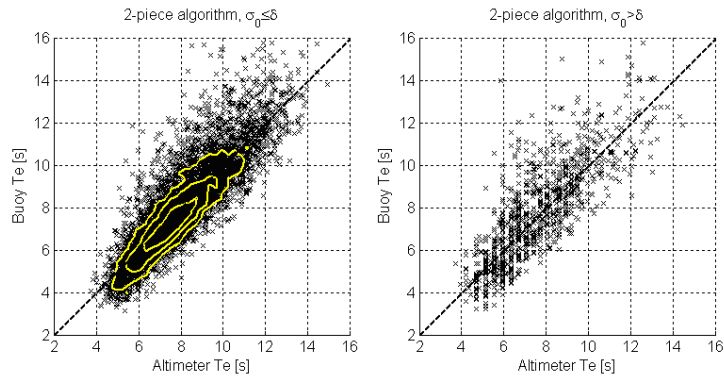


Figure 3.9. Scatter plot of altimeter T_e (two-piece algorithm) against T_e (buoy) for TOPEX data, with contours showing distribution of data.

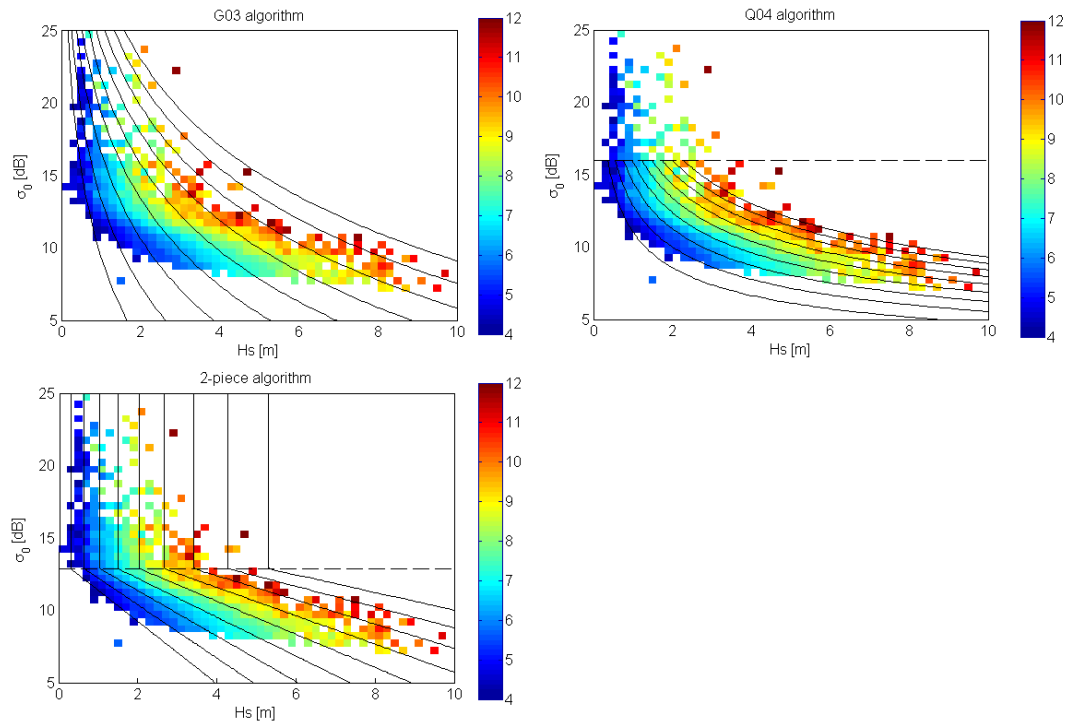


Figure 3.10. Coloured squares indicate mean buoy T_z binned by H_s and σ_0 for TOPEX data with contours of T_z for the two-piece, Q04 and G03 models overlaid. Contours are at 1s intervals, from 4 to 12s.

Figure 3.10 shows the fit of the three models to the collocated TOPEX data. It is clear that the G03 model does not follow the contours of the data. This is a result of the a priori definition of the exponents in their expression for X . The Q04 model follows the contours of the data reasonably well, but has the clear disadvantage that the range of applicability is limited to $\sigma_0 < 16$ dB. The two-piece model follows the contours well

over the entire range of the data, however the sharp corner at $\sigma_0 = \delta$ is likely to be an oversimplification. It should be noted that the two-piece algorithm will give negative values of period if H_s and σ_0 are both low, but these are far outside the normal range of H_s and σ_0 and a negative value of period will probably indicate a bad measurement of either H_s or σ_0 .

The new algorithm displays a marked improvement in the residual errors (see Figure 3.11) with a reduced scatter and less residual trend than the G03 and Q04 algorithms, particularly with the buoy significant steepness and altimeter backscatter. For the two-piece algorithm there is a noticeable residual trend with the buoy T_z . However, there is no residual trend with altimeter T_z (not shown here) so it is not possible to apply a simple correction for this. The reason for the residual trend with buoy T_z is discussed in Section 3.2.4.

In Figure 3.12 the distributions of T_z and significant steepness from buoy data are compared with those derived from the three altimeters models. The distribution of T_z produced by the two-piece algorithm is very close to that of the Q04 algorithm. Both are a slight improvement on the G03 algorithm in terms of the location of the peak. The two-piece algorithm shows the best fit to the buoy data for steepness. Though much improved, the two-piece algorithm still over-predicts steepness occurrence around the mode at 0.04. The reason why steepness distribution is too peaked is that the mean steepness for σ_0 below ~ 13 dB is always greater than about 0.02 (see Figure 3.5) and the lower part of the two-piece model emulates this mean trend. This also explains the residual trend of underestimation for low steepness in Figure 3.11. Note also that while the altimeter distribution declines smoothly to the right of the peak, to the left it features a small hump at around 0.02. This is due to the form of the upper part of the algorithm which is solely dependent on H_s and therefore has no variation in steepness for a given H_s .

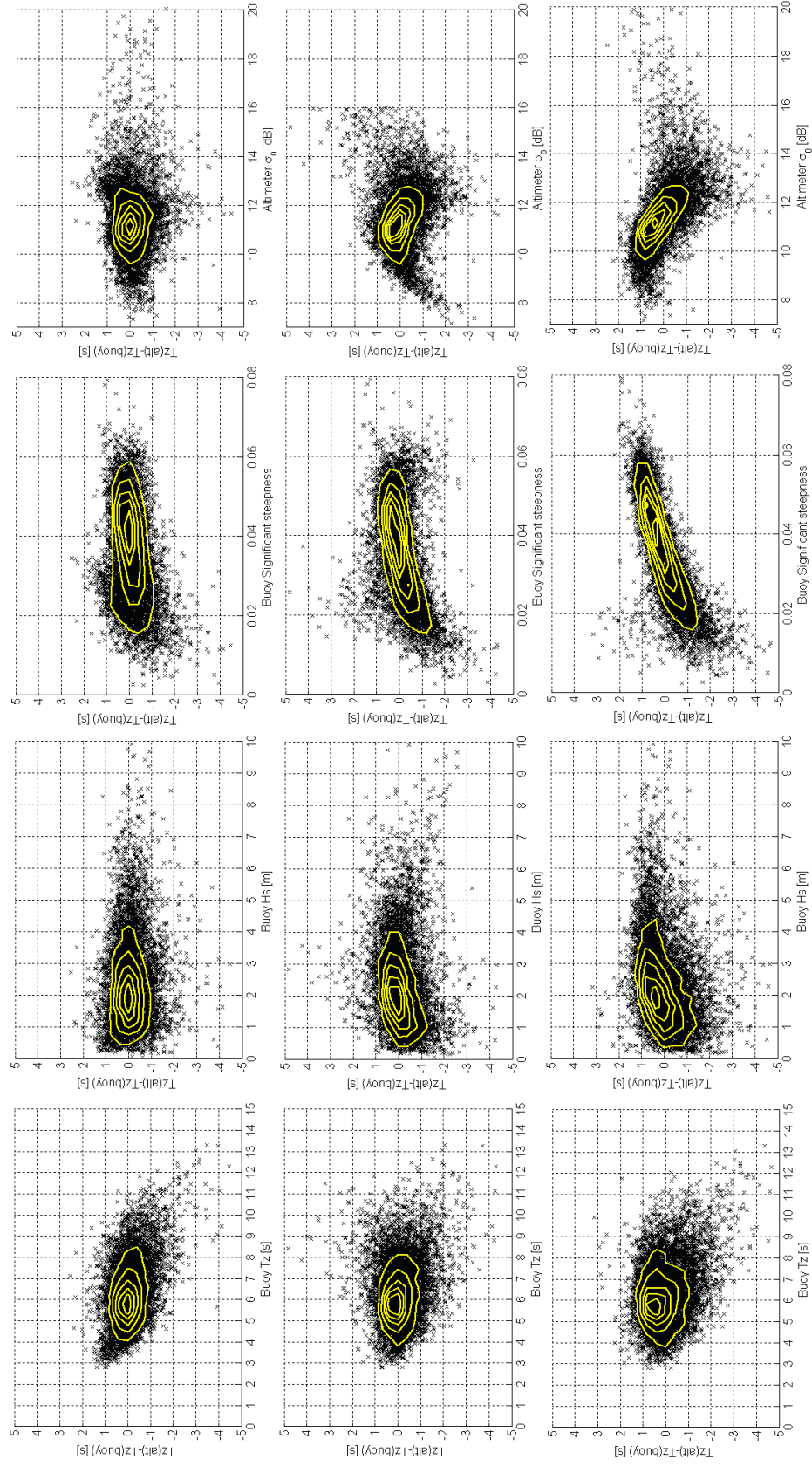


Figure 3.1.1. Residual errors for the two-piece model (top row), Q04 model (middle row) and G03 model (bottom row) for TOPEX data, with buoy T_z , buoy H_s , buoy significant steepness and altimeter σ_0 . Contours show distribution of data.

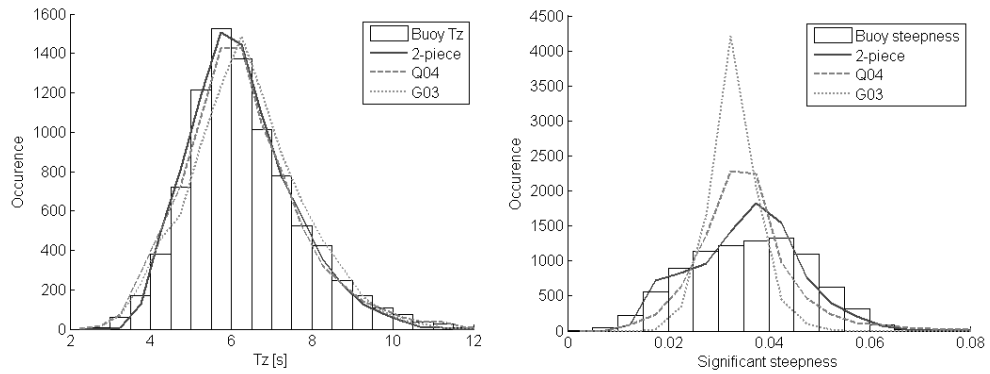


Figure 3.12. Histograms of buoy and altimeter T_z and significant steepness for TOPEX (data is $\sigma_0 < 16\text{dB}$ for comparison with Q04)

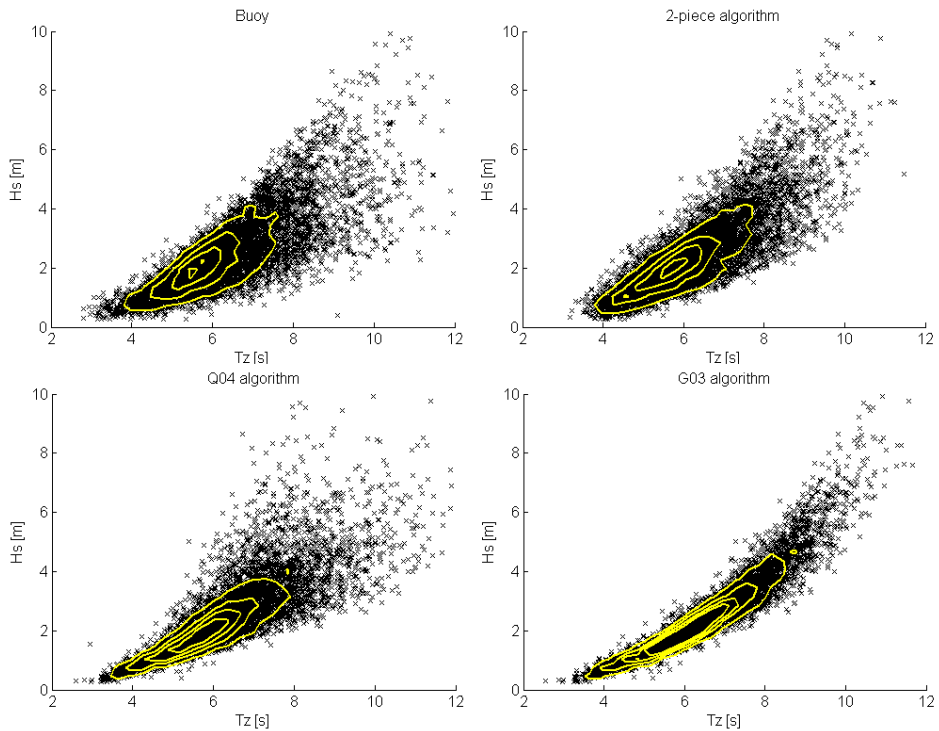


Figure 3.13. Joint distribution of H_s and T_z from buoy and altimeter data (TOPEX, $\sigma_0 \leq \delta$), with contours showing distribution of data.

The joint distribution of H_s with T_z for the buoy data and the 3 models is shown in Figure 3.13. The new algorithm is clearly better than the G03 algorithm in its ability to reproduce the joint distribution and is a better match to the peak of the distribution than the Q04 algorithm. The G03 algorithm's poor reproduction of the joint distribution of

H_s and T_z is a result of its strong dependence on H_s . For $\sigma_0 > \delta$ the two-piece algorithm has no dependence on σ_0 , therefore it is not possible to reproduce the joint distribution of wave height and period in this range. However, the algorithm is able to follow the mean value of T_z , as shown in Figure 3.14.

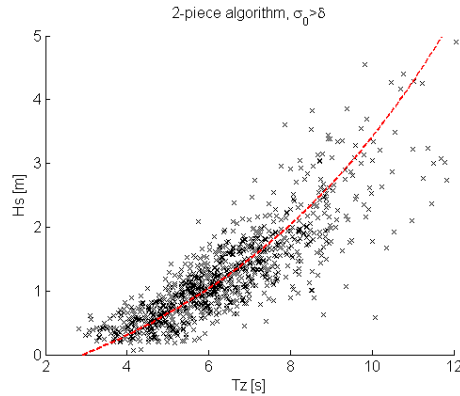


Figure 3.14. The joint distribution of H_s and T_z from buoy data when TOPEX $\sigma_0 > \delta$. The dashed line shows the value of T_z for two-piece algorithm.

3.2.4 Discussion

An altimeter wave period model of the form $T = f(H_s, \sigma_0)$ can only give one value of period for a given H_s and σ_0 . However from the collocated dataset it is clear that for a given H_s and σ_0 there are a range of values of T_e and T_z . In this section we discuss how this will affect the performance of an altimeter wave period model.

Figure 3.15 shows the standard deviation and skewness in the distribution of T_z for the combined collocated data, binned by H_s and σ_0 . It is clear that there is considerable variation of the measured buoy period for a given value of H_s and σ_0 . Because the two-piece algorithm is matched to the mean value of period in each bin, it cannot reproduce the full range of periods observed and will miss low and high values. The positive skewness in the distribution means that period values higher than the mean are more frequent or lie further from the mean than lower values. These two characteristics of the data imply that the residual trend with buoy T_z , for the two-piece model (Figure 3.11) is a result of the physical relationship between H_s , σ_0 and T_z rather than the fit of the model.

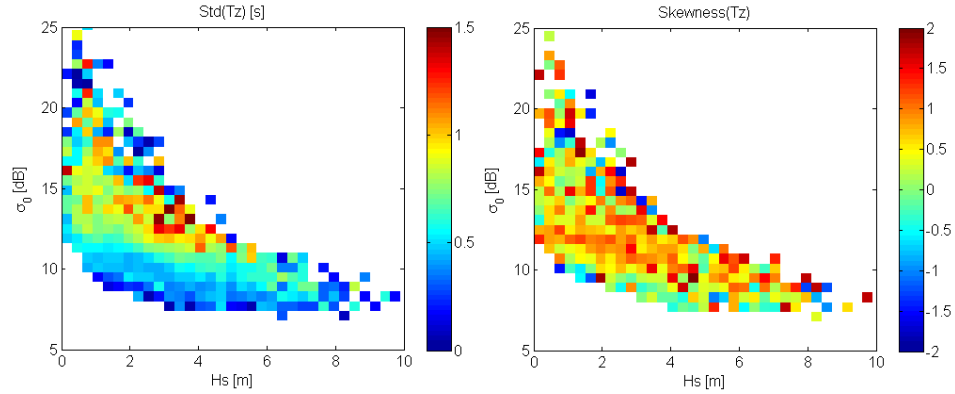


Figure 3.15. Standard deviation and skewness of T_z for data binned by H_s and σ_0 , for combined collocated data.

Measurements with high σ_0 correspond to times of low wind speed ($\sigma_0 = 13\text{dB} \Leftrightarrow U_{10} \approx 4 \text{ ms}^{-1}$) or, equivalently, swell conditions. Since we can only create a period algorithm based on H_s when $\sigma_0 > \delta$, we are forced to create a model in which all swell has same steepness for a given H_s . The limitation posed by the step change in the response of σ_0 around 13 dB does not seem too severe. The range of steepness is in fact quite small for $\sigma_0 > \delta$ (see Figure 3.5b) and from Figure 3.8 we can see that the performance of the model is reasonable for $\sigma_0 > \delta$ with fairly low levels of scatter and an RMS error of less than 0.9 s for T_z . The information that σ_0 is above the threshold is sufficient to infer that the wave conditions are swell dominated and that the period can be reasonably estimated from H_s alone.

The higher RMS error of the model when $\sigma_0 > \delta$ is partly a result of the greater variation in T_z for higher σ_0 values, displayed in Figure 3.15. In swell conditions integral period parameters are only weakly related to the high frequency part of the spectrum on which backscatter is strongly dependent, so it is not surprising that the backscatter is not correlated to wave period in low wind conditions. Conversely, above a certain wind speed, from the good performance of our period model we can infer that integral wave period parameters are strongly correlated to some function of H_s and the shape of the high frequency tail of the spectrum.

Caires et al (2005) noted that the G03 algorithm performs worse in times of high swell component or low wind speed. They suggest this is due to one of the physical

assumptions used to derive the model breaking down for swell conditions. However, from Figure 3.10 we can see that the model contours do not follow the data very well over the rest of the range either, so we suggest that this is not related to the change in response of σ_0 but a mismatch between the model and the physics.

The strong dependence of backscatter on the high frequency components of the spectrum is consistent with the fact that we observe more variability in T_e than T_z for a given value of H_s and σ_0 (see Figure 3.16). T_z is more dependent on the higher frequency components of the spectrum as it varies with m_2 , while T_e depends more on the lower frequency components, since it varies with m_1 . The higher variability for T_e was also evident in the higher rms error for the T_e model compared to the T_z model. Indeed, when we fit the model for T_m we find that $rmse(T_e) > rmse(T_m) > rmse(T_z)$.

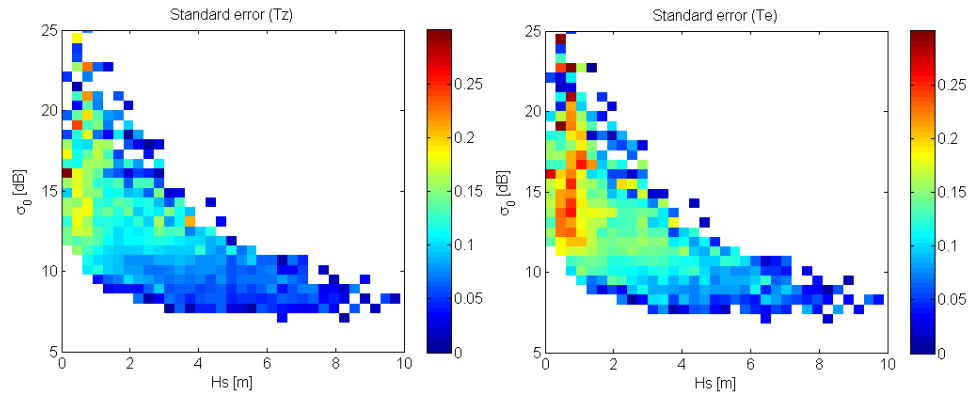


Figure 3.16. Standard error of T_z and T_e (defined as the standard deviation divided by the mean) for data binned by H_s and σ_0 , for combined collocated data.

Figure 3.17 shows scatter plots of T_z against T_e for buoy measurements and the two-piece altimeter model. From the buoy measurements it can be seen that there is not a fixed relationship between T_e and T_z , since the ratio of T_e/T_z depends on the spectral shape. For the altimeter model we see a near-constant relationship between T_e and T_z , implying that the two-piece model is not able to discern changes in spectral shape. This is probably a result of the strong dependence of σ_0 on the high frequency components of the spectrum.

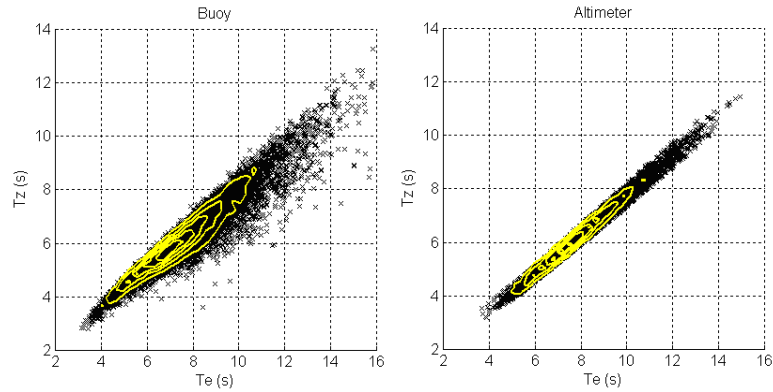


Figure 3.17. Scatter plots of T_z against T_e for buoy measurements and the two-piece altimeter model (TOPEX data).

Part of the discrepancy between the buoy and altimeter estimates of wave period is due to the fact that buoys and altimeters are sensitive to different sea surface length scales. Altimeter backscatter measurements are dependent on centimetric scale waves, whereas the buoys used in this study have a high frequency limits of either 0.4 Hz or 0.485 Hz (see Table A1 of Appendix D) corresponding to wavelengths of 6.6 m and 9.8 m. Buoy measurements of period are subject to systematic errors as a result of their inability to measure the high frequency part of the spectrum. Caires et al (2005) note that T_z is sensitive to the value of the high-frequency cut-off used to calculate the spectral moments. If the moments of the spectrum are calculated as the integral over frequencies from 0 to a finite frequency rather than to infinity then T_z will be overestimated. For example, in the case of a Pierson-Moskowitz spectrum with a cut-off of 0.4 Hz, typical of buoys, T_z will be overestimated 16% for a peak frequency of 0.2 Hz, 4% for a peak frequency of 0.1 Hz and 1% for a peak frequency of 0.05 Hz. The cut off is less important for T_e , with a 4% overestimate for a peak frequency of 0.2 Hz and 0.3% overestimate for a peak frequency of 0.1 Hz.

Quilfen et al (2004) show that using backscatter measurements at C-band and Ku-band frequencies enables a more accurate algorithm to be developed. Since C-band (5.3GHz) measurements are at a lower frequency than Ku-band (13.6GHz), they are dependent on slightly longer waves. Thus by using the measurements at both frequencies, it is possible to extract more information on the shape of the entire spectrum and hence integral period parameters. It is likely that using the S-band (3.2GHz) measurements of

Envisat it will be possible to create a more accurate algorithm still, as the backscatter will depend on even lower frequencies.

From the above discussion it is clear that there is a limit to how accurate a period function of the $T = f(H_s, \sigma_0)$ can be. To benchmark the performance of our parametric two-piece model we can use a basic non-parametric model such as a look-up table of values. That is, the altimeter period is defined to be the mean buoy period from the collocated data for a given bin of H_s and σ_0 . The choice of bin size is a compromise between having sufficient data in each bin to give a smooth distribution of period across the look up table, and increasing the retrieval error from having too coarse a resolution. From limited experimentation it was found that bins of size 0.1m by 0.2dB, gave adequate results.

Splitting the data into development and validation datasets, and using the development dataset to form the look-up table for the validation dataset proved always to give a higher rms error than the two-piece function. This was due to not having sufficient data to both have a good resolution and smooth distribution, even when the development data set is defined to be 80% of the entire collocated dataset.

When the dataset is not split, the rms retrieval error gives an idea of the limit of the accuracy of a function of the form $T = f(H_s, \sigma_0)$. The results are given below in Table 3.3. When looking at these results, it is important to remember that this method of defining the altimeter period is circular (i.e. the same data is used for development and validation) and, as stated above, when the data is split in two this method does not perform as well as our model. We also note that the results for Poseidon are spuriously low. This is because a large number of bins in the look up table contain only one data point, so the retrieved value for that bin will have zero error.

The lowest possible rms error will lie somewhere between the values in Table 3.3 and the values for the two-piece function. It is reassuring to see that these values are close: a difference of 0.11s on average for T_z and 0.14s for T_e (both ignoring Poseidon). The plots of residual errors for the look-up table method (not shown here) display the same trends as for the two-piece model (see Figure 3.11). This implies that these trends are a

result of the relationship between the backscatter and wave period, rather than the fit of the model.

	T_z RMS [s]	T_e RMS [s]
TOPEX	0.51	0.94
POSEIDON	0.26	0.53
JASON	0.44	0.86
ERS-2	0.50	0.93
ENVISAT	0.44	0.78
GFO	0.46	0.87

Table 3.3. RMS errors for the look-up table method.

If there was sufficient data then a look-up table method could possibly give a lower rms error than our function, but in the present case we would need to smooth and interpolate the look-up table. The two-piece model has the advantage that it effectively does this by assuming a model function of the form of equation 3.4.

From the above discussion it can be concluded that it is not possible to create an altimeter wave period function of comparable accuracy to in-situ measurements, from Ku-band H_s and σ_0 alone. However, we must also bear in mind that we are comparing to measurements of a random process, subject to instrumental error, that are separated by both time and space. Calculation of the expected differences, in a similar manner to Section 3.1 for H_s , is beyond the scope of this study, but we note that period parameters are subject to higher sampling variabilities than H_s so we should expect a certain amount of variability from this alone. Since the two-piece model is fitted by finding parameters A , α , β , γ , and δ , which minimise the sum of squared residuals, we are implicitly assuming that there is no error in the buoy measurement of period. This is clearly not true, but is a fair approximation given that the error in the altimeter period measurement is likely to be much higher.

3.2.5 Conclusions

It has been demonstrated that the two-piece altimeter wave period model presented here performs better than the Q04 and G03 models in all metrics considered. The relationship between H_s , σ_0 and wave period has been discussed. It can be concluded that there is no fixed relationship between these three variables, however there is a strong correlation, which allows a reasonable estimate of period to be calculated.

It has been shown that there is a limit to the accuracy it is possible to achieve from an altimeter period function of Ku-band H_s and σ_0 alone and that the two-piece model comes close to this. It may be possible to achieve a more accurate function if the user is only concerned with data for certain ranges of H_s and period, but the improvement which is possible is likely to be small. In particular the sharp corner in the two-piece function is likely to introduce some error in this range.

For a given value of H_s and σ_0 there is considerable variation in the period measured by the buoy. This is likely to be due to the dependence of σ_0 on the shape of the whole spectrum rather than a single integral parameter. Validation of the model is therefore required in other areas, particularly in the Southern Ocean, since the fit may depend on the range of spectral shapes at the buoys used in the collocation.

4. Large Scale Resource Mapping Using Altimeter Data

The work presented in this chapter has been published as: Mackay EBL, Retzler CH, Challenor PG, Bahaj AS, 2008. “Wave energy resource assessment using satellite altimeter data”. Proc. ASME 27th Int. Conf. Offshore Mech. Arctic Eng. Paper number OMAE2008-57976. The paper is included as Appendix E. The co-authors listed above provided advice on the manuscript, but the work presented here is my own.

4.1 Introduction

The first stage in wave energy resource assessment is to select the best sites for development. The ability for a wave energy developer to be able to provide spatial maps of WEC yield at any location in the world, with a quantified accuracy and at a low cost will enable the highest yielding sites to be identified.

Wave measurements from in-situ instrumentation are relatively sparse around the world’s oceans. Wave energy developers wanting to know the resource in locations without nearby in-situ measurements are left to choose from numerical wave model data or satellite remote sensing measurements. Wave model data is normally purchased on a point-by-point basis. A 10-20 year hindcast for a single location typically costs several thousand pounds. This makes spatial mapping of the wave resource using multiple model grid points very costly for a feasibility study.

The global coverage of altimeter data makes it well suited to spatial mapping of oceanographic properties and its use for mapping wave climate in terms of H_s has been demonstrated by numerous authors (e.g. Challenor et al, 1990; Carter et al, 1991; Young, 1994; Barstow and Krogstad, 1995; Young and Holland, 1996; Woolf et al, 2003; Queffeulou and Bentamy, 2007). Barstow et al (1998) describe the use of altimeter data to map wave power. Their estimates of T_e were based on altimeter H_s alone, using a relationship derived from buoy data. The use of altimeter data to estimate the power produced by a WEC has not been studied before.

The work presented in this chapter will provide the following developments on previous studies:

- It will be shown that accurate estimates of WEC power can be obtained from altimeter measurements of H_s and the new period algorithm presented in the previous chapter.
- The accuracy of long-term along-track mean values of WEC power from altimeter measurements is calculated. The limitations imposed by the variability in wave conditions and the sampling patterns of satellite altimeters are investigated.

It will be shown that despite the limited temporal sampling, multi-year mean values of WEC power from along-track averages are of a useful accuracy for wave farm site selection. Also, the spatial resolution provided by altimeter maps using data from several missions is good in comparison to global model data.

The chapter is organised as follows: in Section 4.2 the accuracy of individual measurements of instantaneous power produced by the Pelamis is examined. In Section 4.3 measurement of monthly and annual means over $2^\circ \times 2^\circ$ squares, in offshore locations is discussed. In Section 4.4 we investigate the variation in power along individual altimeter tracks in order to gauge spatial variability close to shore due to topographic sheltering and shallow water effects. In Section 4.5 an example of the use of altimeter data for resource assessment around New Caledonia is presented. Finally, conclusions are presented in Section 4.6.

4.2 Comparison of individual power estimates

To establish the accuracy of estimates of WEC power from altimeters, the altimeter estimates can be compared to collocated buoy estimates. The collocated dataset described in the previous chapter uses only deep water (>100 m) buoys in open ocean, at least 200 km from land. In contrast, the first generation of wave energy farms will be located within a few kilometres of the coast, in a water depth generally less than 100 m. Therefore, in addition to the 28 deep water buoys used in the last chapter, data from 11

buoys in shallow water are used here. The shallow water buoys are located in depths between 28m and 96m and are also located closer to land than the deep water buoys, the closest being 30km from the coast. Apart from these additional buoys, the collocated dataset is prepared in the same way as the previous chapter. The locations of the buoys are shown in Figure 4.1.

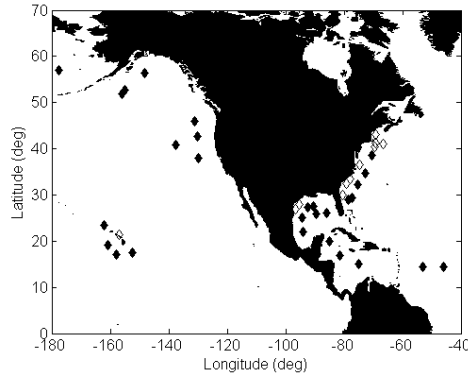


Figure 4.1. Locations of NDBC buoys used in the collocated dataset. Solid diamonds denote buoys in depths $>100\text{m}$, hollow diamonds denote depths $<100\text{m}$.

The altimeter H_s is calibrated using the relationships established in Section 3.1 and altimeter T_e is estimated using the two-piece algorithm developed in Section 3.2. For each pair of collocated altimeter and buoy measurements of H_s and T_e , the power produced by the Pelamis has been calculated from the power matrix, shown in Table 1.1, interpolated to a resolution of 0.1m H_s and 0.1s T_e . The bias and RMS errors of the altimeter estimates compared to the buoys are shown in Table 4.1. Differences in accuracy between different altimeters were found not to be significant at the 95% level (using a bootstrap method to estimate confidence) therefore measurements from all six altimeters are treated as one dataset. However, the accuracy was found to depend on whether σ_0 was above or below the threshold value used in the period algorithm, so results are presented for both $\sigma_0 \leq \delta$ and $\sigma_0 > \delta$. The shallow water buoys provide an independent validation of the period algorithm, as they were not used in its development. It is reassuring to see that the algorithm's performance is similar in shallow water to deep water. The same collocation criteria of 100km and 30 minutes were used for the shallow water buoys as for the deep water ones, so the higher RMS error in power for the shallow water buoys is probably due to the higher spatial

variability in these areas. Scatter plots of altimeter estimates of Pelamis power against buoy estimates are shown in Figure 4.2.

	Deep		Shallow	
	Bias [kW]	RMSE [kW]	Bias [kW]	RMSE [kW]
$\sigma_0 \leq \delta$	6.4 (± 0.7)	55.7 (± 0.8)	6.5 (± 1.4)	63.8 (± 1.4)
$\sigma_0 > \delta$	0.1 (± 0.8)	29.1 (± 1.3)	0.4 (± 0.8)	22.5 (± 2.3)
Overall	5.3 (± 0.6)	52.2 (± 0.8)	4.8 (± 1.0)	55.3 (± 1.8)

Table 4.1. Bias and RMS error of altimeter estimates of Pelamis power with 95% confidence intervals in brackets.

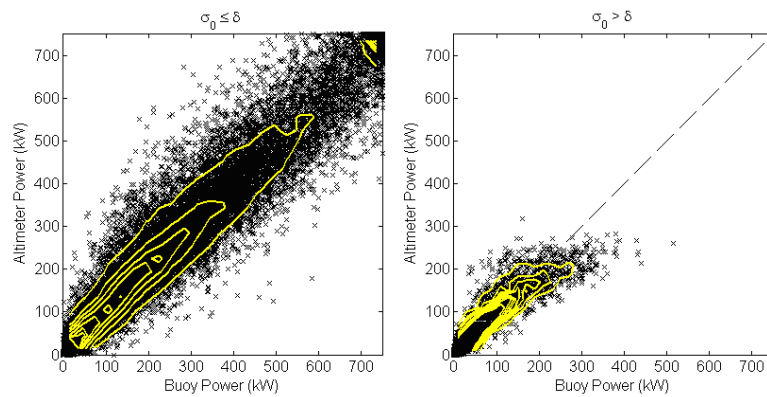


Figure 4.2. Scatter plots of altimeter Pelamis power against buoy Pelamis power, with contours showing density of occurrence, for $\sigma_0 \leq \delta$ (left) and $\sigma_0 > \delta$ (right).

For $\sigma_0 \leq \delta$ the level of scatter is fairly high, but the relationship appears to be linear. There is a small positive bias in the altimeter estimates of around 6 kW. When $\sigma_0 > \delta$ the altimeter underestimates the highest values of Pelamis power. However the bias is not significantly different from zero and these high energy swell conditions represent only a very small percentage of the data. It is interesting to note that the RMS error in Pelamis power is lower when $\sigma_0 > \delta$, despite the fact that the period algorithm performs worse here (see Section 3.2). This is most likely because this corresponds to times when H_s is low and therefore power is low also. Figure 4.3 shows a quantile plot of altimeter against buoy Pelamis power, for the entire dataset. It is clear that the altimeter is capable of properly reproducing the distribution of Pelamis power measured by the NDBC buoys.

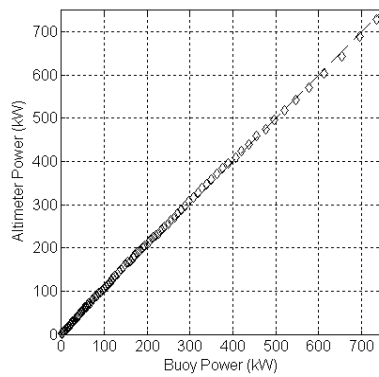


Figure 4.3. Quantile-quantile plot of Pelamis power measured by altimeter and buoys.

Figure 4.4 shows the mean difference altimeter and buoy in power, binned by the differences in H_s and T_e . It can be seen that the difference in power is more sensitive to differences in H_s than differences in T_e . This is not surprising since Pelamis power increases approximately linearly with H_s , while above 7.5 s it decreases approximately linearly with T_e .

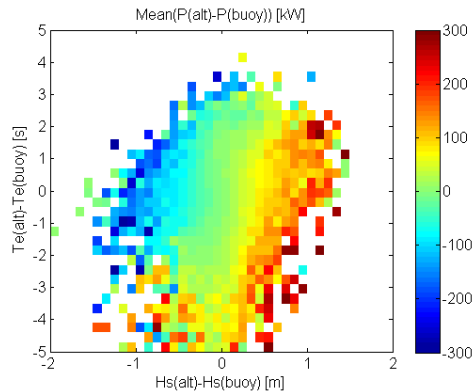


Figure 4.4. Mean difference in power against difference in H_s and T_e .

So far the differences due to spatial and temporal separation of the measurements and sampling variability have not been considered. The sampling variability of buoy estimates of Pelamis power was discussed in Section 2.1.3. It was shown that the coefficient of variation is around 11% on average for a half hour record, but that the value varies with both H_s and T_e . The short-term temporal variability in Pelamis power was discussed in Section 2.1.4. It was shown that the standard deviation between two half hour averages, separated by interval τ , increases with the average power of the two measurements, until around 500-600 kW, and then decrease again. This decrease is due

to the capping of the Pelamis power output at 750 kW. The value at which the standard deviation of the differences reaches its peak depends on the separation τ . In Section 2.2.4 it was shown that modelling the spatial variability of H_s is complicated by the effects of along-track smoothing of altimeter measurements. Modelling the spatial variability of Pelamis power would be further complicated by the uncertainty in the altimeter estimates of T_e .

Because of these complications, a precise examination of the random effects of sampling and separation will not be attempted in the same way as in Section 3.1. Instead, some observations of the effects of spatial and temporal separation can be made by examining measurements made by altimeters flying in tandem orbits. The same collocated data from the tandem orbits, described in Section 2.2.3, will be used here. This gives a temporal separation of 1 minute for TOPEX and Jason measurements and 28 minutes for ERS-2 and ENVISAT. Scatter plots of the data from these tandem orbits are shown in Figure 4.5. The plot of T/P phase A orbit against Jason-1 (both along the same ground tracks) shows low scatter indicating good precision of both altimeters. The standard deviation of the differences is 13.8 kW. The scatter between the ERS-2 and ENVISAT measurements is slightly higher due to the increased temporal separation, and the standard deviation of the differences is 26.8 kW. There is also a slightly non-linear relationship at low power levels, indicating that there may be some difference in calibration of either H_s or T_e at low values.

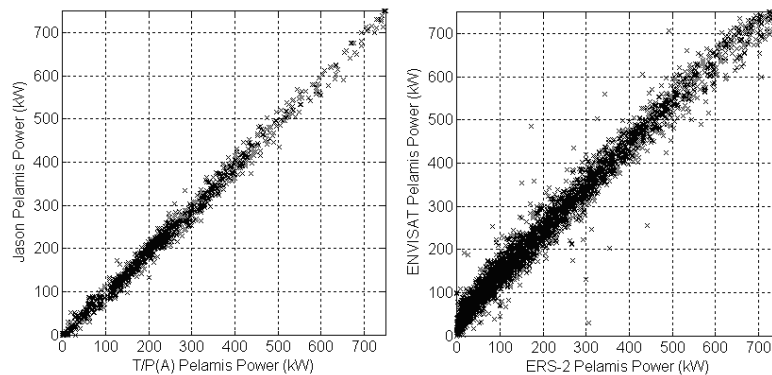


Figure 4.5. Scatter plots of collocated altimeter estimates of Pelamis power from tandem orbits. Left: T/P phase A and Jason-1. Right: ENVISAT and ERS-2.

The effect of spatial separation can be examined by comparing data from TOPEX and Jason-1 after TOPEX was manoeuvred its phase B orbit. This orbit followed a parallel set of ground tracks, half way between the phase A ground tracks, separated by about 150 km at the equator and about 100 km at 50° latitude. Figure 4.6 shows data from this period, collocated exactly in time but separated in space. The standard deviation of the differences in this case is 46.9 kW, indicating that the effect of a spatial separation of 100-150 km is greater than that of a temporal separation of 30 minutes.

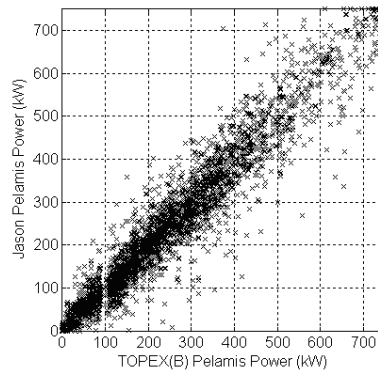


Figure 4.6. Scatter plot of collocated altimeter estimates of Pelamis power from Jason-1 and TOPEX phase B orbit.

The collocated altimeter-buoy dataset uses the median values of the altimeter measurements within 100 km of the buoy, so the effects of spatial separation and sampling variability will be reduced from the examples shown here, but the effects of temporal separation will be similar. From the comparisons of altimeter estimates of Pelamis power from the tandem orbits, it appears that the scatter in the altimeter-buoy comparisons are broadly consistent with the expected differences due to sampling variability and spatial and temporal separation.

4.3 Mean values over $2^\circ \times 2^\circ$ squares

It has been demonstrated by numerous authors that satellite altimeter data can be used to obtain accurate estimates of monthly and annual mean H_s in offshore locations, averaged over squares of 2° latitude by 2° longitude (e.g. Carter et al, 1991; Young, 1994; Woolf et al, 2003). Cotton and Carter (1994) show that the monthly mean H_s

calculated from 5 or more altimeter transects of a $2^{\circ} \times 2^{\circ}$ square surrounding a buoy compares well to the continuous measurements made by the buoy, with an RMS error of around 0.2 m. From 1992 onwards there have been at least 2 altimeters flying at all times. This means that using the combined data from TOPEX, Poseidon, Jason, ERS-2, ENVISAT and GFO, there are a minimum of 7 transects per month through each $2^{\circ} \times 2^{\circ}$ square surrounding the NDBC buoys. The mean number of transects per month is 21, with only 1.5% of squares having less than 10 passes per month. However, the sampling rate of a given geographical area depends on the latitude, on the number of satellites operating at that time and on the relative phasing of the various satellite orbits (Queffeuou and Croizé-Fillon, 2007).

In this section the use of altimeter data as a large-scale tool for identifying areas of interest for wave energy development is investigated. The monthly mean Pelamis power calculated from buoy data is compared to the monthly mean from the altimeter measurements in the surrounding $2^{\circ} \times 2^{\circ}$ square. Only the deep water buoys have been considered in this comparison, since the assumption of stationarity on this scale is not valid in shallow water. Again, the median value of the altimeter transect through the square has been used to reduce sampling variability. Since the data from the tandem missions are so close in time, these effectively represent duplicate measurements. Therefore the average of the data from the tandem missions has been used so as not to bias the estimate of monthly mean. In the case of the TOPEX phase B orbit, some additional information is gained where the phase B ground track falls within the square and the phase A track does not. For our analysis we have discarded months where the buoy is recording for less than 90% of the time.

Figure 4.7 shows scatter plots of altimeter monthly and annual mean Pelamis power against the values from the NDBC buoys. There is evidence that the variance of the error in monthly mean power increases with the mean power, however this is not observed so strongly for the annual mean power. The error in monthly mean is a function of the error in individual measurements, the number of measurements and the autocorrelation structure of the monthly time series. Typically, as the monthly mean power increases, the monthly variability also increases, meaning that more samples are required for a given accuracy. The relationship between sampling frequency, autocorrelation in the data and accuracy of monthly means is discussed in detail by

Challenor and Carter (1994) for stationary distributions sampled at regular intervals. Their analytic method is not appropriate here, since time series of wave parameters are non-stationary due to seasonal variation. Also, using altimeter data from multiple missions produces irregular sampling intervals. It is still useful to examine the effect of sampling rate empirically: Figure 4.8 shows the correlation of the altimeter monthly mean with the buoy monthly mean against number of altimeter transects. There is a slight increase in correlation from $20 < n \leq 30$ to $n > 30$ transects, but it is not significant at the 95% level. It can be inferred that, due to the autocorrelation in the data, sampling at a greater rate than once daily brings only marginal improvement.

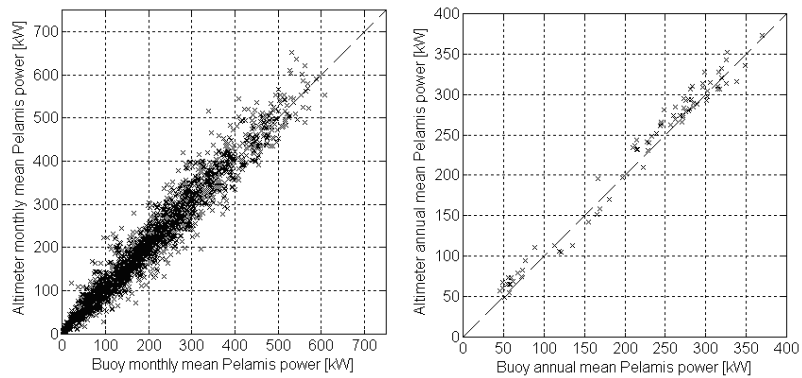


Figure 4.7. Scatter plots of altimeter against buoy monthly and annual mean Pelamis power.

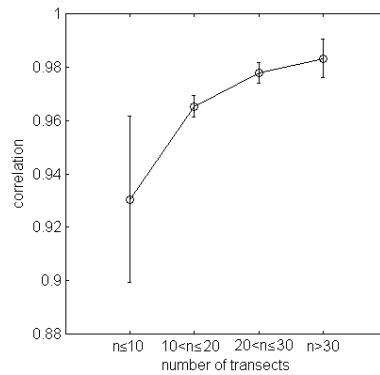


Figure 4.8. Correlation of altimeter monthly mean Pelamis power with buoy monthly mean Pelamis power against number of transects, with 95% confidence limits.

The reason that the error in annual mean is not as strongly dependent on the annual mean value as was observed for the monthly means is probably a result of the seasonal

variability. In our dataset, there is large seasonal variability at the higher power locations. Over the entire dataset the altimeter monthly mean was found to have a bias of 8.2 ± 1.5 kW and RMSE of 32.6 ± 1.4 kW. The annual mean was found to have a bias of 7.1 ± 2.8 kW and RMSE of 12.9 ± 1.6 kW. Since using altimeter data in $2^\circ \times 2^\circ$ squares is only indicative of the resource in that area, there is little use in being more precise about the uncertainty in relation to sampling and variability of the resource.

There is not enough buoy data to test the accuracy of the long term, multi-year averages in $2^\circ \times 2^\circ$ squares. However, the errors in annual mean are approximately normally distributed so if it assumed that the error each year is independent of the previous year, then the standard deviation in error will decrease as $1/\sqrt{n}$, where n is the number of years the data is averaged over. Figure 4.9 shows a global map of the annual mean Pelamis power in $2^\circ \times 2^\circ$ squares for the period 1996-2005. Since this average is taken over ten years, the standard deviation of the error is $12.9/\sqrt{10} = 4.1$ kW. As discussed above, this value is only indicative and dependent on the level of variability in the resource.

From Figure 4.9 it is immediately obvious that the most energetic areas are in the Southern Ocean, followed by the North Atlantic, North Pacific and Southern Indian Ocean. Figure 4.10 shows a global map of the mean Pelamis power over the periods December-February and June-August, between 1996 and 2005. It is clear that the North Atlantic and North Pacific show a much stronger seasonal variability than the Southern Ocean. Also the effect of the summer monsoon winds in the Arabian Sea is clearly visible.

These maps differ from other satellite climatologies in that they show the mean power produced by a WEC rather than the mean H_s . WEC power depends on both H_s and T_e and will reach a maximum (the rated power of the device) at some value. This means that maps of mean values of H_s do not translate directly to maps of mean WEC power. The maps produced in this section make it is possible to directly compare estimates of energy yield from wave farms situated in different areas.

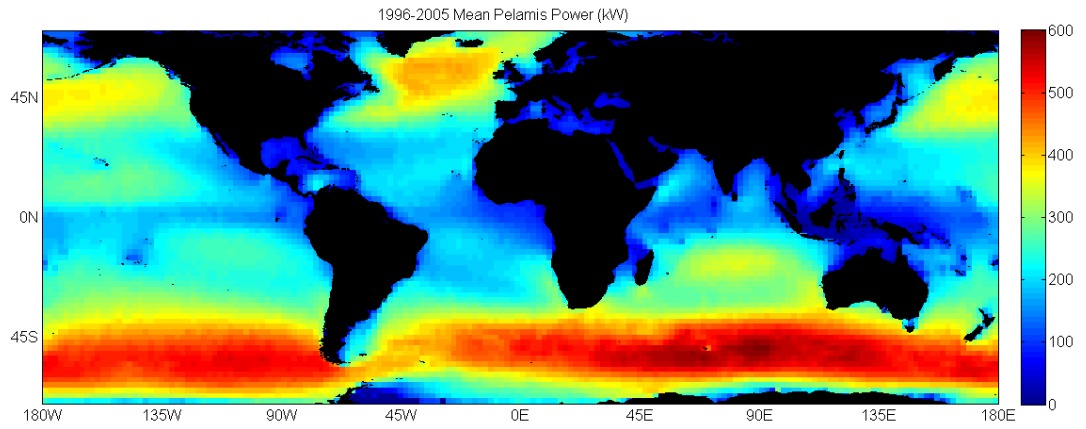


Figure 4.9. Annual mean Pelamis power in $2^{\circ} \times 2^{\circ}$ squares for the period 1996-2005 from the combined altimeter dataset.

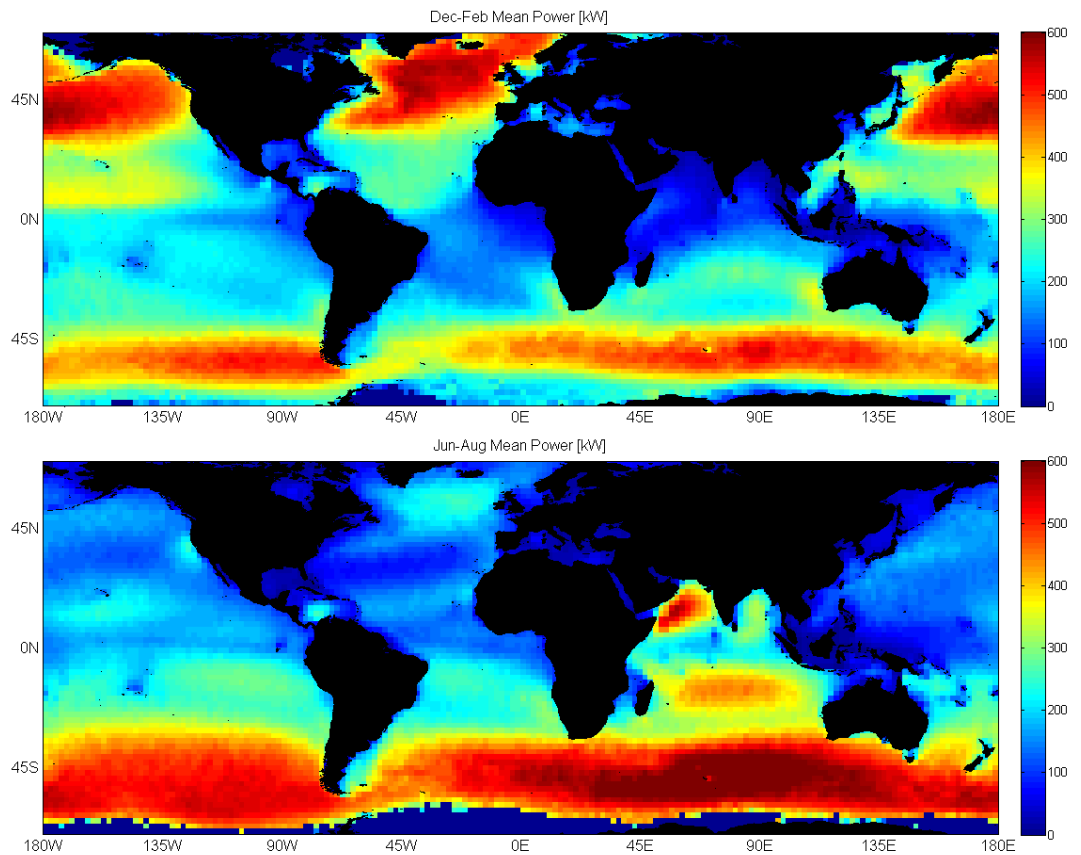


Figure 4.10. Mean Pelamis power in $2^{\circ} \times 2^{\circ}$ squares over December-February (top) and June-August (bottom) for the period 1996-2005 from the combined altimeter dataset.

4.4 Along-track averages

Maps of the wave climate in $2^\circ \times 2^\circ$ squares are useful for locating areas of interest for wave energy development. However, in coastal areas there is considerable spatial variability over smaller scales, so it is of benefit to analyse data along individual satellite passes to give finer resolution nearer shore. Even though measurements along individual tracks are sparse, with TOPEX/Poseidon and Jason on a 10 day repeat orbit, GFO 17 days, and ERS-2 and ENVISAT 35 days, there are many years of data for each satellite so it would be expected that the long-term along-track averages are of a reasonable accuracy. Indeed, when the mean power along a section of track is plotted a smooth along-track variation is observed, with values at cross over points agreeing well. Figure 4.11 shows the along-track mean Pelamis power for T/P and Jason (phase A) for the period Jan 1992 – Dec 2007. Again, data from the tandem period of the missions has been averaged so as not to bias the mean.

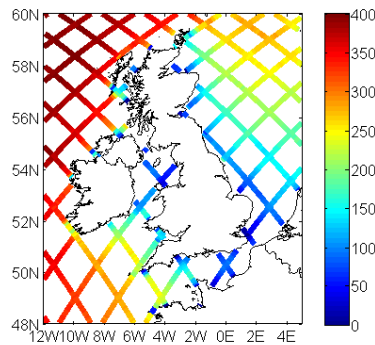


Figure 4.11. Mean along-track Pelamis power for T/P and Jason data for the period Jan 1992 – Dec 2007

The use of along-track averages of TOPEX/Poseidon data to estimate monthly and seasonal mean H_s is discussed by Queffeuilou and Bentamy (2007). They show that even using an average over 13 years, there is still significant scatter in estimates of climatological monthly means at track cross-over points. In this section the accuracy of along-track annual mean values is examined. Figure 4.12 shows the difference in annual mean power measured by the buoy and TOPEX/Poseidon (phase A) and Jason passes against the separation between the ground tracks and the buoys. We see that for the deep water buoys there is no significant change up to 100 km, but for the shallow water

buoys the difference increases at distances greater than 50 km. Therefore, for the shallow water buoys the spatial collocation criterion is set as 50km so as not to introduce differences from spatial variability in wave conditions.

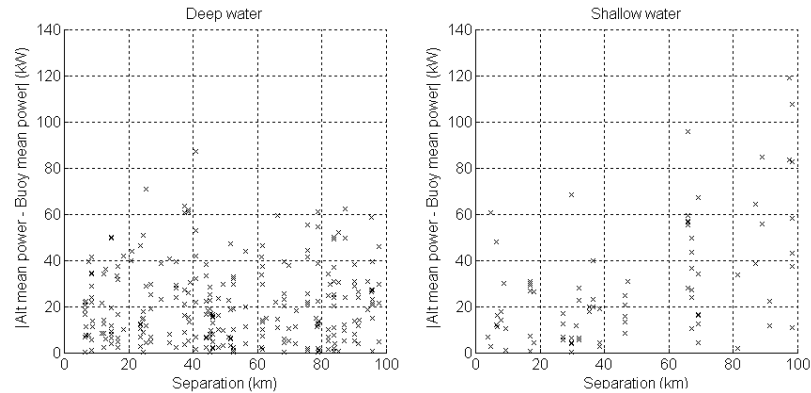


Figure 4.12. Difference in annual mean Pelamis power against separation between ground tracks and buoys for deep water buoys (left) and shallow water buoys (right).

Figure 4.13 shows scatter plots of the along-track annual mean Pelamis power measured by the altimeters against buoy measurements. The bias and RMS error for each set of tracks are given in Table 4.2. As would be expected from the sampling frequency, the TOPEX/Poseidon and Jason tracks have the lowest errors. It is surprising to see that although the RMS error for the GFO tracks is lower than for the ERS-2 / ENVISAT tracks, this is not significant at the 95% level, despite GFO having double the sampling frequency. This is probably a consequence of both the limited size of our dataset and the fact that power levels are strongly seasonal, so one sample every 35 days still gives a reasonable estimate of the annual mean.

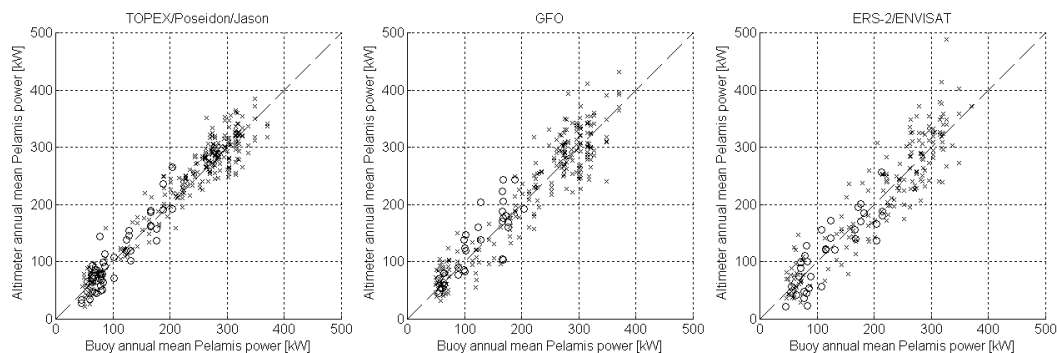


Figure 4.13. Annual mean Pelamis power from altimeter along-track averages against buoy measurements. Values for the shallow water buoys are marked with circles.

	Bias (kW)	RMSE (kW)
T/P & Jason	-4.7 (± 2.8)	25.2 (± 2.1)
GFO	-4.2 (± 4.2)	34.1 (± 3.1)
ERS-2 & ENVISAT	-1.5 (± 5.1)	38.6 (± 4.5)

Table 4.2. Bias and RMS error in along-track annual mean Pelamis power compared to buoy measurements, 95% confidence limits given in brackets.

The effect of limited temporal sampling can be examined by simulation, using hindcast data. As discussed in Section 4.3, the uncertainty due to limited sampling is dependent on the level of variability at the site, which will vary around the world. Therefore hindcasts for several locations are used: Orkney - 14 year hindcast; Cornwall - 15 years; Aguçadoura (Portugal) - 10 years; and New Caledonia - 10 years. The two scales of variability relevant here are: synoptic (from passing weather systems, on the scale of a few days) and seasonal. As a metric for synoptic variability we use the average value of the standard deviation of Pelamis power within a month (hereafter referred to as the intra-monthly STD) divided by the monthly mean Pelamis power. Figure 4.14 shows scatter plots of the intra-monthly STD in Pelamis power against the monthly mean Pelamis power. (Values have been divided by the annual mean Pelamis so that the scales are similar). The relationship is not absolutely linear, but the ratio between intra-monthly STD and monthly mean serves to discriminate between sites.

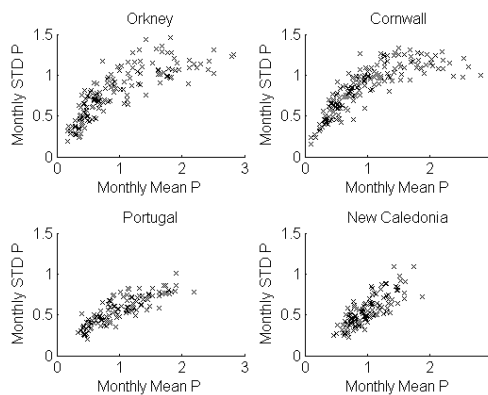


Figure 4.14. Scatter plots of intra-monthly standard deviation against monthly mean Pelamis power. Values have been normalised by the annual average Pelamis power.

Two metrics for seasonal variability are defined: the first is the standard deviation of individual monthly mean Pelamis power, and the second is the standard deviation of the climatological monthly mean Pelamis power. This second figure gives a measure of the

seasonal cycle. Figure 4.15 shows plots of the individual and climatological monthly mean Pelamis power throughout the year. The metrics of variability defined above are given in Table 4.3. Orkney and Cornwall have similar levels of both synoptic and seasonal variability. Portugal and New Caledonia have similar levels of synoptic variability, but whilst the standard deviation of monthly means is roughly equal, Portugal has a stronger seasonal cycle.

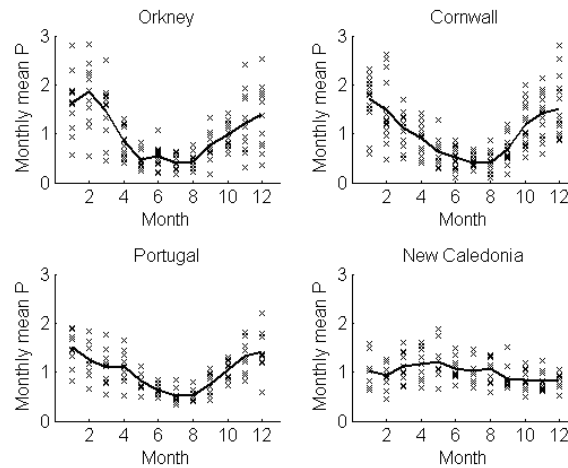


Figure 4.15. Variation in monthly mean Pelamis power: crosses are individual months, line is climatological monthly mean. Values have been normalised by the annual average Pelamis power.

	Orkney	Cornwall	Portugal	New Caledonia
Synoptic variability	0.96	1.03	0.60	0.55
STD of monthly means	0.38	0.37	0.27	0.27
Seasonal cycle	0.51	0.47	0.35	0.13

Table 4.3. Variability Pelamis power on different scales.

The effect of limited temporal sampling on the error in the annual mean is tested by sampling one value every 1, 2, 3, etc. days, starting from the 1st, 2nd, 3rd, etc. sample. The uncertainty resulting from limited temporal sampling is defined as the RMS error in annual mean Pelamis power divided by the mean Pelamis power over the entire hindcast. The results are shown in Figure 4.16. Since these results are based on sampling from a limited number of years, the results have some scatter, so a line of the form $y = ax^b$ has been fitted to each dataset. As would be expected from the similar

levels of variability, the uncertainty from limited sampling is comparable for Orkney and Cornwall. The effects are weaker for Portugal and New Caledonia, consistent with the lower levels of synoptic and seasonal variability. From Figure 4.16 it is clear that the difference in the strength of the seasonal cycles between Portugal and New Caledonia has little effect. This is because the synoptic variability is below the sampling frequency of the altimeter whereas seasonal and interannual variability are below the sampling frequency.

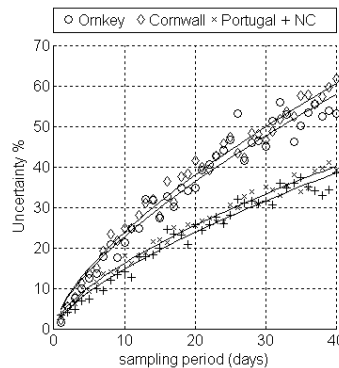


Figure 4.16. Percentage uncertainty from limited sampling for various sites

Despite this site dependency, the RMS error in the multi-year along-track mean Pelamis power is calculated for the entire dataset. This gives an idea of the accuracy of the along-track maps on the whole. Again, it is observed that the error in annual mean Pelamis power is approximately normally distributed. If it is assumed that the errors each year are independent then the standard deviation of the errors will decrease with $1/\sqrt{n}$, where n is the number of years of data. The attainable accuracies in along-track annual mean Pelamis power (defined as half the width of the 95% confidence interval), given the length of data available for the four sets of ground tracks, are shown in Table 4.4.

	Years of data available	Accuracy (kW)
T/P & Jason (phase A)	15	13.0
TOPEX (phase B)	3	29.1
GFO	8	24.1
ERS-2 & ENVISAT	13	21.4

Table 4.4. Attainable accuracy, given the length of data available, for along-track averages of Pelamis power.

4.5 Example and discussion

In this section an example is presented of the use of altimeter data for wave energy resource assessment around New Caledonia, in the South Pacific Ocean. Figure 4.17 shows the along-track annual mean Pelamis power for each set of altimeter ground tracks. Data from individual passes with samples removed by quality control have been interpolated for gaps less than 3 samples in order to give smoother along-track averages. The spatial variability within each $2^{\circ} \times 2^{\circ}$ square is evident, especially close to the coast, and a lot of useful information can be discerned. For example, the sheltering effect in the lee of the main island is clearly visible, as are the dissipative effects of the shallow reefs around the south-east and north-west corners of the main island.

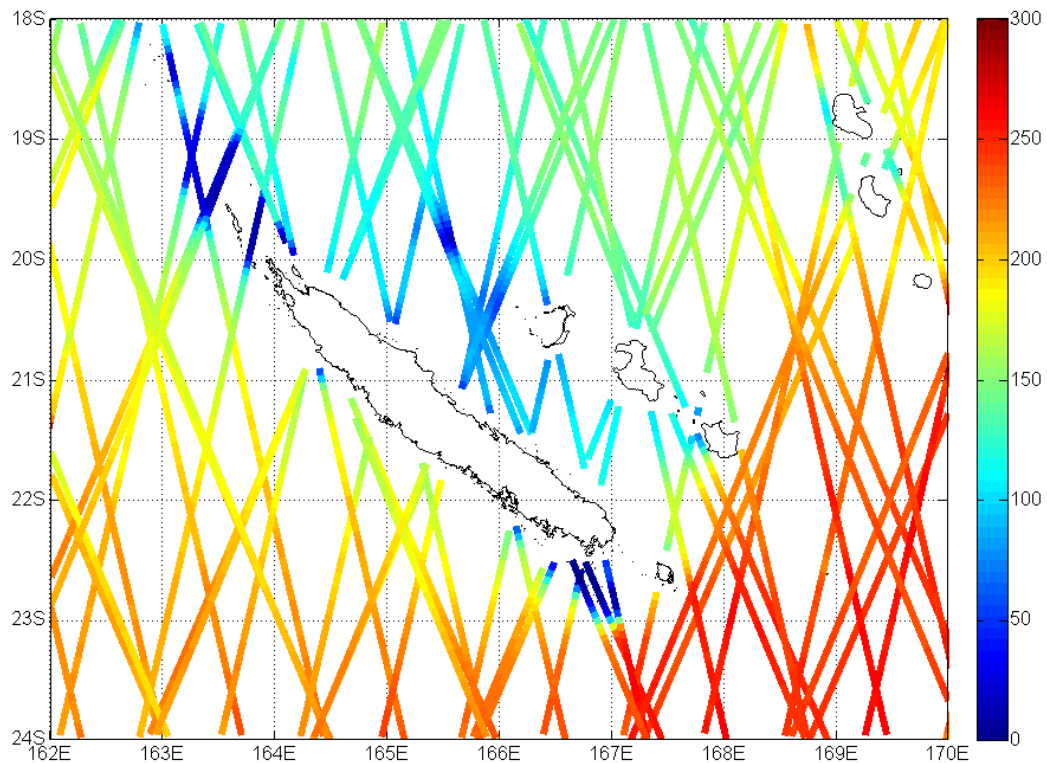


Figure 4.17. Annual mean Pelamis power around New Caledonia for combined altimeter tracks.

Individual tracks are limited by altimeter measurement problems close to shore. The waveform is distorted if there is land within the radar footprint (around 5 km in diameter) and when the satellite is tracking from land to sea it can travel up to 30 km

before regaining lock on the sea surface. Often no data are obtained, but sometimes spurious measurements are recorded so robust quality checking is required.

Despite the nearshore limitations, the track maps provide an attractive resolution. The resolution of global wave model data varies between about 0.5° and 1.5° (about 50km to 150km). From Figure 4.17 it can be seen that altimeter maps can provide information on scales shorter than 0.5° . The along-track resolution is about 10km (of the order of the size of the footprint of a 1Hz measurement). Ultimately though the resolution is limited by separation between tracks, but when data from multiple altimeter missions is combined, the distance of a point to the nearest altimeter track rarely exceeds about 30km. To provide maps of a comparable resolution from model data would require additional nearshore modelling, further increasing the cost of a study.

The uncertainty in the along-track averages is visible from the differences between nearby tracks. The along-track mean values are based on different, but overlapping periods, dependent on the length of data available for each altimeter. Individual tracks may be too high or too low from randomly sampling a greater or lesser proportion of storms. The uncertainty in the long-term along-track average limits the accuracy to which two sites can be compared. For instance from Figure 4.17 it is clear that the area to the south east of Mare (the island located at 21.5°S 168°E) would produce a higher energy yield than a location on the south west facing coast of the main island. However, due to the uncertainty in the estimates of mean power and the distance between the tracks, it is not clear from the figure which part of the south east facing coast has the highest power.

It may be possible to reduce the uncertainty in individual tracks by incorporating information from nearby tracks using a spatio-temporal interpolation. However, the scheme would require a careful analysis of the spatial and temporal variability in the wave field and may be difficult to implement in practice. Moreover, the scheme would not be able to interpolate accurately between tracks in nearshore areas where there is high spatial variability due to bathymetry or sheltering. If information is required on a finer scale than about 30km then a nearshore model would need to be used, which could account for shallow water and sheltering effects. The use of altimeter data to drive nearshore models is discussed in Section 5.3.

4.6 Conclusions

Satellite altimeter measurements can be used to provide a robust estimate of the power produced by a WEC. Although individual altimeter measurements show a large scatter compared to buoy measurements, the long record of altimeter data available allows the monthly and annual means to be calculated accurately for offshore locations. Closer to land, where the spatial variability is higher, measurements can be averaged over individual altimeter ground tracks. Despite the sparse temporal sampling, the long-term mean values are of a useful accuracy. The spatial resolution of altimeter ‘track-maps’ is better than is currently available from global wave model data. Depending on the location of altimeter tracks within the area of interest, altimeter maps are useful on scales upwards of 30-50 km. In areas where high resolution wave model data is not available, or where it is only available at a significant cost, altimeter maps provide an attractive alternative for producing regional scale maps of WEC yield.

5. Resource Estimation from Model Data

In this section the estimation the long term resource a specific site is considered. It is rare that there will be a long record of in-situ measurements at or close to the site of interest, so an alternative is needed. In the previous section it was shown that the usefulness of altimeter data on its own is limited by low temporal sampling, the distance between ground tracks and problems measuring close to shore. Wave estimates from large scale wave models can be used as boundary conditions for nearshore models, enabling high-resolution mapping of the resource close to the coast.

In this chapter two such nearshore models for the EMEC test site in Orkney are examined. Over an 8 year period, covered by both datasets, the values of the mean power produced by the Pelamis calculated from each model differ by 20%. It is clear that one or both models produce significantly biased estimates. In Section 5.1 the calibration of model data using in-situ measurements is discussed and a method is proposed to calculate confidence bounds for estimates of WEC yield from calibrated model data. This is compared to the limiting accuracy due to sampling variability in Section 5.2, and to the accuracy achievable from altimeter data in Section 5.3.

5.1 Calibration and confidence bounds

Errors in model data for a given sea state can be thought of as having a mean and a random component. For example, for an H_s of 2 m, the mean model value could be 2.1 m, with a standard deviation of 0.2 m. The calibration problem for model data is to determine the mean model estimate for a given sea state. Estimating confidence bounds requires the determination of the random model response. It can be difficult to distinguish between the mean and random model errors, since the error at a given location is the integrated effect of mean (predominantly internal) and random (predominantly external) errors over the whole wave field. Moreover, biases can have

complex dependences on multiple parameters and may be non-stationary with both location and time.

It is necessary to use an array of different techniques to understand the behaviour of the model. However, the way in which the data is examined can affect the results. This section begins with some notes on the different techniques which have been used to examine the performance of model data and points out some potential pitfalls. A method is then proposed to model the errors and uncertainties in the two EMEC hindcasts, accounting for the error characteristics described in Section 2.3.3.

5.1.1 Techniques for estimating model errors

5.1.1.1 Review of techniques

Various approaches can be taken to estimate model errors. For example, if there is reason to believe that the model bias may be a linear function of H_s , then linear regression can be used (e.g. Bidlot et al, 2002; Tolman et al, 2002). To test for non-linearities, the bias and scatter index of model data can be plotted against integrated buoy parameters such as H_s and T_p (e.g. Bidlot et al, 2002) or the bias can be calculated in discrete frequency bands (e.g. Rogers et al, 2005; Janssen, 2008).

Alternatively, if three or more concurrent datasets are available then a multiple collocation technique can be used to explicitly calculate the bias (relative to one dataset) and error variance of each dataset (e.g. Caires and Sterl, 2003; Janssen et al, 2007). A more sophisticated approach was implemented by Caires and Sterl (2005), in which corrections are estimated using a non-parametric method, based on analogues in a learning dataset.

Another approach is the comparison of distribution functions via quantile-quantile plots (e.g. Swail and Cox, 2000; Cox and Swail, 2001; Swail et al, 2000; Caires & Sterl, 2005; Swail et al, 2006). Using distribution functions has the advantage that the effects of random errors and temporal offsets (jitter errors) are smoothed out.

5.1.1.2 A note on the interpretation of results

In model validation studies, the objective is usually to determine the model response for a given sea state. For the purposes of estimating WEC yield we would like to know

what the actual sea state is for a given modelled estimate. These two problems are subtly different. It may seem logical to determine the mean value reported by a buoy for a given model estimate, since this is what we want to know. However, this method will lead to a calibration which is dependent on the distribution of the parameter of interest (H_s or T_e) during the calibration period.

Consider a comparison of H_s from an idealised model with a buoy. Suppose that the model has normally distributed errors with zero mean and a standard deviation of $0.2+0.1H_s$. We assume that sampling errors in the buoy data are minimal (a reasonable assumption for 3 or 6 hour averages) and simulate buoy and model data for summer and winter distributions. These have been estimated from 5 years data from the EMEC buoys, with lognormal distributions providing a good fit to both summer and winter data. The mean H_s in summer is 1.3m, with a variance 0.67 m^2 , the winter mean is 2.71 m, with a variance of 2.10 m^2 . The fitted distributions are shown in Figure 5.1

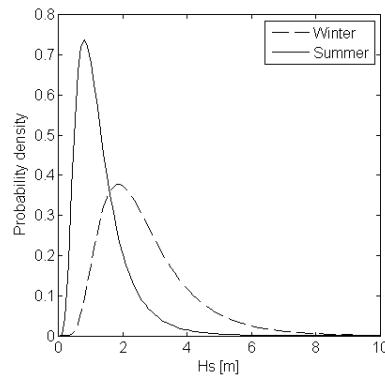


Figure 5.1. Summer and winter distributions of H_s at EMEC.

Figure 5.2 shows plots of the mean value of model H_s binned by buoy H_s , mean buoy H_s binned by model H_s and q-q plots for the summer and winter data. Since the model is unbiased, the mean value of model H_s binned by buoy H_s is equal to the buoy H_s and the line is straight. However, it can be seen that the mean value of the buoy for a given model value differs from summer to winter, with a larger bias for low H_s in winter and the location at which the lines cross changing. Similarly, the shape of the q-q plot is dependent on the distribution of buoy H_s . This is because the distribution of model H_s is a convolution of the model error distribution with the true distribution of H_s . The

situation is similar to that described by Tolman (1998), in the context of observation errors.

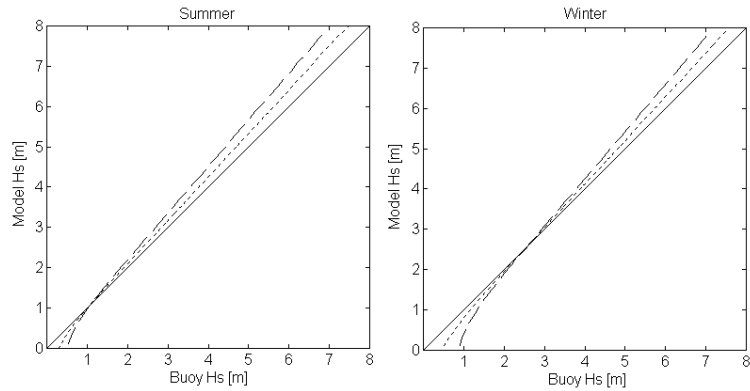


Figure 5.2. Solid line: mean model H_s binned by buoy H_s ; dashed line: mean buoy H_s binned by model H_s ; dotted line: q-q plot. For distributions of H_s shown in Figure 5.1, left – summer; right – winter.

So despite the fact that the model is unbiased and does not change calibration, this example demonstrates that it can appear to change calibration throughout the year. It should be noted that the changes between the summer and winter distributions are much larger than interannual changes in distributions, so the differences would be much smaller if we compared bin-average and q-q plots using data for whole years. However, it will be shown the next section that there are actual changes in the performance of the model throughout the year, and these changes should not be confused with the apparent changes shown here.

5.1.1.3 The calibration problem

A further problem arises when a calibration is applied to the model data. Again we can consider a simple hypothetical situation to illustrate the problem. Suppose we have a modelled estimate X_m of a real variable X and that

$$X_m = X + \varepsilon \quad [5.1.1]$$

and

$$\varepsilon \sim D(\mu(X), \sigma^2(X)) \quad [5.1.2]$$

where D is some distribution specified by its mean and variance, both of which are dependent on X . Suppose that $\mu(X)$ and $\sigma(X)$ are stationary in time and can be determined from a bin average analysis. In this case a functional relationship, g , can be defined between the real and modelled values:

$$\begin{aligned} X_m &= X + \mu(X) + \delta \\ &= g(X) + \delta \end{aligned} \quad [5.1.3]$$

where

$$g(X) = X + \mu(X) \quad [5.1.4]$$

and

$$\delta \sim D(0, \sigma^2(X)) \quad [5.1.5]$$

We then calibrate the model by applying the inverse function:

$$\begin{aligned} Y &= g^{-1}(X_m) \\ &= g^{-1}(g(X) + \delta) \end{aligned} \quad [5.1.6]$$

where Y denotes the calibrated model values. We need to determine whether the mean of the calibrated model, Y , is equal to the mean of the real variable X . In the case that g is a linear function, $g(X) = aX + b$, we have $Y = X + \delta/a$. So the mean of X is equal to the mean of Y , since δ has zero mean. However, if g is non-linear, then the situation is more complicated. From simulation, it can be demonstrated that mean value of Y is not necessarily equal to the mean of X , the difference being dependent on both the distribution of X and the error distribution.

If instead we calibrate the model using the mean value of X for a given X_m , then by definition the mean values of X and Y will be equal within the calibration dataset. However, we are left with the problem that mean value of X for a given X_m is dependent on the distribution of X , so if the distribution of X changes outside the calibration period then the mean values of X and Y will not be equal.

A possible solution to this would be to use a method similar to that proposed by Tolman (1998) for estimating the true distribution of a variable which is observed with error.

This method involves estimating the true distribution of X from the distribution of X_m and the distribution of X_m given X . An estimate of the distribution of X given X_m , outside the calibration period, can then be made and used to calibrate the model. However, this method is complicated to implement and was found to make only a small difference to results. Moreover, it will be shown in the next section, model performance is normally dependent on multiple parameters, so these arguments become somewhat academic. Nevertheless, they illustrate that determining and applying a calibration to a model is not straight forward.

5.1.2 Assessment of EMEC hindcast errors

In this section an assessment of two independent modelled datasets for the EMEC test site is presented. One dataset is supplied by OCEANOR, it covers the period 01/01/1997 – 31/12/2004 with 6 hour time steps. The data are produced using the SWAN model (Booij et al, 1999), with boundary conditions from an archive of operational data from the ECMWF WAM model. The other dataset is supplied by ARGOS and covers the period 01/01/92-31/7/2005 with 3 hour time steps. It is produced using an in-house nearshore model, with boundary conditions obtained from an in-house hindcast using WaveWatch III.

The model data is compared to measurements from the EMEC buoys (as described in Section 2.1.3.2) averaged to 3 hours for the comparison with ARGOS and 6 hours for the comparison with OCEANOR. The model is assumed to be of sufficiently high spatial resolution that spatial representativeness errors are not significant. However, since the input data for the nearshore models comes from global scale models, this assumption may be somewhat optimistic. The buoy data has a sampling variability of about 2% for a 3 hour average of H_s and about 1% for a 6 hour average. From the results of Tolman (1998) it can be assumed that this level of sampling variability will have negligible impact on our results.

There are a number of different approaches which can be taken when calibrating model data. These are:

Method A: To directly calibrate the estimate of WEC power from the model against the power estimated from the buoy. This approach has the advantage that only one variable

is involved. However, the calibration will be dependent on the joint distribution of H_s and T_e in the calibration period. For example the power response of a WEC will reach a maximum at some given H_s , so if the proportion of time that the WEC is operating at maximum power is different outside the calibration period, then a calibration based on model power alone may not be appropriate.

Method B: To define a look-up table of the value of power estimated from the buoy, binned by model H_s and T_e . This would be a more flexible approach than calibrating by power alone, but suffers from the problems of estimating the mean buoy value for a given model value described in Section 5.1.1.2.

Method C: To calibrate the model H_s and T_e independently, using a bin-average method (binned by buoy values). This method is still susceptible to problems when applying non-linear calibrations, as described above, but these effects are relatively small. The other point to be aware of is that errors in H_s and T_e may be correlated, so adjusting parameters independently may change the shape of the joint distribution.

This last method will be used to calibrate the EMEC hindcasts.

5.1.2.1 Analysis of trends

The first step in assessing the hindcasts is to examine the time series. Figure 5.3 shows plots of H_s from the models and the buoy over a two month period, but the trends shown here are reasonably representative of the whole calibration period. On the whole, the models seem to reproduce the time series of H_s quite well and temporal offsets appear small. The ARGOS data is consistently lower than the buoy data and OCEANOR data is higher, although both models underestimate the most intense storm in this period. A 3 hour average of buoy data is used in this plot, but it is clear that there is still more short term variability in the buoy data than in the ARGOS model. This is likely to be a result of the tidal modulation of the waves, discussed in Section 2.1.3, and the fact that the nearshore model data is based on estimates from large scale models which will give smoother time series.

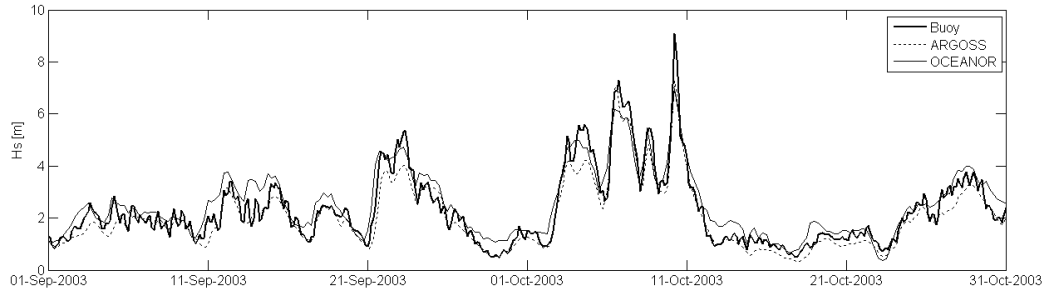


Figure 5.3. Time series plots of H_s from buoy and models.

The next step is to examine scatter plots of the parameters. Figure 5.4 shows scatter plots of model H_s against buoy H_s and model T_e against buoy T_e . It is instructive to colour the plots by the buoy H_s and T_e , to see if the performance of model H_s is dependent on buoy T_e or model T_e on buoy H_s . The scatter is reasonably low for H_s , but it is visible that the OCEANOR model tends to overestimate H_s between 2m and 4m at longer periods. For both models there is more scatter for T_e , especially for low H_s .

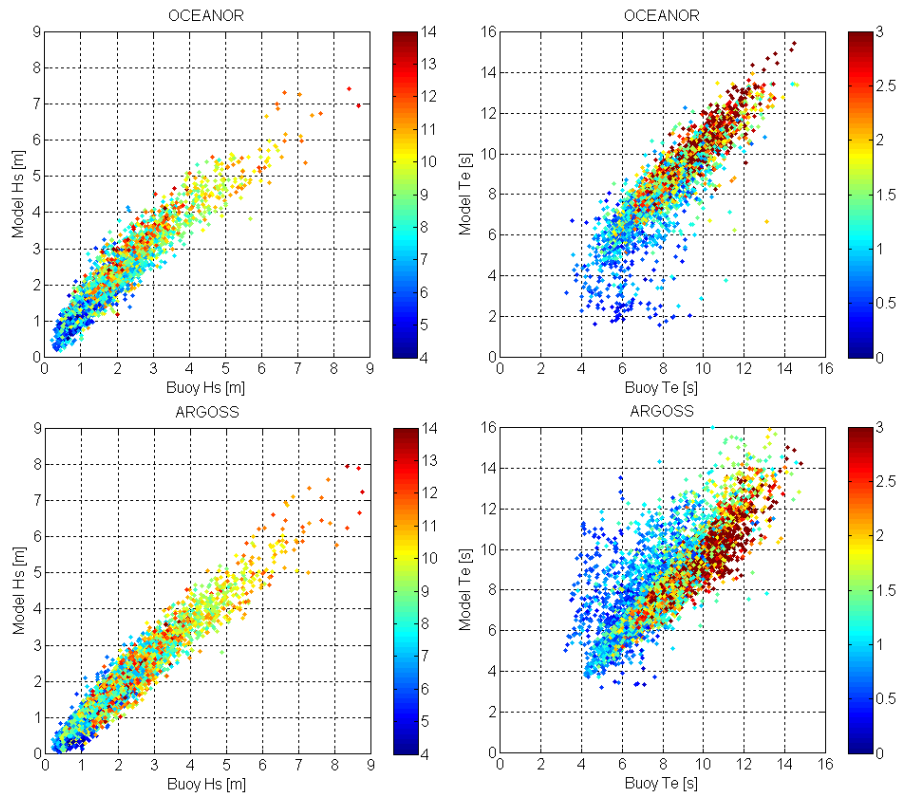


Figure 5.4. Scatter plots of buoy and model H_s (left) and T_e (right), colour denoting buoy T_e (left) and buoy H_s (right).

Figure 5.5 shows the bias in the OCEANOR model, binned by buoy H_s and T_e . As was seen in the scatter plots, the OCEANOR model is observed to over-predict H_s more for swell events with buoy T_e above about 12s and H_s below 5m. This counts for less than 5% of our dataset, and for the remaining data the bias in H_s appears to be dependent on H_s only. The poor performance of model T_e in low H_s is also clear. A trend is observed with buoy steepness, but not with model steepness, and therefore is difficult to correct for. Since the poor performance occurs at low H_s and hence low WEC power, no attempt is made to correct for it and instead only points with buoy $H_s > 1$ m are used to calibrate OCEANOR T_e . However, although these data are not used in the calibration of T_e , they are used for the assessment of the derived WEC power.

Figure 5.6 shows similar plots for ARGOSS. Note that a different colour scale has been used in order to highlight the trends in the data. The dependence of error in model H_s on buoy T_e does not appear to be as strong as for OCEANOR. There is some trend visible in the error in model T_e on buoy H_s . However, if the performance of ARGOSS T_e is examined in terms of model parameters the trend is much stronger. Figure 5.7 shows the bias in model T_e against model H_s and T_e , and also against model steepness (here steepness is defined in terms of T_e rather than T_z , as $\text{steepness} = 2\pi H_s / gT_e^2$). The model is effectively over-predicting T_e for low-steepness swell events. A new model period is defined, with an exponential correction in steepness (shown in Figure 5.7). From hereon this definition is used for ARGOSS T_e .

This correction in terms of model parameters is subject to the effects of changing distributions, discussed in the last section. However there is little that can be done about it, since the trend is not evident with buoy parameters. The correction is also remarkably effective in decreasing the level of scatter, with the standard deviation of the differences decreasing from 1.17s to 0.85s for the new definition.

The performance of both models is likely to be dependent on numerous other factors as well, such as frequency, swell age, wind sea component, etc. Full directional spectra are calculated by the models but only integral parameters were provided from the suppliers, so it is difficult to make a more detailed assessment. Dependence on direction was

tested for, but no trend was found. Strictly speaking, it is only fair to assume that model errors are a purely random when there is no residual dependence on other factors.

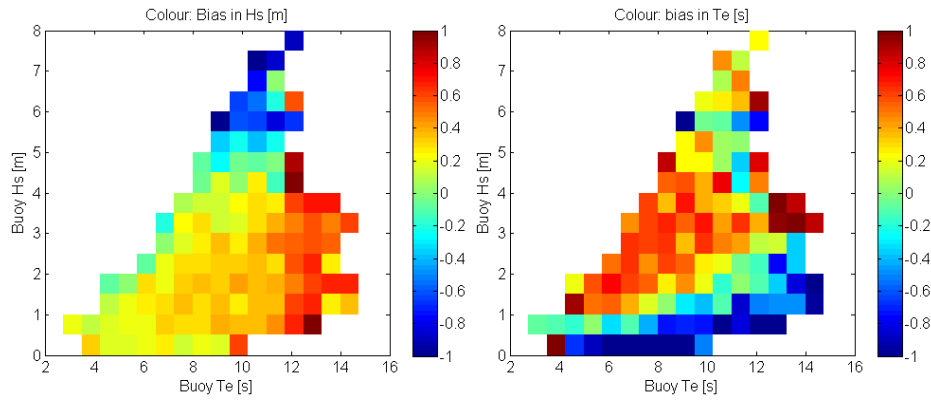


Figure 5.5. Bias in H_s and T_e for OCEANOR model, binned by buoy H_s and T_e .

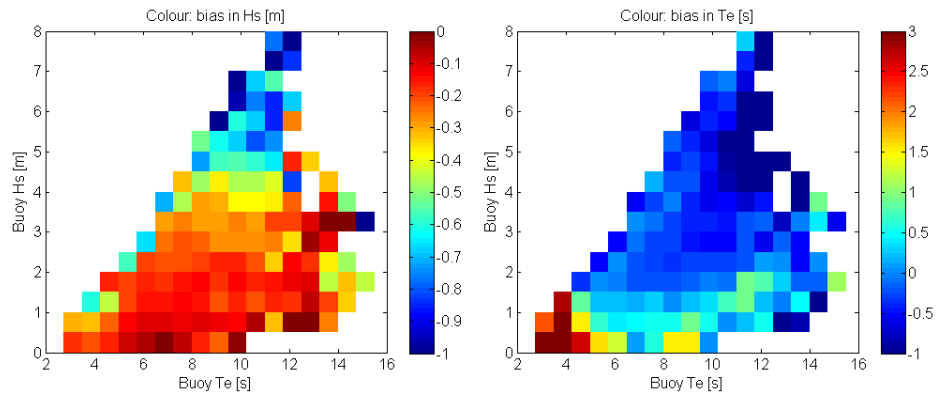


Figure 5.6. Bias in H_s and T_e for ARGOSS model, binned by buoy H_s and T_e .

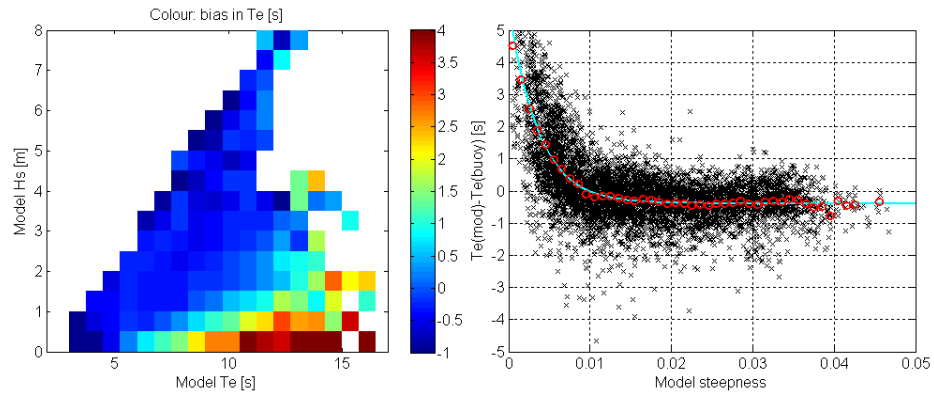


Figure 5.7. Left: bias in ARGOSS T_e , binned by model H_s and T_e . Right: bias in ARGOSS T_e against model steepness, black crosses – individual points, red circles – bin average, cyan line – fitted exponential curve.

Figure 5.8 shows how the bias in model H_s changes throughout the year. The OCEANOR model over predicts low H_s in the winter, but is almost unbiased at low H_s in the summer. This is contrary to the results of Janssen (2008) who showed that averaged over a number of NDBC buoys, the ECMWF WAM model overestimates low frequency energy in the summer. Since we are binning by H_s rather than frequency, our results are not directly comparable, but the changing bias observed here may be a result of the tuning of the model to compensate for biases elsewhere. Note that since we are binning results by buoy parameters, the changing calibration is not a result of changing distributions between summer and winter, as described in the previous section. The ARGOSS model does not appear to perform differently in summer and winter, despite the shorter colour scale used in the plot.

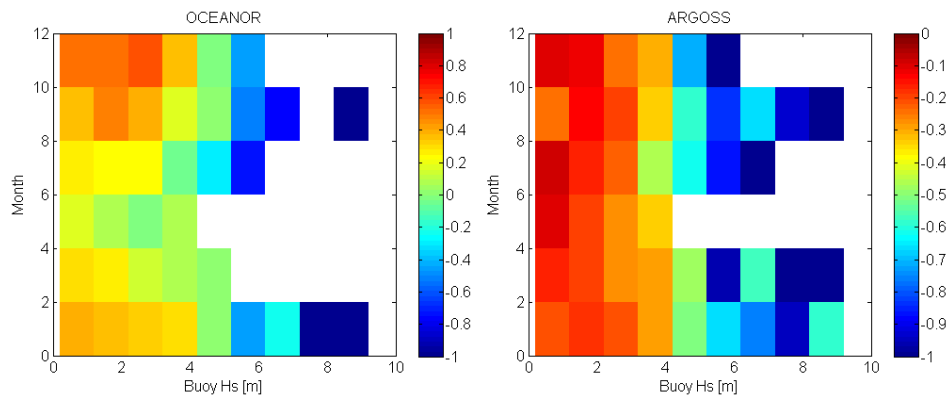


Figure 5.8. Bias in model H_s in binned by month and buoy H_s . Left: OCEANOR, right: ARGOSS.

Using a seasonal calibration for the OCEANOR data was tried and found to perform worse outside the calibration period, than a non-seasonal adjustment. This is thought to be because calibrating for each season reduces the number of points and therefore increases the uncertainty in estimating trends.

Finally, we can test for correlation in the model errors in H_s and T_e . Overall the correlation is low, about 0.2 for OCEANOR and 0.1 for ARGOSS. However, if we examine if errors in specific circumstances are correlated then some patterns emerge. Figure 5.9 shows the correlation in errors in model H_s and T_e , binned by buoy H_s and T_e . Note that only bins containing 10 or more points have been displayed. For OCEANOR a stronger correlation is apparent for at low H_s , which may be related to the poor

performance of model T_e at low H_s . For ARGOSS the correlation in the errors is strongest in steep seas. This is a result of the limiting steepness, necessitating that an increase in H_s for a steep sea is accompanied by an increase in period. There is also some positive correlation of errors in swell events. For the highest occurrence sea states the correlation is low. The pattern of correlations in errors in the ARGOSS data is similar to the correlation observed in differences between two buoys, shown in Figure 2.5.

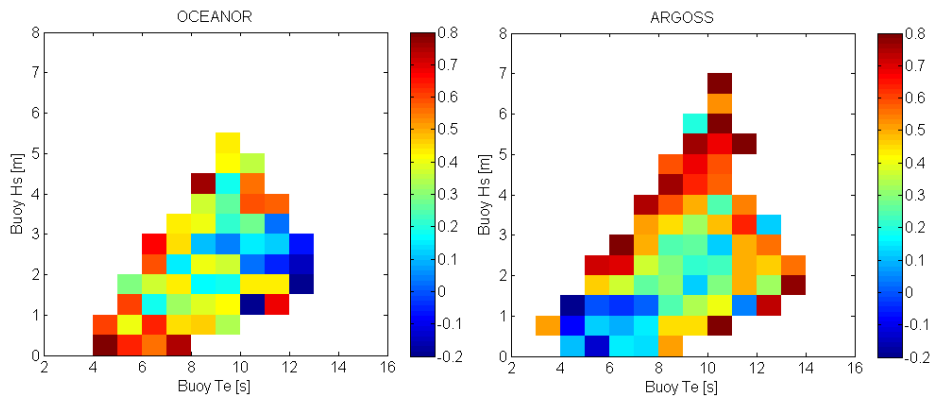


Figure 5.9. Correlation in errors in model H_s and T_e , binned by buoy H_s and T_e .

5.1.2.2 Calibration of the models

Figures 5.10 and 5.11 show bin-average plots of the bias and standard deviation in the model errors. We model the bias in H_s as quadratic, and the bias in T_e as linear. The standard deviation is modelled as linear in H_s and constant in T_e . At higher values of H_s and T_e there are few data points, which makes the estimates of the standard deviation in model errors uncertain. Therefore the points which are away from the trend lines on the far left of Figures 5.10 (b), 5.10 (d), 5.11 (b) and 5.11 (d) are not considered significant. The use of a quadratic calibration for H_s means that there will be a maximum model response at some point. For the OCEANOR this occurs when the buoy H_s is 13.2m and model H_s is 7.9m. Clearly this is not a realistic assumption, since the OCEANOR hindcast contains storms outside the calibration period, exceeding this value, with a maximum of 8.4m. The situation is not as severe for the ARGOSS model, with the maximum occurring when the buoy H_s is 32.3m and model H_s is 15.7m. This does not present a problem for the estimation of WEC power, but clearly is not satisfactory for the estimation of extremes. A slightly different method for calibrating model data at extremes is presented in Chapter 7.

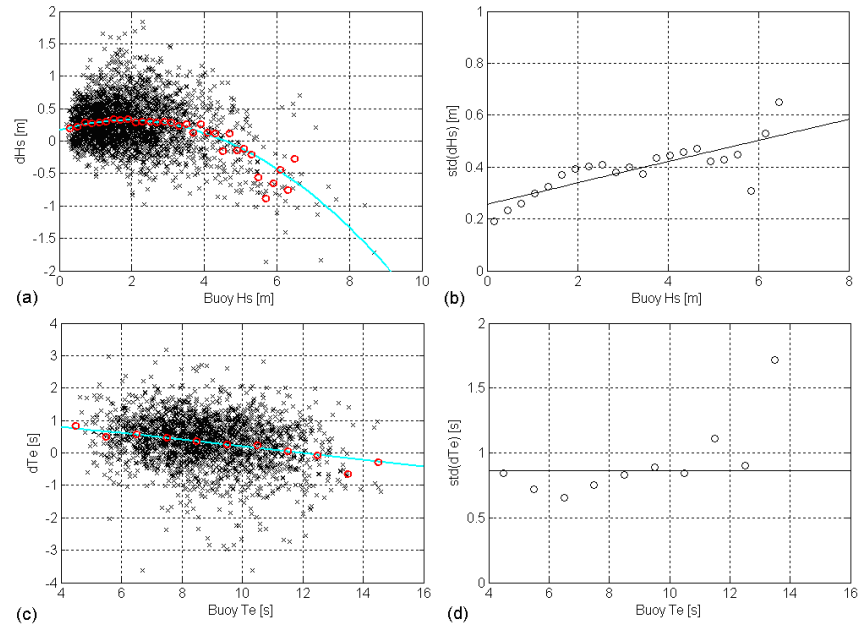


Figure 5.10. (a) Error in model H_s against buoy H_s ; black crosses: individual points, red circles: bin average, cyan line: fitted quadratic curve. (b) Standard deviation of error in model H_s ; circles: bin average, line: fitted linear relationship. (c) Error in model T_e against buoy T_e , for buoy $H_s > 1\text{m}$; black crosses: individual points, red circles: bin average, cyan line: fitted linear relationship. (d) Standard deviation of error in model T_e ; circles: bin average, line: average over dataset. All plots for OCEANOR model.

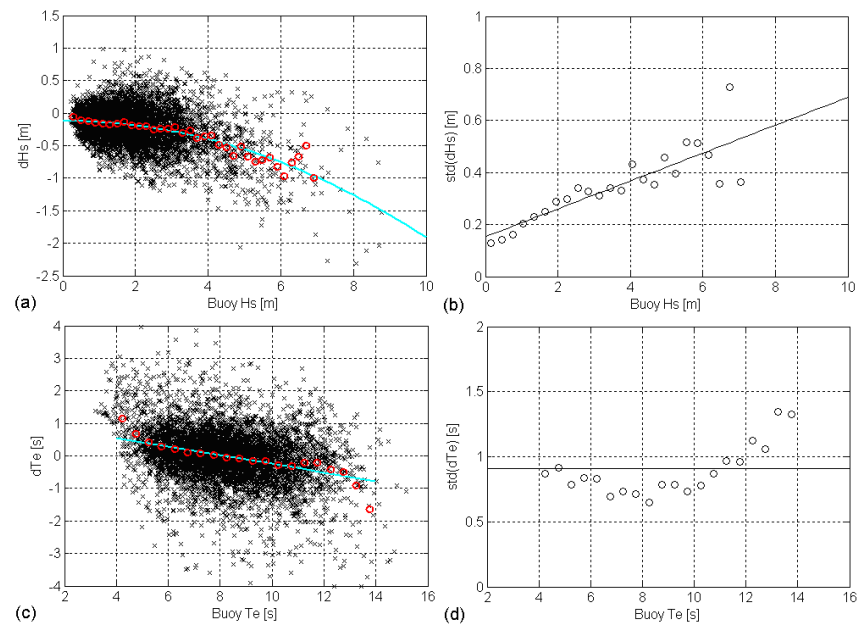


Figure 5.11. As previous figure, but for ARGOSS model.

Figure 5.12 shows q-q plots of Pelamis power for the calibrated and uncalibrated models, calculated from the power matrix, shown in Table 1.1, interpolated to a resolution of 0.1m H_s and 0.1s T_e . There is a clear improvement for both models after calibration, but with some small discrepancies remaining. This is most likely because the parametric correction that was applied does not entirely describe the model behaviour. But it could also be a result of correlation in the errors in H_s and T_e or an effect of using a non-linear calibration, described in Section 5.1.1.3. Considering the models are calibrated in terms of H_s and T_e and the Pelamis response is calculated afterwards, the result is good. For OCEANOR, the bias before calibration is 30.1 kW and -4.0 kW after calibration. For ARGOSS, the bias before calibration is -24.4 kW and -2.3 kW after calibration. Figure 5.13 shows scatter plots of monthly mean Pelamis power for the calibrated models against buoy values. It is clear that the agreement is better for the ARGOSS model. The standard deviation is 18.1 kW for OCEANOR and 7.9kW for ARGOSS.

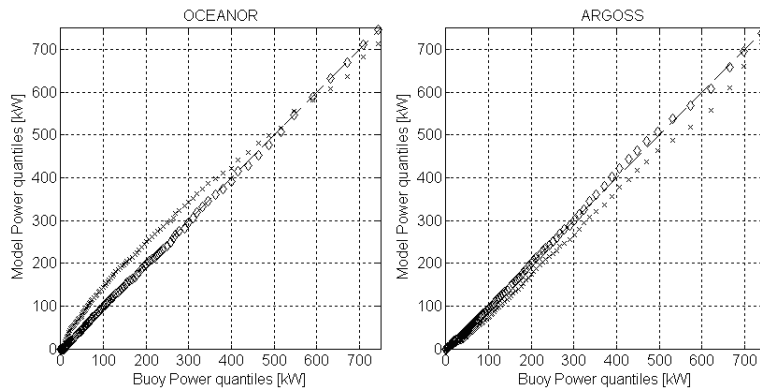


Figure 5.12. Quantile plots of model against buoy Pelamis power. Crosses: uncalibrated models; diamonds: calibrated.

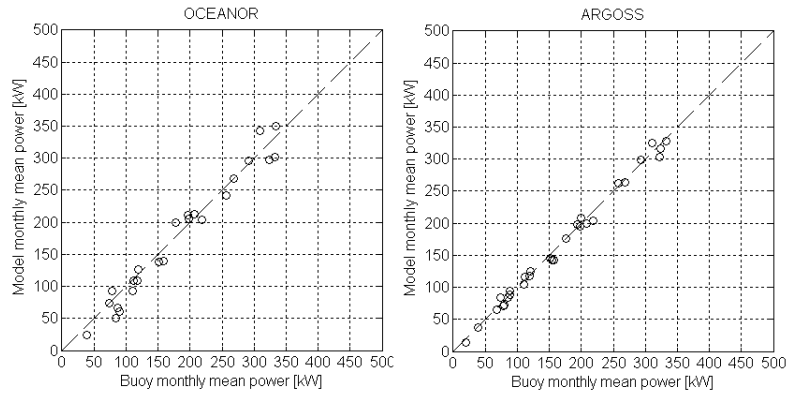


Figure 5.13. Scatter plots of monthly mean Pelamis power for calibrated models against buoy values.

Figure 5.14 shows the monthly mean Pelamis power from calibrated hindcasts for the 8 year period that they overlap. The mean power over the entire period is 188.4 kW for ARGOSS and 179.4 kW for OCEANOR, a difference of 5%, compared with 167.9 kW and 212.9 kW before calibration. This is an improvement, but it is clear from Figure 5.14 that some residual trends remain. In particular the calibrated OCEANOR model gives consistently lower powers in the summer months, a consequence of the seasonal change in calibration mentioned before. Moreover, since the boundary conditions for the OCEANOR hindcast came from an archive of operational data from the ECMWF WAM model, changes to the WAM model made over the years are likely to affect the calibration. These include:

- June 1998: wave model integrated into the atmospheric model allowing two-way interaction of wind and waves.
- April 2002: average effects of gustiness on wave growth included in wave model to make up for low variability in modelled surface winds.
- February 2004: wavenumber dependent blocking factor introduced to account for unresolved islands (mainly affects Pacific Ocean).
- March 2005: New formulation of dissipation source term implemented (this is outside the period covered by our dataset, but is noted here for interest).

It is difficult to see the effects of these changes on our dataset, but it is likely that they make some impact on the calibration.

There is also some difference during the calibration period. The calibrated OCEANOR model is lower than the ARGOSS model during the period June-August 2004. However, the agreement in the previous summer (also within the calibration period) was good. The ARGOSS model is in much closer agreement with the buoy during June-August 2004, so this is further evidence of changing biases in the OCEANOR model.

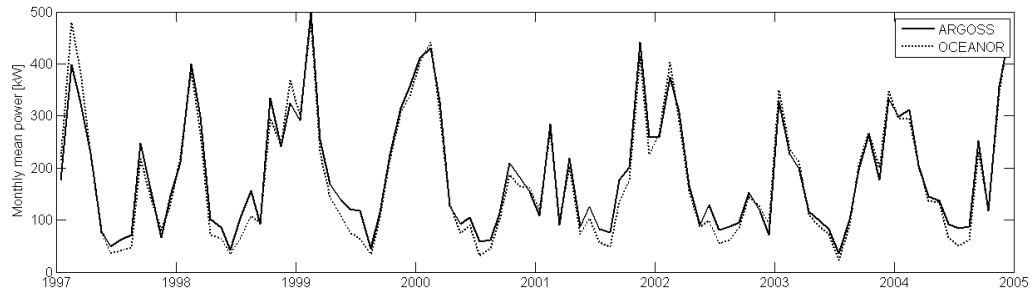


Figure 5.14. Monthly mean Pelamis power from the calibrated models.

5.1.3 Estimating uncertainty in WEC yield

The error in the estimate of Pelamis power from each model exhibits correlation over short time scales. This suggests the use of time series models for representing the evolution of errors and estimating confidence bounds for the model estimates of power. Some notes on time series models are presented in Appendix F. The procedure we will follow to fit the time series model consists of the following steps:

- Estimate distributions of errors in model H_s and T_e
- Calculate the distribution of errors in model WEC power.
- Normalise the error in model power.
- Fit time series model

To estimate confidence bounds we can then generate a large number of simulations using the fitted time series model, which are the length of the hindcast. We then un-normalise to the series to get a number of simulated realisations of the error over the entire hindcast. From this we can calculate error bounds for monthly, annual or multi-year averages of WEC power.

Figure 5.15 shows the distribution of the errors in model H_s and T_e , normalised by the standard deviations (shown in Figure 5.10 and 5.11). The normalised errors are approximately normally distributed, apart from ARGOSS T_e which shows a slightly more peaky distribution. However, we will approximate this with a Gaussian.

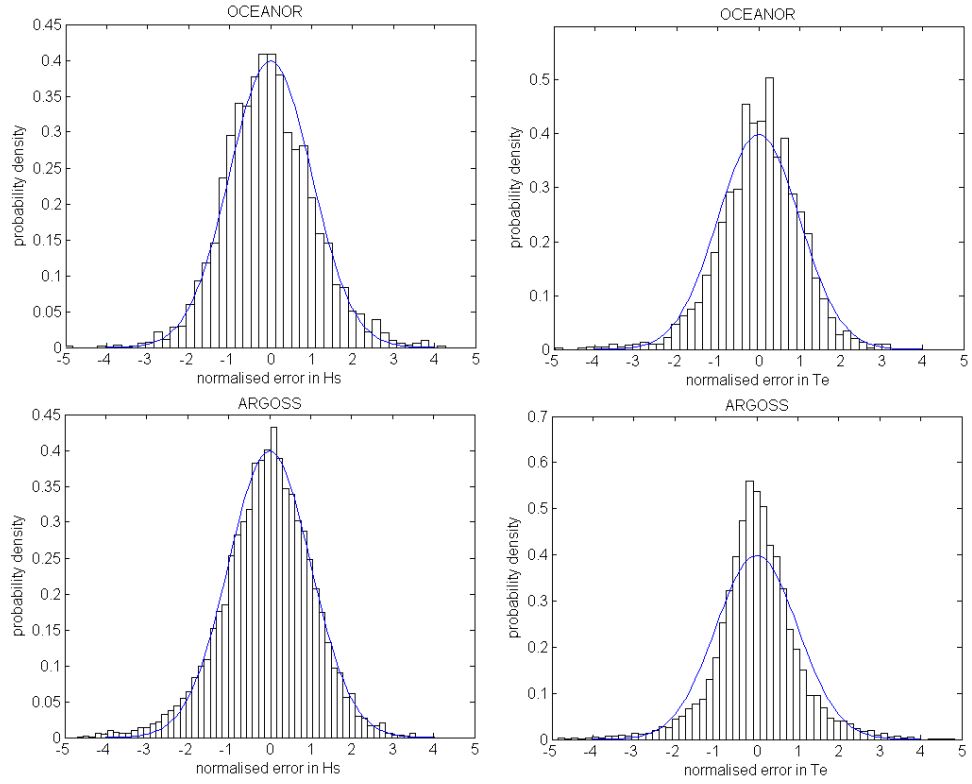


Figure 5.15. Distribution of normalised errors in model H_s and T_e (histograms) with fitted normal distribution (lines).

The error in model estimates of Pelamis power is a function of both H_s and T_e . Figures 5.16 (a) and 5.16(c) show the standard deviation of the error in model power, binned by the buoy values of H_s and T_e . More formally, let $H_b(t_i)$ and $T_b(t_i)$ denote the buoy measurements at time t_i , and $H_m(t_i)$ and $T_m(t_i)$ denote the model estimates. Let $P(H, T)$ denote the Pelamis power response calculated by linearly interpolating the values shown in the power matrix (Table 1.1). If we define the set S as all values of i such that $H_s - dh/2 \leq H_b(t_i) < H_s + dh/2$ and $T_e - dt/2 \leq T_b(t_i) < T_e + dt/2$, then the values shown in Figures 5.16(a) and 5.16(c) are given by

$$\sigma(H_s, T_e) = \sqrt{\sum_{i \in S} [P(H_m(t_i), T_m(t_i)) - P(H_b(t_i), T_b(t_i))]^2} \quad [5.1.7]$$

In Figure 5.16 a bin size of $dh = 0.5\text{m}$ and $dt = 0.75\text{s}$ has been used. The bin size is a compromise between resolution and having enough data to accurately estimate the

standard deviation. The standard deviation of the error in model power can also be calculated from the estimates of the error distributions of model H_s and T_e . The model errors in H_s and T_e are correlated in some places, so strictly this should be accounted for when calculating the distribution of the error in estimated Pelamis power. However, it was found that accounting for the correlation made little difference in practice and they are assumed to be independent here. Let $f_{H_m|H_s}$ and $f_{T_m|T_e}$ denote the density function of the model values, given the real values. The pdf $f_{H_m|H_s}$ is modelled as normal with standard deviation increasing linearly with H_s , and the pdf $f_{T_m|T_e}$ is modelled as normal with constant standard deviation. Then the variance of the model power for a given H_s and T_e is given by

$$\sigma^2(H_s, T_e) = \int_0^\infty \int_0^\infty f_{H_m|H_s}(h_m) f_{T_m|T_e}(t_m) [P(h_m, t_m) - P(H_s, T_e)]^2 dh_m dt_m \quad [5.1.8]$$

Figures 5.16(b) and 5.16(d) show the standard deviation of model error calculated using equation 5.1.8. The agreement with the values calculated from equation 5.1.7 is good, indicating that approximations which have been used for $f_{H_m|H_s}$ and $f_{T_m|T_e}$ are reasonable. This method of calculating the model error in Pelamis power has the advantage that the resolution can be made as high as required, so that the standard deviation can be calculated more precisely for a given H_s and T_e . This method will be used to normalise the model errors in power.

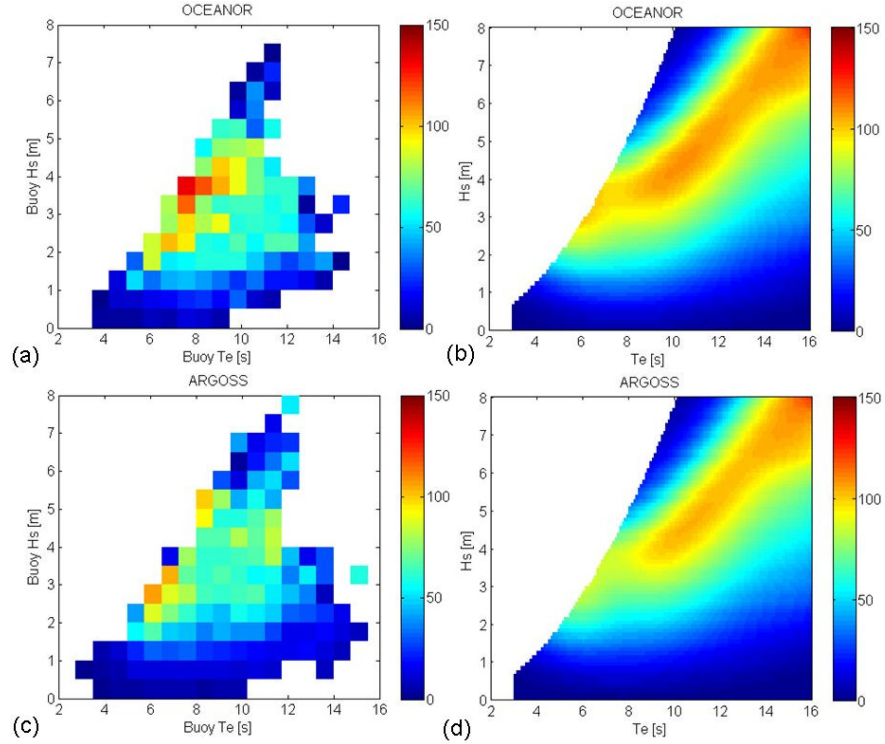


Figure 5.16. Standard deviation of the error in model power for OCEANOR (top) and ARGOSS (bottom). Left: from equation 5.1.7. Right: from equation 5.1.8.

If the uncertainty in WEC response were known, it could be factored in at this point. As was discussed in Section 1.4, a WEC will likely have a range of responses for a given H_s and T_e due to variation in spectral shape and directional spreading. We define Q to be the actual power generated by a WEC in a given sea state, and the probability that $Q = q$, given that $H_s = h$ and $T_e = t$, as $f_{Q|H_s, T_e}(q)$. Note that the power generated in a given sea state is not a random quantity, but rather $f_{Q|H_s, T_e}$ accounts for the effect of parameterising the power response in terms of H_s and T_e . The distribution $f_{Q|H_s, T_e}$ will typically vary from site to site, depending on the distribution of different spectral shapes which occur for a given H_s and T_e . Suppose that $f_{Q|H_s, T_e}$ is known for the site in question, then equation 5.1.8 can be modified to include this additional level of uncertainty:

$$\sigma^2(H_s, T_e) = \int_0^\infty \int_0^\infty \int_0^\infty f_{H_m|H_s}(h_m) f_{T_m|T_e}(t_m) [(P(h_m, t_m) - q) f_{Q|H_s, T_e}(q)]^2 dh_m dt_m dq \quad [5.1.9]$$

Where, as before, $P(H, T)$ is defined to be the WEC power given in the power matrix.

Returning to the time series modelling, since the error in model power is dependent on H_s and T_e , the errors need to be normalised before fitting a time series model. Each value of model power error is divided by the standard deviation calculated from the estimated distributions of errors in model H_s and T_e (the right hand plots in Figure 5.16). The resultant distribution of normalised errors is slightly non-Gaussian so we use the transformation:

$$z = \Phi^{-1}(F_X(x)) \quad [5.1.10]$$

where Φ is the distribution function of the standard normal distribution and F_X is the empirical distribution function of X . This transformation forces the empirical distribution of z to be exactly Gaussian.

ARMA models are fitted to the normalised errors in power using the method described by Priestley (1981), based on minimising Akaike's Information Criterion (see Appendix F for further details). An ARMA(2,3) model was found to provide the best fit for the OCEANOR residuals and an ARMA(3,2) was found to give the best fit for ARGOSS. Figure 5.17 shows the auto-correlation series for the errors in normalised hindcast power and the fitted ARMA model. It is clear that both ARMA models are in good agreement with the observed auto-correlations. The error caused by the tidal modulation of the wave field is also clearly visible. It is less pronounced for OCEANOR because of 6 hour averages are used instead of 3 hour averages for ARGOSS. When the ARGOSS model was averaged to give 6 hour values, the auto-correlation series was very close to that for the OCEANOR model (not shown).

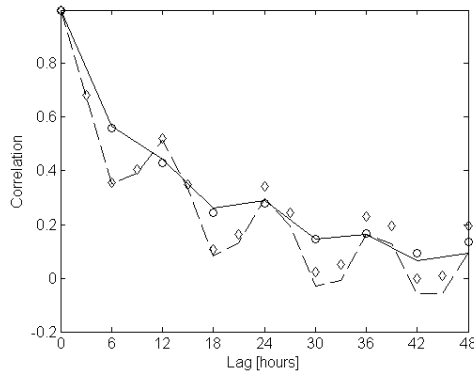


Figure 5.17. Auto-correlation series of normalised errors. Circles and solid line: values for OCEANOR and fitted ARMA(2,3) model. Diamonds and dashed line: values for ARGOSS and fitted ARMA(3,2) model.

To estimate confidence bounds for the calibrated hindcasts the following procedure is followed:

- Generate 1000 ARMA simulations, the same length as the hindcast.
- Apply the inverse transformation of equation 5.1.10.
- Multiply by the standard deviation of the error in model power obtained from the look-up table.

Note that here we are substituting the standard deviation in error for a given model estimate, for the standard deviation for a given buoy value. However, comparison of the two distributions showed that they are almost identical.

The differences between the monthly mean power from the buoy and calibrated ARGOSS model fall within the 95% limits obtained from the ARMA simulations, but the monthly OCEANOR errors are not within the range from the ARMA simulations. This is likely to be due to the changing seasonal calibration, which it was not possible to capture with the low-order ARMA model.

Figure 5.18 shows a scatter plot of the standard deviation of the error in monthly mean power from the ARMA simulations against estimated monthly mean power from the calibrated hindcasts. The OCEANOR hindcasts has higher monthly errors due to slightly higher error in individual estimates and slightly longer correlation times in the errors. The relationship between monthly mean power and the standard deviation in the model estimate is slightly non-linear, with the gradient decreasing with higher monthly

mean power. This is because when monthly mean power is high there is a high proportion of time when the Pelamis power is at maximum, and the standard deviation of the model estimate is lower.

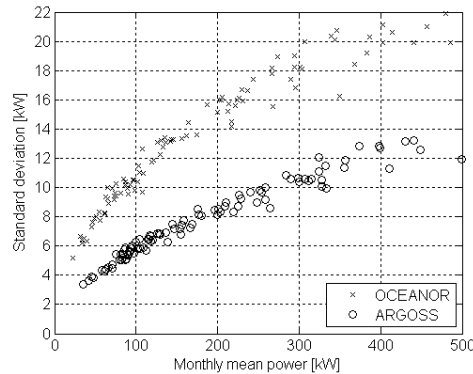


Figure 5.18. Standard deviation of the error in monthly mean power from the ARMA simulations against estimated monthly mean power from the hindcasts.

The 95% confidence interval for the mean power over the 8 year period from the ARMA simulation, is ± 1.6 kW for ARGOSS and ± 3.0 kW for OCEANOR. The actual difference in the 8 year mean power is 10 kW, outside the predicted bounds from the ARMA simulations. Moreover, in 24 of the 96 months that the hindcasts overlap, the differences between the monthly mean values are outside the 95% bounds from the combined ARMA models. We have already seen that the ARMA model does not capture the uncertainty from changing seasonal calibration in the OCEANOR model, and it will not account for any changes to the WAM model.

The bias in the mean power from the calibrated ARGOSS model over the 2 year calibration period was -2.3 kW and the 95% bounds from the ARMA simulations are ± 3.4 kW. So it is possible that the ARMA model is a valid representation of the uncertainty for the ARGOSS model, seeing as errors for individual months were also within the bounds from the ARMA model. However, it is possible that there could be some component of bias which is not captured by the ARMA model (which represents a zero-mean random process) which may affect the accuracy outside the calibration period.

5.1.4 Comparison of calibrated hindcasts

To understand better the reasons for the differences between the two hindcasts, we can compare the calibrated data. Figure 5.19 shows scatter plots of H_s and T_e for the calibrated hindcasts. It is clear that there is still some residual dependence of H_s on T_e and vice versa. The disagreement in T_e between the two models at low H_s is not surprising, since we ignored points with $H_s < 1\text{m}$ for the OCEANOR calibration. If these points are removed, the agreement is good. Figure 5.20 shows the mean and standard deviation of differences between calibrated T_e s, for average $H_s > 1\text{m}$. There is a small bias of 0.25s which seems constant over the entire dataset. The standard deviation of the differences in T_e increases approximately linearly with T_e . This trend was not so evident in the comparisons with the buoy, probably because there were fewer data points.

For H_s the dependence on period is consistent with the trend observed between OCEANOR and the buoy. There is a much larger disagreement between the models at high H_s . From inspection of time series, it is clear that this is not a result of jitter errors, but differences in the estimation of the peak H_s in a storm. This disagreement is not so important for estimating WEC power, but is much more serious for the analysis of extremes. Figure 5.21 shows the mean and standard deviation of differences in H_s between calibrated models. There is a small bias of 7cm over the entire hindcast, but which varies slightly with H_s . The standard deviation in the differences increases linearly with H_s up to about 6m, at which point it increases sharply due to the increased uncertainty in large storms.

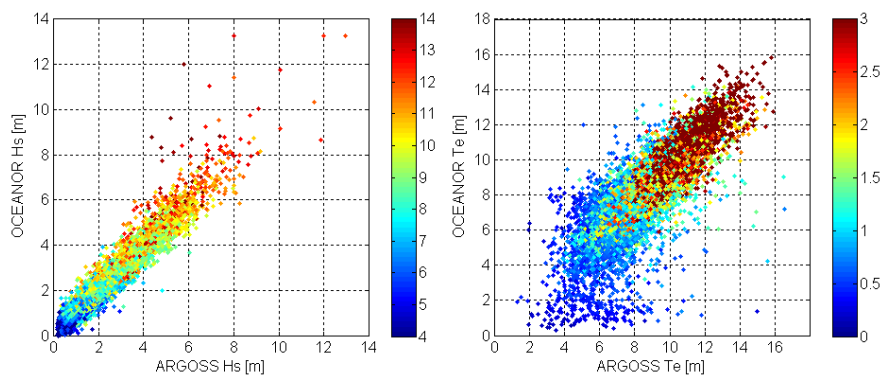


Figure 5.19. Scatter plots of H_s coloured by T_e (left) and T_e coloured by H_s (right) for the calibrated hindcasts.

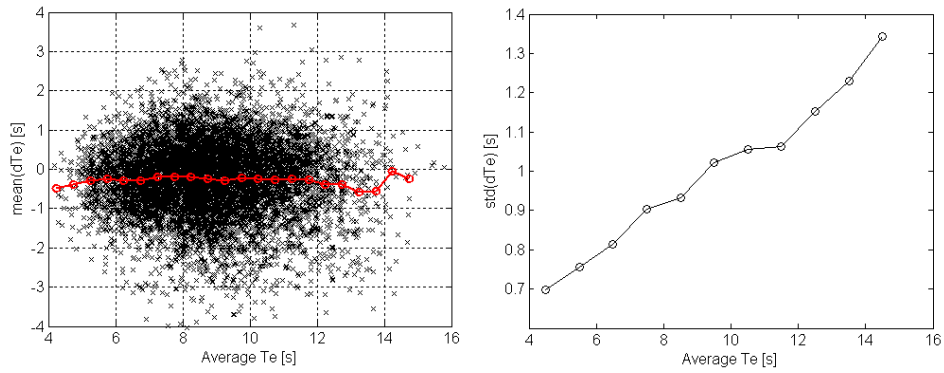


Figure 5.20. Mean and standard deviation of differences in T_e between calibrated models, for average $H_s > 1\text{m}$.

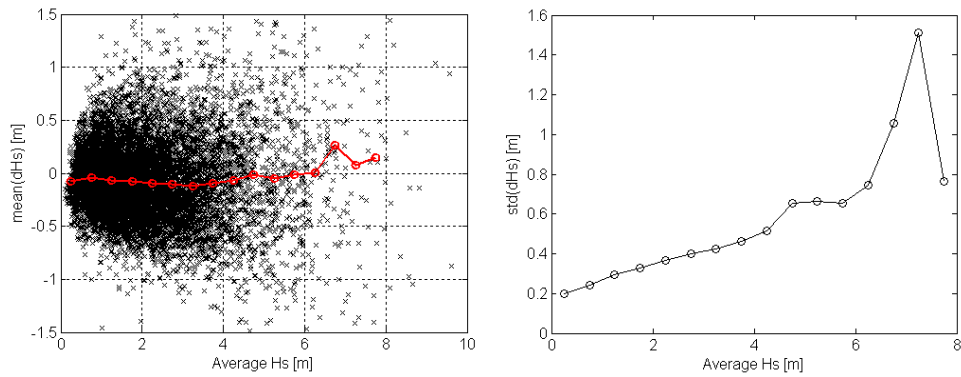


Figure 5.21. Mean and standard deviation of differences in H_s between calibrated models.

Figure 5.22(a) shows the mean difference in H_s , binned by H_s and T_e . It is clear that the ARGOSS model gives higher estimates in steep seas and lower estimates at longer periods. The tendency for OCEANOR to over-predict at longer periods was evident in the buoy data, but a trend with steepness was not evident for either model.

Figure 5.22(b) shows the mean difference in H_s , binned by H_s and month. There are clear seasonal changes in the differences. The trend observed is consistent with that observed between OCEANOR and the buoy.

From the buoy data we know that there are seasonal changes in the mean T_e and steepness for a given H_s (see Figure 5.23), with storms in summer generally steeper than those in winter. However, these changes are not wholly responsible for the differences

in calibration. Figure 5.24 shows the mean difference in H_s between the calibrated models, binned by H_s and T_e , broken down into 4 seasons. It is clear that the dependence on steepness varies with season. This could be due to seasonal changes of parameters we are not considering, such as swell age, mean direction, or spread. Alternatively it could be due to seasonal changes in conditions over the whole model domain, causing different amounts of error to occur and propagate through the model to the EMEC site.

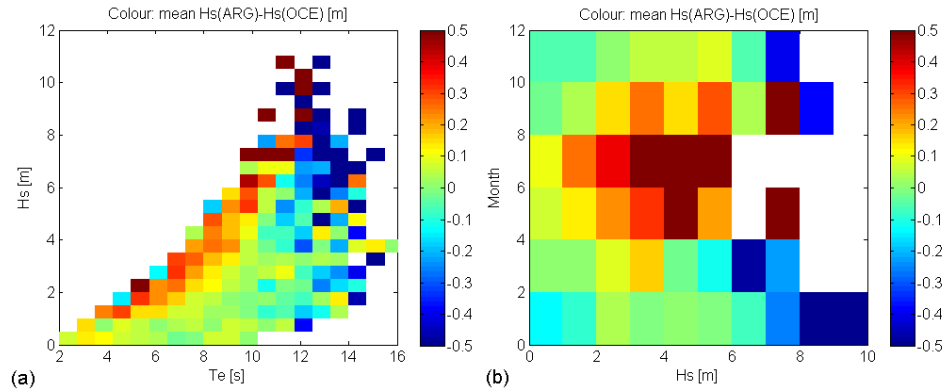


Figure 5.22. (a) Mean difference in H_s , binned by H_s and T_e . (b) Mean difference in H_s , binned by H_s and month.

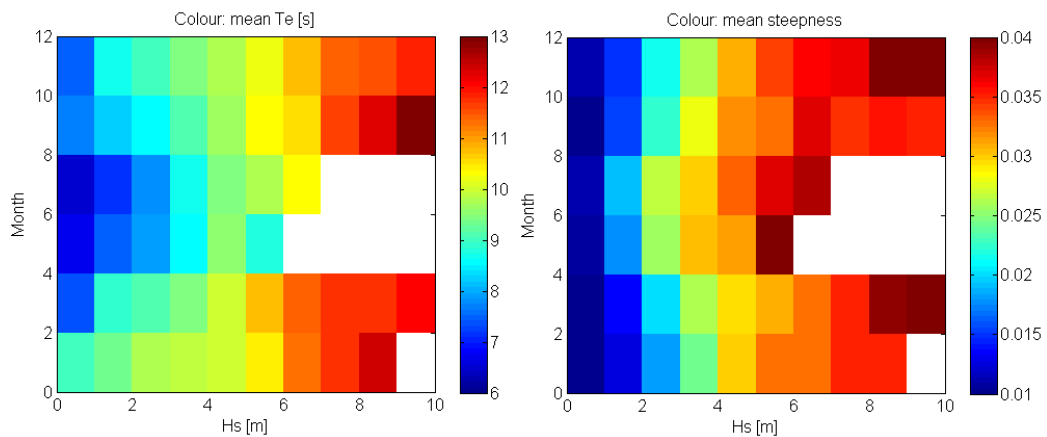


Figure 5.23. Mean T_e (left) and steepness (right) binned by H_s and month, from 5 years of EMEC buoy data.

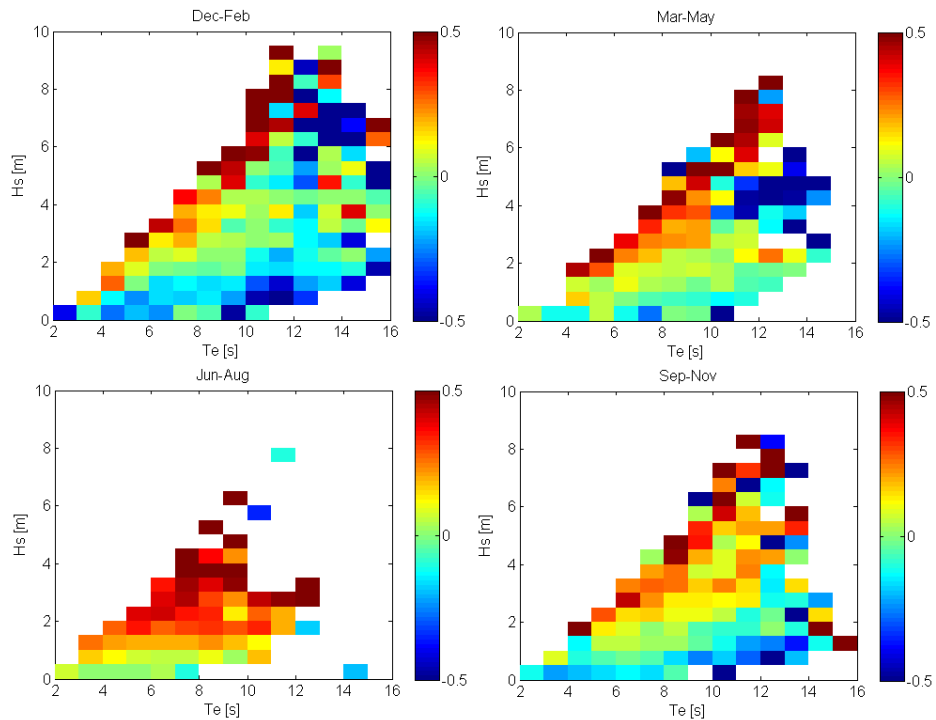


Figure 5.24. Seasonal mean difference in H_s between the calibrated models, binned by H_s and T_e .

If we remove this seasonal dependence then we can examine any interannual changes in calibration. Since the pattern of seasonal differences between the calibrated hindcasts is more consistent with the OCEANOR–buoy comparison, we will re-calibrate the OCEANOR hindcast relative to ARGOSS. This is not to imply that the calibrated ARGOSS hindcast is without systematic errors, but because one dataset must be chosen as reference. Figure 5.25 shows the differences between the hindcasts after the seasonal dependence has been removed from OCEANOR. The dashed lines are 95% bounds from the combined ARMA models. There are still 5 months which exceed the 95% bounds from the combined ARMA models, and 3 months where the difference exceeds 3 times the standard deviation from the ARMA models. This indicates that aside from mean seasonal changes, there are interannual changes in behaviour which exceed those from short-term correlated processes which can be represented by the low-order ARMA models.

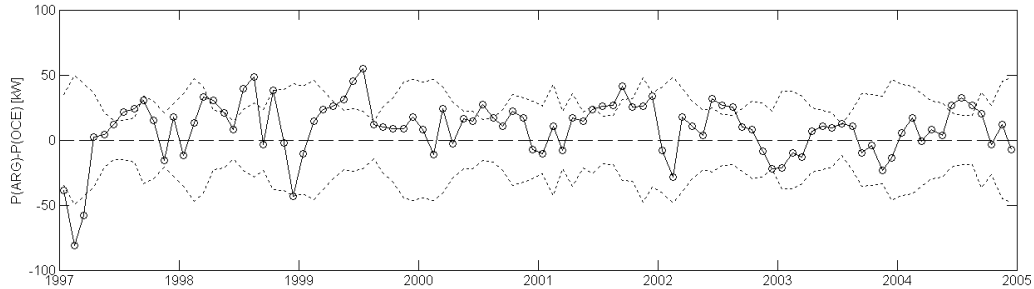


Figure 5.25. Solid line with circles: differences between hindcasts after seasonal recalibration. Dashed lines: 95% bounds from combined ARMA models.

5.1.5 Discussion and conclusions

It has been shown that the main features of the errors in model data that it is necessary to account for when estimating WEC power are:

- Non-linear dependence of model parameters on multiple factors, such as H_s , T_e and steepness.
- Correlation of errors in H_s and T_e
- Short-term temporal correlation of random errors
- Seasonal and interannual changes in biases

The specific method used to calibrate a particular model will vary depending on the model. For a given model, the appropriate calibration may also vary depending on location, due to varying performance of the model in different wave climates. It is therefore difficult to generalise about the performance of WAM versus WW3 for use in wave energy resource assessments, since we have only examined data for one location. Moreover it is not possible to separate the errors caused by the global models from those caused by the nearshore models. We can conclude, however, that it is preferable to use data from a hindcast rather than an archive of operational data, since this rules out changes in model performance due to changes in the operational model.

In the two datasets examined here, both had significant biases before calibration. After calibration, the ARGOS model seems to perform better, with no evidence of varying seasonal performance. The differences in estimate of monthly mean power between the calibrated ARGOS model and the buoy fall within the bounds predicted using the ARMA model of the error.

The use of an ARMA model proved not to be appropriate for estimating the errors in the calibrated OCEANOR model. This is most likely because the effects of changing seasonal performance were not accounted for initially. After the seasonal effect was removed, the two calibrated models still showed differences which exceed those expected from a short-term correlated process, represented by the ARMA models. This indicates that there are interannual changes in the calibration of one or both of the models.

Since there are only two years of buoy data concurrent with the models it is not possible to be sure what the causes are for the discrepancies between the models outside the calibration period. One possibility is that changes to the operation WAM model at ECMWF may be responsible for some changes in the performance of the OCEANOR model. Despite the fact the ARGOS near-shore model is driven by hindcast data, rather than operational data, we do not know whether the wind fields used to drive the WW3 hindcast are of consistent quality throughout. So we cannot rule out changes in the performance of the ARGOS model outside the calibration period.

Another reason for the observed differences between the models is that wave model performance is dependent on the wave conditions over the entire model domain, and that changes in the seasonal or annual distributions of these conditions causes changes in model biases. The error in a model estimate of wave conditions at a particular time is the cumulative result of errors which have occurred over the model grid and propagated to that location. We have seen that model biases vary depending on H_s and T_e (and doubtless on other variables not considered in this study), therefore changes in the distributions of these parameters over the entire domain will cause varying amounts of error to occur and propagate to the location in question. We have seen that the large changes in wave conditions with seasons cause seasonal changes in calibration. Therefore we would expect interannual changes in wave conditions to cause interannual changes in calibration. However, these should not be confused with the pseudo-effects described in Section 5.1.1.2.

The seasonal and interannual changes in the calibrations of the models make it difficult to quantify the uncertainty in the estimate of WEC yield. Although the ARMA representation of the ARGOS errors appears valid for the calibration period, we cannot

conclude that it gives a valid estimate of the uncertainty over the entire hindcast. A validation over a much longer period, 10 years say, would be necessary before we could draw conclusions about the long term accuracy.

Calibrating the models in this way is a pragmatic solution to wave resource assessment using the data that is currently available. Improving the performance of the input wave models would be preferable, but this is a much larger task and outside the scope of this study. Both the WAM and WW3 models include assimilated altimeter measurements already, so it is difficult to see how any significant improvements could be made quickly. Another topic which deserves attention is the transformation of the data from the global models using nearshore models. It would be interesting to validate both the offshore and nearshore data, using a procedure similar to that outlined above, to see if any significant improvements could be made by adjusting the set up of the nearshore models.

5.2 The limiting accuracy due to sampling variability

In Section 5.1 we discussed the accuracy which could be achieved in estimates of WEC yield from calibrated wave model data. In this section we will compare this to the accuracy which is achievable from a continuous record of in-situ measurements, limited by sampling variability.

Suppose we have a long record of accurate in-situ measurements, from a buoy say, for a potential site of a wave farm. If a WEC had been placed close to the buoy, but not in the exact location, sampling variability will cause the power generated by the WEC to differ from that estimated from the buoy, even if we knew the exact response of a WEC to that sea state. This situation would occur if several devices were to be deployed over a small area. In Section 2.1.3 the sampling variability of Pelamis power was estimated by comparing measurements from two buoys moored about 1km apart. Although averages over a 30 minute or even a 3 hour period are quite high, we would expect the differences to average out over a period of about a month.

The estimate of sampling variability for Pelamis power shown in Figure 2.6b comes from a finite number of buoy records and therefore does not show an entirely smooth plot. To obtain a smoother estimate we can generate a look-up table in a similar way to Section 5.1.3 in the case of model errors. We will use the parametric representation of sampling variability in buoy H_s and T_e from Section 2.1.3. We will assume errors follow a bivariate normal distribution with a correlation of 0.4 everywhere (i.e. the correlation is not dependent on the value of H_s and T_e). The resulting synthesised look-up table is in good agreement with that shown in Figure 2.6b.

In order to test the effect of sampling variability we also need to know the distribution of the differences between the buoys. Obviously the distribution will vary with H_s and T_e , so we normalised them by dividing by the standard deviation from the look-up table. The resulting distribution is shown in Figure 5.26. The distribution is slightly heavier-tailed than a normal distribution, but is well fit by a Student's t -distribution with zero mean, scale parameter $\sigma = 0.796$, shape parameter (degrees of freedom) $\nu = 3.855$.

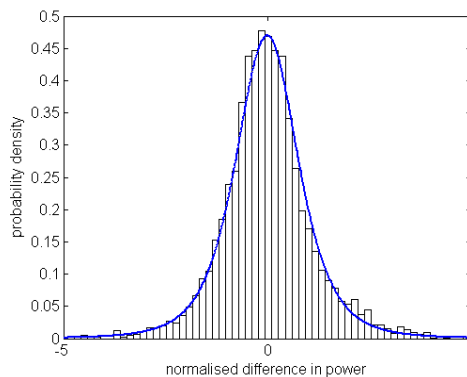


Figure 5.26. Histogram: Distribution of normalised differences in Pelamis power estimated from concurrent buoy data. Line: Fitted Student's t -distribution.

We will use the calibrated hindcast data from Section 5.1 to examine what errors can be expected in monthly mean power. This is done as follows: We generate a large number of series of independent t -distributed variables, the length of the hindcast. For each point in the hindcast we find the corresponding value of standard deviation in Pelamis power for that H_s and T_e , from the look-up table. Each series of independent variables is then multiplied by the series of standard deviations in Pelamis power, giving a series of errors due to sampling variability. From this large number of error series we can

calculate statistics for the uncertainty in monthly mean power. The standard deviation in monthly mean power from 1000 trials is shown in Figure 5.27, plotted against monthly mean power. The standard deviations are relatively small, between 0.5 and 2.5 kW over a month, and are much smaller than the errors in the calibrated model data. It was found the distribution of errors in monthly mean power due to sampling variability are very nearly normally distributed, but with slightly heavier tails. However, 99.7% are still within ± 3 standard deviations of the monthly ‘true’ monthly mean power from the hindcast.

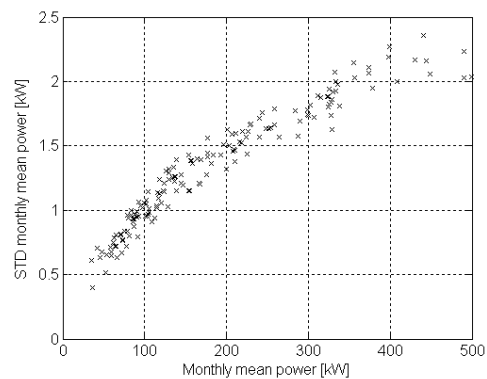


Figure 5.27. Standard deviation in monthly mean Pelamis power from sampling variability against monthly mean power.

The effect of sampling variability over a month is relatively small, so it does not seem worth investigating the dependence on the level of variability in wave conditions in a manner similarly to Chapter 4. Since the Orkney data was the most variable of the four hindcasts examined in Chapter 4, we would expect monthly standard deviations to be less elsewhere.

5.3 Comparison of altimeter and model accuracy

We have shown that it is difficult to quantify the uncertainty in WEC yield estimated from model data, due to the changes in model biases with time. In Chapter 4 we saw that altimeter data gave almost unbiased estimates of Pelamis power, but with high

variance due to limited temporal sampling. In this section we investigate the variance of estimates of monthly and annual WEC yield, when combined altimeter tracks are used.

Some experimentation for the EMEC site has shown that offshore altimeter measurements of H_s and T_z can be used as boundary conditions for the SWAN model, yielding reasonably accurate estimates of nearshore Pelamis power. We will assume that offshore measurements can be transformed without error and investigate the uncertainty that arises due to the altimeter sampling pattern only. This will give a limiting accuracy due to sampling, which will inform us whether further investigation of the use of altimeter data to drive nearshore models is worthwhile, or if results from offshore wave models are more accurate. First we need to discuss altimeter sampling patterns in slightly more detail.

5.3.1 Altimeter sampling patterns

A point along a certain altimeter track will be sampled at regular intervals determined by the satellite orbit, but the times at which tracks cross each varies with location. For example, a cross over point on the T/P orbit maybe sampled twice within an hour and then not again for nearly 10 days, or it maybe sampled roughly every 5 days, or somewhere in between, e.g. 3 days then 7 days. If we combine measurements from different altimeters, then sampling patterns become even more complex.

Figure 5.28 shows altimeter sampling patterns, with the colour denoting day of the cycle on which the track is sampled. For TOPEX/Poseidon and Jason (T/P/J), moving eastward, adjacent tracks are sampled 3 days after the preceding one (or 76 passes later). For GFO, also moving eastward, the adjacent track is sampled 3 days or 86 passes later. For ERS-2 and ENVISAT it is easiest to describe the pattern in two sections (see Figure 5.28 b and c). In the first half of a cycle, every other pass is sampled and in the second half the gaps are first half is repeated with a shift of one pass. So if a cross over point is sampled twice on day 1, then adjacent crossover point is sampled twice on day 19. In pass numbers, moving westward, the next but one track is sampled 86 passes later (or 3 days) and the adjacent track is sampled 544 passes later (or 19 days). This alternating pattern is shown in Figure 5.29.

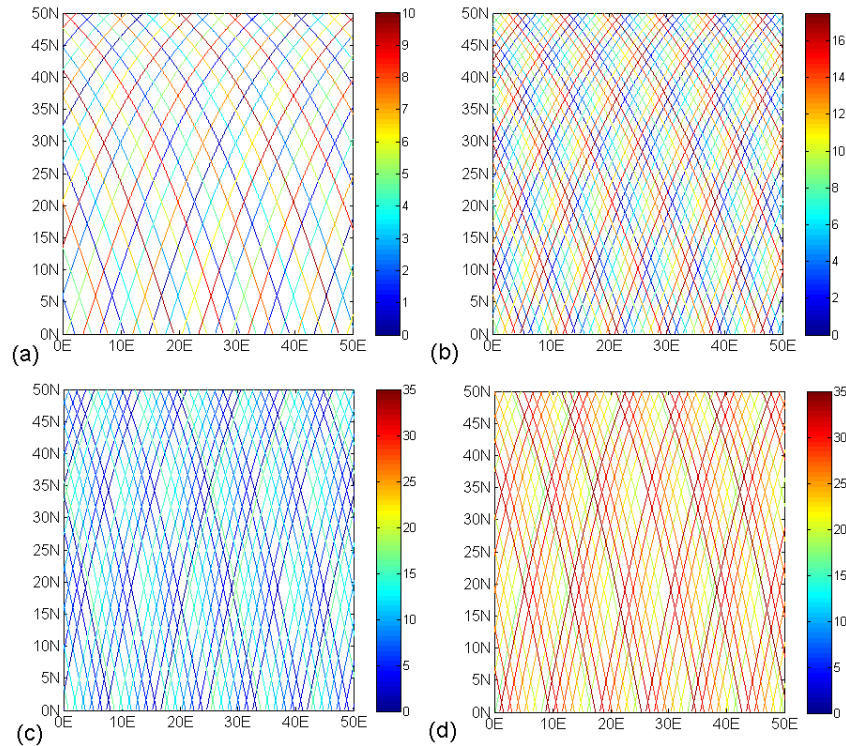


Figure 5.28. Altimeter sampling patterns. Colour denotes day of the cycle on which the track is sampled. (a) TOPEX/Poseidon and Jason (b) GEOSAT/GFO (c) ERS-2/ENVISAT days 1-17, (d) ERS-2/ENVISAT days 18-35.

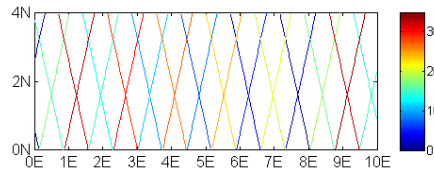


Figure 5.29. Zoom of ERS-2/ENVISAT sampling pattern, showing alternating sampling of crossover points. Colour denotes day of the cycle on which the track is sampled.

When tracks from different altimeters are overlaid the pattern becomes very irregular. The density of tracks varies with location, with some points close to 3 cross over points whilst others sparsely sampled. Moreover, the distance between ground tracks varies with latitude. T/P/J tracks are separated by 315km at the equator and 157km at 60°N/S, GEOSAT and GFO (phase B) tracks are separated by 163km at the equator and 82km at 60°N/S and ERS-2/ENVISAT tracks are separated by 78km at the equator and 39km at 60°N/S (see Figure B.2 in Appendix B for more details). In the next section we give some specific examples of sampling patterns in areas of interest.

5.3.2 Uncertainty from sparse temporal sampling

Due to the irregular nature of sampling from combined missions, it is very difficult to give general results on the effect of limited temporal sampling. If a nearshore model were to be used for a particular location, with boundary conditions specified by altimeter data, the set up would depend on the location and the tracks which passed nearby. It may be reasonable to take tracks from a wide area and transform the data, but if the coastline and bathymetry is complex, it may be better to specify the boundary conditions using just one or two tracks. Increasing the area that tracks are chosen from also increases uncertainty due to spatial variability in the wave field.

We will give 3 examples of how a nearshore model could be set up using altimeter data for boundary conditions and examine the limitations to accuracy imposed by the altimeter sampling patterns at these locations.

5.3.2.1. EMEC

The first site we consider is the EMEC test site. Figure 5.30 shows altimeter tracks in the vicinity. The target location – the EMEC test berth – is marked on the figure with a black cross. We will assume that boundary conditions for a model are specified using the three nearest crossover points, circled in black in the figure. There is one closer crossover point for ERS-2/ENVISAT, but this involves a track which has just passed from land to sea, so in practice not much data is obtained close by. It could be argued that other tracks could be included as well, but this is a hypothetical example, so we won't consider this further. We must also assume that the nearshore model could accommodate the quite significant changes in bathymetry the tracks used.

The sampling pattern from the combined tracks is shown in Figure 5.31. From the launch of TOPEX/Poseidon in September 1992 until the launch of ERS-2 in April 1995, there are only data once every 4 or 6 days. (We are not considering data from ERS-1 since the orbit changed quite often and was only in the phase G, ERS-2 orbit from March 1995 onwards. We are also not considering data from TOPEX or Jason phase B since there is relatively little data). After the launch of ERS-2 the time between sampled varies between a few hours and 6 days, with the pattern repeating after about a year and a half. When GFO data are included, the sampling is much denser, but there can still be up to 6 days between some samples.

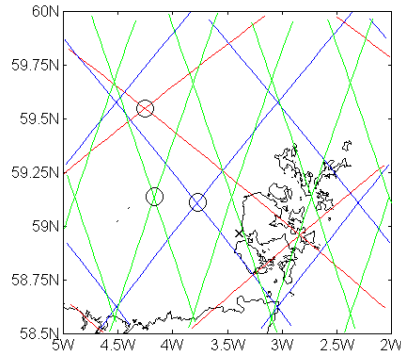


Figure 5.30. Altimeter tracks near Orkney. Red lines: TOPEX/Poseidon and Jason (Phase A). Blue lines: GFO. Green lines: ERS-2 and ENVISAT. Black circles show locations of data considered. Black cross marks target location.

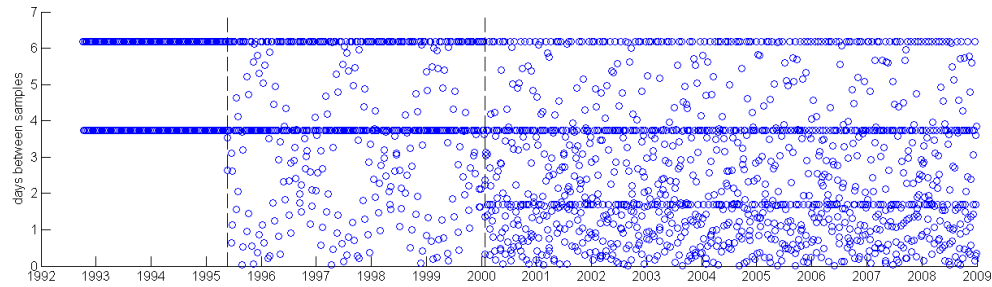


Figure 5.31. Days between altimeter samples from altimeter indicated in Figure 5.30. Dashed lines indicate the dates of the launch of ERS-2 and GFO.

We will use the calibrated ARGOS data from Section 5.1 and examine the effect that the 3 sampling patterns has on the accuracy of the monthly mean power. We start by applying the pattern at the first 3 hour sample and calculate monthly mean powers. This process is repeated starting at the second sample, third sample etc. For T/P/J the pattern repeats after 10 days, so this gives 80 different values of each monthly mean from the sampled data. For the combined data we vary the starting point over a year, giving $8 \times 365 = 2920$ different values of sampled monthly means. Figure 5.32 shows the standard deviation in the monthly mean Pelamis power, calculated from the altimeter sampling patterns, plotted against the monthly mean power from the hindcast. As expected, using only T/P/J data gives the highest standard deviation, but it is not improved significantly when data from the other altimeters are introduced.

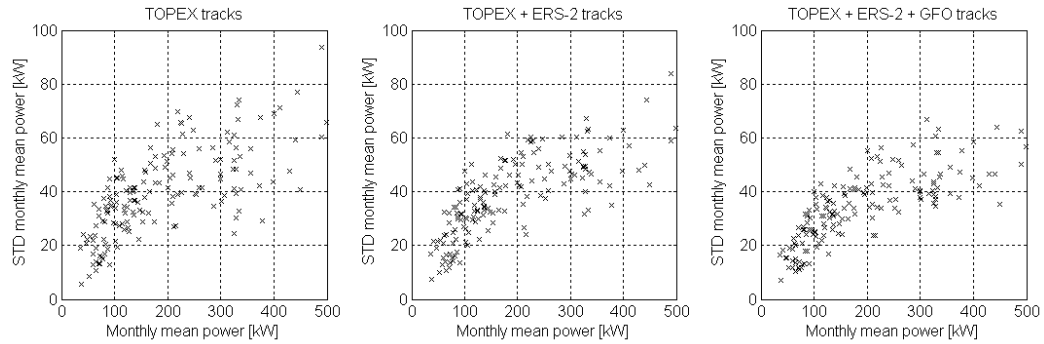


Figure 5.32. Standard deviation in the monthly mean Pelamis power, calculated from altimeter sampling patterns shown in Figure 5.31, against the monthly mean power from hindcast.

5.3.2.2 Wave Hub

The next example is for the Wave Hub development, off the coast of Cornwall. Altimeter tracks over South West England are shown in Figure 5.33. The proposed Wave Hub site is marked with a black cross. For this example we have chosen to use data from altimeter passes in the direction of the prevailing waves, coming from the Atlantic. It could be argued that a model could be set up to infer the ‘upstream’ conditions from passes to the east of the site, but again, since this is a hypothetical example we will not consider this further. The location of the data used is circled on Figure 5.33. It comprises two ERS-2/ENVISAT crossover points, one GFO crossover point and two T/P/J tracks, one of which passes directly over the site. All passes are within ~100km of the site. Again, we assume perfect transformation of these data and investigate the effects of limited temporal sampling only.

The sampling pattern for the combined tracks is shown in Figure 5.34. In contrast to the EMEC example, the sampling is much denser after the launch of GFO, with few samples separated by more than 6 days, and most by less than 3 days.

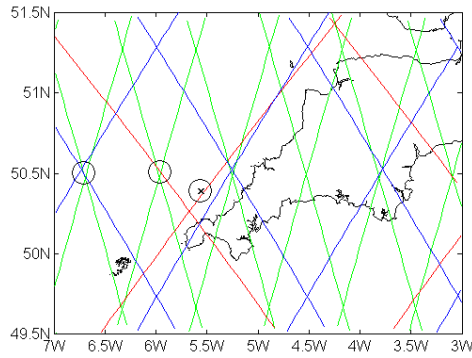


Figure 5.33. Altimeter tracks over South West England. Red lines: TOPEX/Poseidon and Jason (Phase A). Blue lines: GFO. Green lines: ERS-2 and ENVISAT. Black circles show locations of data considered. Black cross marks target location.

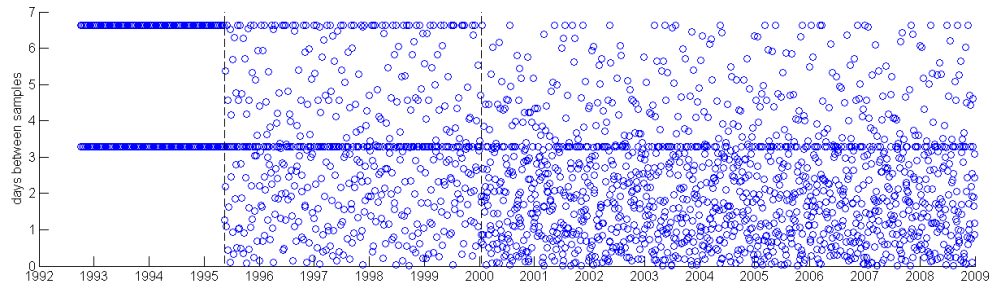


Figure 5.34. Days between altimeter samples from tracks indicated in Figure 5.33. Dashed lines indicate the dates of the launch of ERS-2 and GFO.

The effect of limited sampling is calculated in the same way as for the EMEC example, except this time the hindcast is supplied by the UKMO European waters model, described in Chapter 4. Figure 5.35 shows the standard deviation in the monthly mean Pelamis power, calculated from the altimeter sampling patterns, plotted against the monthly mean power from the hindcast. Again we see that only using data from the T/P/J tracks results in the highest standard deviation. In contrast with the EMEC example, the standard deviation does show a marked decrease with both the introduction of the ERS-2/ENVISAT and GFO tracks.

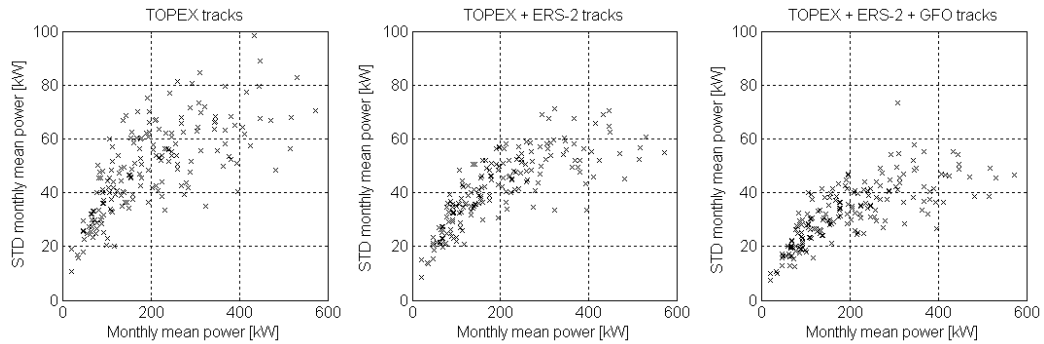


Figure 5.35. Standard deviation in the monthly mean Pelamis power, calculated from altimeter sampling patterns shown in Figure 5.34, against the monthly mean power from hindcast.

5.3.2.3. Aguçadoura

The final example is for the site of the first Pelamis wave farm in Aguçadoura, Portugal, located about 50 km south of the northern Portuguese border. Altimeter passes in the area are shown in Figure 5.36, and the location of the wave farm is marked with a cross. It is unfortunate that the site is in an area with relatively few altimeter passes nearby. No T/P/J data will be used in this example, since it is thought that the nearest tracks are too far north or south and may represent different wave conditions. Again, this is just an example, so it could be argued that they could be included. There is an ERS-2/ENVISAT track which passes almost directly over the site from which data will be used. The ERS-2/ENVISAT track just to the south has just passed from land to sea, so will not be used. The other data used in this example comes from one GFO crossover point and another ERS-2/ENVISAT crossover point, circled in the figure.

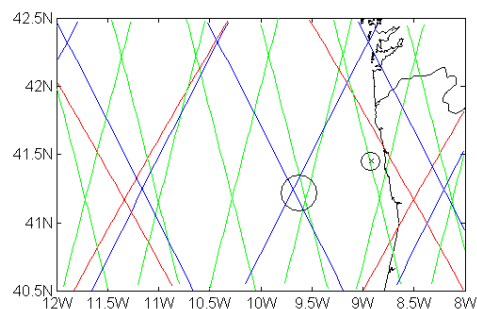


Figure 5.36. Altimeter tracks over Northern Portugal. Red lines: TOPEX/Poseidon and Jason (Phase A). Blue lines: GFO. Green lines: ERS-2 and ENVISAT. Black circles show locations of data considered. Black cross marks target location.

The sampling pattern is shown in Figure 5.37. Due to the lack of T/P/J data there is a much larger separation between samples, with 19 days between some samples before the launch of GFO. After the launch of GFO, some samples are still separated by over 10 days.

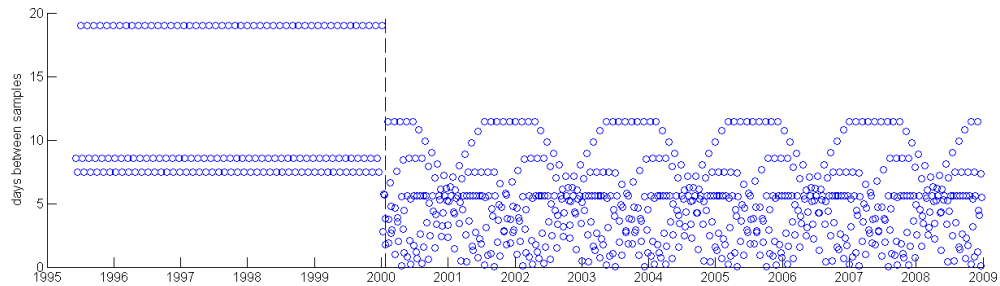


Figure 5.37. Days between altimeter samples from tracks indicated in Figure 5.36. Dashed line indicates the date of the launch of GFO.

To calculate the effect of the sampling pattern, we use the 10 year hindcast for the site, provided by OCEANOR, describe in Chapter 4. The standard deviation of the monthly mean Pelamis power is shown in Figure 5.38. Note that the vertical scale is twice as large as the previous plots, and that the variance of the estimates of monthly mean power is very high. This is not surprising considering that in some cases there are only one or two samples per month.

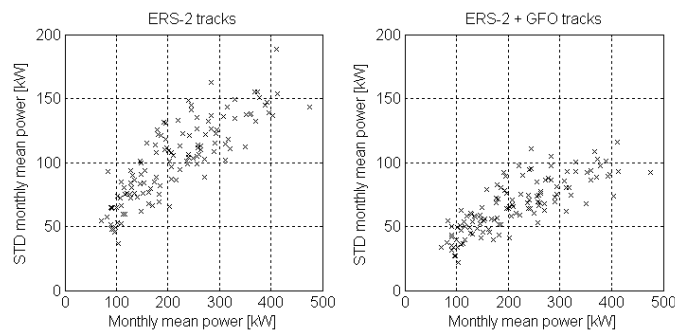


Figure 5.38. Standard deviation in the monthly mean Pelamis power, calculated from altimeter sampling patterns shown in Figure 5.37, against the monthly mean power from hindcast.

5.3.3 Discussion and conclusions

It is clear that in the three examples we have considered, the uncertainty in monthly mean power which results from limited temporal sampling is much higher than the uncertainty from the calibrated model data considered in Section 5.1. Due to the irregular sampling patterns of combined altimeter tracks it is difficult to make generalised statements about the accuracy which is achievable in any location.

However, it is likely that the use of model data will result in more accurate estimates of historic WEC yield in most locations. Especially considering that we have not taken into account that altimeter data does not provide any directional or spectral information. Moreover, the uncertainty will vary over time because the sampling rate changes depending on the number of altimeters in orbit. It should be noted here that GFO was switched off permanently in November 2008, although other altimeter missions are planned within the next few years, which could improve sampling rates.

It should also be noted here that the autocorrelation in wave conditions has not been considered. Monthly mean powers have been calculated as an average of all the samples within a month, regardless of the separation between samples. Since wave conditions are correlated over several days, taking an average of two samples within two days and one ten days later does not take into account that the first two samples are likely to be correlated. However, developing methods to account for this is likely to be a fairly involved process and it seems unlikely that it could improve results dramatically.

Asides from assimilation in to global-scale wave models, altimeter data could still be useful in estimating WEC yield at nearshore sites. Further analysis of along-track data could provide valuable information on the variability of boundary conditions of a nearshore model. Moreover, the tracks which fall within the boundaries of the nearshore model could be used to provide validation at multiple points, as opposed to just a single buoy location.

The use of model data in absence of in-situ calibration has not been considered here, and the use of altimeter data to calibrate/validate nearshore models is something which could be considered in future work. This is a problem which is likely to arise in actual wave energy resource studies, since at the onset of a project it is unlikely that in-situ data will exist for the location in consideration. It will not be possible to perform the

same kind of calibration/validation exercise using altimeter data as with in-situ data. The temporal structure (autocorrelation) of the model errors cannot be determined because of the limited temporal sampling from altimeters. Also altimeters provide no spectral or directional information. Moreover, it is unlikely that a track will pass directly over the site in question, so a direct calibration may not be possible because of variability in the wave conditions caused by changes in bathymetry and sheltering. It may be better to calibrate offshore data and check the transformation at the locations of the tracks within the nearshore model domain. It may then be possible to determine the accuracy of the transformation at the location in question, if further generic results on nearshore model accuracy were available.

6. Variability and Predictability of Wave Energy Resource

6.1 Introduction

Chapter 5 investigated the question of how accurately the historic resource can be estimated. In this chapter we will investigate how accurately the future resource can be predicted, based on the historic resource.

The wave resource is variable on multiple scales relevant to wave energy production: wave-to-wave (sampling variability), synoptic (weather systems), seasonal, interannual and climatic. This variability imposes limitations on the accuracy to which the future resource can be predicted over a given time scale. For instance, the mean power produced by a WEC over a given month will vary from year to year. Similarly, the annual mean power will vary from year to year. Moreover, it is well documented that the wave climate exhibits variability on decadal scales.

Such changes in wave climate could have a significant impact for an estimate of the energy yield of a potential wave farm that is based on historic data and assumes that long term climatic mean levels are stationary. This assumption is at the core of the Measure-Correlate-Predict approach which is widely used in the wind industry to estimate the yield of a proposed wind farm, discussed in Section 1.5.

The evidence that mean wave heights in the North Atlantic were increasing in the latter part of the 20th century was first presented by Neu (1984). He noted an upward trend in North Atlantic wave heights from analysis of manual wave charts. Carter and Draper (1988) and Bacon and Carter (1991) confirmed this trend using data from the Seven Stones Light Ship and Ocean Weather Station Lima. Bacon and Carter (1993) went on to make a connection between mean wave heights and atmospheric pressure gradients in the North Atlantic. Since then there have been numerous studies of changes in North Atlantic wave climate using numerical model data (e.g. Kushnir et al, 1997; Gunther et al, 1998; The WASA Group, 1998; Wang and Swail, 2001; Wang and Swail, 2002; Caires and Swail, 2004, Wang et al, 2006a), altimeter data (Woolf et al, 2002), VOS

data (Gulev and Hasse, 1999; Gulev & Grigorieva, 2006) and micro-seismological data (Grevemeyer et al, 2000). Broadly, the results have shown an increase in North Atlantic wave heights from the mid-1950s to the mid-1990s. Vikebo et al. (2003) confirmed this trend using a 118-yr wave hindcast of the Norwegian Meteorological Institute (DNMI), but noted that the increase is not more dramatic than the decrease which occurred from 1881 towards the beginning of the 20th century. Similarly, increasing trends in wave heights in the Pacific have been noted (e.g. Allan & Komar, 2000; Graham and Diaz, 2001; Graham et al, 2002; Gower, 2002; Bromirski et al, 2005).

Changes in wave climate are due to changes in storm activity, in terms of both intensity and location of the storm tracks. Pinto et al (2007) note that there have been contradictory reports on significant changes of storm activity in the second half of the twentieth century based on reanalysis and observational data. While some authors reported increased activity (e.g., Geng and Sugi 2001; McCabe et al 2001; Paciorek et al 2002; Wang et al, 2004; Alexander et al, 2005; Weisse et al, 2005), others mention that storminess has been remarkably stationary in the last 200 years, with little variation on time scales of more than one or two decades (e.g., WASA group 1998; Barring and von Storch 2004). Moreover, Bengtsson et al (2004) reported that these trends may not be reliable because of inhomogeneities in the reanalysis data series. An incremental increase is found in many atmospheric variables in the extra-tropics around 1978/1979, coinciding with the introduction of the global observing system.

To assess the impact that variability in the wave climate can have on WEC yield, we can break the problem down to several representative scales. The shortest scale of variability in wave conditions is sampling variability. This has been discussed in Section 5.2 and will not be considered further here. Modelling synoptic and seasonal variability in wave conditions and WEC power production is necessary for the purposes of planning operations and maintenance schedules, and for the integration of wave energy into the electrical grid. This topic has received quite a lot of attention in the literature. A recent review of stochastic models for wave parameters on these time scales is given by Monbet et al (2007). In this section we focus on modelling interannual and climatic variability and the effect it has on the predictability of WEC yield.

We use the term ‘interannual variability’ to refer to the changes in monthly or annual mean values from year to year and ‘climatic variability’ to refer to changes in averages over a number of years. When modelling climatic variability we face two challenges. The first is to establish a model for the ‘natural’ climatic variability in wave conditions. The second is to estimate what effect forcing on the climate system from anthropogenic emissions of green house gases (GHGs) may have on wave climate and hence WEC yield.

It remains uncertain whether observed changes in wave and storm climates in the latter part of the 20th Century are part of natural long slow variations or a result of anthropogenic forcing on the climate system. Trenberth et al (2007) note that anthropogenic forcing is likely to have contributed to changes in wind patterns, affecting extra-tropical storm tracks and temperature patterns in both hemispheres, but that the observed changes in the Northern Hemisphere circulation are larger than simulated by climate models in response to 20th century forcing. Wang et al (2006b) investigated changes in wave climate using pressure fields from ensembles of integrations (45 in total) from nine coupled atmosphere-ocean global circulation models (AOGCMs) forced with historical levels of greenhouse gases and sulphate aerosols obtained from the IPCC Fourth Assessment Report model output archive. Using the optimal detection method of Allen and Stott (2003) they conclude that the upward trends in North Atlantic wave heights in the latter half of the twentieth century can be attributed to anthropogenic forcing.

Projections of future wave climates have been made which directly use the projected pressure fields output by AOGCMs directly (e.g. STOWASUS Group, 1998; WASA Group, 1998; Perrie et al, 2004; Wang et al, 2004; Wang and Swail, 2005; Wang and Swail, 2006). However, there is high uncertainty in pressure fields from AOGCMs at grid-point scale (Doblas-Reyes et al, 2003), which will make predictions for specific sites of potential wave farms less useful.

Harrison & Wallace (2005) have investigated the effect of climate change on wave energy. They use a relationship between wind speed and the Pierson-Moskowitz wave spectrum to investigate how changes in wind speed may effect wave energy production. A more detailed investigation is made by Wolf and Woolf (2006), who use a numerical

model to examine the effect that the storm frequency, intensity, track and propagation speed has on the mean and maximum monthly wave heights in the North-east Atlantic. They find that the strength of the westerly winds has the greatest effect on mean wave height, but that the intensity, track and speed of the storms all significantly affect maximum wave height. A number of recent studies, project storm frequency and intensity to increase with GHG emissions, with a slight poleward shift in tracks (e.g. Bengtsson et al, 2006; Leckebusch et al, 2006; Pinto et al, 2007).

An alternative approach to downscaling projections from AOGCMs is proposed by Woolf and Coll (2006). They suggest that downscaling via general structural changes in the atmosphere may be more suitable for predicting changes in storminess than analysing winds in global or regional circulation models. Low frequency variability in climate tends to occur in large spatial patterns associated with changes in atmospheric circulation patterns (Trenberth, 1995). Woolf et al (2002) demonstrated that the leading mode of interannual variability in monthly mean wave height in the North Atlantic correlates strongly with an atmospheric pattern called the North Atlantic Oscillation (NAO). The NAO is one of the most prominent and recurrent patterns of atmospheric variability of the Northern Hemisphere atmosphere (Hurrell et al, 2003). It can be described as an irregular, oscillatory, large-scale net displacement of atmospheric mass between two centres of action: the Icelandic Low and the Azores High, known as the Atlantic dipole (Hastenrath 2002). It is particularly important in the boreal winter, when it exerts a strong control on the climate of the Northern Hemisphere, causing large changes in strength and path of storm systems crossing the Atlantic (Hurrell, 1995; Hurrell and van Loon, 1997; Rogers, 1997; Marshall et al, 2001; Wanner et al, 2001; Hurrell et al, 2003).

The NAO can be described by an index of deviations or ‘anomalies’ of sea level pressure from climatic mean values. A positive NAO index indicates that the Atlantic dipole is more intense than normal and the Icelandic Low and the Azores High also tend to be located slightly further north and east (Glowienka-Hensa 1985; Serreze et al 1997). This results in a stronger mean westerly flow over the North Atlantic which creates an eastward-propagating wave field, increasing in size towards the North East Atlantic. Woolf et al (2002) show that the influence of the NAO on wave height peaks at the eastern edge of the Atlantic basin, with the correlation coefficient in this region

greater than 0.8. Figure 6.1 shows a contour map of the correlation of winter mean wave height with the NAO index of Jones et al (1997).



Figure 6.1. Contour map of the correlation of winter mean wave height with NAO index (from Woolf et al, 2002).

The NAO is a mode of variability that is present in every month of the year (Barnston and Livezey 1987). However, it is most pronounced in amplitude and areal coverage during winter (December to February) when it accounts for more than one third of the interannual variance in sea-level pressure (Doblas-Reyes et al, 2003). Despite the pronounced influence of the NAO on the Northern Hemisphere climate, many open issues remain about which climate processes govern NAO variability and how it may be affected by climate change (Hurrell et al, 2003).

We will use this link between wave climate and the NAO to model both the natural climatic variability in WEC yield and the potential effects of anthropogenic climate change. The chapter is organised as follows: Section 6.2 describes the data used in this section. In Section 6.3 a stochastic model is proposed to describe the long-term variability in WEC yield, based on the link between the NAO and wave climate. In Section 6.4 this stochastic model is used to examine the effect that long-term variability has on the predictability of WEC yield, and discuss how this relates to the uncertainty in the historic data and the uncertainty from the potential effects of anthropogenic climate change. Conclusions are presented in Section 6.5.

6.2 Data and validation

6.2.1 Wave data

The wave data used in this chapter is from a 50 year reanalysis undertaken by Oceanweather Inc. We use one point from this hindcast, located at $60^{\circ} 0' N$, $5^{\circ} 0' W$, about 150 km north of Cape Wrath (the northwest tip of mainland Scotland), covering the period 1954-2005. The location is shown in Figure 6.2. The hindcast was performed on the OWI-3G model, a third generation model, including shallow water physics, similar to WAM, driven by manually reanalysed wind fields. The model uses a $0.5^{\circ} \times 0.5^{\circ}$ grid with a 3 hour time step. Swail et al (2006) describe the setup in detail and also present a validation of the model against in-situ and altimeter data. From comparison with the in-situ data they show that the bias and scatter index remain nearly constant from 1978 to 2005. Prior to 1978 there is little validation data. Cox and Swail (2001) presented a validation of a global hindcast using an earlier version of the OWI-3G wave model and use in-situ measurements from Ocean Weather Stations Bravo and Papa to show that model biases were approximately the same in 1958 and 1967 as in the 1980s and 1990s.

Since model performance can change with location, we present a brief validation of the data for this grid point, using altimeter measurements as the reference. The altimeter passes in the vicinity of the grid point are shown in Figure 6.2. We will use the median value of the altimeter data within 50km of the hindcast point. Analysis of along-track altimeter data shows no detectable trends over this area. Moreover, the hindcast point is located on the edge of the continental shelf and the water depth is greater than 100m for most of this area. The altimeter data is quality checked and calibrated as described in Chapters 2 and 3. For each altimeter pass we find the nearest 3 hour record from the hindcast, giving a maximum separation of 90 minutes. This gives a total of 2129 collocated data points, over the period September 1992 – December 2005.

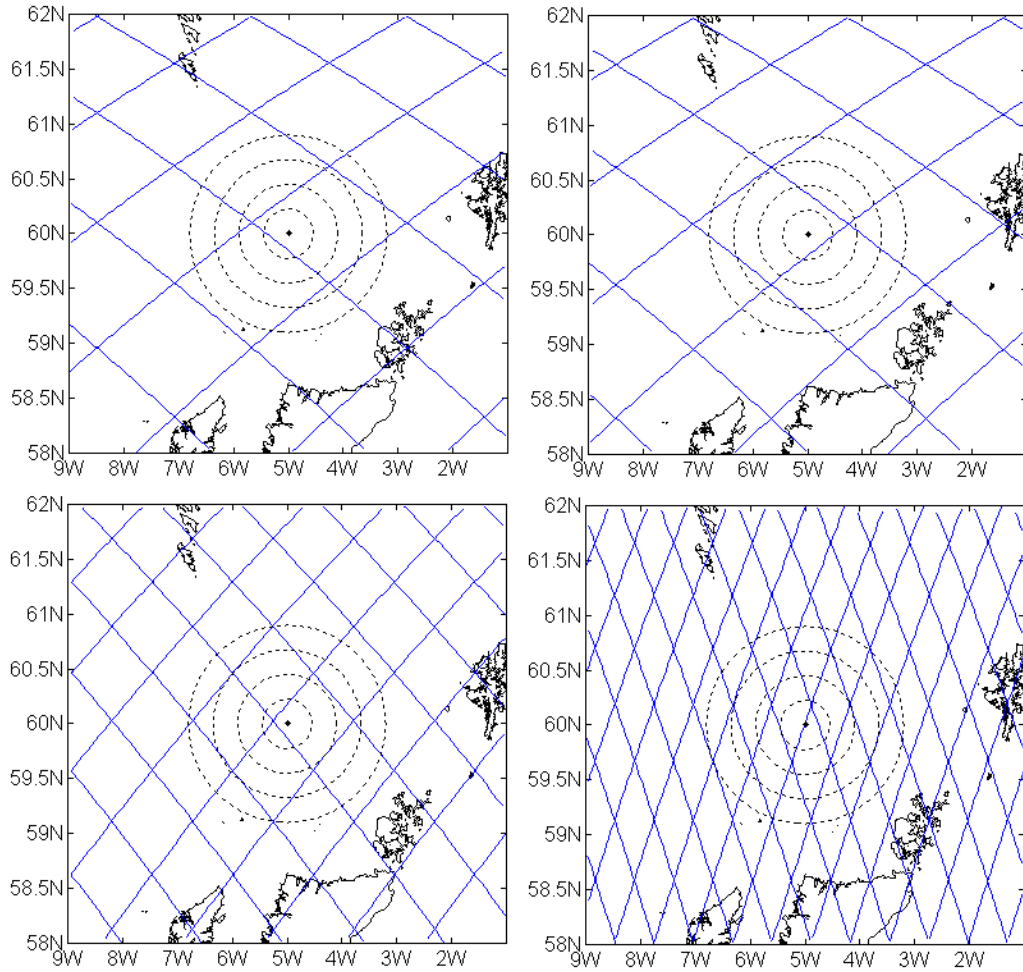


Figure 6.2. Altimeter tracks near the hindcast point. Top left: TOPEX/Poseidon/Jason phase A. Top right: TOPEX phase B. Bottom left: GFO. Bottom right: ERS-2/ENVISAT. Concentric circles at 25, 50, 75 and 100km from hindcast point.

Figure 6.3 shows a scatter plot of the collocated altimeter and model H_s . The level of scatter is low and there are few outliers. There is good agreement even in very large seas, up to nearly 14m. Figure 6.4 (a) shows the average difference between the model and altimeter H_s , binned by altimeter H_s . There is a small bias at low H_s , which may be a result of the problem with altimeter measurements at low H_s which were discussed in Sections 2.2 and 3.1. At higher H_s the bias is low compared to the level of scatter and the model does not show the underestimation of high H_s which was noted for the hindcasts examined in Chapter 5. Overall the bias in the model H_s is 5cm, agreeing with the results of Swail et al (2006). The altimeter estimate of T_z and T_e is not used to

validate the model, since the uncertainty of the altimeter estimates is deemed to be too high to be useful. The hindcast is therefore used without calibration.

Figure 6.4 (b) shows the standard deviation of the differences between model and altimeter H_s against altimeter H_s . As in Chapter 5, a linear increase in standard deviation with H_s is observed. The standard deviation is slightly higher than for the ARGOSS hindcast at EMEC. This could be a result of the temporal separation and the higher sampling variability of the altimeter data relative to the buoy data. The median value of the altimeter pass within 50km of the hindcast point was used, so spatial variability should not add too much to the standard deviation.

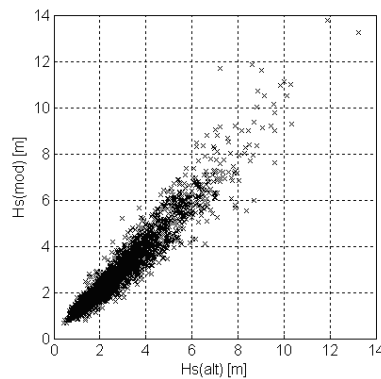


Figure 6.3. Scatter plot of collocated altimeter and model H_s .

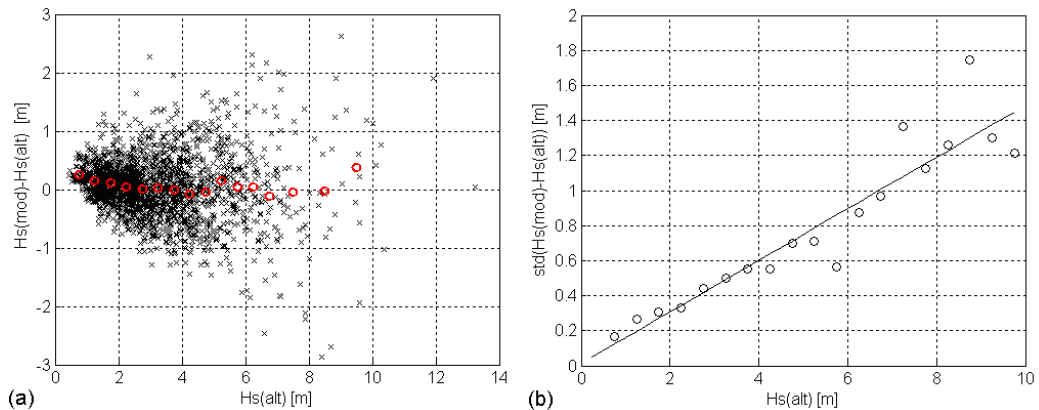


Figure 6.4. (a) Difference in model and altimeter H_s against altimeter H_s . Black crosses: individual values; red circles: bin average. (b) Standard deviation of difference in H_s against altimeter H_s and fitted linear relationship.

Due to the sparse temporal sampling from the altimeter measurements it is not possible to see if there are small changes in model biases with season or between years, as were noted in Chapter 5. Moreover, we can only check the model performance from 1992 onwards. However we assume that the results of Cox and Swail (2001) on the stationarity of the earlier OWI-3G model apply here as well.

Since we cannot check the temporal correlation of the model errors either, we assume that they are of a similar level to the OCEANOR and ARGOSS hindcasts discussed in Chapter 5. It seems reasonable to assume that the accuracy of estimates of monthly mean Pelamis power from this hindcast are somewhere between those from the ARGOSS and OCEANOR hindcasts, shown in Figure 5.18. The effect of uncertainty in the estimate of historic resource is discussed in Section 6.4.2.

6.2.2 NAO index

Several difference indices have been proposed to describe the behaviour of the NAO. Much of the nature of the NAO can be described by anomalies in pressure at a single pair of sites reasonably close to each centre of action (e.g. Jones et al, 1997). A disadvantage of station-based indices is that they are fixed in space. The NAO centres of action move through the annual cycle (Machel et al, 1998; Jonsson and Miles, 2001), so station-based indices can only adequately capture NAO variability for parts of the year (Hurrell and van Loon, 1997; Portis et al, 2001; Jones et al, 2003). Moreover, pressure at individual stations is significantly affected by short-scale noise from passing weather systems, not related to the NAO (Trenberth, 1984). Hurrell and van Loon (1997) showed that the signal-to-noise ratio of station-based indices is near 2.5 in winter, but by summer it falls to near unity.

An alternative description of NAO behaviour is obtained from the leading Empirical Orthogonal Function (EOF) mode of monthly pressure fields north of 20 °N, (e.g. Hurrell, 1995; Osborn et al. 1999; Ambaum et al. 2001; Wanner et al. 2001). An advantage of the EOF time series approach is that such indices better represent the full NAO spatial pattern.

Stephenson et al (2006) proposed a simple index based on gridded monthly mean sea level pressure (SLP) data dating back to 1899 (Trenberth and Paolino, 1980). It is

defined as the difference between the December–February mean SLP spatially averaged over two large rectangular latitude–longitude regions: 90W–60E, 20N–55N and 90W–60E, 55N–90N. This definition of NAO index has the advantage that it uses SLP information covering a large part of the Atlantic from the tropics up to the North Pole and is robust to modest changes in the position of centres of action. Unlike other indices, this index is not non-dimensional, and has units hPa.

Since the NAO is a genuinely robust feature the various definitions of NAO index correlate well, especially in winter when the pattern is strongest. The correlation of the Jones et al (1997) and Hurrell (1995) indices averaged over December–March have a correlation of 0.86; the Jones et al (1997) and Stephenson et al (2006) indices have a correlation of 0.84; and the Hurrell et al (1995) and Stephenson et al (2006) indices have a correlation of 0.96. We will use the index of Stephenson et al (2006), so that their results on the sensitivity of the NAO index to GHG increase can be used.

6.3 A stochastic model for long-term variability in WEC yield

6.3.1 Observed variability in WEC power levels

As with many statistical analyses, the first questions we ask about WEC power levels are: what is the mean value over a given period and what is the range of expected values? This information is summarised in Figures 6.5 and 6.6. Figure 6.5 (a) shows individual and climatological monthly mean Pelamis power calculated from the hindcast. We use the term individual monthly mean to refer to the average power over a month in a particular year, January 1990 say. The term climatological monthly mean refers to the average in that month over a number of years, over all Januaries from 1954 to 2005 in this case. (The term ‘climatological mean’ may be slightly misleading, since these values are non-stationary and depend on the years that the data are averaged over. However, their variability is much lower than the individual monthly mean values.) From Figure 6.5 (a) we see that there is a strong seasonal cycle, with the climatological mean power levels nearly three times higher in the winter than in the summer. The variability of individual monthly means about the climatological mean level is also large, power levels with a factor of 3 difference between the lowest and highest summer

power levels and a factor of 2 in the winter, but the range of monthly mean power levels is highest in winter. The distribution of the individual monthly mean power levels about the mean value is approximately normal. Figure 6.5(b) shows the distribution of the normalised monthly power anomaly, defined as the individual monthly mean minus the climatological monthly mean, divided by the standard deviation of the individual monthly mean values.

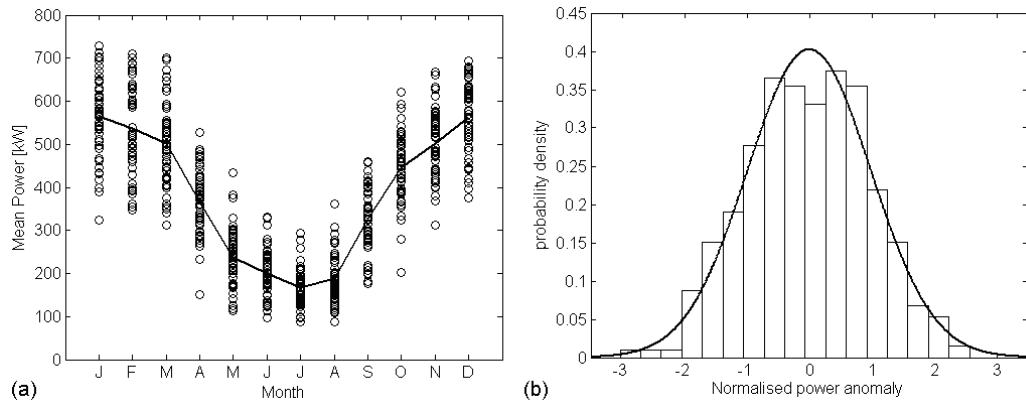


Figure 6.5. (a) Circles: Individual monthly mean power; Line: Climatological monthly power. (b) Histogram of anomalies in monthly mean power and fitted normal distribution.

Figure 6.6 shows annual mean power levels with 5, 10 and 20 year moving averages. Because of the effect of aggregation, the variability of the annual mean values is less than the monthly means. It is, however, still significant, with the highest and lowest power years being $\pm 15\%$ of the mean over the entire hindcast. The multi-year mean values remain fairly constant until around 1970 where they start to rise, peaking in the early 1990s and then starting to decrease again. This is consistent with the trends in wave height in the North Atlantic, noted in Section 6.1.

Suppose that a wave farm was built in 1980 that operated for 20 years, with the yield estimated from data for the preceding 20 years. The mean power level for the historic data (1960-1980) was 369 kW, whereas the mean power whilst the farm operates (1980-2000) was 402 kW, an increase of 9%. Obviously this would be a boon to the operators of the wave farm, but such trends are not necessarily monotonic and hence this uncertainty must be quantified.

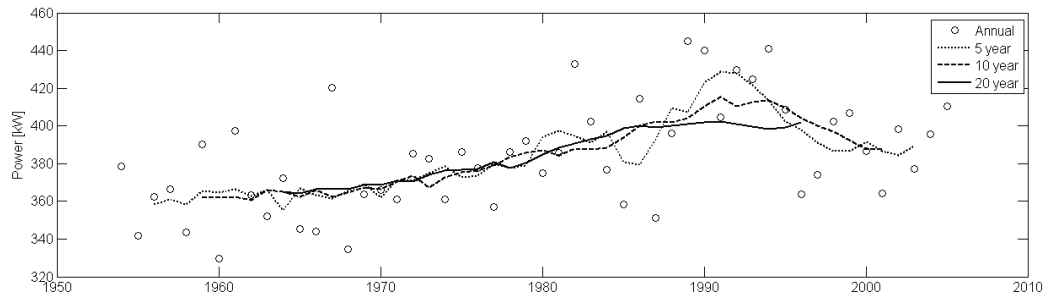


Figure 6.6. Annual mean Pelamis power and running 5, 10 and 20 year mean values.

A linear regression of the annual mean wave height against time shows that the increase in annual mean wave height shown in Figure 6.6 is significant at the 95% level under the null hypothesis that annual mean wave heights are independent Gaussian variables. However, care should be taken when making inferences about future wave conditions. Before concluding that we are seeing evidence for a shift in the mean value, we must rule out the possibility that we are seeing purely random fluctuations expected from stationary time series with long-range dependence. Wunsch (1999) gives examples of trends which appear significant when only short sections of climate records are examined, but which in fact arise from stationary time series. Even the 50 years of data we are using here may not be enough to properly model the long-term variations in wave conditions and WEC power levels. We can improve our understanding though, by using the NAO as a proxy for wave conditions.

6.3.2 The relationship between the NAO and power anomalies

The dependence of North Atlantic wave heights on the NAO was clearly demonstrated by Woolf et al (2002). They note that the relationship is strongest in the winter, when the influence of the NAO is greatest. Figure 6.7 shows the correlation of the monthly mean Pelamis power from the hindcast with the NAO index. All correlations are significant at the 95% level, with correlation strongest in winter months, consistent with the results of Woolf et al (2002).

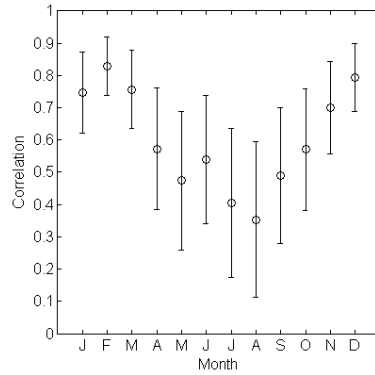


Figure 6.7. Correlation of monthly mean power level with NAO index and 95% error bars.

Figure 6.8 shows a scatter plot of the monthly anomalies in power against the monthly anomalies in NAO index. Anomalies are defined as the difference between the individual and climatological monthly means (note that in contrast to Figure 6.5 (b) they have not been normalised by the standard deviation). Linear regressions have been performed for anomalies over all months and over each season, with seasons being defined as three month periods December-February (DJF), March-May (MAM), June-August (JJA) and September-November (SON). Since we are using anomalies from the mean values, all the intercepts are zero. The slopes of the regression lines over each season are all within 95% error bounds of each other and also within 95% error bounds of the regression over all months. In fact the slopes for winter and spring almost coincide with the slope for the regression over all months.

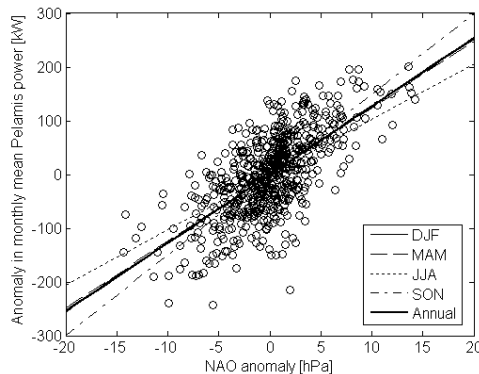


Figure 6.8. Linear regression over various periods of monthly power anomalies on NAO anomalies.

The standard deviation of the residuals from the regression is approximately constant throughout the year. This indicates that the relationship between power anomalies and NAO anomalies is constant throughout the year, but that the smaller variation of the NAO index (i.e. zonal pressure gradient) in summer makes signal to noise ratio (and hence correlation) lower.

The noise on the NAO and power signals results from synoptic variability. Anderson et al (2001) note that there are roughly the same number of North Atlantic storms in winter and summer, of the order of one new storm each week. They also note that winter storms are more intense (as defined by the sea level pressure gradient to the centre of the storm) than summer storms but travel faster and so endure for shorter periods than summer storms. The balance between intensity and duration of storms may result in roughly the same ‘noise’ level throughout the year.

Figure 6.9 shows the relationship between anomalies in annual mean power levels and the annual NAO anomaly. The correlation is 0.84, a result of the strong correlation in winter months when power levels are highest.

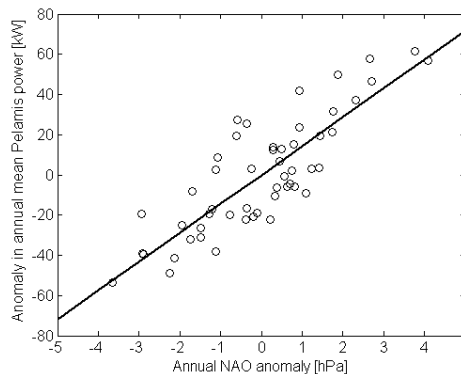


Figure 6.9. Linear regression of annual power anomalies against annual NAO anomalies.

So we have a linear relationship:

$$\text{Annual power anomaly} = A \times (\text{Annual NAO anomaly}) + \varepsilon \quad [6.1]$$

where $A = 14.4 (\pm 2.6)$ kW/hPa and ε is normally distributed with standard deviation $\sigma_\varepsilon = 15.4$ kW. The residuals, ε , show no significant autocorrelation. This means that we only need to model the temporal variability of the NAO index to model interannual variability in Pelamis power levels at this location. It does not imply that NAO explains all predictable interannual variability, only that it accounts for enough that over a 50 year period, any residual signal is not detectable and we can approximate ε with a series of independent random variables. Figure 6.10 shows the power from the hindcast and the predictable component from equation 6.1. The agreement is reasonable, and the relative size of the predictable and random components of the variability can be seen.

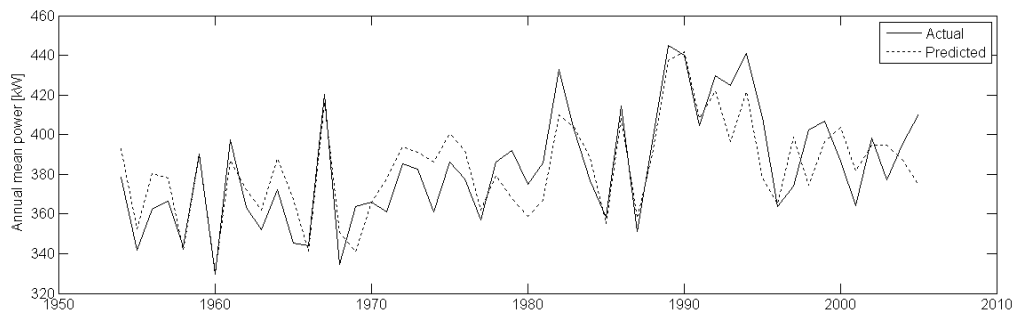


Figure 6.10. Linear predictor for annual mean Pelamis power from NAO anomaly.

6.3.3 Temporal variability of the NAO

Although the NAO is the dominant pattern of variability in atmospheric circulation over the North Atlantic, most winters are not dominated by any particular regime and there can be large changes in the NAO index from year to year (Nakamura, 1996). There are, however, periods when anomalous NAO-like circulation patterns persist over quite a few consecutive winters. A plot of the annual NAO anomaly (from the S06 index) and averages over various periods is shown in Figure 6.11. The interannual variability is high but some longer term trends are visible. There is a decrease in the 5, 10 and 20 year averages between 1920 and 1960 and a increase of roughly the same magnitude between 1960 and 1990.

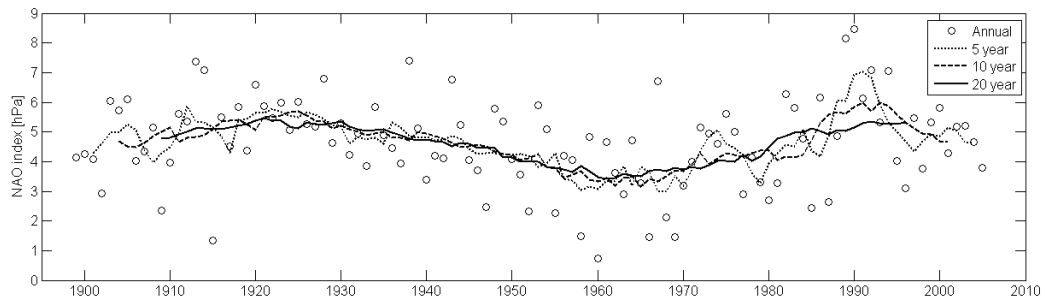


Figure 6.11. Annual NAO anomaly with 5, 10 and 20 year moving average.

There is some debate over which physical processes are responsible for the observed low frequency variability. Candidate mechanisms include sea surface temperature and ocean dynamics (Paeth et al, 2003; Visbeck et al, 2003; Hurrell et al, 2004), processes internal to the atmosphere (Thompson et al, 2003; Scaife et al, 2005) and external forcing from GHGs (Gillett et al, 2003; Osborn, 2004). Wunsch (1999) discusses the possibility that the observed trends are an effect of finite sampling of a random process. He simulates several 138-year sequences from the estimated spectrum of the NAO index (which appears to be weakly red) and finds that a number of simulations show extended periods with values away from the mean. He concludes that although this does not rule out the possibility that external forcing may have caused the upward trend in NAO index in recent years, it should be tested against the null hypothesis that it arises from a simple stochastic superposition or “climate noise” (random year-to-year fluctuations in monthly and seasonal means caused by random day-to-day changes in weather). Feldstein (2000) further examined the effect of climate noise properties of the NAO using daily data. He found that the short scale properties were consistent with a first-order autoregressive process, with a fundamental time scale of about 10 days. However, the interannual variability was in excess of that expected from climate noise alone.

Various stochastic models have been proposed to describe evolution of the NAO index. (An introduction to the time series models discussed here is given in Appendix F). A random walk model has been rejected for the evolution the NAO index (Stephenson et al, 2000), but owing to its statistically rather featureless structure, there is still some debate over the appropriate model. Stephenson et al (2000) test a ‘red noise’ first-order AR(1) autoregressive model, a higher order AR(10) autoregressive model and a ‘long-

range' fractional differenced FAR(1) model. They conclude that the FAR(1) model is the most appropriate, having only one parameter and providing a good fit to the index.

Mills (2004) uses a structural time series model to identify three components: a slowly oscillating level exhibiting long swings, a stable cycle having a period of about 7.5 years (consistent with the cycle found by Wunsch (1999) using spectral techniques), and an irregular component that dominates the variation of the index. The presence of this irregular component makes accurate forecasting of the index difficult, since the structural model is found to explain less than 15% of the variation in the index. Mills (2004) also notes that the value for the fractional difference parameter found by Stephenson et al (2000) may not be statistically significant, but that due to the short length of the record it is difficult to distinguish between the models using statistical tests. Barbosa et al (2006) uses wavelet analysis to examine the Lisbon and Gibraltar station-based NAO indices. They find a value of the fractional difference parameter consistent with Stephenson et al (2000) and that it is statistically significant for the Lisbon index, but not for Gibraltar.

We will use a FAR(1) model to describe the evolution of the NAO and hence WEC yield. Fractionally differenced models exhibit long-term persistence, with correlation decaying more slowly than ARMA models. They have been used to describe long-term variations in wind power by Haslett and Raftery (1989). Since the NAO has a strong influence on storm parameters in the eastern North Atlantic, it is not surprising that similar stochastic models can be used to describe NAO and wind power variability. Haslett and Raftery (1989) also noted that wind speeds in Ireland displayed long-range dependence and that modelling only the short-term correlation structure leads to underestimates of interannual variability.

The FAR(1) model is given by the recurrence relation

$$(1 + \alpha B)\Delta^d X_t = e_t \quad [6.2]$$

where B is the backward shift operator, $BX_t = X_{t-1}$, α is a constant and e_t is a white noise process. Δ^d is the fractional difference operator, defined in the natural way, by a binomial series:

$$\Delta^d = (1 - B)^d = 1 - dB + \frac{d(d-1)}{2!}B^2 - \frac{d(d-1)(d-2)}{3!}B^3 + \dots \quad [6.3]$$

For $|\alpha| < 1$ and $0 < d < \frac{1}{2}$ this process is stationary and capable of modelling long-term persistence (Hosking, 1981).

We fit a FAR(1) model to the series of annual NAO indices shown in Figure 6.11 using the `fracdiff` package for R which implements the maximum likelihood method of Haslett and Raftery (1989). The parameters are found to be $d = 0.19$, $\alpha = -0.07$, $\sigma_e = 1.46$. The value of d is close to that found by Stephenson et al (2000) and Barbosa et al (2006), with the small difference probably due to the fact that we are using a different index. The small value of α is to be expected, since the short term correlation of the annual NAO index is very low.

6.4 Predictability of WEC yield

6.4.1 Distribution of multi-year mean values

By combining the time series model for the NAO (equation 6.2) with the relationship between the NAO and Pelamis power we can generate sequences of annual anomalies in Pelamis power of arbitrary length. An example 500 year simulation is shown in Figure 6.12 with 5 and 20 year moving averages. There are extended periods when the 20 year moving average is above or below zero, for over 50 years at times. It should be reiterated though, that this is a stationary process, but one that has long-range dependence.

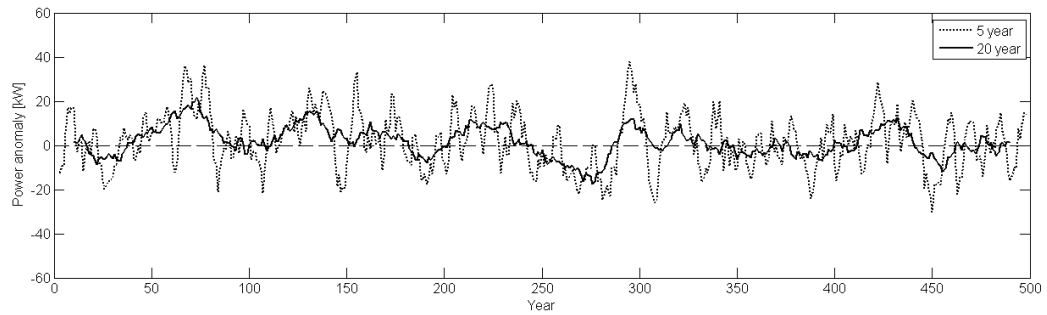


Figure 6.12. 5 and 20 year moving averages of simulated anomalies in annual mean Pelamis power from FAR(1) model.

A measure of the predictability of the wave resource can be obtained from the distribution of differences in average power between consecutive periods. This tells us the uncertainty in the future resource, if the estimate is based on the historic resource. To do this we generate a long series (1 million years in this case) of power anomalies as described above. The series is then divided into 5, 10, or 20 year blocks and the difference in mean power between each block is calculated. The differences were found to be normally distributed, with standard deviations of 17.5 kW, 13.3 kW and 10.3 kW between consecutive 5, 10 and 20 year mean values respectively.

How does this compare to the assumption that annual power anomalies are uncorrelated noise? The standard deviation of the annual anomalies is 28.6 kW, so under the assumption that interannual variability is a white noise process the standard deviations of differences between mean power over consecutive 5, 10 and 20 year periods are 18.0 kW, 12.8 kW and 9.0 kW respectively. So the variance in this case decreases slightly faster than for the FAR(1) model. The difference is small since the FAR(1) model for NAO variability is dominated by irregular fluctuations with only a small level of long-range dependence. Moreover, the influence of the residuals in equation 6.1 is of roughly the same magnitude as that from the NAO: the residual standard deviation is 15.4 kW compared to the value for the slope of 14.4 kW / hPa and the NAO index varying between ± 4 hPa. This means that a lot of the structure of the modelled NAO variability will be masked by the random noise term in 6.1. Moreover the assumption that ε in 6.1 is a white noise process may not be accurate and there may be a small amount of temporal correlation which we were not able to detect from the relatively short record.

A similar finding was made by Pitt (2006a). In order to study the variability of the wave power climate at the Wave Hub site in South West England, Pitt (2006a) constructed a predictor based on an ‘Index of Westerlies’ over the North Atlantic, analogous to the NAO index. Despite the reasonable correlation (0.79) between monthly mean wave power and the Index of Westerlies, there was a large uncertainty in the resulting predictor and he concluded that the use of a longer hindcast is likely to give more accurate results.

This uncertainty in our NAO-based predictor may explain why the observed difference of 33 kW in mean power levels between 1960-1980 and 1980-2000 exceeds that expected from the FAR(1) model. A difference of 33 kW between mean power over consecutive 20 year periods corresponds to the 99.93 percentile of the distribution of differences from the FAR(1) model. From this we can conclude one of two things: either that the combined use of equations 6.1 and 6.2 is not an appropriate model for annual anomalies in WEC power levels at this location, or that a statistically significant change in wave climate occurred between the 1960s and 1990s. There is a large uncertainty related to both conclusions. As noted before detection and attribution of human influence on the NAO and wave climate is made difficult by the short length of climate record available and the differing results between climate models on the effects of GHG forcing. Nevertheless, the evidence is building to suggest that the observed increase in the NAO index and corresponding increase in North Atlantic wave heights in the latter part of the twentieth century are the result of increasing greenhouse gas concentrations (Gillett et al, 2003; Wang et al, 2006b).

With regard to the appropriateness of the stochastic model, fitting a ‘long-range’ dependence model to a series of only 100 years results in quite a high uncertainty in the maximum likelihood estimate of the fractional difference parameter. This uncertainty in the choice of model for the NAO is reflected in the fact that there is still no consensus in the appropriate choice of model (Stephenson et al, 2000; Mills, 2004; Barbosa et al, 2006). Moreover, fitting a stochastic model to the NAO record to explain ‘natural’ variability may not be appropriate since the record may already contain some effect of anthropogenic forcing.

Finally, Woolf et al (2002) have observed that the residual anomalies in winter wave heights in the north-east North Atlantic, once the NAO signal has been removed, are correlated with the “East Atlantic pattern” in atmospheric pressure (see e.g. Rogers, 1990; Zveryaev, 1999). This may mean that our assumption of independent residuals in equation 6.1 is not strictly valid. However there is little literature on the temporal variability of the East Atlantic pattern, so this will not be investigated further here.

6.4.2 The effect of uncertainty in historic data

In Chapter 5 we saw that over an 8 year period the mean Pelamis power calculated from the two calibrated hindcasts differed by 10 kW. The differences in annual mean power over the 8 years concurrent period had a standard deviation of 9 kW, with a maximum of 20 kW and a minimum of -5 kW. It is difficult to say which hindcast these differences resulted from, or if the hindcast data used in this chapter has similar behaviour, but we can make some general remarks on the effect that any errors in the historic data would have on the predictability of WEC yield.

The first observation to make is that a bias in the estimate of the historic resource will result in a bias in the mean value of the predicted future resource. Whether this is a constant bias each year or the net effect of zero-mean random errors in the annual mean (as might arise from the use of altimeter data), the effect on the mean predicted resource will be the same. However, whether the errors in the historic data are predominantly bias errors or random errors will effect the estimated distribution of possible future resource. The observed distribution of annual power anomalies is the convolution of the true distribution of annual power anomalies with the distribution of errors in the estimate of annual mean power. This will result in a positive bias in the estimate of the standard deviation of power anomalies. If we assume that the errors in annual power have a standard deviation of 8 kW, as for the hindcasts in Chapter 5, and the true annual anomalies have a standard deviation of 28 kW, as found above, then the observed annual anomalies would have a standard deviation of 29 kW - only a small increase.

The effect of random errors in the historic wave data on the stochastic model described in Section 6.3 is slightly more subtle. The uncertainty in the estimate of the slope in equation 6.1 results both from errors in the wave data and from sampling effects from having only 50 years of data. The standard deviation of the residuals in equation 6.1 is

15.4 kW, so even if the standard deviation in the estimates of annual power is 8 kW (which is probably an overestimate), then the true residual standard deviation would be 13.2 kW. Therefore finite sampling effects are likely to be the main source of uncertainty in the estimated relationship between power anomalies and the NAO in this case.

So we can conclude that the main effect of errors in the estimate of the historic resource is to bias the estimate of the mean future resource and that the effect on the estimate of interannual variability is small. In relation to a $\pm 20\text{-}30$ kW uncertainty in the predicted mean power over a 20 year period, a 10 kW bias is still significant, but whether it is worth investing further time and money to improve estimates of the historic resource will depend on the sensitivity of the economics to uncertainty in the predicted yield.

6.4.3 Sensitivity to climate change

We investigate the sensitivity of WEC yield at this location to climate change through the link with the NAO. The output of climate models has been used to examine the effect of increased atmospheric concentrations of GHGs on the NAO by several authors (e.g. Gillett et al, 2003; Osborn, 2004; Terray et al, 2004; Kuzmina et al 2005; Stephenson et al, 2006; Pinto et al, 2007). Results have varied depending on the climate model used. An estimate of the uncertainty in the model representation of climate physics can be made by using a multi-model approach (Collins et al, 2006; Tebaldi and Knutti, 2007).

Stephenson et al (2006) have used the output from 18 AOGCMs to investigate the response of wintertime NAO to increasing concentrations of atmospheric carbon dioxide (CO₂). They examine the model simulations of the NAO over 80 year periods with both constant forcing and transient forcing at 1% per year increasing CO₂, (other possible anthropogenic forcing, such as changes in the concentration of other greenhouse gases, aerosols, or ozone are not included). Of the 18 models compared, 15 appeared to be able simulate the main features of NAO, but there was much model-dependent variation in how the models simulated the amplitudes, spatial patterns, and future trends of the NAO. Of the 15 models able to simulate the NAO pattern, 13 predicted a positive increase in NAO with increasing CO₂ concentrations, but generally with only a small response and large variations between models. Stephenson et al

(2006) estimate the NAO sensitivity at 0.0061 ± 0.007 hPa per %CO₂ and note that this result is relatively robust to the exclusion of the models without the NAO dipole. They note that the true confidence interval is likely to be larger than this since the model sensitivities are neither independent nor normally distributed, but since even this interval includes zero, the null hypothesis that there is no effect of CO₂ increase on the NAO index, cannot be rejected at the 5% level of significance. Since the combined results from 18 models cannot be used to reject the no-effect hypothesis, caution should be used when drawing conclusions from studies using smaller subsets of models (e.g. Gillett et al, 2003; Osborn, 2004; Terray et al, 2004; Kuzmina et al 2005; Pinto et al, 2007).

The results of Stephenson et al (2006) are for the response of the winter (Dec-Feb) index, so in order to use them to investigate the effect of climate change on wave energy, we must assume that they apply equally to the annual index that we have used. Since the highest power levels are in winter anyway, this should capture most of the response.

At present, atmospheric concentrations of CO₂ are rising at around 1.9ppm per year or approximately 0.5% per year, with current (February 2009) levels around 387ppm. This gives an increase of around 10% in a 20 year period. So even if we assume that the NAO will respond with the most extreme sensitivity of the models reported by Stephenson et al (2006), of 0.04 hPa per %CO₂ (estimated by the ECHAM4 model), then in a 20 year period the NAO could increase by 0.4 hPa. So under our model for the relationship of Pelamis power with the NAO, equation 6.1, this would result in an increase of 5.7 kW. Assuming this happens gradually over the 20 year period, this would result in a net increase of around 2.9 kW over the entire period. Considering that we calculated the standard deviation of the differences between mean power levels over consecutive 20 year periods as 10.3 kW, this increased power caused by the increasing mean value of the NAO would be undetectable amongst the ‘natural’ variability. This implies that changes in WEC power levels related to anthropogenic emissions of GHGs will probably not effect the predictability of the future resource based on historic estimates, since the change in the NAO over timescales we are interested in is much less than the ‘natural’ noise level. However, whether the increase in wave power between the 1960s and 1990s was natural variability or not is debatable.

This is, of course, based on many assumptions which are difficult to justify. Firstly, the response of the NAO to increased levels of CO₂ is highly uncertain and will almost certainly not be a linear increase over time. Future CO₂ emissions are also uncertain. Moreover, we are assuming that the response of wave power to the NAO will remain the same in a changed NAO state. Wang and Swail (2006) give a similar analysis of the uncertainty in predictions of future wave conditions and note that the uncertainty due to differences among the emissions scenarios is much smaller than that due to differences between predictions from different climate models.

Since there are such high uncertainties in predictions of future climate, it may be more useful to note the effect on WEC yield under various NAO change scenarios. If the mean value of the NAO index increases by 1 standard deviation (about 1.5 hPa for the index used here), then the mean Pelamis power at the location in question here would increase by 21.6 kW (5.6%). A mean increase of 2 standard deviations in the NAO index would result in a mean increase of 43.2 kW (11.2%). Since the NAO has an affect on storm track, frequency and intensity it may be naïve to assume that residuals ε in equation 6.1 will not be affected by a change in the NAO state. Nevertheless, the NAO accounts for about 70% of the interannual variability in Pelamis power at this site, so we can certainly expect some response to changes in the mean NAO state.

6.5 Discussion and conclusions

The long term variability and predictability of WEC yield for a site in the north of Scotland has been examined. The main conclusions for this location are:

1. Observed changes in multi-year mean values of Pelamis power exceed those expected if annual anomalies were uncorrelated Gaussian noise.
2. Annual power anomalies are strongly correlated with the NAO, but the stochastic model for long-term variability in WEC yield, based on the FAR(1) model for the NAO does not explain all observed variability.

3. GCM predictions for the NAO are too uncertain to forecast changes in wave climate, but some increase in wave power with increased GHGs seems likely at this location.
4. Improvements in the accuracy of historic data will improve the bias, but not variance of predictions of future WEC yield. These bias and random error components are of roughly the magnitude.

The site which has been studied in this chapter is in an area where wave parameters are strongly and positively correlated with the NAO (see Figure 6.1). In areas with strong negative correlation, the opposite results can be expected. However, in areas with lower correlation with the NAO or for locations outside the North Atlantic a different approach will be necessary to examine the sensitivity of wave power to climate change. Whether the best approach is to use pressure fields output by AOGCMs directly, or to investigate changes in general storm parameters (e.g. intensity, frequency and track) remains to be seen.

Improvements in the accuracy of predictions of future WEC yield can be made through improving the quality of the historic data. In particular it seems likely that improvements could be made to the quality of modelled data and the descriptions of its long-term uncertainties.

A related problem which is worth mentioning here is the seasonal predictability of wave energy yield. Seasonal forecasts of the wintertime NAO index have been discussed by Doblas-Reyes et al (2003) and Fletcher and Saunders (2006). The empirical predictors presented by Fletcher and Saunders (2006), based on factors such as Northern Hemisphere snow cover or sea surface temperature are slightly more accurate than those based on climate model output, discussed by Doblas-Reyes et al (2003). However, even these only have a correlation of around 0.5 with the winter NAO index. Some tests of these predictors on our data improved the RMS error in prediction of winter WEC yield by about 15% (over the climatological mean value). It seems doubtful though, that this level of predictability would be of any practical use to wave farm operators.

7. Extreme Wave Analysis

7.1 Introduction

In severe storms the forces exerted by ocean waves can be enormous. Wave energy converters must be designed to utilise the available power from the waves under normal operating conditions whilst withstanding the forces in the most severe storms. Generally speaking the larger the forces that a WEC must be designed to cope with the more expensive it will be. Therefore machines are designed to survive the most extreme conditions expected in their lifetime, but no more than this.

Future wave conditions cannot be predicted more than a few days in advance, so a probabilistic approach must be taken to estimate the distribution of possible future extreme conditions. It is then up to the discretion of the engineers and project developers to decide on design value which presents an acceptable level of risk.

The distribution of possible future extreme conditions is estimated from the historic extreme conditions. However this usually requires extrapolation from the observed range of the historic data. For example, if the lifetime of a wave farm is 20 years, it may be required that the WEC is designed to withstand the most severe conditions in 95% of the possible future 20 year periods. If it is assumed that annual maxima are independent then we can make the following calculation. Let X denote the annual maximum H_s and let $F(x) = \Pr\{X < x\}$ be the distribution function of X . Let Y denote the maximum H_s in a 20 year period and $G(x) = \Pr\{Y < x\}$ be the distribution function of Y . Then

$G(x) = F(x)^{20}$. So the H_s which is only exceeded in 5% of 20 year periods corresponds to the value x for which $G(x) = 0.95$, or equivalently the x for which

$F(x) = 0.95^{1/20} = 0.9974$. This is a value which is exceeded on average every $1 / (1 - 0.9974) = 390.4$ years (see the note on return values in Section 7.3.2).

There are no historic datasets of this length. Therefore extrapolation outside the observed range of values is required in this example. This can be done either on a

physical or statistical basis. In energetic sites it may not be possible to rule the possibility of very large waves on physical grounds alone. Extreme value theory provides a mathematically rigorous framework for the extrapolation of historical data.

In this chapter we discuss the estimation of the distribution of extreme H_s using extreme value theory. Because of the size of this topic and the large volume of existing work, it is not possible to cover the whole field in this chapter. In particular there are two topics relevant to wave energy which we will not be examining here. These are: the distribution of individual waves given a certain sea state and the estimation of multivariate extremes, such as H_s and T_z . For an introduction to recent work on the distribution of individual wave heights see, for example, Tayfun and Fedele (2007) and references therein. The problem of combining long-term and short-term distributions of wave heights has been discussed by Foristall (2008). He compares the various methods which have been proposed and shows that the most appropriate is that of Tromans and Vanderschuren (1995).

Multivariate analysis of extreme conditions is important for the design of WECs since the WEC response may be tuned to certain frequencies. It is therefore possible that the largest wave may not be the most damaging to the machine, but a lower wave with a longer or shorter period may be more dangerous. An introduction to the theory of multivariate extreme value analysis can be found in Coles (2001) and examples of applications to wave data are given by Morton and Bowers (1997) and Repko et al (2004).

However, the first problem which is likely to be encountered when assessing a site for the deployment of a wave farm is the prediction of the anticipated maximum H_s . Within this problem two issues are focused on in this chapter. The first is the method used to estimate the parameters of the distribution and the second is the effect of seasonal variability in wave heights. These problems are dealt with theoretically to start with, before using buoy data to give practical examples and illustrate particular points. The chapter is organised as follows: In 7.2 an overview of methods for estimating extreme values of H_s is presented, together with the motivation for using a Peaks Over Threshold (POT) approach, fitted with a generalised Pareto distribution (GPD). In 7.3 the main features of the GPD are described. In section 7.4 methods used to estimate GPD

parameters are discussed and a simulation study is presented to show how these methods perform in practice. The effect of seasonality, directionality and other covariates is discussed in 7.5, and some methods which have been proposed for modelling seasonality and directionality are reviewed. In 7.6 the examples are presented using buoy data, to show how the theory translates to practical situations. The results of the study using buoy data are used to construct realistic case studies, so that the performance of seasonal and non-seasonal models can be tested using realistic simulations. Finally, in 7.7 the conclusions are presented.

7.2 Overview of methods for estimating extreme H_s

In this section we give an overview of some of the models which have been proposed for distributions of extremes and their application to wave data. The aim is to describe the motivation for the Peaks Over Threshold (POT) method which is commonly used at present. For brevity the mathematical details have been omitted from this section, and the reader is referred to Coles (2001) for these.

Before the advent of long term wave data sets, a popular approach for estimating extremes was to fit a parametric distribution to the entire dataset and extrapolate into the tail. This is sometimes referred to as the initial distribution (ID) method. There are numerous problems with this approach for wave data. Firstly, it is normally assumed that the data are independent and identically distributed (i.i.d.), which is not the case for wave data. Consecutive measurements are highly correlated (in the case of in-situ or model data) and therefore not independent. Also conditions generally exhibit seasonal variability, meaning that data are not identically distributed during the year. Most importantly though, a fit based on the bulk of the data does not necessarily imply a good fit to the highest values in which we are interested.

This point has been well illustrated by Ferreira and Guedes Soares (1999). They model the distribution of H_s using Beta and Gamma distributions. The distributions are very flexible and cover the three limiting forms of tail behaviour (see Coles, 2001). The Gamma distribution has an exponential tail (type I) and the Beta distribution can have

either long tails (type II) or short tails (type III). They show that all three types of distribution fit H_s data from the Portuguese coast very well. Kolmogorov–Smirnov tests for goodness-of-fit do not reject any of the distributions as not fitting the data. The three distributions are very close to each other over range of the bulk of the data but differ remarkably at high probability quantiles. This leads to estimates of return values differing by over 5m between the two types of Beta model. Since there is no *a priori* reason to suppose that H_s follows one distribution rather than another, the ID method is not recommended for predicting extreme H_s (Mathiesen et al, 1994).

Extreme value theory does not require assumptions about the distribution of the bulk of the data. Roughly speaking, the theory states that the distribution of the maximum of a sample of n independent, identically distributed observations will tend to one of the three tail types mentioned above, as $n \rightarrow \infty$. These three types of tail are all members of the Generalised Extreme Value (GEV) distribution. For a large enough sample size, n , this suggests the use of the GEV family for modelling extremes. This is referred to as a ‘block maxima’ method since it is used to model the maximum value in a ‘block’ of fixed size such as a year or a month (or alternatively over a fixed unit of length).

By definition, extreme conditions are rare; therefore making maximal use of the data is of great importance. Block maxima methods where only one value is used per block is wasteful of data. For instance several large (and independent) storms may occur in one year which are all more severe than storms in another year. R largest order statistics models come some way to addressing this problem, by using the 1st, 2nd, ..., r^{th} largest measurements in each block (see e.g. Sobey and Orloff, 1995; Guedes Soares and Scotto, 2004, for applications of this method to wave data). A more complete description of the upper tail of a distribution is given by a threshold model. In a threshold model the data are not separated into blocks, but instead extreme events are defined as exceedances of some high threshold. The analysis of only storm data exceeding a threshold is known as the Peaks Over Threshold (POT) method.

Threshold analyses of extremes and analyses based on block maxima are consistent with each other (see Coles 2001, p75), but threshold analyses have the advantage that they use a greater proportion of the data. Again, roughly speaking, if block maxima have an approximating distribution in the GEV then excesses of a ‘large enough’

threshold will have an equivalent approximating distribution within the generalised Pareto family. The issue of choosing a ‘large enough’ threshold is non-trivial and is analogous to the choice of block size for the GEV method. Too small a threshold will mean that approximation by the asymptotic limit model is likely to be poor, leading to bias in estimation and extrapolation. Too large a threshold gives fewer data leading to large estimation variance. Threshold selection is discussed in Section 7.3.2.

Van Vledder et al. (1993) and Guedes Soares and Scotto (2001) have compared the use of annual maxima (AM) and POT methods using a dataset for a location on the Norwegian continental shelf. They conclude that POT is to be preferred over AM since it uses a greater number of data points. It is now common practice to use the POT method for the estimation of extreme H_s , see for example Goda et al (1993), Mathiesen et al (1994), Elsinghorst et al (1998), Ferreira and Guedes Soares (1998), Naess (1998), Taylor & Goh (2000), Guedes Soares et al (2003), Caires and Sterl (2005b).

Both block maxima and threshold models are special cases of point process models (see Morton et al, 1997; Anderson et al, 2001). The point process model provides an elegant formulation of the extreme value behaviour of process. However, it does not lead to anything new in terms of statistical models, since any inference made using a point process method could equally be made using a threshold or block maxima method (Coles, 2001). For simplicity of the exposition, we will therefore not consider the point process formulation further.

It is important to be aware of the limitations implied by the use of extreme value theory. The models are developed using asymptotic arguments and care is needed in treating them as exact results for finite samples. Naess and Haug (2008) argue that it is hard to verify the correctness of such assumptions and their experience using asymptotic models has been mixed. This has led them to develop a model which attempts to capture the sub-asymptotic behaviour of extreme value data. Another approach is taken by Bernardino et al (2008) who attempt to derive extreme value statistics for a location by studying storm parameters over an entire ocean basin. However, both of these approaches are at preliminary states of development and will not be considered further here.

It is also important to check that the other assumptions made in the models are not violated by the data. Two important assumptions are that the data are independent and identically distributed. The assumption of independence can be relaxed by requiring independence of extremes which are sufficiently separated in time (this is known as the $D(u_n)$ condition, see Coles, 2001, p93). This is entirely plausible for wave data, with the occurrence of storms separated by several days being roughly independent. Short term dependence is dealt with by declustering. That is, we only consider the maximum value in a single storm, rather than all data points within a storm above the threshold. The declustering of wave data is discussed in Section 7.6.2.

The assumption that the data are identically distributed is not strictly valid due to seasonal and climatic variability. For example the distribution of storm peak H_s in summer is different to the distribution in winter. However, if a threshold is chosen so that only winter storms exceed it then this assumption may be appropriate. Alternatively, terms to describe non-stationary effects can be incorporated into the statistical model. The effect of seasonal variability is discussed in Sections 7.5 and 7.6.

So in summary, the POT method will be used for the estimation of extreme H_s , whereby the generalised Pareto distribution is fit to declustered exceedances of a high threshold. Attention will be given to testing the validity of the assumptions of the model or examining the effect of violating assumptions. These issues we consider are:

- Declustering the data
- Assessing the performance of various estimators of the GPD
- Threshold selection
- The effect of non-stationarity in the data

7.3 The generalised Pareto distribution

7.3.1 CDF and PDF

Let Y be a random variable and $X = Y - u$ be the exceedances of Y over some high threshold u . Then X has a generalised Pareto distribution if and only if the distribution function of X , conditional on Y exceeding u , is

$$F(x) = \Pr\{X < x | Y > u\} = \begin{cases} 1 - (1 + \xi x / \sigma)^{-1/\xi} & \text{for } \xi \neq 0 \\ 1 - \exp(-x / \sigma) & \text{for } \xi = 0 \end{cases} \quad [7.1]$$

for $\sigma > 0$ and $0 \leq x < \infty$ for $\xi \geq 0$ and $0 \leq x \leq -\sigma / \xi$ for $\xi < 0$. The density function is given by

$$f(x) = \frac{dF(x)}{dx} = \begin{cases} \sigma^{-1} (1 + \xi x / \sigma)^{-(1+1/\xi)} & \text{for } \xi \neq 0 \\ \sigma^{-1} \exp(-x / \sigma) & \text{for } \xi = 0 \end{cases} \quad [7.2]$$

The parameters σ and ξ are called the scale and shape parameters respectively. The family of generalised Pareto distribution contains the uniform distribution when $\xi = -1$ and the exponential distribution when $\xi = 0$. The density functions of the generalised Pareto distribution for various values of ξ are shown in Figure 7.1.

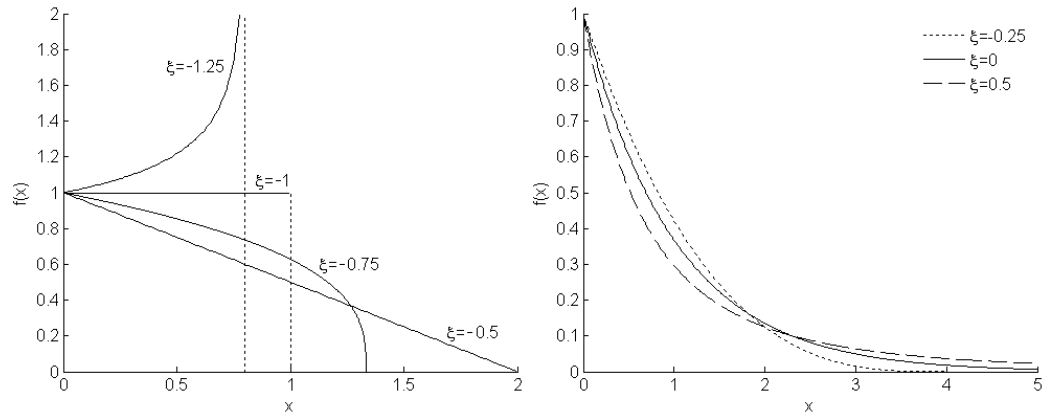


Figure 7.1. Probability density function of the generalised Pareto distribution for scale parameter $\sigma = 1$ and various values of shape parameter ξ .

The case $\xi = 0$ is an exponential tail (type I) as referred to above. When $\xi < 0$ the distribution has a finite end point and is referred to as “short-tailed” (type III). When $\xi > 0$ the distribution is referred to as “heavy-tailed” or “long-tailed”. In this case the r^{th} central moment exists only if $\xi < 1/r$ and in particular we have that

$$E(X) = \frac{\sigma}{(1-\xi)} \quad [7.3]$$

and

$$\text{var}(X) = \frac{\sigma^2}{(1-\xi)^2(1-2\xi)} \quad [7.4]$$

so the when $\xi \geq 1$ the mean is not defined and when $\xi \geq 0.5$ the variance is not defined.

The GPD is a valid probability distribution for all values of ξ , however, we will restrict our interest to the range $-0.5 < \xi < 0.5$ since these are the values which are commonly observed for distributions of extreme H_s .

7.3.2 Return values

The N -year return value is the value that, on average, is exceeded once every N -years. Or more precisely, it is the level which is exceeded in a given year with probability $1/N$. If X is a GP variable, the N -year return level for $Y = X + u$ is the solution of

$$\frac{1}{Nm} = \Pr\{Y > x_N\} \quad [7.5]$$

where m is the number of observations per year. We have that

$$\Pr\{Y > x_N \mid Y > u\} = 1 - F(x_N - u) \quad [7.6]$$

So

$$\Pr\{Y > x_N\} = \Pr\{Y > u\}(1 - F(x_N - u)) \quad [7.7]$$

If we equate 7.7 with 7.5, substitute 7.1 (the GP distribution function) and rearrange, this gives

$$x_N = \begin{cases} u + \frac{\sigma}{\xi} [(Nm\zeta_u)^\xi - 1] & \text{for } \xi \neq 0 \\ u + \sigma \log(Nm\zeta_u) & \text{for } \xi = 0 \end{cases} \quad [7.8]$$

where $\zeta_u = \Pr\{Y > u\}$. For dependent data, such as time series of wave height ζ_u is estimated by n_c / n , where n_c is the number of clusters above u , and n is the total number of samples.

Return values are a useful single parameter to gauge the risk associated with a particular distribution. However, they should not be confused with the largest value that is expected in a given period. In fact for large N the probability of exceeding x_N in an N -year period is about 0.63. To see this we can consider, without loss of generality, annual maxima. Each year is a random trial with probability of exceeding the return value $p = 1 - 1/N$. The probability that x_N is not exceeded in N years is p^N , so the probability that x_N will be exceeded at least once in N -years is $1 - p^N$. Figure 7.2 shows a plot of $1 - p^N$ against N . From the example given in the introduction we can see that the level which is not exceeded in 95% of 20 year periods is in fact the 390.4 year return value.

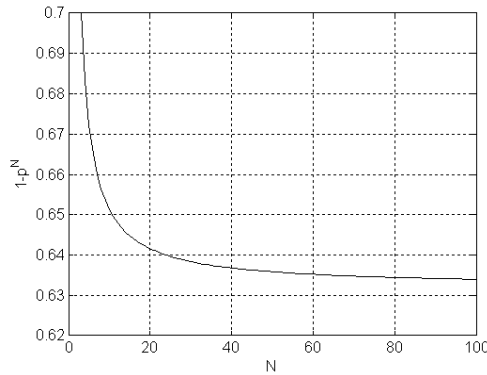


Figure 7.2. Probability that the N -year return value is not exceeded in N years.

7.3.3 Threshold choice

It is possible to use statistical techniques to estimate the threshold from the data, however the method preferred by most practitioners is to estimate parameters for a

range of thresholds and examine the variation of certain statistics with the threshold. The disadvantage to this approach is that it makes threshold choice somewhat arbitrary. However the advantages are that it can illustrate whether the GPD provides a good fit and highlights the uncertainty in the threshold choice.

If Y is a random variable and $X_0 = Y - u_0$ has a generalised Pareto distribution with scale parameter σ_{u_0} and shape parameter ξ , it can be shown that (see e.g. Coles, 2001) for any $u > u_0$, $X = Y - u$ has a generalised Pareto distribution with the same value of ξ and

$$\sigma_u = \sigma_{u_0} + \xi(u - u_0) \quad [7.9]$$

Therefore the variable

$$\sigma^* = \sigma_u - \xi u \quad [7.10]$$

is constant with respect to u . Therefore if we plot estimates of ξ and σ^* against u we should observe a minimum threshold u_0 above which the parameter estimates are constant. In practice finite sampling effects lead to variability of these parameters with threshold, so it is rare to see a completely straight line with threshold. Moreover, as the threshold increases the number of samples will decrease, thus increasing the variance of the estimates.

From 7.3 and 7.9 we have that

$$E(X) = \frac{\sigma_{u_0} + \xi u}{1 - \xi} \quad [7.11]$$

So if the GPD is a valid model for exceedances over u_0 then the mean of the exceedances over threshold $u > u_0$ are a linear function of u with slope $\xi/(1 - \xi)$ and intercept $\sigma_{u_0}/(1 - \xi)$. This provides another diagnostic tool for choosing the threshold level, known as the mean residual life plot. The threshold is then chosen as the lowest

value for which estimates of ζ and σ^* approach constant values and $E(X)$ satisfies 7.11.

Plots of ζ , σ^* and $E(X)$ against u can be made either by calculating values at regular increments of u or by removing one sample at a time and specifying the threshold as the lowest remaining sample. The first method can be quicker for large samples, but in small samples it can result in a loss of information. In the case of estimating extreme H_s samples are nearly always small enough for the second method to be used. Another advantage of removing one point at a time is that it can explicitly show the effect of discrete data on the estimates. For example if values of H_s are reported to the nearest 0.1m then if there are multiple samples with the same value then removing the lowest sample from the set and recalculating will result in multiple estimates for the same threshold and produce a saw-tooth type graph. Depending on whether the data were round up, down or to the nearest 0.1m, an idea of the shape that the graph should take if the data had not been rounded can be made from this saw-tooth shape graph. If estimates are calculated only at specific values of u then this effect will be missed.

7.3.4 Model diagnostics

Once a threshold has been chosen, it is important to check that the GPD provides a good fit to the data. If a model does not provide a good fit to the extremes which have been observed so far then there is little hope that it will accurately model future conditions. Probability plots and quantile plots are useful diagnostic tools for checking the fit of a model. They provide a graphical comparison of the estimated distribution \hat{F} to the empirical distribution \tilde{F} .

7.3.4.1 The empirical distribution function and plotting position

Consider a sample $\mathbf{x} = x_1, \dots, x_n$ of observations from a common population with unknown distribution function F , and let $x_{(1)} \leq x_{(2)} \leq \dots \leq x_{(n)}$ denote the order statistics. For the largest sample in the set, $x_{(n)}$, there are $n-1$ samples which are smaller than it so we could assign it the probability $\Pr\{X < x_{(n)}\} = (n-1)/n$. Conversely, zero observations are larger than it so we could assign it the probability $\Pr\{X > x_{(n)}\} = 0$. As

$n \rightarrow \infty$ the difference in these two approaches tends to zero, but for finite samples both approaches will introduce bias. The empirical distribution function is defined by

$$\tilde{F}(x) = \frac{i+a}{n+b} \text{ for } x_{(i)} \leq x < x_{(i+1)} \quad [7.12]$$

for constants a and b . Various formulas have been proposed in the literature but they generally give very similar results. We will use the formula $a = 0.35$ and $b = 0$ as advocated by Hosking and Wallace (1987). The empirical distribution function evaluated at $x_{(i)}$ is known as the plotting position of $x_{(i)}$ and is denoted as $p_i = \tilde{F}(x_{(i)})$. Plotting positions proposed by other authors are noted in Section 7.4.

7.3.4.2 Probability plots

A probability plot consists of the points

$$\{(\hat{F}(x_{(i)}), \tilde{F}(x_{(i)})) : i = 1, \dots, n\} \quad [7.13]$$

where \hat{F} is the estimated distribution function and \tilde{F} is the empirical distribution function. If \hat{F} is a good model for the data then the points should lie close to the unit diagonal. Substantial departures from this line indicates that the model does not describe the data well.

7.3.4.3 Quantile plots

A quantile plot consists of the points

$$\{(\hat{F}^{-1}(p_i), x_{(i)}) : i = 1, \dots, n\} \quad [7.14]$$

It provides the same information as a probability plot, but on a different scale. In a quantile plot most of the points are bunched towards the lower quantiles, giving a better view of the fit of the model to the higher quantiles, whereas in a probability plot the points are spread evenly between 0 and 1. Both plots provide useful information since a fit which looks reasonable on one scale may look poor on the other.

7.4 Estimation of GPD parameters

Various methods have been proposed for estimating the parameters of the GPD. It is desirable for estimators to have the following properties:

- (a) Estimators always exist
- (b) Easy and fast to compute
- (c) Low bias and standard deviation of model parameters and quantiles
- (d) Estimators are consistent with the observed data
- (e) Low sensitivity to threshold choice

Properties such as existence and consistency with the observed data would seem like minimum requirements for an estimator, but they are not satisfied by all the methods which are commonly used. In this section we compare various estimators which have been proposed for the GPD in terms of the properties listed above. In 7.4.1 the various estimation methods are described. In 7.4.2 the results of a simulation study are presented from which a critical comparison of the estimators can be made. This study expands on those given in presented in the literature in two ways:

1. New results are given on the existence of the maximum likelihood estimators
2. A new hybrid estimator is studied which is shown to give the best results in terms of the criteria listed above.

7.4.1. Methods

This section describes estimators which have been proposed for the GPD. Several ‘robust’ methods have been proposed which are less sensitive to outliers e.g. Dupuis (1998), Peng and Welsh (2001) and Juarez and Schucany (2004). Davison and Smith (1990) caution against the use of robust methods in extremes, arguing that the highest observations are those which are most informative and that careful checking of the data by the analyst is preferable. Therefore robust methods are not considered further here.

Throughout this section a caret “ \wedge ” will be used to denote an estimate of the true parameter.

7.4.1.1 Maximum likelihood

The maximum likelihood (ML) method is recommended by numerous authors, e.g. Coles (2001), as it has many desirable properties. Asymptotically, it is unbiased and has the minimum possible variance (this is known as an efficient estimator). However, Hosking and Wallis (1987) showed that the ML estimates do not display this asymptotic property for sample sizes less than 500. They also noted that sometimes the solutions to the ML equations do not exist and that at other times when the solutions do exist there can be convergence problems with the algorithm they used to find them. There has been some progress since the study of Hosking and Wallis (1987) on the problem of finding the ML estimates, so it is worth revisiting here.

The log-likelihood of the GPD is given by

$$\ell = \begin{cases} -n \log \sigma - (1 + 1/\xi) \sum_{j=1}^n \log(1 + \xi x_j / \sigma) & \text{for } \xi \neq 0 \\ -n \log \sigma - \frac{1}{\sigma} \sum_{j=1}^n x_j & \text{for } \xi = 0 \end{cases} \quad [7.15]$$

By taking partial derivatives of ℓ with respect to σ and ξ it is straight forward to show that the maximum of the log-likelihood function is equivalent to a zero of the function

$$h(\rho) = 1 + \frac{1}{n} \sum_{j=1}^n \log(1 + \rho x_j) - \left[\frac{1}{n} \sum_{j=1}^n \frac{1}{(1 + \rho x_j)} \right]^{-1}, \quad \rho > -1/x_{(n)} \quad [7.16]$$

where $\rho = \xi / \sigma$. This reduces the problem to a one-dimensional search. The ML estimates of σ and ξ are then given by

$$\hat{\xi} = \frac{1}{n} \sum_{j=1}^n \log(1 + \rho x_j) \quad [7.17]$$

$$\hat{\sigma} = \hat{\xi} / \rho \quad [7.18]$$

However, finding the zeros of $h(\rho)$ is not as straight forward as it may appear. Grimshaw (1993) and Chaouche and Bacro (2006) have gone some way to characterising the behaviour of the function $h(\rho)$. They have shown analytically that

$$h(\rho) \rightarrow -\infty \text{ as } \rho \rightarrow -1/x_{(n)} \quad [7.19]$$

$$h(0) = 0 \quad [7.20]$$

$$h(\rho) \rightarrow -\infty \text{ as } \rho \rightarrow \infty \quad [7.21]$$

Grimshaw (1993) showed that $\rho = 0$ corresponds to the maximum likelihood solution if and only if $S(\mathbf{x}) = 0$, where

$$S(\mathbf{x}) = n \left(\sum_{j=1}^n x_j^2 \right) - 2 \left(\sum_{j=1}^n x_j \right)^2 \quad [7.22]$$

The following properties of $h(\rho)$ have been established through simulation by Grimshaw (1993) and Chaouche and Bacro (2006), but have not been proved analytically:

1. If $S(\mathbf{x}) \neq 0$ the zero of $h(\rho)$ which corresponds to the ML solution will have the same sign as $S(\mathbf{x})$.
2. If $S(\mathbf{x}) > 0$ then $h(\rho)$ has just one positive root
3. If $S(\mathbf{x}) < 0$ then $h(\rho)$ has 0 or 2 negative roots.
 - a. Contrary to the conjecture of Chaouche and Bacro (2006) it is relatively easy to generate a sample where no non-zero solution of $h(\rho)$ exists. This occurs most frequently for small sample sizes and negative ζ (see Figure 7.3).
 - b. In the case that there are 2 negative roots, one is very close to $-1/x_{(n)}$ and is not the ML solution.

This information can be used to construct an algorithm to search for the roots of $h(\rho)$, avoiding the trivial solution at $\rho = 0$ and moving toward the solution which corresponds to the solution of the ML equations.

As noted above, samples with no ML solution occur quite frequently when the sample size is low and ζ is negative. Figure 7.3 shows the occurrence of samples with no ML solution for sample sizes of 25 and 50, with ζ between -0.5 and 0.5. 10,000 samples were generated for each value of ζ . For $n = 100$ no failures were found for any value of ζ . The results agree with those of Hosking and Wallis (1987).

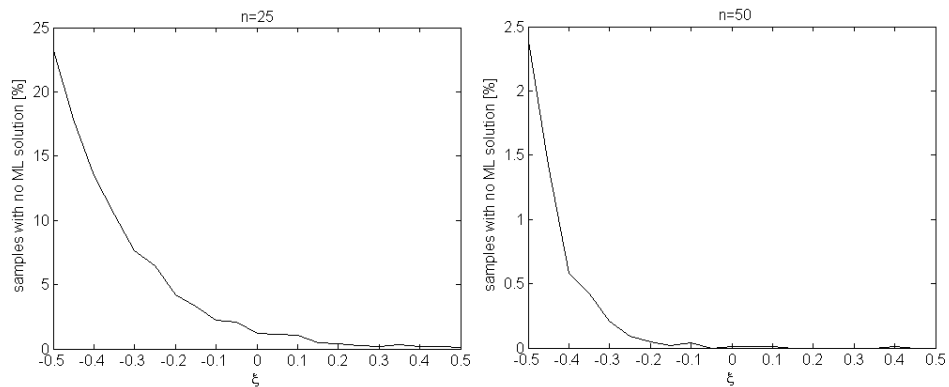


Figure 7.3. Percentage of samples with no ML solution against ζ for $n = 25$ (left) and $n = 50$ (right).

Luceno (2006) proposed a quasi-maximum likelihood (QML) method as a solution to the problem of non-existence of the ML estimates. He notes that substituting $\sigma = -\zeta x_{(n)}$ into the log-likelihood equations and maximising with respect to ζ gives an estimate $\tilde{\zeta}$ given by

$$\tilde{\zeta} = \frac{1}{n-1} \sum_{j=1}^{n-1} \log(1 + x_j / x_{(n)}) \quad [7.23]$$

Luceno (2006) also defines a second parameter

$$Z = \frac{-S(\mathbf{x})}{2 \left(\sum_{j=1}^n x_j \right)^2} \quad [7.24]$$

For $\xi = -1$ the asymptotic value of Z is $1/3$ and for $\xi = 0$ the asymptotic value of Z is 0 . Based on this reasoning he proposes that the ML solutions should be used when $\tilde{\xi} > -0.75$ and $Z > 0.2$, otherwise estimates should be given by $\tilde{\xi}$ and $\tilde{\sigma} = -\tilde{\xi}x_{(n)}$.

Further investigation of the existence of ML solutions in relation to these criteria has yielded some interesting results in addition to those of Luceno (2006). These are:

1. There is a critical value of $\tilde{\xi}$, $\tilde{\xi}_c$ say, above which the ML solutions always exists. This value is a function of sample size only.
2. The probability that the ML solutions exists and $\tilde{\xi} < \tilde{\xi}_c$ is very low (typically less than 1%).
3. The existence of ML solutions does not depend on the value of Z .
4. $\tilde{\xi} \rightarrow \tilde{\xi}_c$ as $\hat{\xi} \rightarrow -1$, where $\hat{\xi}$ is the ML solution.

The results are based on extensive simulation but despite some effort, analytic proofs could not be found. However the range of parameters tested and the number of trials used (over 10,000 for some parameter combinations) gives confidence that they are valid. Figure 7.4 shows a scatter plot of $\tilde{\xi}$ against $\hat{\xi}$ for 1000 samples of size $n = 25$ from a GP distribution with $\xi = -0.5$ and $\sigma = 1$. It can be seen that $\tilde{\xi} \rightarrow -0.74$ as $\hat{\xi} \rightarrow -1$ and that there are only 11 samples for which $\tilde{\xi} < -0.74$ and $\hat{\xi}$ exists. In this case there were a total of 233/1000 samples where $\tilde{\xi} < -0.74$. Crucially though, in the 777 samples where $\tilde{\xi} > -0.74$ the ML solution always exists.

A plot of the critical value $\tilde{\xi}_c$ against n is shown in Figure 7.5. Critical values were found from simulation with various n , σ and ζ , and found to be dependent on n only. The value of ζ effects the distribution of $\tilde{\xi}$, with lower ζ giving a lower mean value of $\tilde{\xi}$. Also when ζ is lower, the probability that the ML solution exists given that $\tilde{\xi} < \tilde{\xi}_c$ decreases. For example when $\xi = -0.5$ and $n = 25$ there were 233 samples with $\tilde{\xi} < \tilde{\xi}_c$

and of these 11 where the ML solution existed, but when $\xi = 0$ and $n = 25$ there were 15 samples with $\tilde{\xi} < \tilde{\xi}_c$ and of these 5 where ML solution existed. However, the joint probability that $\tilde{\xi} < \tilde{\xi}_c$ and the ML solution exists was always less than 1.5%. From this we can conclude that condition $\tilde{\xi} > \tilde{\xi}_c$ is a sufficient and nearly always necessary condition for the existence of ML solutions. Moreover this criterion can be calculated from the data before an attempt is made to solve the ML equations, thus speeding up calculation.

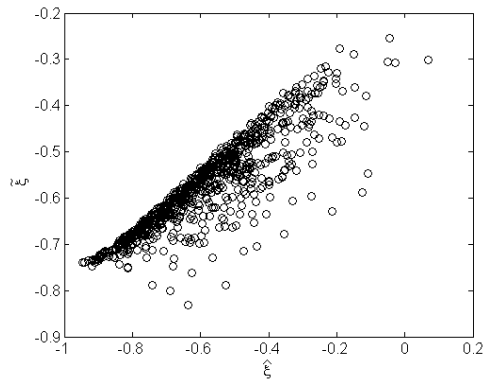


Figure 7.4. Scatter plot of $\tilde{\xi}$ against $\hat{\xi}$ for 1000 samples of size $n = 25$ for $\xi = -0.5$ and $\sigma = 1$.

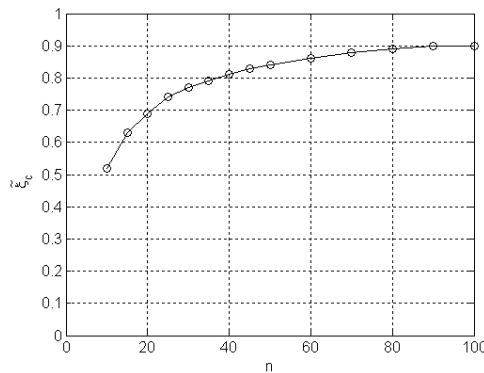


Figure 7.5. Critical value $\tilde{\xi}_c$ against sample size n .

7.4.1.2 Maximum entropy

Maximum entropy (ME) estimates of the GPD parameters are discussed by Sing and Guo (1995). In the case that the threshold is chosen before the parameters are estimated,

the ME solutions are equivalent to the ML solutions. Therefore they will not be considered further.

7.4.1.3 The method of moments, probability weighted moments and hybrids

Moment estimators for the GPD are found by substituting the sample mean \bar{x} and variance s^2 into the formulas for the population mean and variance (equations 7.3 and 7.4) and rearranging. The moment (MOM) estimators are then given by:

$$\hat{\sigma} = \frac{1}{2}\bar{x}(1 + \bar{x}^2 / s^2) \quad [7.25]$$

$$\hat{\xi} = \frac{1}{2}(1 - \bar{x}^2 / s^2) \quad [7.26]$$

Hosking and Wallis (1987) introduced probability weighted moment (PWM) estimators for the GPD. They are given by

$$\hat{\sigma} = \frac{2\alpha_0\alpha_1}{\alpha_0 - 2\alpha_1} \quad [7.27]$$

$$\hat{\xi} = 2 - \frac{\alpha_0}{\alpha_0 - 2\alpha_1} \quad [7.28]$$

where

$$\alpha_r = \frac{1}{n} \sum_{j=1}^n (1 - p_j)^r x_{(j)} \quad [7.29]$$

and $p_j = (j - 0.35) / n$ is the empirical non-exceedance probability of $x_{(j)}$.

MOM and PWM estimators always exist and are easy to compute. Moreover, Hosking and Wallis (1987) showed that they have lower standard deviation and bias than ML estimators for sample sizes less than 500. However, there are two disadvantages with this method. The first is that they can sometimes produce estimates which are not consistent with observed data, in that there are samples for which $\hat{\xi}$ is negative and $x_{(n)} > -\hat{\sigma} / \hat{\xi}$, violating the definition given in equation 7.1. Dupuis (1996) refers to

these as non-feasible parameter estimates and discusses the probability of these occurring. He shows that when $\xi = -0.5$ about 30% of samples result in non-feasible MOM and PWM parameter estimates for sample sizes between 500 and 10,000. However, the occurrence decreases with increasing ξ .

Dupuis and Tsao (1998) introduced hybrid estimators based on PWM and MOM which are always feasible. These hybrid estimators take the value of the MOM or PWM estimators if the results are feasible and set $\hat{\xi} = -\hat{\sigma} / x_{(n)}$ otherwise.

The second disadvantage of the PWM estimators, which does not seem to have been noted in the literature, is their sensitivity to the threshold. From equation 7.29 it can be seen that the parameter α_1 is most sensitive to the lowest order statistics, since these have the greatest weight. This means that a small change in threshold can have a larger effect on the PWM parameter estimates than for other methods.

7.4.1.4 Likelihood-Moment Estimation

Zhang (2007) has proposed a likelihood-moment (LM) estimator for the GPD. This estimator always exists, is always feasible and is simple to compute. It is given by solving the equation

$$\frac{1}{n} \sum_{j=1}^n (1 - bx_j)^p = \frac{1}{1-r} \quad [7.30]$$

where

$$p = \frac{rn}{\sum_{j=1}^n \log(1 - bx_j)} \quad [7.31]$$

and the parameter $r < 1$ is chosen before the estimation. Having solved for b the GPD parameter estimates are given by

$$\hat{\xi} = \frac{1}{n} \sum_{j=1}^n \log(1 - bx_j) \quad [7.32]$$

$$\hat{\sigma} = \hat{\xi} / b \quad [7.33]$$

Zhang (2007) shows that the solution to 7.30 is simple to obtain since the function

$$g(b) = \frac{1}{n} \sum_{j=1}^n (1 - bx_j)^p - \frac{1}{1-r} \quad [7.34]$$

is a smooth monotone function of b with a unique solution in $(-\infty, 1/x_{(n)})$, unless $r = 0$ or $x_1 = x_2 = \dots = x_n$. He also provides a Newton-Raphson algorithm for computing the root of $g(b)$ which usually converges within 4-6 iterations to a margin of relative error less than 10^{-6} .

Zhang (2007) also shows that if the parameter r is close to the true value of ζ then the LM estimators will approximately equal the ML estimators. Results were presented for several fixed values $r = -2, -0.5$ and 0.25 , but no results were presented for the case that r is estimated from the data. Instead the following question was proposed: Given an initial estimate for ζ , it can be used as the value of r in 7.30 and used to obtain a new estimate. If this procedure is iterated and each step uses the new estimate of ζ as r , then will the LM estimates converge to the ML estimates when they exist?

This hypothesis was tested, using the hybrid-PWM estimate of ζ as the initial guess for r and iterating until $\hat{\xi}$ converges to r or $\hat{\xi} > 1$ (at which point the algorithm fails, but this happens very rarely). It was found that the iterated LM estimates did not converge to the ML estimates and that the performance was not significantly better than the ordinary LM estimates with the hybrid-PWM estimate of ζ as the initial guess for r . An investigation was also made of the performance of the LM estimator using the hybrid-MOM estimate of ζ as the initial guess for r . The performance was very similar but with marginally larger RMS error in small samples. In the following the LM estimate will refer to the non-iterated version using the hybrid-PWM estimate of ζ as the initial guess for r .

7.4.1.5 The Empirical Percentile Method

Castillo and Hadi (1997) proposed an estimator found by equating the empirical and theoretical distribution functions:

$$F(x_{(i)}) = p_i \quad [7.35]$$

They recommend using $p_i = i/(n+1)$ as the plotting position. Then substituting 7.1 in 7.35 and taking the logarithm they obtain

$$\ln(1 - x_{(i)} / \delta) = -\xi \ln(1 - p_i) \quad [7.36]$$

where $\delta = -\sigma / \xi$. Equating pairs of these equations and solving for ξ gives

$$\ln(1 - p_j) \ln(1 - x_{(i)} / \delta) = \ln(1 - p_i) \ln(1 - x_{(j)} / \delta) \quad [7.37]$$

They show that this equation has a unique solution $\hat{\delta}$ from which $\hat{\xi}$ can be estimated using equation 7.36 and $\hat{\sigma} = -\hat{\delta}\hat{\xi}$. They also provide an algorithm for solving 7.37. When $i = n/2$ and $j = n/4$ the estimators of Pickands (1975) are obtained. Castillo and Hadi (1997) recommend fixing $j = n$ and calculating $\hat{\delta}$ for $i = 1, \dots, n-1$. The empirical percentile method (EPM) estimators are then obtained as the median value of all estimates. The EPM estimators always exist and are always feasible but they can be computationally intensive for larger samples.

7.4.1.6 Maximum goodness of fit

Luceno (2006) proposed estimators based on maximising various “goodness of fit” statistics and called the resulting estimators maximum goodness of fit (MGF) estimators. These goodness of fit statistics essentially quantify how well the fitted distribution function matches the empirical distribution function. Various goodness of fit statistics were examined, but the ones which performed the best were the Cramer-von Mises statistic (CM), the Anderson-Darling statistic (AD) and the right-tail weighted Anderson-Darling statistic (ADR). These are given by

$$\text{CM:} \quad W^2 = n \sum_{i=1}^n [F(x_i) - p_i]^2 \quad [7.38]$$

$$\text{AD:} \quad A^2 = n \sum_{i=1}^n \frac{[F(x_i) - p_i]^2}{F(x_i)[1 - F(x_i)]} \quad [7.39]$$

$$\text{ADR:} \quad R^2 = n \sum_{i=1}^n \frac{[F(x_i) - p_i]^2}{1 - F(x_i)} \quad [7.40]$$

Luceno (2006) recommends the use of $p_i = (i - 0.5)/n$. The MGF estimators of σ and ζ are found by substituting 7.1 in the above equations minimising these equations using numerical methods. These estimators effectively give the best fit in the probability plots.

7.4.1.7 Least Squares

In a similar manner to the MGF method, estimators can be found which give the best fit in terms of quantile plots, i.e. by minimising

$$\sum_{i=1}^n [x_i - \hat{x}_i]^2 = \sum_{i=1}^n \left[x_i - \frac{\sigma}{\zeta} [(1 - p_i)^{-\zeta} - 1] \right]^2 \quad [7.41]$$

This method was first proposed Moharram et al (1993), who recommend using $p_i = (i - 0.4)/(n + 0.2)$. Moharram et al (1993) used the method to estimate the threshold as well as the GPD scale and shape parameters and noted that their algorithm sometimes had convergence problems. No such problems have been encountered in this case, when the threshold is chosen before the parameters are estimated.

7.4.2 Simulation study

The performance of the estimators detailed above has been compared in a simulation study. Since the results are invariant to the value of σ , we have arbitrarily chosen $\sigma = 1$. Trials have been made with $n = 25, 50, 100, 200$ and 500 and $\zeta = -0.5, -0.45, \dots, 0.45, 0.5$. For each value of n and ζ , 10,000 samples were generated and the estimators of σ and ζ were calculated using each method, and the bias and RMS error of quantiles at

probabilities of 0.99 and 0.999 were recorded. Quantiles of the GPD are given by rearranging equation 7.1:

$$x(F) = \begin{cases} \frac{\sigma}{\xi} [(1-F)^{-\xi} - 1] & \text{for } \xi \neq 0 \\ -\sigma \log(1-F) & \text{for } \xi = 0 \end{cases} \quad [7.42]$$

Hosking and Wallis (1987) gave a formula for the variance of quantile estimates in terms of the variance and covariance of $\hat{\sigma}$ and $\hat{\xi}$. However, results will be presented here in terms of the quantile estimates rather than the parameter estimates, since most often we are interested the accuracy of the predicted extreme values rather than the parameters of the distribution. Moreover, the methods which performed best in terms of the accuracy of quantile estimates were also those which performed best in terms of the parameter estimates.

The EPM, MGF and LS estimates did not perform as well as the others on the whole, although for $n = 500$ there was very little difference between any of the methods. Therefore, to avoid over-cluttering, results are presented only for the other methods.

The bias and RMS error for the ML, LM, hybrid-MOM and hybrid-PWM are shown in Figures 7.6 - 7.10. The RMS error is used in preference to the standard deviation as it gives a better idea of the absolute accuracy. (Note that $\text{RMS}^2 = \text{bias}^2 + \text{std}^2$). The bias is presented as well to differentiate between methods with roughly equal RMS errors. Both the bias and RMS errors shown in these figures have been divided by the values of the quantiles to give relative figures, e.g. the bias shown is given by $\text{mean}(\hat{x} - x) / x$.

The values shown for the ML estimates for $n = 25$ and 50 are for those samples where the solutions exist. This may introduce a slight bias since the samples where no ML solution existed corresponded to samples where other methods gave large negative values of $\hat{\xi}$, often less than -0.5 . The effect for $n = 50$ will be quite small but may be more significant for $n = 25$ and $\xi < 0$.

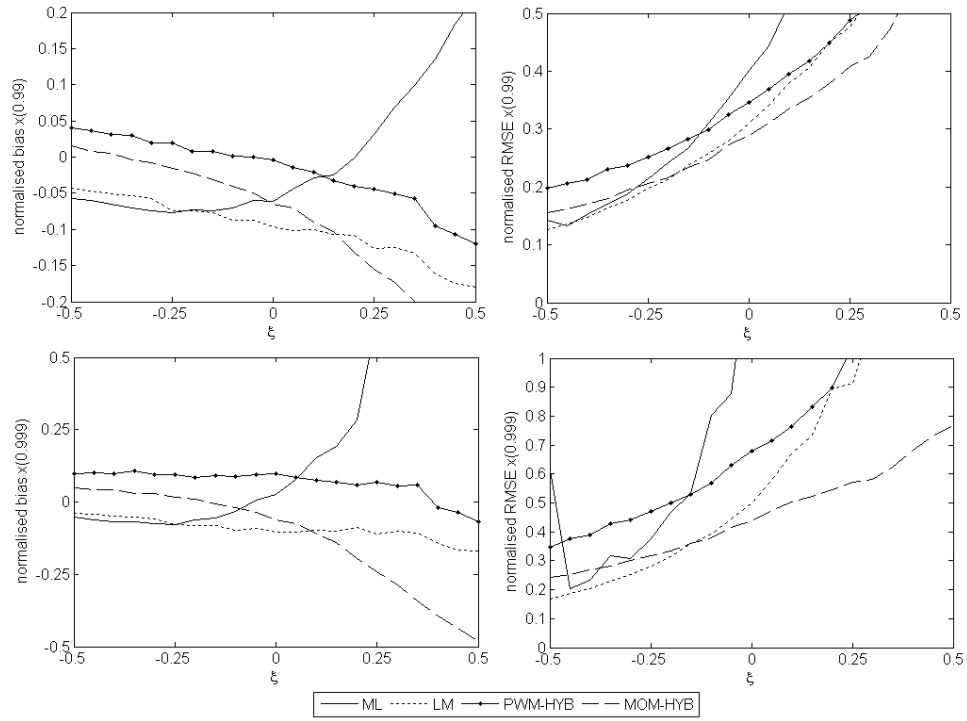


Figure 7.6. Normalised bias and RMS error in quantile estimates at probabilities of 0.99 (top) and 0.999 (bottom) for $n = 25$.

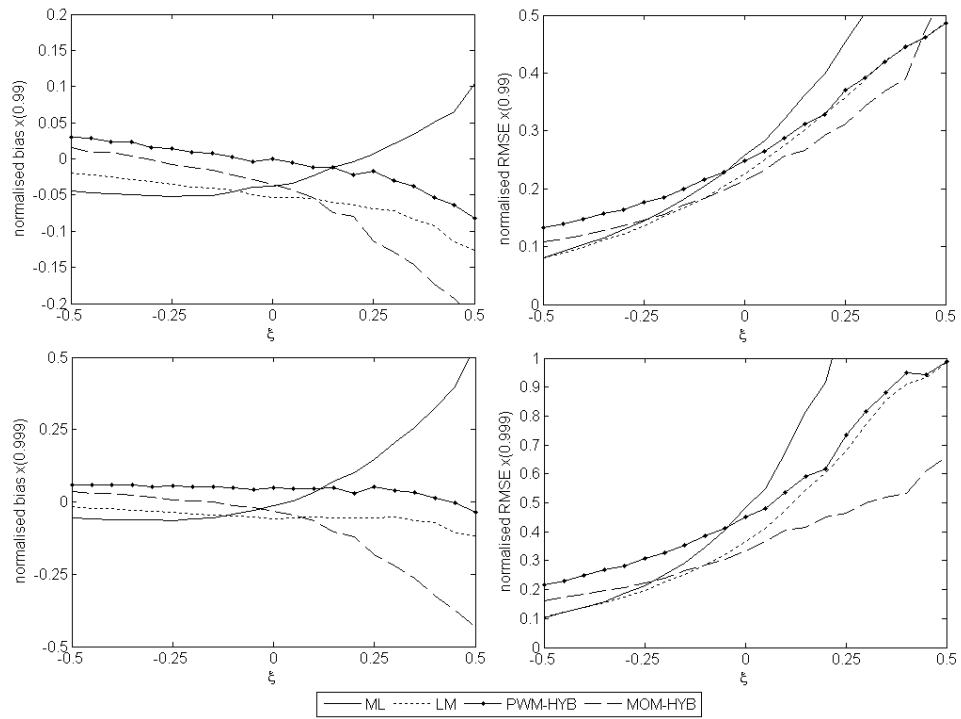


Figure 7.7. As previous figure, but for $n = 50$.

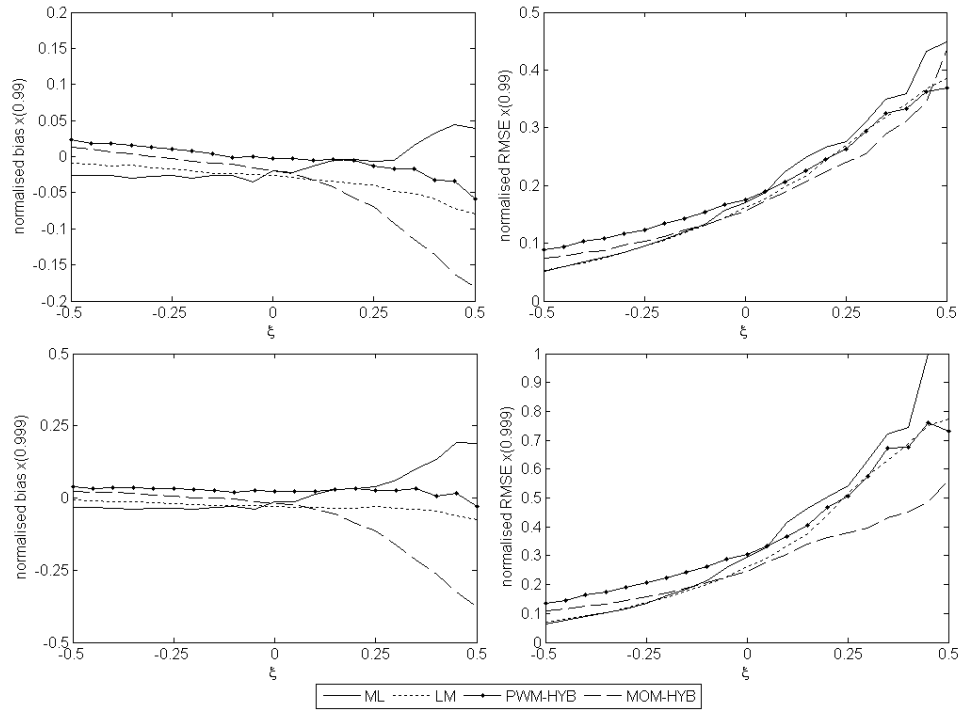


Figure 7.8. As previous figure, but for $n = 100$.

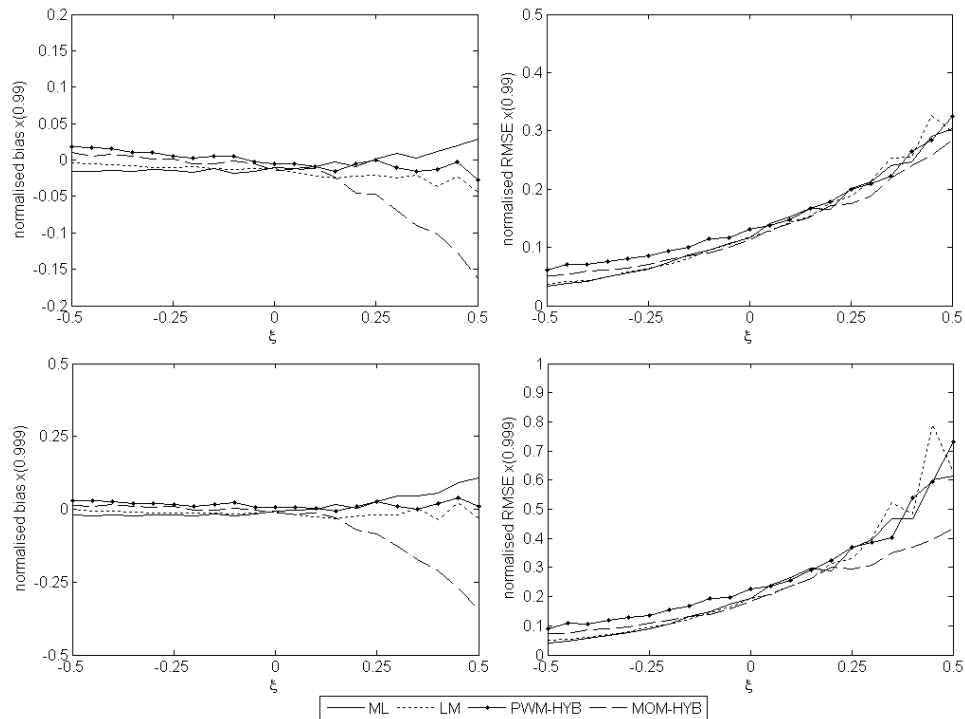


Figure 7.9. As previous figure, but for $n = 200$.

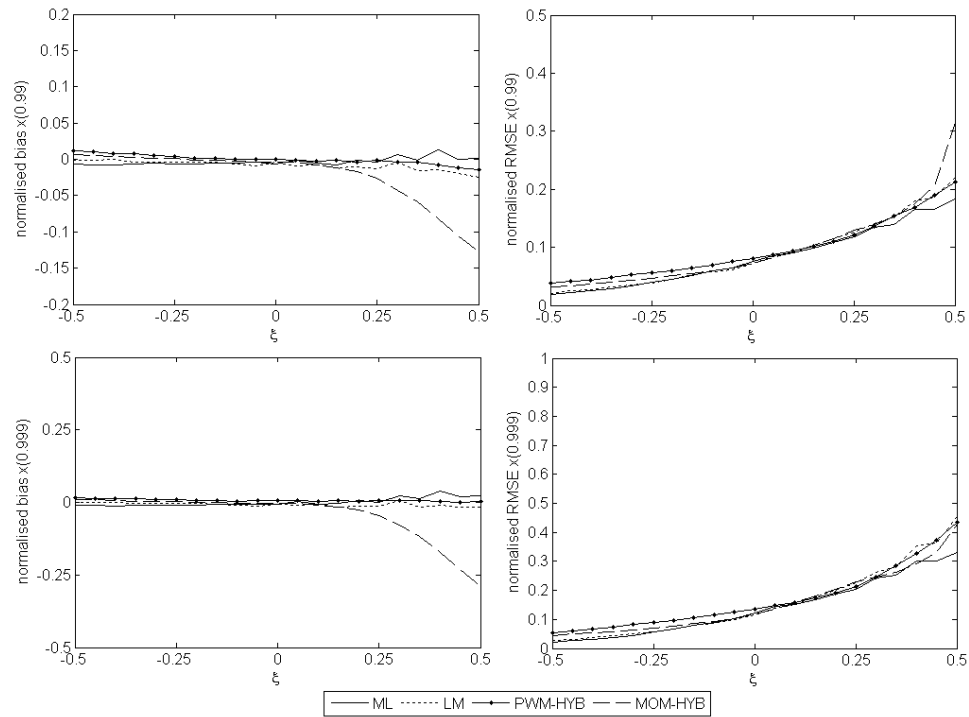


Figure 7.10. As previous figure, but for $n = 500$.

From the above figures it is clear that there is no one method which stands out as being the best in all situations. However it is clear that the ML estimates have a larger RMS error than other methods for $\xi > 0$ and sample sizes ≤ 100 . Moreover, when $\xi < 0$ there are samples where no ML solution exists. It is therefore recommended that ML is not used for sample size when $n \leq 100$.

Of the other methods the hybrid-moment (HM) estimator consistently has one of the lowest RMS errors for $\xi > 0$ and $n = 25, 50$ and 100 . However, for $n = 200$ and 500 a negative bias remains for $\xi > 0$, when it almost vanishes for the other estimators. This bias in the HM estimator for $\xi > 0$, is caused by the fact that $\hat{\xi}_{HM}$ is always less than 0.5 . This can be seen by noting that $\bar{x}^2 / s^2 > 0$ in equation 7.26 (see also Figure 7.11). The LM and hybrid-PWM estimators perform similarly in terms of RMS error for $\xi > 0$, but the LM method has slightly lower RMS for $\xi < 0$. The LM estimator also has the advantage that it is not as sensitive to threshold as the hybrid-PWM estimator (see Figure 7.16 for an example of this).

The results presented here differ from those of Zhang (2007), since he used a fixed value of r in his algorithm, whereas $r = \hat{\xi}_{PWM-Hyb}$ has been used here. This has given better overall results than those reported by Zhang (2007). The results also differ from the simulation study of Hosking and Wallis (1987) in that we have considered the always-feasible hybrid estimators of Dupuis and Tsao (1998).

In summary,

- The LM estimator has close to the lowest bias throughout.
- The LM estimator has close to the lowest RMS error when $\xi < 0$
- The HM estimator has the lowest RMS error when $\xi > 0$ and $n < 500$, but...
- The HM estimator has a large bias when $\xi > 0$

Figure 7.11 shows scatter plots of HM and LM estimators of ξ for various ξ and n . 1000 samples were generated for each plot. It can be seen that unless both estimates are very close to zero, the two methods always give the same sign for estimates of ξ . This would enable us to choose the estimator which has the lowest RMS error. A new estimator, which we will call the hybrid-likelihood-moment (HLM) estimator, can then be defined as follows:

$$\hat{\xi}_{HLM} = \begin{cases} \hat{\xi}_{LM} & \text{if } \hat{\xi}_{LM} + \hat{\xi}_{HM} \leq 0 \\ \hat{\xi}_{HM} & \text{if } \hat{\xi}_{LM} + \hat{\xi}_{HM} > 0 \end{cases} \quad [7.43]$$

The performance of the HLM estimator was tested and it was found that the bias and RMS error does indeed match those of the HM and LM estimators for ξ positive and negative respectively. However, despite the slightly lower RMS error for high quantiles when $\xi > 0$ and $n < 500$, we opt to use the LM estimator over the HM and HLM estimators in all situations, since it is felt that improvement in RMS error does not outweigh the increase in bias. For $n \geq 500$ the LM estimator has approximately the same bias and RMS error as the ML estimate but is much faster to compute.

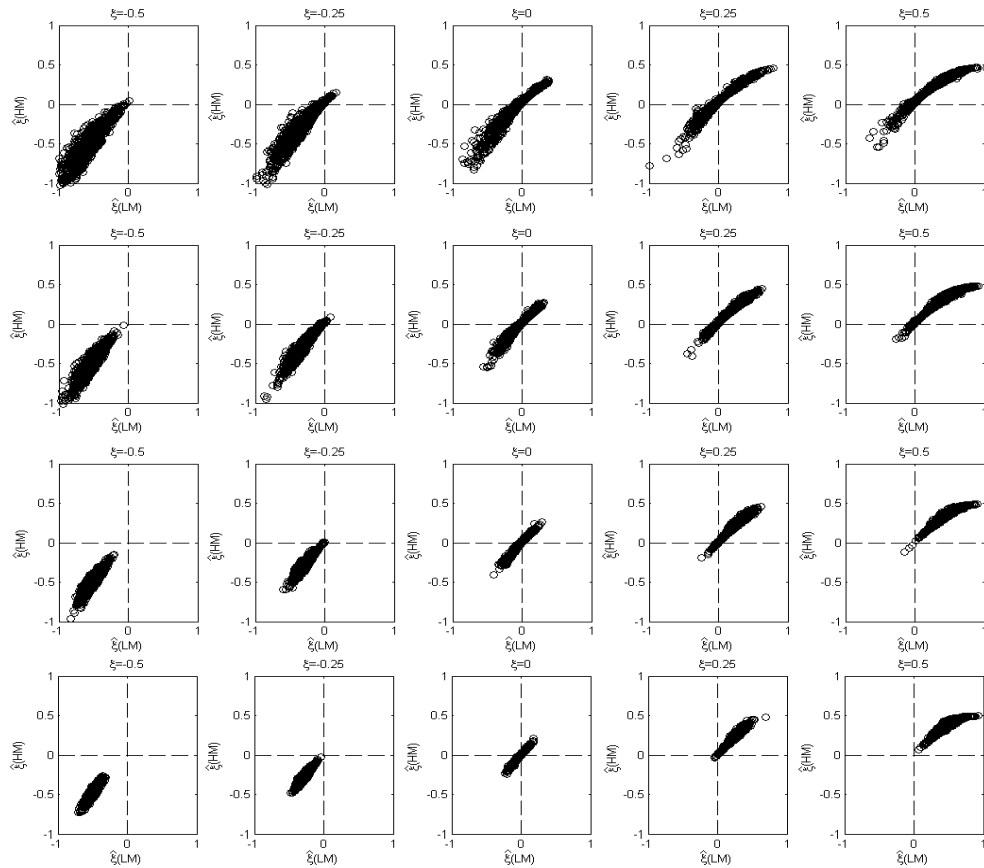


Figure 7.11. Scatter plots of HM estimators against LM estimators for various values of ξ (increasing left to right) and $n = 25$ (top row), 50 (second row), 100 (third row) and 200 (bottom row).

Two points should be noted here. The first is that we have examined the performance of estimators *given* that the data is GPD. This does not answer the question of the best estimator for extremes of *real* data. However, in Section 7.6 it is shown that the GPD is a good fit for extremes of buoy data, so these results should carry over reasonably well. The second point to note is that the results presented above are the bias and RMS errors of quantile estimates for a known ζ . This is not the same as the bias and variance given $\hat{\zeta}$. It is this latter figure which is needed to estimate confidence. Confidence bounds for the estimated parameters and quantiles can be estimated using a bootstrap method, as discussed in Section 7.6.

In conclusion, the following new results have been obtained on estimators for the GPD:

1. A sufficient condition for the existence of ML estimates has been presented.

2. The sensitivity of the PWM and PWM-hybrid estimators to the threshold value was pointed out.
3. New results for the performance of the LM estimator have been presented which use the PWM-hybrid estimate as a first guess. This estimator arguably performed the best of those tested.
4. It was found that the iterated LM estimate does not converge to the ML estimate.

7.5 Seasonality, directionality and other covariates

So far we have not considered that the intensity of storms can depend on other variables, known as covariates, such as the time of year, direction of origin of the storm, or climatic variables such as the NAO. This means that the data cannot be considered as identically distributed, which is an assumption in the POT model. In the case of seasonality or directionality if the most severe storms occur in one season or come from one direction then a threshold could be set such that all the peaks could be considered as coming from the same season or direction. If the highest storm peaks cannot all be considered as coming from the same distribution then it is necessary either to use a model which takes into account the non-stationary effects, or to examine the effect of non-stationarity on the stationary model.

Consider storm parameters which vary throughout the year. A storm peak H_s of 5m may occur with lower probability in summer than in winter (see e.g. Figure 7.14). Using a model where the distribution parameters vary with season can capture this difference in probability through the year. However, it does not immediately follow from this that using models which ignore seasonality (or other covariate effects) will give a less accurate estimate of extremes.

Carter and Challenor (1981) consider estimation of return values from a population composed of a number of distinct homogeneous sub-populations. They prove that when the distribution in each sub-population is known, the return values calculated from a random sampling of the entire population are less than or equal to those obtained when the sub-populations are sampled proportionally, with equality only when the

distributions in each sub-population are equal. This argument has often been used to support the use of covariate models. However, in practice the distribution of each sub-population is not known and must be estimated from the data. Moreover, over a long enough period, sampling from each sub-population will be approximately proportional.

Morton et al (1997) have analysed data from the North Sea both as a whole and split into four separate seasons over which the data is considered reasonably stationary. They suggest that the seasonal model is potentially more accurate but note that they do not have an objective method to compare the accuracy. Splitting the data into seasons results in fewer points in the estimation of distribution parameters for each season and therefore increases uncertainty. It will be shown in Section 7.6.5 that this makes seasonal models less accurate than non-seasonal models.

The alternative is to assume that the distribution parameters vary smoothly with season or direction and to use a Fourier expansion to describe the variation (see e.g. Anderson et al, 2001; Jonathan and Ewans, 2007; Jonathan and Ewans, 2008). For low order expansions this generally involves estimating fewer parameters than when the data is partitioned into seasons and analysed separately. Increasing the order of the Fourier expansion will give a better fit, but will risk ‘over modelling’ the data. Coles (2001) notes that the basic principle in model choice is parsimony: obtaining the simplest model possible which explains as much of the variation in the data as possible. In the case that a simple model is a subclass of the more complex model, the deviance statistic (defined as twice the difference of the maximised log-likelihoods under each model) can be used to choose between models (see e.g. Coles, 2001; Anderson et al, 2001; Jonathon et al, 2008).

Threshold selection is problematic when estimating the variation of parameters using a Fourier expansion. When the data are split into separate seasons or directional sectors the techniques described in section 7.3.3 can be used to select an appropriate threshold for each season or directional sector. However, when the parameters are modelled as varying smoothly throughout the year, examining choice of threshold is more difficult. As far as the author is aware, no objective method for selecting a threshold for this type of model has been proposed. Anderson et al (2001) chose arbitrarily to set the threshold as the 90th percentile of the data for each month. Jonathan and Ewans (2008) use a

variable threshold, estimated for each day of the year as the 50th or 80th percentile of the nearest 300 storm peaks (in terms of season). However, they note that the effect of the choice of threshold appears more influential than incorporation of seasonally varying extreme value parameters. Moreover, there is no *a priori* reason to assume that the threshold for which the GP distribution can be considered a reasonable fit will correspond to the same percentile of the data or storm peaks in each season. The lack of an objective method for selecting a threshold is a serious limitation of this method.

Another approach to modelling the seasonality of extreme sea states has been taken by Stefanakos and Athanassoulis (2006). They assume that the time series of H_s admits the representation

$$H_s(t) = \mu(t) + \sigma(t)W(t) \quad [7.44]$$

where $\mu(t)$ and $\sigma(t)$ are deterministic time-dependent periodic functions representing the seasonal mean and standard deviation of the process, and $W(t)$ is a zero-mean stationary stochastic process, referred to as the residual stochastic process. They then show that extremal properties of the process $H_s(t)$ can be calculated from extremal properties of $W(t)$. Athanassoulis and Stefanakos (1995) have shown that the mean, standard deviation and frequency spectrum of the process $W(t)$ can indeed be considered stationary. However, further information on the extremal properties of $W(t)$ and on the sensitivity of the results to the fit of the time series model is required before this method can be considered as rigorous as other extreme value models.

Reports of the performance of analyses which model directionality or seasonality have been mixed. Morton et al (1997), Anderson et al (2001), and Jonathan and Ewans (2007) all report higher return values from non-stationary models, whereas Stefanakos and Athanassoulis (2006) report lower return values. Jonathan et al (2008) have presented simulation studies where data comes from two separate distributions, representing storms from two directions (but which could equally be interpreted as storms from different seasons). They demonstrate that under these circumstances the non-directional models under-estimate return values. However, in the present authors' opinion the examples presented in their study are rather artificial and do not answer the

question of whether it is better to use non-stationary models in real situations. In Section 7.6.5 we will construct more realistic simulation studies based on buoy data in an attempt to answer this question.

First we need to show how annual return values are calculated from separate seasonal distributions or equivalently how omni-directional return values can be calculated from separate directional distributions. For the simplicity, we will only refer to seasonal analyses from here on.

Suppose that the year can be split into k seasons, not necessarily the same length, over which the distribution of the data can be considered stationary. Let Y_i denote a storm maxima in season in i and Y denote a storm maxima at any point throughout the year, ignoring season. Let $F_i(x) = \Pr\{Y_i < x \mid Y_i > u_i\}$ be the conditional distribution of exceedances in season i , described by a GP distribution with parameters ξ_i and σ_i , with threshold u_i . For simplicity, it is assumed in the following that $\xi_i \neq 0$. In the case that $\xi_i = 0$ for some i , then the CDF should be replaced with the appropriate form from equation 7.1.

The derivation of the ‘annual’ return value parallels that given in Section 7.3.2 and therefore requires an estimate of the ‘annual’ distribution function, i.e. the distribution of all points within a year, ignoring the season. The models for each season are likely to be fitted using different thresholds, so the annual distribution function can only be defined for $Y > u_{\max}$ where $u_{\max} = \max(u_i : i = 1, \dots, k)$. The distribution function for each season, conditional on exceeding u_{\max} , is also generalised Pareto, with the same shape parameter, and scale parameter given by equation 7.9:

$$\Pr\{Y_i < x \mid Y_i > u_{\max}\} = 1 - \left[1 + \xi_i(x - u_{\max}) / \tilde{\sigma}_i\right]^{-1/\xi_i} \quad [7.45]$$

where

$$\tilde{\sigma}_i = \sigma_i + \xi_i(u_{\max} - u_i) \quad [7.46]$$

In the case that $u_{\max} > u_i - \sigma_i / \xi_i$ for some i then, strictly speaking, equation 7.45 does not make sense since $\Pr\{Y_i > u_{\max}\} = 0$. However, inconsistency can be avoided by using only the positive part of the term in the square brackets.

The probability that u_{\max} is exceeded in each season is given by

$$\begin{aligned}\Pr\{Y_i > u_{\max}\} &= \Pr\{Y_i > u_i\} \Pr\{Y_i > u_{\max} \mid Y_i > u_i\} \\ &= \zeta_{u_i} (1 - F_i(u_{\max}))\end{aligned}\quad [7.47]$$

where $\zeta_{u_i} = \Pr\{Y_i > u_i\}$.

To form the annual distribution we must assume that storms in each season are independent. The annual distribution is then given as the weighted average of the distributions from each season, where the weights reflect the probability that a point within the year, which exceeds u_{\max} , comes from season i . The expected number of points exceeding u_{\max} in each season is given by

$$r_i = m_i \Pr\{Y_i > u_{\max}\} = m_i \zeta_{u_i} (1 - F_i(u_{\max}))\quad [7.48]$$

where m_i is the total number of samples each season. Weights for each season are then given by the expected number of points exceeding u_{\max} from each season divided by the expected number of points exceeding u_{\max} each year:

$$w_i = r_i / r\quad [7.49]$$

where $r = \sum_{i=1}^k r_i$. The annual CDF, conditional on exceeding u_{\max} , is then given by the weighted sum of the distribution functions for each season

$$\begin{aligned}\Pr\{Y < x \mid Y > u_{\max}\} &= \sum_{i=1}^k w_i \Pr\{Y_i < x \mid Y_i > u_{\max}\} \\ &= 1 - \sum_{i=1}^k w_i \left(1 + \xi_i (x - u_{\max}) / \tilde{\sigma}_i\right)^{-1/\xi_i}\end{aligned}\quad [7.50]$$

The probability that any point in the year exceeds u_{\max} is given by the expected number of points exceeding u_{\max} each year, divided by the total number of points in a year:

$$\Pr\{Y > u_{\max}\} = r/m \quad [7.51]$$

where $m = \sum_{i=1}^k m_i$. Finally, for $x > u_{\max}$, by equations 7.50 and 7.51 we have that

$$\begin{aligned} \Pr\{Y > x\} &= \Pr\{Y > u_{\max}\} (1 - \Pr\{Y < x \mid Y > u_{\max}\}) \\ &= \frac{r}{m} \sum_{i=1}^k w_i (1 + \xi_i (x - u_{\max}) / \tilde{\sigma}_i)^{-1/\xi_i} \end{aligned} \quad [7.52]$$

For mixed GPD models the N -year return value, x_N , is given by solving

$$\frac{1}{Nm} = \Pr\{Y > x_N\} \quad [7.53]$$

or equivalently

$$\frac{1}{Nr} = \sum_{i=1}^k w_i (1 + \xi_i (x_N - u_{\max}) / \tilde{\sigma}_i)^{-1/\xi_i} \quad [7.54]$$

This reduces to equation 7.8 in the case $k = 1$. The validity of equation 7.54 has been verified by simulation in a wide range of cases, described below.

7.6 Examples using buoy data

7.6.1 Buoy data

To illustrate the points discussed so far in this chapter we will use data from several NDBC buoys on the west coast of the USA. The locations of these buoys are shown in Figure 7.12 and information about the buoy types, locations and coverage are given in Table 7.1. The buoys selected for use here are those for which the record length exceeds 20 years. Also the west coast of the USA is an area with an energetic wave climate, suitable for wave energy farms, and which is not affected by tropical cyclones. This

second point is important since the storms generated by tropical cyclones cannot be considered as coming from the same population as those from extratropical cyclones. Tropical cyclones are much smaller than extratropical storms, so a 20 or 30 year record for one location may only contain one or two tropical cyclone events. Moreover, these events are typically much more intense than those from extratropical cyclones. It is therefore necessary to analyse these two populations separately. Methods for estimating the distribution of extremes from tropical cyclones are discussed by Hardy et al (2003) and Jonathan and Ewans (2006).

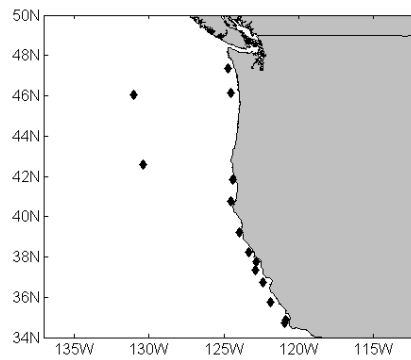


Figure 7.12. Locations of the 14 buoys used in this section.

Buoy number	Lat. (N)	Lon. (W)	Data period	Water depth (m)	Buoy size (m)	Buoy shape
46002	42.60	130.27	1978-2008	3374	6	Nomad
46005	46.05	131.02	1978-2008	2780	6	Nomad
46011	34.87	120.86	1980-2008	204	3	Discus
46012	37.36	122.88	1980-2008	88	3	Discus
46013	38.23	123.32	1981-2008	123	3	Discus
46014	39.20	123.97	1981-2008	274	3	Discus
46022	40.78	124.54	1982-2008	509	3	Discus
46023	34.71	120.97	1982-2008	384	10	Discus
46026	37.76	122.83	1982-2008	52	3	Discus
46027	41.85	124.38	1983-2008	48	3	Discus
46028	35.74	121.89	1983-2008	1112	3	Discus
46029	46.14	124.51	1984-2008	128	3	Discus
46041	47.35	124.73	1987-2008	132	3	Discus
46042	36.75	122.42	1987-2008	2115	3	Discus

Table 7.1. Details of the NDBC buoys used in this section.

One-dimensional spectra have been retrieved from the U.S. National Oceanic Data Centre. The data has already had some quality control applied, as detailed in National Data Buoy Center (1996, 2003). However, a number of clear outliers remained for some

buoy records. These were confirmed by inspection of the individual spectra and removed from the datasets.

The data has been interpolated for gaps less than 3 hours and then smoothed using a 3 hour moving average filter. Smoothing measured data in this way is recommended by Forristall et al (1996). They show that if shorter samples are used then the sampling variability in the measurements will cause the peak H_s in a storm to be biased high.

7.6.2. Declustering

As mentioned in Section 7.2, an important assumption of the POT model is that the peaks to which the GPD is fitted are independent. Wave measurements exhibit strong serial correlation so cannot be considered independent. This problem is circumvented by only considering the peak value of H_s in each storm. It is then assumed that these peak values are independent. The problem is then reduced to identifying which events can be considered as separate and independent storms.

The notion of a storm has a direct physical interpretation: a peak in the time history of H_s at a particular location is associated with winds generated by a weather system. In practice winds may vary as the weather system evolves, causing several peaks over a number of days. If synoptic pressure charts were available it may be relatively easy to see that several consecutive peaks in a record were the result of a single storm, but this may not be so clear from the time history of H_s alone. From a physical point of view, a pressure system which causes a large peak in the H_s record will generally be large in extent and persist for a number of days. It is therefore unlikely that peaks close to each other come from separate storms. Moreover, if two separate storms occur in close proximity then it may not be realistic to assume that their characteristics are independent.

This leads to some authors defining a minimum separation in time between peaks. Tawn (1988) uses a separation of 30 hours between storms in the southern North Sea, whereas Anderson et al (2001) use an interval of 24 hours for a location in the northern North Sea. Another approach is to examine the autocorrelation function of the H_s time series and to select an interval for which the correlation drops below some prescribed value (Guedes Soares and Scotto, 2004).

A slightly different approach is proposed by Soukissian et al (2006). They suggest picking out local maxima and minima and only keeping those for which the change in ‘energy’ between maxima and minima exceeds a certain fraction of the storm peak ‘energy’, where the energy is proportional to H_s^2 .

Both approaches will be investigated here. In contrast to Soukissian et al (2006) we will use a criteria based on the change in H_s rather than H_s^2 . In Section 2.1.4 it was shown that for the EMEC buoy data the standard deviation in H_s between two points separated by time τ is a roughly linear function of H_s , for short-term timescales. Repeating this analysis using the NDBC buoy data, with much longer records, shows that for higher H_s the increase in the standard deviation is slightly non-linear. However, the relationship is much closer to a linear function of H_s than to a function of H_s^2 . It should be noted though that the correlation structure of the time series will change throughout the year. For example, in summer the mean and standard deviation of H_s is lower than in winter, therefore the distribution of H_s at time $t + \tau$, conditional on H_s at time t , will differ in summer and winter. However, tests using data for winter months only still exhibit the linear relationship.

We use the following procedure to identify storm peaks: First, identify all points which are maxima within $\pm\tau$ days, and the minima between each maxima, then starting at first maxima in the series:

1. Check if preceding minima is less than fraction p of the maxima.
If not then discard maxima and the higher of the preceding and following minima.
2. If so, check if following minima is less than fraction p of the maxima.
If not then discard the minima and the lower of the current and following maxima.
3. Move on to next maxima.

This procedure essentially picks out all peaks separated by time τ to nearest maxima, and for which the preceding and following minima are less than fraction p of the maxima.

Testing the independence of storms peaks is complicated by the temporal variation of their distribution. Seasonal variability causes a periodic correlation in peak wave heights and any climatic variability will also result in a small, but potentially significant, correlation in peak wave heights. We propose to use the normalisation given by equation 7.44 to create an approximately stationary series and examine the correlation for different values of p and τ .

The normalisation is performed using the method of Athanassoulis and Stefanakos (1995). First, the mean and standard deviation are calculated for each day of the year, using a moving window of width 10 days. The functions $\mu(t)$ and $\sigma(t)$ are defined as low-order Fourier expansions of the daily mean and standard deviation respectively. The normalised series is defined to be

$$W(t) = \frac{H_s(t) - \mu(t)}{\sigma(t)} \quad [7.55]$$

The procedure is illustrated with an example using data from buoy 46002. Figure 7.13(a) shows 3-hour average H_s against day of the year, together with the daily mean and its Fourier expansion $\mu(t)$. Figure 7.13(b) shows the daily standard deviation and its Fourier expansion $\sigma(t)$. Second order Fourier expansions were found to be adequate for both the mean and standard deviation.

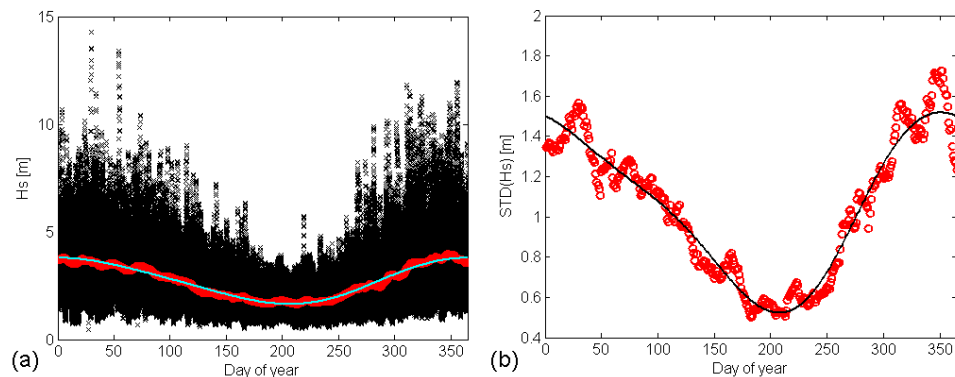


Figure 7.13. (a) 3-hour average H_s (black crosses), daily mean value (red circles), Fourier expansion of daily mean (cyan line). (b) Daily standard deviation in H_s (red circles), Fourier expansion of daily standard deviation (black line).

Figure 7.14(a) shows the storm peaks identified using the criteria $p = 0.75$ and $\tau = 1.5$ days. If we denote these peaks as X_1, \dots, X_n , occurring at times t_1, \dots, t_n , then we can define normalised storm peaks as

$$Y_i(t_i) = \frac{X_i(t_i) - \mu(t_i)}{\sigma(t_i)} \quad [7.55]$$

It should be emphasised that the data is declustered in its original form and the normalisation in 7.55 is applied afterwards. The normalised storm peaks are shown in Figure 7.14(b), their distribution appears to be reasonably stationary throughout the year. This is quite remarkable since the storm peaks have been normalised by the mean and standard deviation of all the data, and lends support to the approach of Stefanakos and Athanassoulis (2006). However, we are using this normalisation to investigate the correlation of the declustered data and further statistical tests are required to show that the normalised distribution can be considered stationary. But it should be noted that, from visual inspection, the normalisation appears satisfactory for all of the buoys considered here.

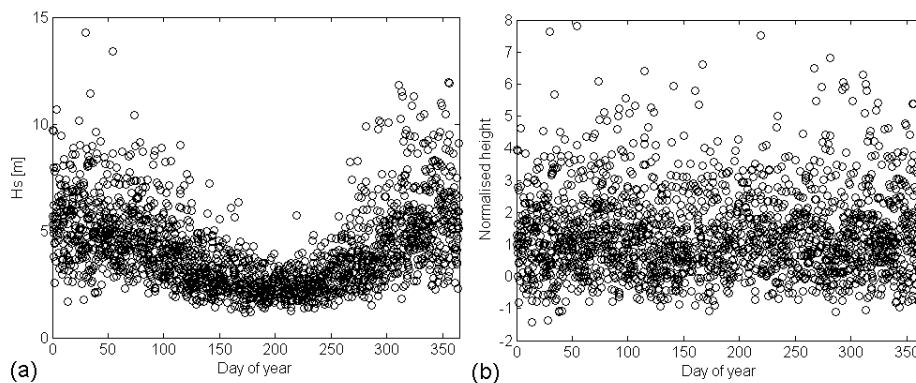


Figure 7.14. (a) Storm peaks identified using declustering criteria $p = 0.75$ and $\tau = 1.5$ days. (b) Normalised values of storm peaks from (a).

Since we are interested in the extremal properties of the distribution of storm peaks, we shall only examine the correlation of those which exceed a high threshold. A variable threshold is used, set as the second-order Fourier expansion of the 90th percentile of all the data, found in the same way as $\mu(t)$ and $\sigma(t)$. The 90th percentile of the data is roughly equal to the median value of the storm peaks, but using a threshold based on all

the data means that it can be chosen before the declustering and allows the same threshold to be used for each value of p and τ . This is not intended to be used as the threshold in the POT analysis. The median value of the distribution of storm peaks is likely to be about the minimum value at which a ‘high’ threshold could be set.

Data for each buoy has been declustered using values of p between 0.5 and 1 and τ between 0 and 5 days. After the declustering we discard any peaks which fall below the variable threshold. The correlation between subsequent peaks is then calculated. To smooth out sampling uncertainties, we take the average over the 14 buoys considered. This assumes that storm properties are the same at each location, and hence that the same declustering criteria will be optimal for each buoy record. This does not seem unreasonable considering that the buoys all experience storms from the same area of the Pacific Ocean. Figure 7.15(a) shows the average correlation for each value of p and τ . Note that the colour scale has been cropped to give contrast in the range of interest. The average correlation for $p = 0.95$ and $\tau = 0$ was 0.28. Figure 7.15 (b) shows the average number of peaks exceeding the threshold for each value of p and τ .

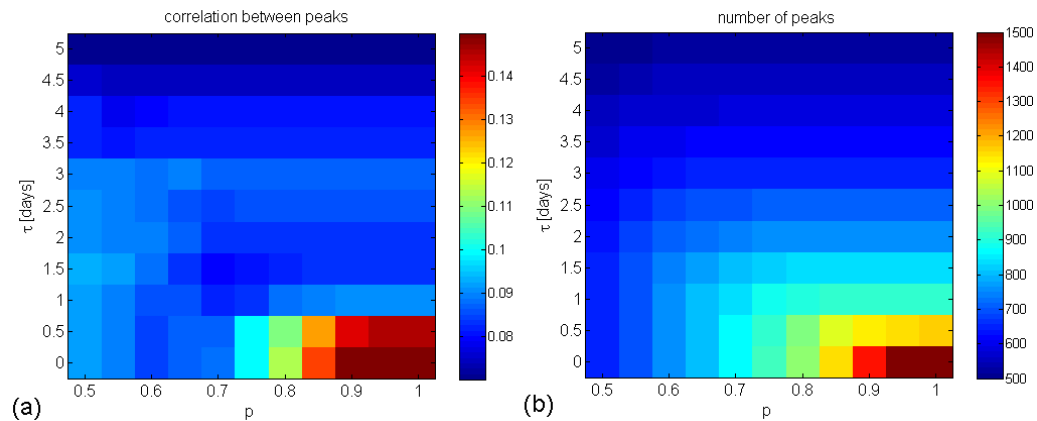


Figure 7.15. (a) Correlation between declustered peaks exceeding the variable threshold for various values of declustering criteria p and τ . (b) Average number of peaks for various values of declustering criteria p and τ .

It is evident that there is little reduction in the correlation for $p < 0.7$ or $\tau > 1.5$. From a visual inspection of time series of H_s it appears that making the declustering criteria stricter than this, removes peaks which appear to be separate storms. Conversely, making them less strict leaves peaks which appear to be from the same storm.

Moreover, using only either the p or τ criteria alone leaves peaks which appear to be from the same storm. It was found that using criteria of $p = 0.75$ and $\tau = 1.5$ provided a good compromise between achieving a low correlation and unnecessarily removing peaks from distinct storms which occur in close proximity. The highest peaks in each season will remain for any choice of declustering criteria, but ultimately the choice of which of the lower peaks to include is somewhat subjective. In the following sections criteria of $p = 0.75$ and $\tau = 1.5$ have been used to decluster the data.

7.6.3. Model fitting and checking

In Section 7.3.3 it was noted that if the GPD is a valid model for the data above a threshold then above this level, estimates of ξ , σ^* and return values should be constant, and the mean exceedance should be a linear function of the threshold u . So to select a threshold we estimate the parameters for a range of thresholds and choose the threshold as the lowest value for which we observe the desired behaviour. In practice sampling variability often makes it difficult to identify a valid threshold. It is therefore desirable that the estimator has a low sensitivity to the threshold used. In Section 7.4 it was mentioned that the PWM estimator is more sensitive to threshold choice than the LM estimator. This is illustrated in Figure 7.16 with data from buoy 46002. It is clear that the LM estimator is less sensitive to threshold than the PWM estimator. However, it is still not obvious from the plots if a valid threshold exists.

To aid the identification of a valid threshold, Naess and Clausen (2001) have suggested a smoothing the threshold plots using a moving average filter. This method does produce smoother plots, but doesn't provide any further information on the data. Moreover, estimates for higher thresholds will have greater uncertainty due to fewer data, and using a moving average does not take this into account.

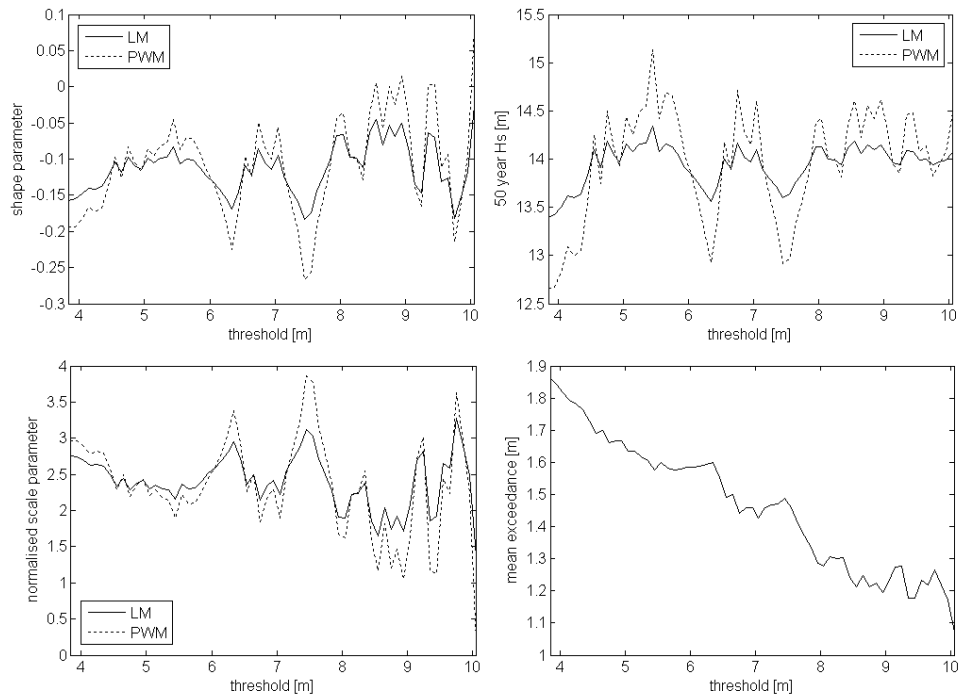


Figure 7.16. Threshold plots using the PWM and LM estimators, for annual data from buoy 46002.

We propose a modified bootstrap method to aid threshold selection which takes into account the uncertainty inherent in the data. When using a bootstrap technique it is assumed that the data represent a realisation of the underlying population. If it is further assumed that the data are independent and identically distributed then it follows that a random sample of the data, drawn with replacement, is an equally likely realisation of the same process. By resampling the data a large number of times we can estimate the effect of sampling variability on estimates of ζ , σ^* , return values and the mean exceedance. This can be used to add confidence bounds to the plots. The bootstrap is used by numerous authors in this context (e.g. Elsinghorst et al, 1998; Naess and Clausen, 2001; Jonathon and Ewans, 2007).

Resampling in this way does not smooth the threshold plots, since the mean bootstrap estimate will tend to the original non-bootstrapped estimate. Incorporating information about the uncertainty of each estimate of storm peak H_s can smooth the plots to a certain extent. The distribution of the estimate of maximum H_s in a storm has been discussed in detail by Forristall et al (1996). Suppose measurements are taken continuously. Since each estimate of H_s is subject to sampling variability the expected value of the

maximum estimate over the storm is greater than the true value of the maximum. The size of the overestimate depends on the spectral shape, storm length and averaging period. If the measurements are not taken continuously then the peak of the storm may be missed, reducing the bias in the estimated storm maximum. NDBC buoys report wave data at hourly intervals, based on measurements over 20 or 40 minutes. A moving three hour average is taken before declustering. Based on the results of Forristall et al (1996), we estimate that the coefficient of variation in the peak H_s is around 3%.

This information is incorporated into the bootstrap in the following way. For each bootstrap trial we draw a random sample $X_{(j,1)}, \dots, X_{(j,n)}$ from the original data X_1, \dots, X_n and generate n standard normal variables e_1, \dots, e_n . The bootstrap sample is defined to be $X_{(j,1)}(1+0.03e_1), \dots, X_{(j,n)}(1+0.03e_n)$. This is a natural extension of the bootstrap method, since samples generated in this way are an equally likely realisation of the underlying process. The fact that the data are not identically distributed can be dealt with by dividing the data into seasons, and resampling each season separately. The use of seasons of various length has been tested and it was found that two months is reasonable compromise between sample size and the distribution being reasonably stationary within each season.

The use of this modified bootstrap technique is illustrated in Figure 7.17. The mean bootstrap estimate is considerably smoother than the original non-bootstrapped estimates. Bootstrapping cannot rectify any inherent bias in the empirical distribution (i.e. differences between the shape of the sample distribution and the underlying population distribution), but uncertainty can be gauged through the confidence bounds.

From these plots the threshold has been selected as 6.2m. After this point the mean exceedance becomes approximately linear, with slope -0.11 and intercept 2.2. From equation 7.11 this is equivalent to $\hat{\xi} = -0.12$ and $\hat{\sigma}_{u_0} = 2.5$. The estimates of ξ , and σ^* display stability and from around 6.2m until around 7.5m, with values consistent with those from the mean excess plot. The variability displayed after this point is likely to be due to decreasing sample size. Despite the variability in $\hat{\xi}$ and $\hat{\sigma}^*$ above 7.5m the estimate of the 50 year return value of H_s is reasonably constant from 6.2m onwards.

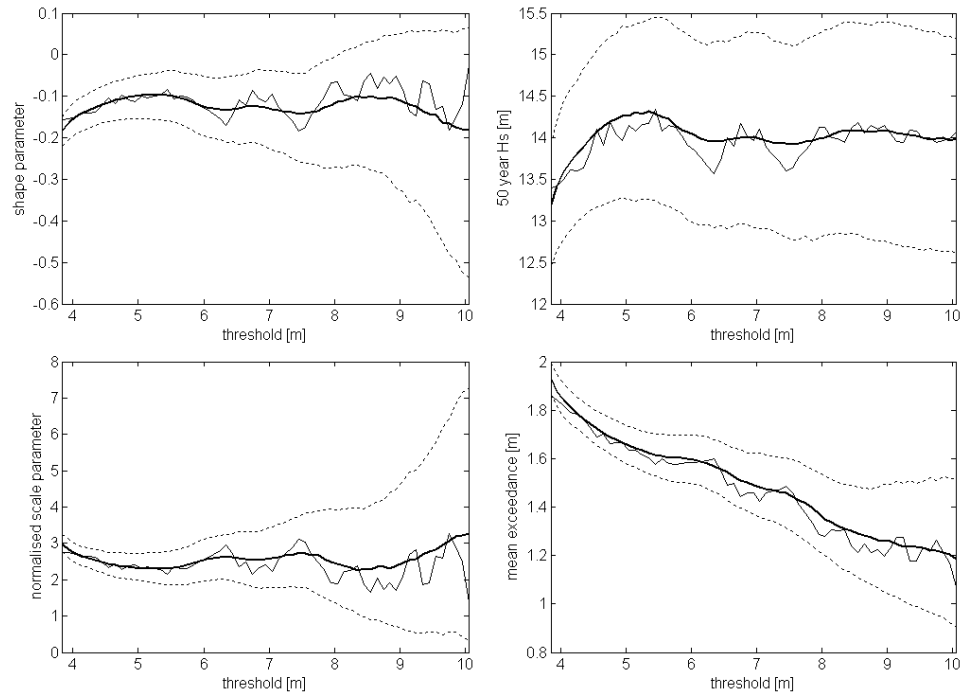


Figure 7.17. Threshold plots for data from buoy 46002. Thin solid line: estimates without resampling. Bold line: mean of modified bootstrap estimates. Dotted line: 95% confidence bounds from modified bootstrap trials.

Probability and quantile plots for the fitted model are shown in Figure 7.18. The quantile plot shows excellent agreement for all but the highest 3 points. The probability plot shows good agreement for the higher probability points, with some small deviations below a probability of 0.6. Overall it appears that the fit is good and that the GPD can be considered as a valid model for the data.

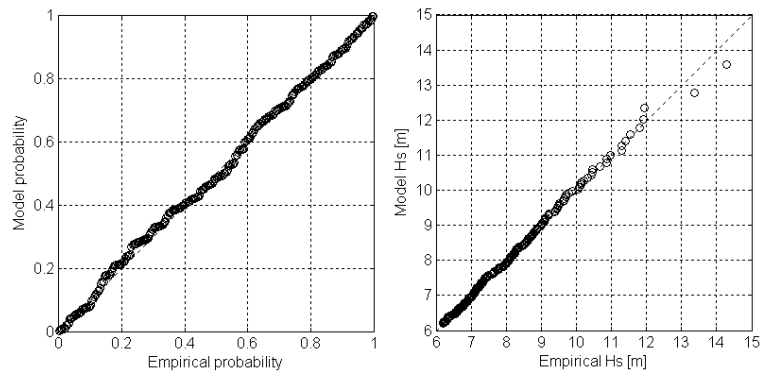


Figure 7.18. Diagnostic plots for model fitted using LM estimators with a threshold of 6.2m. Left: Probability plot; right: quantile plot.

7.6.4 Results

The method described in the previous section has been used to fit the GPD to data for each of the 14 buoys, both for the data considered as a whole and for separate seasons. Again, a season length of 2 months has been selected as a reasonable compromise between sample size and stationarity. Annual return values have been calculated from the seasonal parameters using equation 7.54. Estimated model parameters, 50 and 100 year return values of H_s and confidence bounds are presented in Appendix G.

The GPD was found to provide a good fit for both annual and seasonal data in most cases, although in some cases it was more difficult to identify a valid threshold for the seasonal data due to the smaller sample sizes. The 50 and 100 year return values from the seasonal analysis were generally close to those calculated from the non-seasonal analysis, but the confidence bounds for the return values from the seasonal analysis were wider in all cases. For buoys 46002 and 46042 the return values from the seasonal analysis were slightly lower to those from the non-seasonal analysis. For the other buoys the return values from the seasonal analysis were higher.

For buoy 46005 the 50 and 100 year return values from the seasonal analysis were 1.0 and 1.5m higher than those from the non-seasonal analysis. It appears that this was due to the fitted distribution in September-October. Figure 7.19 shows the distribution of storm peaks throughout the year. It is clear that the distribution cannot be considered stationary though September-October. The result is that the distribution appears heavier tailed, leading to a positive estimate of the shape parameter.

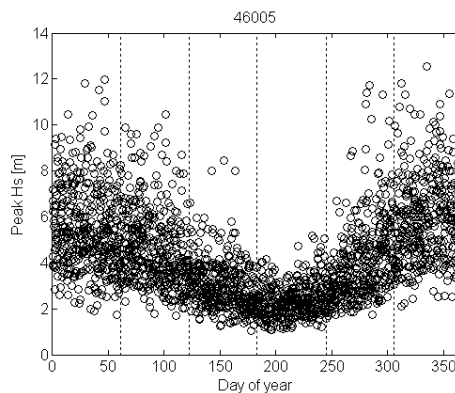


Figure 7.19. Storm peak H_s against day of year for buoy 46005. Dashed lines indicate seasonal boundaries.

Figure 7.20 shows threshold plots for September-October. From these plots a threshold of 4.5m was chosen, since the scale and shape parameters appear constant after this point, until about 6m. Also the mean exceedance plot changes at 4.5m and could be considered linear after this points if the confidence bounds are taken into account. The estimated 50 year return value only shows stability after 7.3m. However, above 6m the estimated shape and normalised scale parameters are not stable.

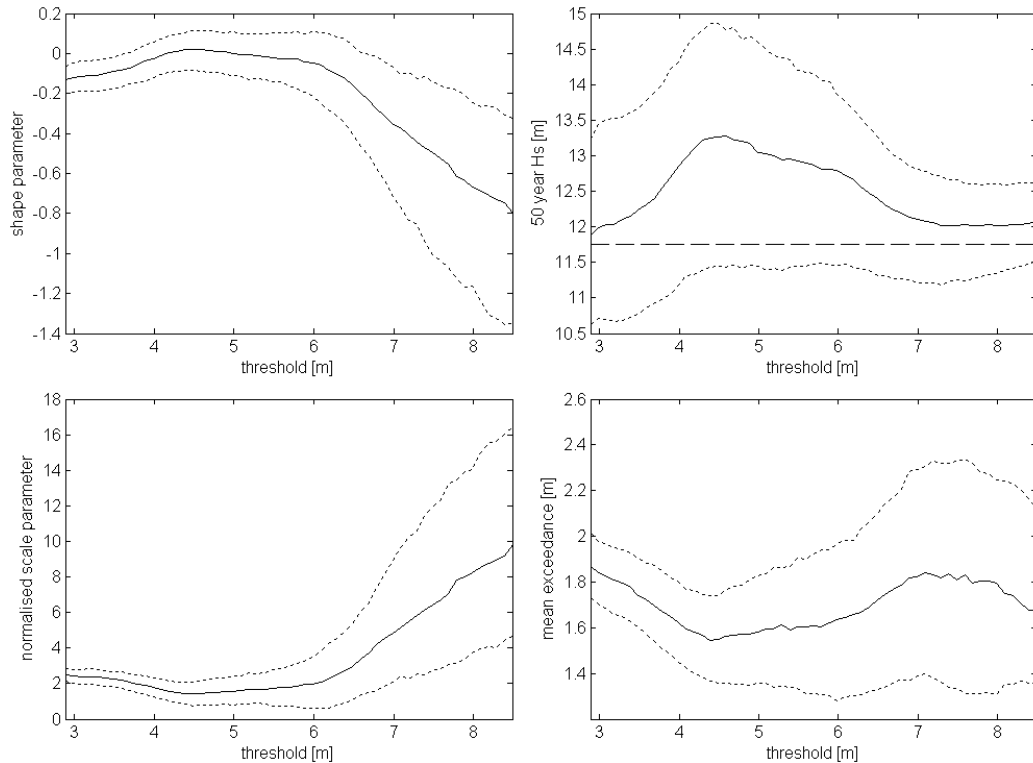


Figure 7.20. Threshold plots for data from buoy 46005, September-October. Solid lines: mean bootstrap value; dotted lines: 95% confidence bounds. Dashed line on upper right plot is the maximum observed H_s between September-October.

Figures 7.21 and 7.22 show probability and quantile plots for models fitted using thresholds of 4.5m and 7.3m. The model fitted using a threshold of 4.5m uses 117 points and gives $\hat{\xi} = 0.05$ and the 50 year return value for the season as 13.2m. The model fitted using a threshold of 7.3m uses 18 points and gives $\hat{\xi} = -0.46$ and the 50 year return value for the season as 12.0m. From the probability plots both fits seem reasonable. From the quantile plots, it is evident that the fit at higher quantiles is slightly better using the threshold of 7.3. Using the higher threshold, the annual return values

from the seasonal analysis become $H_{s,50}=13.0\text{m}$ and $H_{s,100}=13.4\text{m}$, less than 0.2m different from those from the non-seasonal analysis.

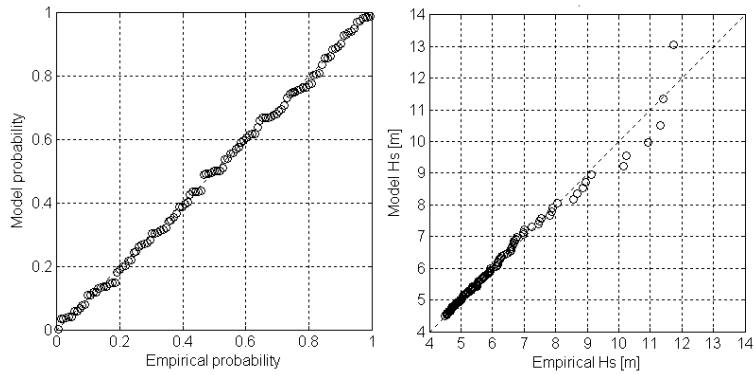


Figure 7.21. Probability and quantile plots for data from buoy 46005, Sep-Oct, using a threshold of 4.5m.

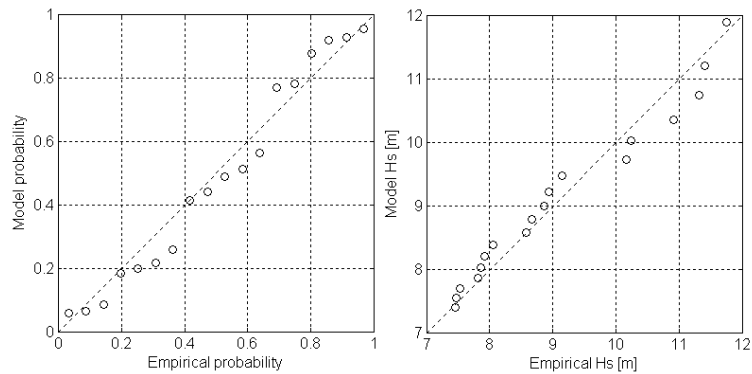


Figure 7.22. Probability and quantile plots for data from buoy 46005, Sep-Oct, using a threshold of 7.3m.

This example illustrates some of the difficulties in implementing the seasonal model. The difficulty in identifying a valid threshold in one season, seriously affects the results of the analysis. In fact, it is not clear if any threshold can be considered valid for this season. However, there are similar difficulties in identifying a valid threshold for the non-seasonal analysis. Figure 7.23 shows threshold plots for the non-seasonal data. A threshold of 5.3m was selected, because from this point until about 8m the estimated shape parameter, normalised scale parameter and return values are roughly constant. Above 8m, the estimates could be considered constant within the confidence limits, but appear to change their behaviour. It is not clear whether this is due to the small number

of data above 8m or if it is because the GPD is not a valid model for the data. Figure 7.24 shows probability and quantile plots for the model fitted using a threshold of 5.3m. Both appear to show good fits, with only small deviations in the quantiles above 10m.

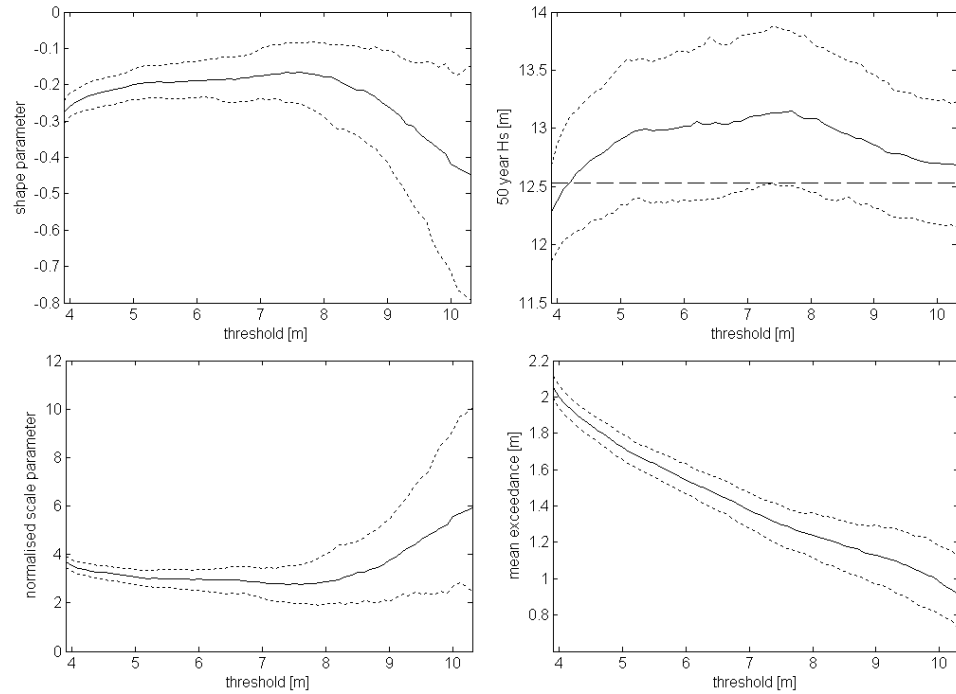


Figure 7.23. Threshold plots for annual data from buoy 46005. Solid lines: mean bootstrap value; dotted lines: 95% confidence bounds. Dashed line on upper right plot is the maximum observed H_s .

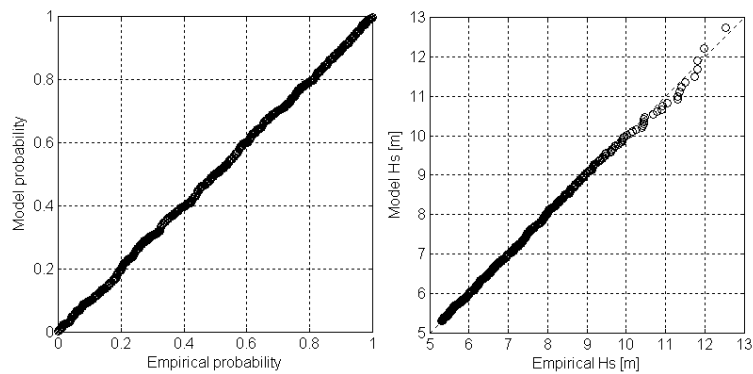


Figure 7.24. Probability and quantile plots for annual data from buoy 46005, using a threshold of 5.3m.

A similar problem occurred for buoy 46027 in September-October. The distribution of storm peaks changes rapidly during this period, so when all the data from September and October are binned together, the distribution appears heavy tailed, and results in the return values from the seasonal analysis being considerably larger than those from the non-seasonal analysis. A solution to this problem would be to use shorter seasons, or to visually estimate seasonal boundaries. However, using shorter seasons would result in few data and therefore greater uncertainty. Visually estimating seasonal boundaries may be more effective, but would introduce a further subjective element to the analysis.

For buoys 46028 and 46041 there are fewer data in the winter months than in summer. Figure 7.25 shows the amount of data in each season, relative to the season with the most data. The missing data in the winter months is likely to have introduced a small bias to the non-seasonal analyses and could be one reason for the discrepancy in the return values with the seasonal analyses. An attempt was made to compensate for this by resampling the data for each season to give equal proportions throughout the year. I.e. if there is $Q\%$ as much data in season S as in the season with the most data and there are n storms in season S , then $100 \times n / Q$ storms are drawn from season S to make up the annual sample. This resampling procedure was found only to make a small difference to the annual analysis, with return values increasing by less than 0.2m. The reason that the difference is small is probably because the storms in the summer months are generally much lower and have little influence on the annual return values. The effect of missing data on estimated return values is tested analytically in the next section and shown to have only a small influence.

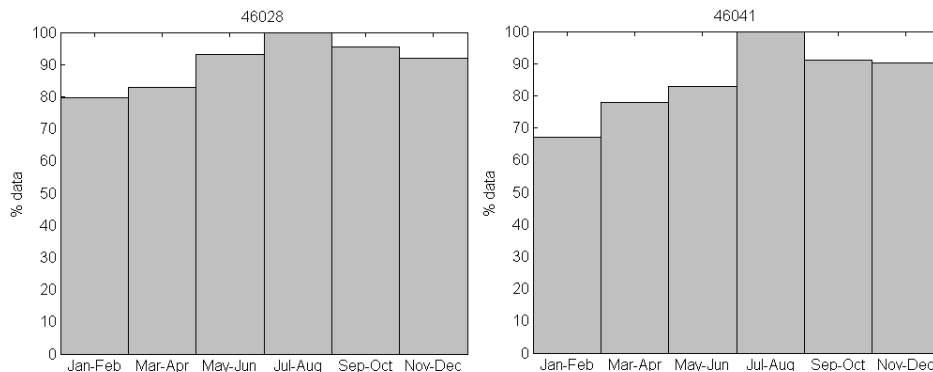


Figure 7.25. Percentage of data in each season relative to the season with the most data, for buoys 46028 (left) and 46041 (right).

7.6.5. Simulation study

In Section 7.5 it was mentioned that results presented by Jonathon et al (2008) were for rather artificial case studies. In this section we shall attempt to define some more realistic case studies, based on the analysis of the NDBC data presented in the last section. Figure 7.26(a) shows the mean number of storms exceeding the threshold (the rate of occurrence of ‘extreme’ events) for each month for each season and buoy. The values range between 0.5 and 4 depending on the buoy, season and threshold. Plots for individual buoys did not show any clear pattern throughout the year, indicating that variations may be due to threshold choice and random variability. We shall use the mean value over all seasons and buoys of 2.0/month as the rate of occurrence in our simulations.

Figure 7.26(b) shows the threshold for each season and each buoy. The smallest range of thresholds was for buoy 46026 with a minimum of 2.7m and maximum of 3.9m. The largest range was for buoy 46005 with a minimum of 2.1m and maximum of 7.0m. Scale parameters are shown in Figure 7.26(d). They varied roughly in proportion to the threshold with a mean value of $\hat{\sigma}/u = 0.26$. There does not appear to be any systematic variation of the shape parameter throughout the year, with the mean and standard deviation of the estimates over all buoys remaining roughly equal in each season. It is possible that the shape parameter may be slightly higher in April-May and September-October, but this may be a result of the rapidly changing distribution, mentioned in the previous section. The mean value of the shape parameter over all seasons and all buoys is -0.15.

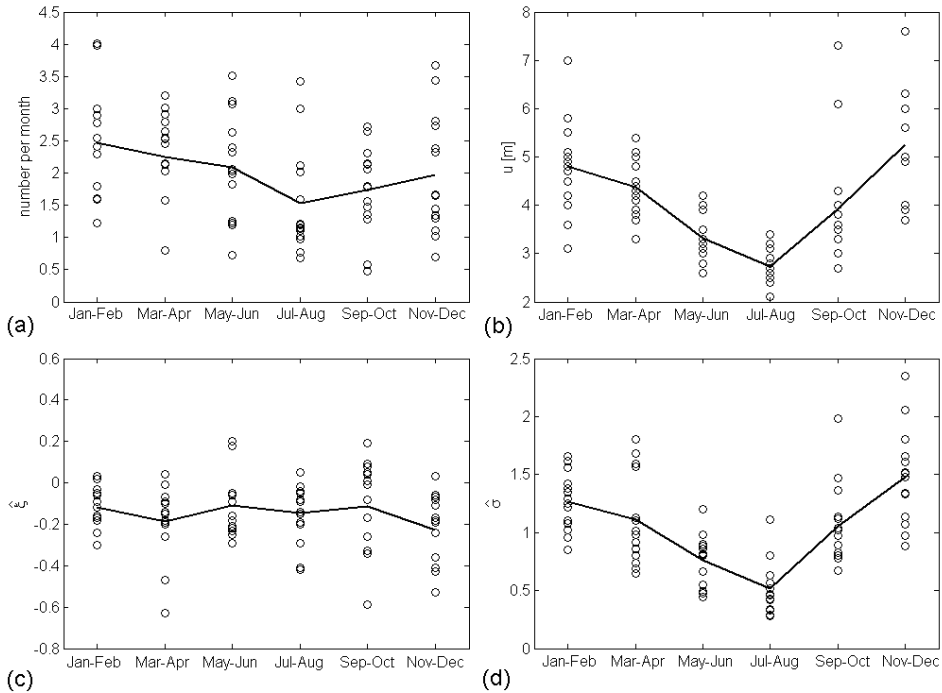


Figure 7.26. (a) Mean number of storms exceeding threshold per month; (b) threshold; (c) estimated shape parameter; (d) estimated scale parameter. For all plots circles indicate estimates for a specific buoy and lines indicate the mean value over all buoys.

Averaging the results over all the buoys may ignore some genuine differences in the distributions due to different exposure to storms and possibly shallow water effects. In order to try to capture some of the possible differences between the distributions four case studies have been examined. In all four cases the parameters of the distribution are assumed to vary smoothly throughout the year. For simplicity, a year is defined to be 360 days and a month to be 30 days. The times between threshold exceedances are modelled as exponentially distributed with a mean of 15 days, so that the number of storms per month is Poisson distributed with a mean of two storms per month, consistent with the buoy data.

In the first two case studies the shape parameter remains constant throughout the year and the shape parameter varies in proportion to threshold. In the first case study the threshold varies between 2m and 4m, and in the second case study it varies between 2m and 6m. In the third and fourth case studies the shape parameter varies throughout the year. This makes the distribution more stretched in spring and autumn as was noticed for some of the buoy records. In case 3 the threshold varies between 2m and 4m, and in

case 4 it varies between 2m and 6m. The parameters of the distributions and return values for the four case studies are given by: (d denotes the day of the year)

Case 1:

$$u = 3 + \cos(2\pi d / 360)$$

$$\sigma = 0.75 + 0.25 \cos(2\pi d / 360)$$

$$\xi = -0.15$$

$$H_{s,50} = 7.69 \text{ m}, H_{s,100} = 7.96 \text{ m}, H_{s,500} = 8.50 \text{ m}.$$

Case 2:

$$u = 4 + 2 \cos(2\pi d / 360)$$

$$\sigma = 1 + 0.5 \cos(2\pi d / 360)$$

$$\xi = -0.15$$

$$H_{s,50} = 11.44 \text{ m}, H_{s,100} = 11.85 \text{ m}, H_{s,500} = 12.68 \text{ m}.$$

Case 3:

$$u = 3 + \cos(2\pi d / 360)$$

$$\sigma = 1 + 0.5 \cos(2\pi d / 360) - 0.25 \cos(2\pi d / 180)$$

$$\xi = -0.15 - 0.1 \cos(2\pi d / 360)$$

$$H_{s,50} = 8.30 \text{ m}, H_{s,100} = 8.53 \text{ m}, H_{s,500} = 9.02 \text{ m}.$$

Case 4:

$$u = 4 + 2 \cos(2\pi d / 360)$$

$$\sigma = 1.5 + 0.75 \cos(2\pi d / 360) - 0.3 \cos(2\pi d / 180)$$

$$\xi = -0.15 - 0.1 \cos(2\pi d / 360)$$

$$H_{s,50} = 12.25 \text{ m}, H_{s,100} = 12.57 \text{ m}, H_{s,500} = 13.16 \text{ m}.$$

Figure 7.27 shows 50 year realisations of the four case studies, together with the theoretical 0.9, 0.99 and 0.999 quantiles for each day. The solid red line indicates the upper limit of the distribution.

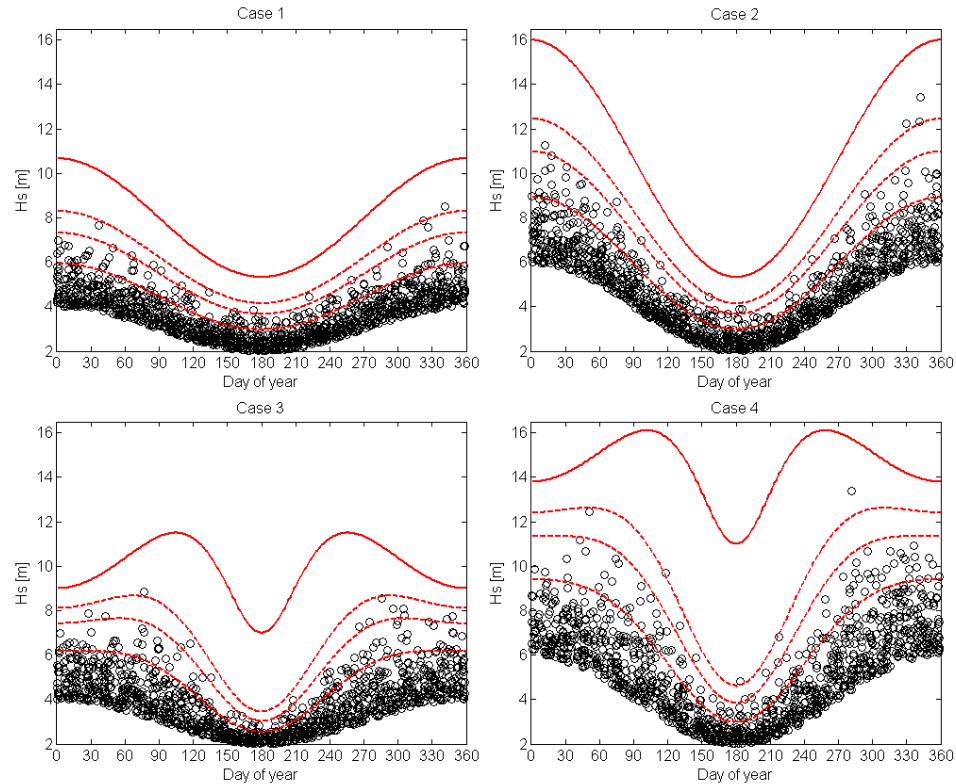


Figure 7.27. Distribution of storm peaks in the four case studies. Black circles: storm peaks from 50 year realisations. Dashed red lines: theoretical 0.9, 0.99 and 0.999 quantiles for each day. Solid red line: upper limit of distribution.

For each case study 1000 simulations have been run, of lengths 10, 20 and 50 years. For each simulation models are fitted using both seasonal and non-seasonal analyses. In the case of the non-seasonal analysis the threshold is chosen as the maximum of u throughout the year, i.e. 4m in cases 1 and 3, and 6m in cases 2 and 4. The seasonal analyses are conducted using seasons of length 1, 2 and 3 months. The midpoint of the first season is defined to be day 0. For each season the threshold is chosen as the maximum of u in that season.

The results of the simulations are presented in Tables 7.2-7.5. In each case the target return values are shown in the second column and the bias and RMS errors of the estimated return values from the non-seasonal and seasonal analyses are shown in subsequent columns. The target return values are calculated using equation 7.54 using season lengths of 1 day.

Return period [years]	Return value [m]	Sim. length [years]	Non-seasonal analysis		1 month seasons		2 month seasons		3 month seasons	
			Bias	RMS	Bias	RMS	Bias	RMS	Bias	RMS
50	7.69	10	-0.05	0.69	0.17	0.75	0.03	0.66	-0.01	0.67
		20	-0.03	0.44	0.10	0.48	0.02	0.49	-0.02	0.46
		50	0.00	0.30	0.04	0.32	0.00	0.31	0.00	0.31
100	7.96	10	-0.03	0.83	0.42	1.06	0.15	0.85	0.06	0.83
		20	-0.02	0.54	0.25	0.65	0.09	0.62	0.02	0.55
		50	0.02	0.37	0.12	0.41	0.03	0.38	0.02	0.37
500	8.49	10	0.03	1.23	1.31	2.31	0.58	1.54	0.38	1.40
		20	0.02	0.77	0.79	1.33	0.36	1.03	0.21	0.90
		50	0.06	0.53	0.40	0.77	0.15	0.59	0.09	0.55

Table 7.2. Bias and RMS errors in estimated return values for case study 1.

Return period [years]	Return value [m]	Sim. length [years]	Non-seasonal analysis		1 month seasons		2 month seasons		3 month seasons	
			Bias	RMS	Bias	RMS	Bias	RMS	Bias	RMS
50	13.31	10	-0.25	1.08	0.13	1.16	-0.05	1.12	-0.22	1.08
		20	-0.11	0.78	0.06	0.78	-0.03	0.79	-0.09	0.78
		50	-0.03	0.48	0.02	0.50	-0.01	0.49	-0.02	0.48
100	13.74	10	-0.28	1.31	0.38	1.57	0.05	1.41	-0.20	1.30
		20	-0.12	0.96	0.24	1.03	0.05	0.99	-0.08	0.95
		50	-0.02	0.59	0.11	0.64	0.02	0.61	-0.03	0.59
500	14.59	10	-0.29	1.92	1.44	3.27	0.57	2.49	0.16	2.20
		20	-0.10	1.42	0.98	2.05	0.46	1.73	0.12	1.52
		50	0.00	0.87	0.46	1.13	0.17	0.94	0.01	0.86

Table 7.3. Bias and RMS errors in estimated return values for case study 2.

Return period [years]	Return value [m]	Sim. length [years]	Non-seasonal analysis		1 month seasons		2 month seasons		3 month seasons	
			Bias	RMS	Bias	RMS	Bias	RMS	Bias	RMS
50	8.30	10	-0.06	0.63	0.40	0.84	0.25	0.75	0.18	0.74
		20	0.01	0.42	0.28	0.57	0.20	0.53	0.16	0.49
		50	0.01	0.27	0.15	0.33	0.09	0.31	0.08	0.30
100	8.53	10	-0.07	0.74	0.78	1.28	0.49	1.07	0.35	0.99
		20	0.00	0.49	0.53	0.85	0.37	0.73	0.29	0.66
		50	0.00	0.31	0.28	0.48	0.17	0.41	0.16	0.41
500	9.02	10	-0.11	0.99	2.10	3.02	1.36	2.35	0.84	1.77
		20	-0.05	0.66	1.37	1.90	0.99	1.59	0.64	1.18
		50	-0.06	0.42	0.72	1.02	0.47	0.82	0.41	0.74

Table 7.4. Bias and RMS errors in estimated return values for case study 3.

Return period [years]	Return value [m]	Sim. length [years]	Non-seasonal analysis		1 month seasons		2 month seasons		3 month seasons	
			Bias	RMS	Bias	RMS	Bias	RMS	Bias	RMS
50	12.25	10	-0.08	0.90	0.59	1.21	0.33	1.02	0.22	1.04
		20	-0.02	0.61	0.37	0.80	0.23	0.70	0.14	0.65
		50	0.02	0.38	0.16	0.45	0.09	0.40	0.08	0.40
100	12.57	10	-0.06	1.06	1.14	1.85	0.65	1.44	0.49	1.42
		20	-0.01	0.71	0.73	1.19	0.46	0.97	0.32	0.89
		50	0.03	0.44	0.35	0.64	0.21	0.53	0.18	0.52
500	13.16	10	-0.03	1.44	3.18	4.48	1.85	3.17	1.32	2.72
		20	0.00	0.95	1.98	2.72	1.33	2.13	0.90	1.70
		50	0.04	0.60	1.02	1.41	0.68	1.09	0.54	1.00

Table 7.5. Bias and RMS errors in estimated return values for case study 4.

The results can be summarised as follows:

- For all the case studies the non-seasonal analysis performs at least as well as the seasonal analyses and in most cases has a smaller bias and RMS error.
- Of the seasonal analyses, the 3-month season models had the best performance, followed by the 2-month season models, with the 1-month season models consistently having the worst performance.
- For the non-seasonal analyses the bias in estimate of the return value remains roughly constant with the return period, whereas for the seasonal analyses the bias increases with the return period.

The finding that the non-seasonal model performs better is contrary to what has been suggested by previous studies on seasonal and other covariate effects. Jonathon et al (2008) constructed examples with two distinct populations, which resulted in a compound distribution that was not well modelled by the GPD. In the case studies constructed here, where the distribution parameters vary smoothly with season, the compound annual distribution is well modelled by the GPD, even at high return values. These examples are a better representation of the change of distribution throughout the year, but could equally be interpreted as a change in distribution with direction.

Despite using more data points in total than the non-seasonal models, the seasonal models had a higher RMS error. This is caused by the partitioning of the data into smaller sets. For each season, the smaller sample size results in greater uncertainty in the estimates of model parameters. The models with longer seasons have larger sample sizes and therefore lower RMS errors.

It is perhaps easiest to understand the reason for the positive bias of the seasonal models in terms of maxima. Let M denote the annual maximum and M_i denote the maximum in season i . Denote the distribution function of the annual maximum $F(x) = \Pr\{M < x\}$, the distribution functions of the seasonal maxima as $F_i(x) = \Pr\{M_i < x\}$ and estimates of these are denoted with a '^' as usual. Then, assuming the maxima in each season are independent, $F(x) = \prod F_i(x)$. Consider a simple example of a two season year, where for some high value x , $F_1(x) = F_2(x) = 0.99$ and $F(x) = 0.99^2 = 0.98$. Suppose when the seasonal distributions are estimated from the data that $\hat{F}_1(x)$ is too low, $\hat{F}_1(x) = 0.95$ say, but $\hat{F}_2(x)$ is accurate or too high, $\hat{F}_2(x) \geq 0.99$. Then $\hat{F}(x) \leq 0.95$. So the effect of an overestimate of the probability of exceeding a high value in one season is not compensated for by underestimates of the probability of exceeding that high value in the other season. Moreover, the sensitivity of the annual distribution to estimates in individual seasons will increase at higher quantiles, as $F_i(x) \rightarrow 1$. Therefore the more seasons that the year is divided into, the greater the chance that there will be an overestimate in one season. Since this overestimate is not compensated for by the estimates in other seasons, the annual distribution becomes biased high at high quantiles. An example of this phenomenon was presented in the previous section, where

the return values for buoy 46005 were strongly influenced by the estimated distribution in September-October.

There is a small negative bias for the non-seasonal model in the 10 year simulations. This may be a result of non-proportional sampling from each season, as described by Carter and Challenor (1981) (see Section 7.5). However, the seasonal models generally had higher RMS errors than the non-seasonal models and comparable biases, so their estimates are not considered more accurate. In the simulations the times between threshold exceedances are modelled as exponential with a mean of 15 days. If we denote the length of the simulation in years as Y and the number of seasons that the year is divided into as NS , then the number of samples in from each season is Poisson distributed with mean $(Y \times 360)/(NS \times 15)$. For a Poisson distribution the variance is equal to the mean, so as the mean increases, the standard deviation as a fraction of the mean decreases. Therefore as the length of simulation increases the sampling becomes approximately proportional.

A simulation has also been run to examine the effect of missing data. Case study 2 was chosen since the seasonal models performed best here. 30% of the data was removed from the period between day 315 and day 45, which corresponds to season 1 in the 3-month season models. The bias and RMS errors for both the seasonal and non-seasonal models are shown in Table 7.6. The non-seasonal estimates are biased low, as would be expected when data is missing from the season with the highest values. The seasonal model shows less bias and has a similar RMS error to the non-seasonal model.

Return period [years]	Return value [m]	Sim. length [years]	Non-seasonal analysis		3 month seasons	
			Bias	RMS	Bias	RMS
50	8.30	10	-0.46	1.26	-0.26	1.31
		20	-0.28	0.88	-0.10	0.91
		50	-0.24	0.59	-0.07	0.59
100	8.53	10	-0.47	1.54	-0.21	1.59
		20	-0.26	1.06	-0.08	1.10
		50	-0.23	0.70	-0.06	0.72
500	9.02	10	-0.40	2.37	0.20	2.61
		20	-0.20	1.58	0.15	1.69
		50	-0.18	1.00	-0.04	1.04

Table 7.6. Bias and RMS errors in estimated return values for case study 2, with 30% missing data in winter.

Returning to the analysis of the buoy data in the previous section, in light of the simulation studies it is clear that the non-seasonal estimates should be considered as more accurate than the seasonal estimates. For 12 of the 14 records, the non-seasonal estimates were lower than the seasonal estimates and in the 2 records where the non-seasonal estimates were higher the difference was less than 0.4m, agreeing with the results of the simulation study. In all cases the estimated confidence bounds for the non-seasonal estimates were narrower than those for the seasonal estimates, again agreeing with the results of the simulation study. For buoys 46028 and 46041 where there was 20-30% missing data in the winter, the return values from the seasonal model are likely to be more accurate.

An alternative to estimating distribution parameters for individual seasons is to estimate them as a smoothly varying function of a time (e.g. Anderson et al, 2001; Jonathon and Ewans, 2008). There has not been time to investigate the use of this method and it would be useful to investigate the bias and RMS error in comparison to non-seasonal models using a similar simulation study as that described here.

7.7 Conclusions

In this chapter motivation for the commonly used Peaks Over Threshold (POT) method for the estimation of extreme values of H_s has been presented. The method is asymptotically justified, and makes fuller use of the data than other extreme value models. Several new results on the use of the POT method have been presented.

The method used to estimate the parameters of the generalised Pareto distribution (GPD) affects the accuracy of the results. The most commonly used estimators for the GPD in wave studies are the maximum likelihood (ML) and probability weighted moment (PWM) estimators. Both of these methods have disadvantages which are documented in the statistical literature, but have not been so widely reported in oceanographic studies. For small sample sizes the ML estimator does not always exist and also has a larger bias and variance than other estimators. In Section 7.4 new results on the existence of the ML estimator were presented. The PWM estimator always exists, and has a lower bias and variance than the ML estimator for smaller sample sizes. However the PWM estimator can sometimes produce non-feasible results and is sensitive to threshold. A hybrid-PWM can be used which is always feasible, but still suffers from sensitivity to threshold.

The performance of a range of estimators has been examined in Section 7.4. Of these, the likelihood moment (LM) estimator was shown to have arguably the best performance overall. This estimator is relatively new and has not been used in this context before. It was shown that by using the hybrid-PWM estimator as a first guess in the estimation procedure, the bias and RMS of the LM estimator are consistently the lowest or close to the lowest of all the estimators, and performs better than the original LM estimator with a fixed first guess, reported by Zhang (2007). The new LM estimator always exists, is always feasible and has a low sensitivity to threshold. For larger sample sizes the bias and variance are very close to those of the ML estimator, but the LM estimator has the advantage that it is easier to compute. It is concluded that the LM estimator, using the hybrid-PWM estimator as a first guess, should be used in preference to other estimators.

The POT model makes several important assumptions which need to be verified for its use in predicting extreme values of H_s . Some new results concerning the verification of these assumptions have been presented in this chapter.

The first assumption discussed was that the data are independent. Wave data have strong serial correlation. This is usually dealt with by declustering. The seasonal variability in wave conditions introduces a further periodic correlation to the data, making it difficult to verify the independence of the declustered data. A new method for examining the correlation of declustered data has been presented in Section 7.6.2 which uses the method of Athanassoulis and Stefanakos (1995) to remove the seasonal component from the time series. This method has been used to examine the efficacy of different declustering procedures. However, there is still some level of subjectivity in the choice of declustering criteria. It is thought that this will not have a large impact on the results since the largest peaks, on which extremes are critically dependent, remain for any choice of declustering criteria.

The second assumption that was discussed was that the data are identically distributed. Seasonal and other covariate effects mean that this is not the case for wave data. The use of seasonal models has been tested using realistic case studies, based on examination of buoy data. Contrary to what would be expected from most literature on the subject, the non-seasonal models performed better than the seasonal models unless there was a significant amount of missing data. In the case studies considered here, under the assumption that the extremes values follow a GPD with parameters varying smoothly throughout the year, the annual distribution is well modelled by another GPD. The seasonal models performed worse because of the greater uncertainty related to smaller sample sizes. It was shown that this introduces a positive bias into estimates from seasonal models and increases their uncertainty, despite using more data than the non-seasonal models.

The asymptotic argument used to justify the use of GPD is difficult to verify directly. If it is shown that the GPD is a good fit for the data then it can be argued that at least the asymptotic argument is not unreasonable. To this end verifying that the choice of threshold is appropriate is of great importance. A new bootstrapping method for aiding threshold choice was presented in Section 7.6.3. It was shown that this method can

smooth the plots used to examine the variation of estimated model parameters and return values with threshold. For the examples using buoy data it was possible to identify a valid threshold in most cases and the GPD was shown to be a good fit. However, it was shown in Section 7.6.4 that in some cases the choice of threshold is not clear and that results can be sensitive to the choice of threshold. In the instances where there is no clear choice of threshold, the use of the GPD is difficult to justify.

It would be desirable to do without some of the subjective choices which are necessary to apply the POT model, especially in relation to threshold choice. Recently Beirlant et al (2009) have proposed a ‘second-order’ peaks-over-threshold model which can be fitted to a larger portion of the data. This model certainly warrants further investigation in its application to wave data. The models of Naess and Haug (2008) and Stefanakos and Athanassoulis (2006) which do not invoke asymptotic arguments would also be worth investigating further, although both models require further details on the fitting procedure before they can be considered as rigorous as the POT method.

The issue of the data source used for estimation of extremes has not been considered in this chapter. It is rare that there will be a long record of high quality in-situ measurements at a site of interest. As with the other topics considered in this thesis, this leaves the choice of data between wave models and satellite altimeters. There are problems with estimating extremes from both data sources. Model data can perform poorly in extreme conditions, which can mean that derived extreme value statistics are highly uncertain. On the other hand altimeter data is sparsely sampled both in space and time. In the open ocean the spatial sampling is not an issue since wave conditions can be considered stationary over large areas. However, close to the coast wave conditions can change significantly between altimeter ground tracks, so some form of interpolation or modelling must be used to infer conditions between tracks. The issue of sparse temporal sampling has been considered by Anderson et al (2001). They propose a method to account for the sparse sampling, but note that it requires further theoretical developments before it can be recommended for practical use. A useful topic for further work would be to compare the accuracy of estimates of extremes from wave model and altimeter data.

8. Conclusions and further work

8.1 Conclusions

The primary aim of the research presented in this thesis was to provide the information on the wave resource necessary for the economic assessment of a wave energy project, using the Pelamis WEC as an example. The problem is split into two stages. The first is to select the best sites for wave energy development in terms of estimated energy yield. This requires spatial maps of WEC yield, so that a comparative assessment can be made. Once a site has been selected for development, the next stage is to provide detailed information on the resource at the particular location. In particular, estimates are needed of the mean power produced by the WEC, the variability of power levels over various timescales and predictions of extreme wave height. In addition, confidence bounds on these estimates are required. Conclusions will be presented separately for each stage.

8.1.1 Spatial mapping of wave energy resource and site selection

The work presented in Chapter 4 has shown that:

1. Using calibrated H_s measurements and the new period algorithm, developed in this work and described in Section 3.2, satellite altimeter data can be used to create accurate spatial maps of the long-term mean power produced by a WEC. The method developed provides a cost-effective alternative to mapping the resource using model data.
2. The accuracy of the long-term mean power from averages along sections of the altimeter ground tracks is limited by sparse temporal sampling. This limits the accuracy to which two sites can be compared. If there are several tracks in close proximity then this can increase the temporal sampling rate and hence increase confidence.
3. The spatial resolution of altimeter ‘track-maps’ is better than that which is currently available from global wave model data. The resolution is limited by the distance between altimeter ground tracks, and problems measuring within 5-10km of the coast (discussed in Section 2.2). By combining tracks from multiple

missions a resolution of around 30km is usually achievable. In areas where high resolution wave model data is not available, or where it is only available at a significant cost, altimeter maps provide an attractive alternative for producing regional scale maps of WEC yield.

8.1.2 Detailed information at selected site

I) Accuracy of historic data

It is rare that there will be a long record of in-situ measurements at the site of a proposed wave farm. The choice of data source for establishing the historic resource at the site is between wave models and satellite altimeters. In Chapter 5 the accuracy of two hindcasts for the same location was examined. This accuracy was then compared to the accuracy that is achievable using altimeter data alone. The following conclusions are made:

1. Without calibration, estimates of the mean WEC power from model data can be biased of the order of 10-20%.
2. The error structure of wave parameters from model data makes calibration complicated. In Section 5.1.2 it was shown that even with two years of buoy data for comparison it was not possible to completely remove the systematic errors from the model data. The most important features of model errors to account for are:
 - Non-linear dependence of model parameters on multiple factors, such as H_s , T_e and steepness.
 - Short-term temporal correlation of random errors
 - Seasonal and interannual changes in biases
3. In Section 5.1.3 it was shown that modelling the short-term correlation of the model errors in Pelamis power, using a low-order ARMA model, was sufficient to explain the errors in estimates of monthly mean Pelamis power in one of the hindcasts considered. In the other hindcast, a precise estimate of the monthly and annual errors in mean Pelamis power could not be given due seasonal and inter-annual changes in model performance. After calibration, the difference between the estimates of mean Pelamis power over a period of 8 years from the two models was 5%. Validation against a longer record of in-situ measurements

is required before more precise results can be given on the accuracy of estimates of WEC power from wave model data.

4. However, in Section 5.3 it was shown that the accuracy which is currently achievable from model data is better than that which is theoretically achievable from altimeter data alone, due to the limited temporal sampling.

II) Accuracy of predictions of WEC yield

The accuracy of predictions in the future resource is limited by the accuracy of the historic resource and the variability in the resource. In Chapter 6 the variability in mean power levels was studied for an area in the north of Scotland. In this location wave parameters are strongly correlated to the NAO. This correlation means that existing work on the temporal variability of the NAO and its sensitivity to climate change can be used to study variability in WEC power levels. The following conclusions are made for this location and are likely to apply equally to other locations with similar levels of interannual variability:

1. The variability in 5, 10 and 20 year mean power levels is greater than would be expected if annual power anomalies were uncorrelated noise (Section 6.4.1). This is due to the strong correlation of the wave climate with the NAO (Section 6.3.2), which exhibits long-range dependence.
2. Predictions from global climate models of potential changes in the NAO are too uncertain at present to forecast changes in wave climate, but some increase in wave power with increased GHGs seems likely at this location (Section 6.4.3). However, the change in wave climate over the life time of a wave farm is likely to be small in comparison to the ‘natural’ variability in the wave climate.
3. Improvements in the accuracy of historic data will improve the bias, but not variance of predictions of future WEC yield (Section 6.4.2). These bias and random error components are of roughly equal magnitude. Therefore improving the accuracy of historic data will improve the predictions of future yield.

III) Extremes

Two specific problems related to the estimation of extreme values have been considered in Chapter 7. The first was the choice of estimator used for the Generalised Pareto distribution (GPD) and the second was the effect of seasonal variability. The main conclusions from the work are:

1. The Likelihood-Moment estimator, using the hybrid-PWM estimator as a first guess, should be used in preference to other estimators for the GPD such as maximum likelihood or probability weighted moments (Section 7.4).
2. Non-seasonal models have a lower bias and variance than models which analyse the data in separate seasons. This is in contrast to the assertions made in many previous studies. The smaller samples sizes in seasonal models increase the uncertainty in estimates of model parameters for each season. An overestimate in one season is not compensated by underestimates in the other seasons. This results in a positive bias in estimates of extremes from seasonal models (Section 7.6.5).

8.2 Further work

The research presented in this thesis has used the Pelamis as an example throughout. The main results should apply equally to other WECs, but it would be useful to verify this directly when power matrices become available. It has also been assumed throughout that the Pelamis power response is completely determined by H_s and T_e . The validity of this assumption was discussed in Section 1.4. When further information is available from device manufacturers on the effect of this parameterisation, then it will be useful to investigate the effect this has on the accuracy of predicted yield. In particular, quantifying the effect of varying spectral shapes and directional distributions on the power produced by a WEC will be important.

It will be a few years before large arrays of WECs are deployed, but before this happens it will be necessary to model the effect of interactions between WECs within a wave farm. Once the effect of interaction between WECs is known more precisely this information can be combined with the information on the wave resource to obtain a more accurate estimate of the yield from a whole farm.

There are also ways in which the work presented here can be developed further. As in the previous section, these will be split into the two stages of resource assessment.

8.2.1 Spatial mapping of wave energy resource and site selection

Comparison of sites from the altimeter ‘track-maps’ is limited by the accuracy of the along-track mean values and the spatial resolution of the data. Site selection on a finer scale requires the use of nearshore models. Further work is required to address the following problems:

- Nearshore models can account for physical processes such as refraction, bottom dissipation, triad interactions, wave-current interactions, etc. The more processes which are accounted for, the more time it takes to compute results. It would be useful to see which processes are relevant to compute for various water depths, relevant to different WECs.
- Similarly, it can take a long time to compute the nearshore conditions at 6 hour intervals over a 20 year period. It would be useful to investigate if a set of transfer coefficients can be generated and applied to the boundary conditions instead of running the model for each time step.

8.2.2 Detailed information at selected site

I) Accuracy of historic data

It was noted in Chapter 5 that 2 years of buoy data was not enough to properly examine the long term uncertainties in wave model data. It would be useful to validate a hindcast using a record of in-situ measurements of 10 years or more.

Estimation of confidence in model estimates in absence of in-situ data was not considered in detail. It is possible to compare H_s from model and altimeter data in order to calibrate the boundary conditions to a nearshore model, but the accuracy of altimeter T_e and T_z from Ku-band data is too low for calibration purposes. It would be useful to investigate the estimation of T_e and T_z from dual frequency measurements to see if these could be used for calibration of model data. Alternatively, it may be worth trying to determine a more precise estimate of the relationship between altimeter σ_0 and the wave spectrum. For example, if it can be shown that σ_0 is only dependent on frequencies in a certain range and a more precise relationship can be established between σ_0 and the energy at these frequencies, then this information could be used for calibration and validation purposes.

The best route to improving the accuracy of estimated WEC yield from wave model data is not through calibration, but improvements in the accuracy of the model data itself. This is a broad subject that was touched on in Section 2.3. The sources of errors in wave model data can be split into three categories: input data, numerical resolution and model physics. It is likely that improvements can be made to the current generation of models in all three of these categories and there is currently much research ongoing on these subjects. It will be important for wave energy developers to keep up to date with developments in these fields and investigate the impact they have on estimated WEC yield.

II) Accuracy of predictions of WEC yield

In Chapter 6 a study of variability and predictability of WEC yield for a location in the north of Scotland was presented. The results relied on the strong correlation between the wave climate and the NAO in this location. In other areas it will either be necessary to identify a climatic index which can be used in lieu of the NAO or to adopt another approach to study long-term variability and potential impacts of climate change. Other studies have used the pressure fields output by AOGCMs to investigate trends in wave climate, but these remain highly uncertain at present. The other option is to investigate the effect on wave climate of changes in storm parameters such as intensity, frequency and track position.

III) Extremes

There remain numerous problems in the estimation of extreme wave parameters, such as declustering of data, threshold selection and the validity of asserting asymptotic distributions. All of these would benefit from further research to remove subject interpretation from the calculations.

Another important problem which there was not time to consider was the effect of uncertainties in the data source. In practical situations it is unlikely that there will be a long-term record of buoy measurements, as used in Chapter 7. In this situation the choice is, again, between model and altimeter data. Estimates from wave models are highly uncertain in extreme conditions. Altimeter measurements are accurate, but may not measure some extreme events due to their sampling patterns. It would be useful to

conduct a study to investigate which data source it is preferable to use for the estimation of extremes.

Appendix A: Quality controls for DWR data

There were several problems which were noticed in the data from the two Datawell Directional Waverider (DWR) buoys at EMEC. This section describes these problems and the procedures which have been developed to screen for them and correct where possible.

The Datawell software used to decode the signal transmitted by the buoy records an ASCII text format file containing hexadecimal vectors, known as an HXV file. These files contain 7 series of variables:

1. A status signal, to indicate whether the transmission was received without error.
2. A cyclically repeated index signal
3. A system word, containing information on buoy system parameters
4. Heave displacement
5. North displacement
6. West displacement
7. Parity bits, from which the transmission status is ascertained.

The checks described in this section use the three displacement signals, the index signal and the status signal. Checking the displacement time series is the first step in the quality check procedure. It should reduce the number of records failing post-processing checks, but does not replace the need for checking the processed data. We first describe the problems observed in the displacement time series and the QC procedures which have been developed, in the order that they are applied to the data. We then give a summary of the entire QC procedure and finish by presenting a validation.

A.1 Scrambling of index signal

In a number of files from the EMEC buoys it was noticed that the index signal had become scrambled. An example of a corrupt index signal is shown Figure A1. At points the index signal jumps back and forth. The cause of this problem is unknown. Figure A2 shows the original heave signal (red line) and ‘unscrambled’ heave signal (blue line) calculated from the sorted index signal. The index signal and the data are both

scrambled, thus sorting the record by the index signal appears to correct the problem. The algorithm used to unscramble the signal finds the longest section of the HXV file with no discontinuities in the index signal of greater than 30 samples, and then sorts the file by the index signal. It also inserts blank lines for missing indices.

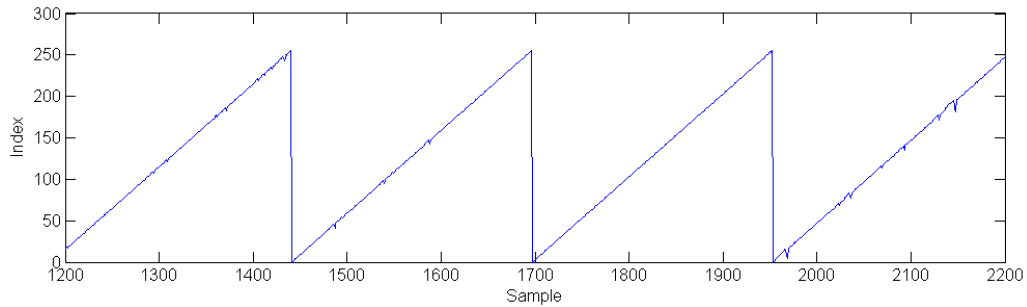


Figure A1. An example of a corrupt index signal from EMEC buoy B.

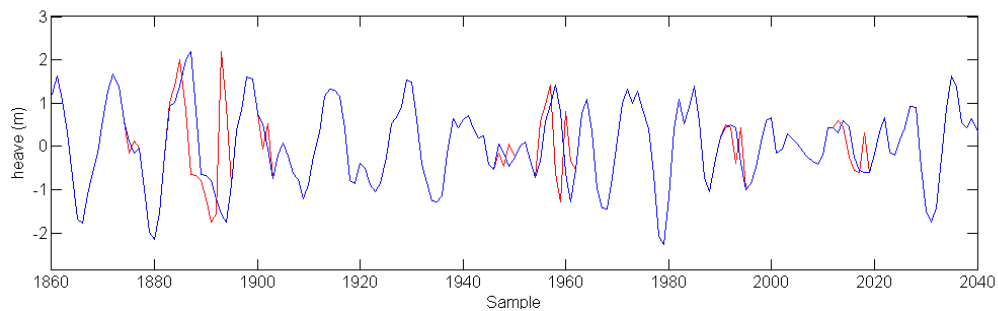


Figure A2. Heave signal for original (red) and unscrambled (blue) signal, corresponding to index signal shown in preceding figure.

A.2 Spikes in the displacement signals

Many of the records from the EMEC buoys showed spikes in the heave, north or west signals. Many of these spikes result from transmission errors and removing data where the status signal is greater than 1 (which indicates an irreparable transmission error) removed a lot of the spikes in the signals. However, some spikes remained after the data was screened for transmission errors. These spikes are detected from the velocity time series of each signal (i.e. the difference between successive displacements). All three velocity signals are approximately normally distributed and a spike is defined as a point where the velocity exceeds 5 times the standard deviation (the standard deviation of the velocity signal is estimated as 0.74 times the inter-quartile range, the ratio for the normal distribution). This limit has been chosen empirically. A visual inspection of a

large number of files has shown that this limit is sufficient to pick up all large spikes, with very few false positives. Spikes identified using this method are removed from the displacement signals.

A.3 Near-zero records

In addition to buoy outages documented by the operator, a number of periods of buoy failure were noted where one or more of the displacement signals reverted to zero with occasional spikes. These are flagged by setting a lower limit on the IQR of each signal of 0.05m. Records with one or more signals having lower IQR than this are flagged as bad.

A.4 Cross-correlation with double integration filter

A problem in the displacement signals was identified in some HXV files from the EMEC buoys, which caused unrealistically large, but realistically shaped waves. An example is shown in Figure A3.

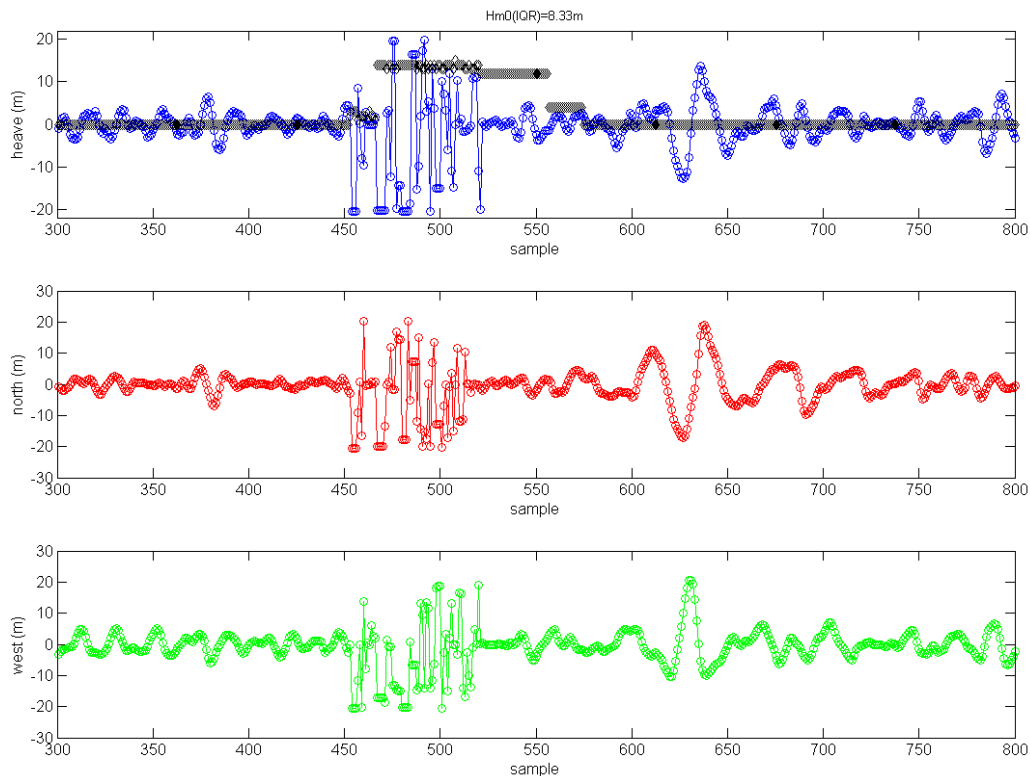


Figure A3. Example of heave, north and west signals for a record exhibiting the ‘filter problem’. The status signal is marked in black diamonds on heave plot.

After a period of bad transmission between samples 450-575, large displacements occur between samples 600-650. The trough-to-crest height of the wave is 26.6m and the zero-crossing period is 19.5s, giving a steepness of 0.045, which is well below the limiting steepness of 1/7. However, H_s calculated from the IQR is 8.3m, giving $h / H_s = 3.2$. Based on a Rayleigh distribution of wave heights, the probability of this occurring in a half hour record is

$$\Pr(H_{\max} \geq h) = 1 - [1 - \exp(-2h^2 / H_s^2)]^{1800/T_s} \approx 2.6 \times 10^{-7}$$

So there is strong cause to suspect this wave to be bad data. However, we do not wish to exclude the wave based on pre-assumed statistics, since the wave statistics are precisely what we are interested in.

The wave is in fact a result of a spike in the one of the acceleration signals measured by the buoy. The acceleration signals recorded by the buoy are double integrated using a digital filter (an array of real numbers, $u[j]$, $j = -m, -m+1, \dots, -1, 0, 1, \dots, m$). The acceleration signal is sampled, yielding the array $a[j]$, $j = -\infty, \dots, \infty$. The array $z[j]$ of displacement values is the convolution of the acceleration $a[j]$ and the filter $u[j]$:

$$z[j] = \sum_{k=-m}^m a[j-k]u[k]$$

Hence a spike in the acceleration signal at time i will result in the filter pattern appearing in the displacement signal from time $i-m$ to $i+m$. If there are multiple spikes in the acceleration signal, the resulting displacement signal will be the sum of shifted filter arrays (plus a smaller contribution from the other terms without spikes in the acceleration signal).

It is possible to test whether this has occurred by examining the cross-correlation of the displacement signal and the filter (see Figure A4). For each displacement signal, peaks occur in the cross-correlation at the time of the large displacement, indicating that the large displacements are a result of one or more spikes in the acceleration signals. Note that wrongly transmitted data and spikes in the displacements must be removed before

calculating the cross-correlation with filter array in order to avoid spuriously high correlations.

From examination of over 5 years of data from the EMEC buoys, it was found that if the maximum absolute value of cross-correlation of the heave and filter signals exceeds 0.2, then this indicates the presence of the filter pattern in the heave signal. A limit of 0.3 is applied for the north and west signals (see Figure A5). All data between the first and last points where the cross-correlation exceeds the threshold are removed. These limits were found to be remarkably robust. All occurrences of the filter pattern which had been manually identified were flagged by this method, and out of a total of over 200 records flagged there were only 2 false positives and these were both for instances where $H_s < 1\text{m}$.

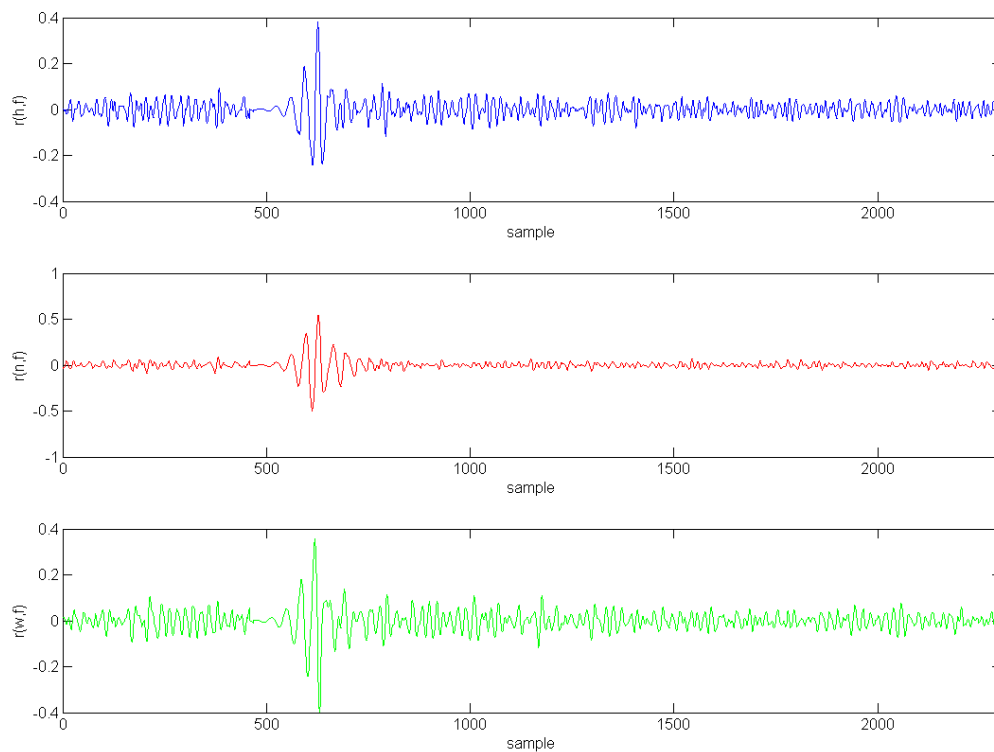


Figure A4. Cross-correlation of displacement signals with double integration filter.

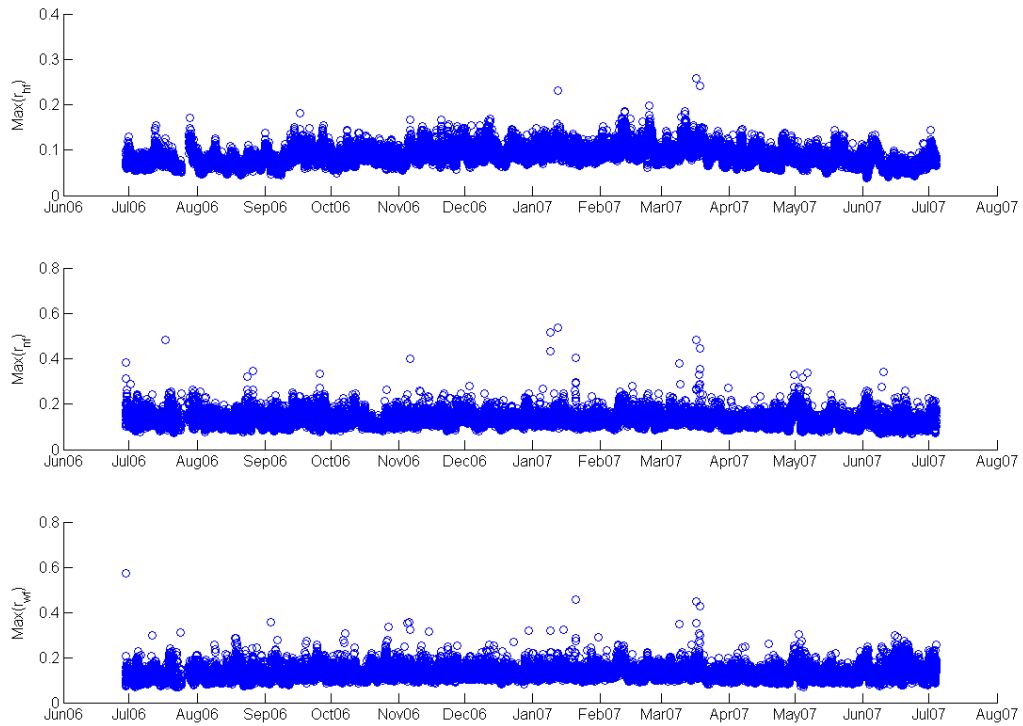


Figure A5. Maximum absolute value of cross-correlation of displacement signals with filter array for EMEC buoy C.

A.5 Trimming procedure

When bad data is removed from the HXV file, the question arises as to how to analyse the remaining signal with missing values. Simply joining either side of the gap together will result in jumps appearing in the displacement signal. The approach taken in this case is to trim either side of the gap to the nearest zero-crossing point, ensuring that crests are joined to troughs and vice versa. Typically only a small amount of data is removed by this procedure, of the order of 10-20 samples in a record of 2304 samples.

A.6 Overview of QC procedure

The quality checks are applied in the following order:

1. Check index signal for continuity and unscramble if necessary
2. Remove all data with status >1
3. Remove spikes in heave, north or west signals
4. Make 3 signals consistent (e.g. if a spike has been removed from the north signal, the same sample is removed from the heave and west signals)
5. Reject records with near zero displacements

6. Remove sections of record with high cross-correlation with double integration filter
7. Linearly interpolate gaps shorter than 2 points
8. Trim heave signal to zero crossing points
9. Reject records with less than 10 minutes of good data.

A.7 Validation of QC procedure

The quality control procedures described above have been checked using data spanning a 5 year period from data from 3 different DWR buoys (1 of the buoys was a replacement for an earlier buoy that failed). The maximum H_s recorded in this period exceeded 12m. The displacement series for all records with H_s exceeding 8m have been inspected by eye. This comprises 14 separate storms and 128 half hour records.

All occurrences of the filter pattern which had been manually identified were flagged by the QC procedure. Additional records exhibiting the filter problem were also identified and out of a total of over 200 records flagged there were only 2 false positives, both for instances where $H_s < 1\text{m}$.

Various plots were inspected to see if there were any obvious problems with the quality checked data:

- Time series of H_s , T_e , T_z , direction, etc., looking for outliers, flat periods or rapid changes.
- Scatter plots of H_s against T_e
- Scatter plots of H_{max} against H_s
- Scatter plots of concurrent data from each buoy

No obvious outliers remained after QC and all plots inspected appeared to follow realistic distributions.

The percentage of records with each flag, binned by H_{m0} , are shown in Tables A1-A3. Flag 0 indicates that no errors were detected, flag 1 indicates errors were identified and removed (scrambling or spikes), flag 2 indicates that the filter problem was detected,

flag 3 indicates that the record was removed as bad. It is evident that the occurrence of flags 1 and 2 increases with H_{m0} , but the occurrence of flag 3 decreases.

	Flag 0	Flag 1	Flag 2	Flag 3	# records
$0 \leq H_{m0} < 2\text{m}$	82.5	16.8	0.1	0.5	14993
$2 \leq H_{m0} < 4\text{m}$	77.9	21.7	0.1	0.4	9069
$4 \leq H_{m0} < 6\text{m}$	45.0	54.3	0.6	0.2	1815
$6 \leq H_{m0} < 8\text{m}$	27.6	68.4	3.9	0.0	228
$H_{m0} \geq 8\text{m}$	5.6	88.9	5.6	0.0	18

Table A1. Percentage of flags for buoy A.

	Flag 0	Flag 1	Flag 2	Flag 3	# records
$0 \leq H_{m0} < 2\text{m}$	80.4	18.7	0.1	0.9	46201
$2 \leq H_{m0} < 4\text{m}$	76.4	23.3	0.1	0.2	26818
$4 \leq H_{m0} < 6\text{m}$	45.8	53.2	0.8	0.2	4935
$6 \leq H_{m0} < 8\text{m}$	16.9	80.4	2.3	0.4	813
$H_{m0} \geq 8\text{m}$	2.2	89.0	8.8	0.0	91

Table A2. Percentage of flags for buoy B.

	Flag 0	Flag 1	Flag 2	Flag 3	# records
$0 \leq H_{m0} < 2\text{m}$	76.9	22.1	0.2	0.7	10127
$2 \leq H_{m0} < 4\text{m}$	75.3	24.3	0.1	0.3	5806
$4 \leq H_{m0} < 6\text{m}$	56.9	41.8	0.5	0.8	1508
$6 \leq H_{m0} < 8\text{m}$	41.5	53.4	2.0	3.2	253
$H_{m0} \geq 8\text{m}$	21.1	63.2	15.8	0.0	19

Table A3. Percentage of flags for buoy C.

Appendix B: Summary of altimeter missions to date

This section makes some notes on the altimeter missions to date, with the exception of GEOS-3 (launched in 1975) and SEASAT (launched in 1978) which only provided short periods of data that have not been used in this study. The notes focus on orbital information and dates, and are intended to illustrate the spatial and temporal availability of data from each altimeter.

B.1 US Navy satellites: GEOSAT & GEOSAT Follow-On (GFO)

The first altimeter to provide a continuous dataset of over a year was the US Navy's GEOSAT. As indicated by its name (GEOdetic SATellite), the satellite's primary purpose was to measure the marine gravity field with high precision. Launched in March 1985, the for the first year and a half GEOSAT's orbit was based on a 3-day near-repeat orbit which was permitted to drift, ultimately producing a tightly spaced ground track pattern, with a 168 day exact repeat period. The main goal was to obtain a densely sampled map of the marine geoid.

Upon completion of the geoid-mapping objective, GEOSAT was manoeuvred into an exact repeat orbit with a period of 17.05 days for the observation of geodetic parameters of the oceans. The exact repeat mission (ERM) officially started on Nov. 8, 1986 and continued until the satellite failed in January 1990; but it began to malfunction early in 1989, and there was a significant decline in global coverage from about March 1989.

Descriptions of the GEOSAT system characteristics were collected in two special issues of the Johns Hopkins APL Technical Digest (Vol. 8(2), 1987; Vol. 10(4), 1989). Extensive references and collections of ocean science results were presented in special issues of the Journal of Geophysical Research devoted to GEOSAT (Vol. 95(C3), 1990; Vol. 95(C10), 1990). Further details on GEOSAT are given in the User Handbook (Cheney et al, 1987).

In February 1998 the GEOSAT Follow-On (GFO) satellite was launched by the US Navy as part of their initiative to develop an operational series of radar altimeter satellites to maintain continuous ocean observation from the GEOSAT Exact Repeat Orbit. The RADS data record begins in January 2000. After an onboard problem in September 2008, GFO's transmitter was turned off on 26 November 2008 and the orbit manoeuvred for spacecraft disintegration in early December 2008. More information can be found on the GFO homepage: <http://gfo.bmpcoe.org/Gfo>.

Both the GEOSAT and GFO altimeters operate at 13.5 GHz (Ku-band)

B.2 NASA/CNES satellites: TOPEX/Poseidon, Jason-1 & Jason-2

The TOPEX/Poseidon satellite was a joint French (CNES) and American (NASA) satellite system designed to study global ocean dynamics. Launched on August 10, 1992, TOPEX/Poseidon (T/P) made altimetric sea level measurements using either the dual-frequency NASA altimeter which operates simultaneously at 13.6GHz (Ku-band) and 5.3GHz (C-band) or the CNES single frequency Ku-band altimeter (13.65 GHz). Since the two altimeters share a common antenna, they cannot be operated simultaneously. The NASA TOPEX altimeter, the primary mission instrument, is operated about 90% of the time, and the CNES Poseidon altimeter is operated about 10% of the time. The Poseidon altimeter was switched off permanently on 12th July 2002 (cycle 361). The T/P mission ceased operations in May 2006 after spacecraft lost its ability to manoeuvre. For more information see the TOPEX homepage: <http://TOPEX.wff.nasa.gov>.

The TOPEX altimeter was run on the “A-side” circuitry until 10/02/1999 (end of cycle 235) and switched to the “B-side” circuit from 11/02/1999 (start of cycle 236). Measurements of significant wave height began to drift towards the end of the A-side circuit.

Jason-1 was launched on December 7, 2001 in an orbit identical to that of T/P. The satellite is another joint CNES and NASA project and has inherited a lot of T/P's main features. In particular it carries a dual frequency 13.6GHz (Ku-band) and 5.3GHz (C-band) altimeter. TOPEX and Jason were flown in tandem, along the same orbit,

separated by about 1 minute for a period of 6 months. After this TOPEX was manoeuvred into its phase B orbit: a parallel orbit, half way between Jason's ground tracks.

The Geophysical Data Record (GDR) for Jason-1 begins at cycle 1, pass 2, equator crossing time 15-Jan-2002 06:35:10, this corresponds to TOPEX cycle 344, pass 2, equator crossing time 15-Jan-2002 06:36:22. When TOPEX was flying in the phase B orbit, the lag increased to about 7 minutes, due to the manoeuvre into the new orbit.

The Jason-2 satellite was launched in June 2008. At the time of writing Jason-2 is still in its commissioning phase, flying in the same orbit as Jason-1 and leading by 60 seconds. After 4 months Jason-1 is scheduled to be manoeuvred into a parallel orbit, coinciding with the TOPEX phase B orbit.

B.3 ESA satellites: ERS-1, ERS-2 & ENVISAT

The ERS (European Remote Sensing) missions, built by European Space Agency (ESA) carry several instruments, including a radar altimeter and synthetic aperture radar (SAR). ERS-1 was launched on July 1991 and operated until June 1996. It flew on three different orbits: a 3-day period for calibration and ice-sea observation, a 35-day period for multi-disciplinary ocean observations, and a 168-day period for geodetic applications.

ERS-2 was launched in April 1995 and was flown in tandem with ERS-1, their identical orbits having a one-day shift. The tandem orbit lasted until June 1996 when ERS-1 was switched off. On 22 June 2003 (cycle 85) the ERS-2 tape recorder failed. From this point on ERS-2 data is only available within the visibility of ESA ground stations over Europe, North Atlantic, the Arctic and western North America, see the figure B.1. The altimeters on both ERS-1 and ERS-2 operate at 13.8 GHz (Ku-band).

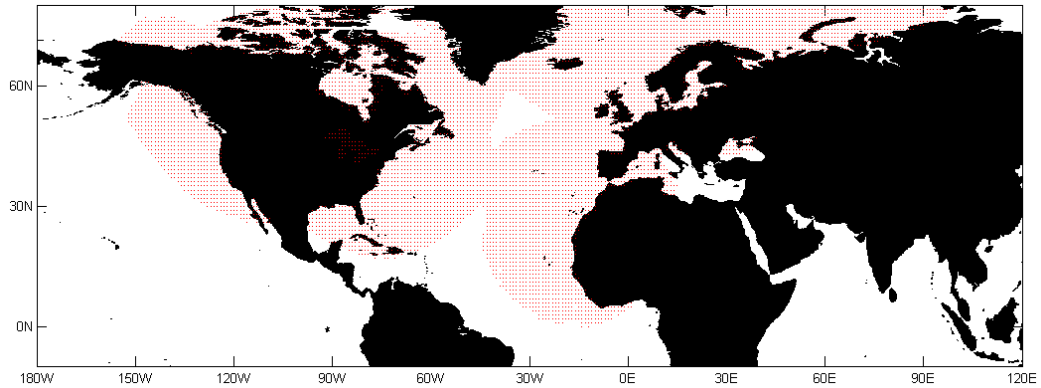


Figure B.1. Availability of ERS-2 data from 22 June 2003 (cycle 85) onwards.

In March 2002, ESA launched ENVISAT (ENVironmental SATellite) to provide continuity of the measurements from the ERS missions. ENVISAT carries a dual frequency 13.6 GHz (Ku-band) and 3.2 GHz (S-band) altimeter. It flies in the same orbit as ERS-2 and ERS-1 phases C and G. The GDR for ENVISAT begins at cycle 9, pass 834, equator crossing time 00:18:51 25/09/02, corresponding to ERS-2 cycle 77, pass 834, equator crossing time 00:47:24 25/09/02. From this point onwards data from ERS-2 lags ENVISAT by about half an hour.

B.4 Summary of altimeter orbit information

The distance between ground tracks and their cross over angles are shown in Figure B.2 as functions of latitude. Table B.1 presents a summary of dates and orbit information for each altimeter. Note that the dates in the table refer to the availability of data rather than satellite launches.

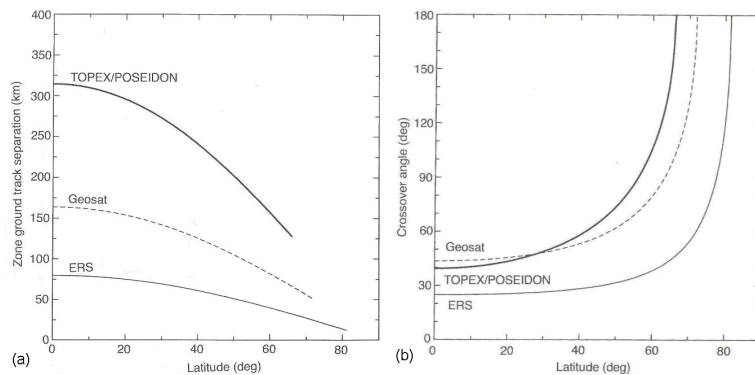


Figure B.2. Separation of ground tracks (a) and cross over angles (b) as functions of latitude (From Fu & Cazenave, 2001).

Table B.1. Summary of altimeter orbit information

Satellite	Phase	Start date	End date	Start Cycle	End Cycle	Period (days)	Passes per cycle	Direction of travel	Lat./Lon. coverage (km)	Altitude	Notes
GEOSAT	A	31-Mar-85	30-Sep-86	1	25	168	660	Westward	72°N/S	800	3-day near-repeat orbit
	B	08-Nov-86	30-Dec-89	26	93	17.05	488				Ends Jan 90, but poor quality data from Mar 89 onwards
TOPEX / Poseidon	A	25-Sep-92	11-Aug-02	1	364	9.92	254	Eastward	66°N/S	1336	Poseidon switched off 12/07/2002, cycle 361
	N	11-Aug-02	20-Sep-02	365	368	9.92	254				Orbit transition period. Changed to offset JASON
	B	20-Sep-02	08-Oct-05	369	481	9.92	254				
ERS-1	A	01-Aug-91	14-Dec-91	1	46	3	86	Westward	81.5°N/S	785	
	B	14-Dec-91	25-Mar-92	47	81	3	86				
	R					35.00					Experimental roll-tilt mission
	C	14-Apr-92	20-Dec-93	83	101	35.00	1002				
D		24-Dec-93	10-Apr-94	103	138	3	86				
	E	10-Apr-94	28-Sep-94	139	140	168	4822				8 km shift from phase E
F		28-Sep-94	21-Mar-95	141	143	168	4822				
	G	24-Mar-95	02-Jun-96	144	156	35.00	1002				Exact repeat orbit, ends Jun 96
ERS-2	A	29-Apr-95	Present	0	118	35.00	1002		81.5°N/S	785	Same orbit as ERS-1 phases C & G.
GFO	A	07-Jan-00	26-Nov-08	37	177	17.05	488	Westward	72°N/S	800	Same orbit as GEOSAT
JASON-1	A	15-Jan-02	Present	1	173	9.92	254	Eastward	66°N/S	1336	Same orbit as T/P phase A
ENVISAT	B	24-Sep-02	Present	9	51	35.00	1002	Westward	81.5°N/S	785	Same orbit as ERS-1 & 2

Appendix C: Notes on linear regression

Notes in this section are based on the book ‘Statistical Regression with Measurement Error,’ Cheng CL & Van Ness J, Arnold, London, 1999.

C.1 Introduction

The basic premise of linear regression is that two variables ζ and η are related by

$$\eta = \alpha + \beta\zeta \quad [\text{C.1}]$$

However the variables ζ and η are unobservable due to measurement error. Thus instead of observing ζ and η directly, one observes the variables

$$x = \zeta + \delta \text{ and } y = \eta + \varepsilon \quad [\text{C.2}]$$

where the errors, δ and ε , are independent and identically distributed. A sample of size n for this model would be

$$\begin{pmatrix} x_1 \\ y_1 \end{pmatrix}, \dots, \begin{pmatrix} x_n \\ y_n \end{pmatrix} \quad [\text{C.3}]$$

The method used for estimating α and β depends on the assumptions made about the ratio of the error variances

$$\lambda = (\sigma_\varepsilon / \sigma_\delta)^2 \quad [\text{C.4}]$$

where σ_δ^2 and σ_ε^2 are the variances of δ and ε respectively.

In this document we discuss some common models for different values of λ and when it is appropriate to use each type.

The following notation will be used for the variance and covariance of x and y :

$$s_{xx} = \frac{1}{n} \sum (x_i - \bar{x})^2 \quad [\text{C.5}]$$

$$s_{yy} = \frac{1}{n} \sum (y_i - \bar{y})^2 \quad [\text{C.6}]$$

$$s_{xy} = \frac{1}{n} \sum (x_i - \bar{x})(y_i - \bar{y}) \quad [\text{C.7}]$$

C.2 Error in one variable only

The simplest case is that one of the variables, ζ say, is observed without error. In this case the process of estimating α and β is known as the regression of y -on- x , ordinary least-squares regression, or sometimes simply as linear regression.

The model is fitted by finding the coefficients which minimise the sum of squared residuals:

$$R^2 = \sum \varepsilon_i^2 = \sum (y_i - (\alpha + \beta x_i))^2 \quad [\text{C.8}]$$

The values of α and β which minimise R^2 are given by

$$\hat{\beta} = \frac{s_{xy}}{s_{xx}} \quad [\text{C.9}]$$

$$\hat{\alpha} = \bar{y} - \hat{\beta}\bar{x} \quad [\text{C.10}]$$

It is not necessary to make any assumptions on the distributions of ζ , η or ε in order to derive these estimates. However, to estimate confidence intervals for the slope and intercept it is necessary to assume that the errors are independent and identically distributed normal variables. Then a $1-\alpha$ confidence interval for the slope and intercept are given by:

$$\hat{\alpha} \pm t_{\alpha/2} \hat{\sigma}_\varepsilon \sqrt{\frac{1}{n} + \frac{\bar{x}^2}{ns_{xx}}} \quad [\text{C.11}]$$

$$\hat{\beta} \pm t_{\alpha/2} \frac{\hat{\sigma}_\varepsilon}{\sqrt{ns_{xx}}} \quad [\text{C.12}]$$

where $t_{\alpha/2}$ is the value for a $1 - \alpha$ confidence interval for a Student's-t distribution on $n-2$ degrees of freedom and the estimated error variance, $\hat{\sigma}_\varepsilon$, is given by

$$\hat{\sigma}_\varepsilon = \frac{1}{n-2} \sum (y_i - (\hat{\alpha} + \hat{\beta}x_i))^2 \quad [\text{C.13}]$$

Note that if the errors are not independent (e.g. errors in subsequent observations are correlated) or not identically distributed (e.g. the variance of the errors depend on x or y) or not normal, then these formulas are not valid.

C.3 Errors in both variables

In the case that the ratio of the error variances λ is not known, it is not possible to indentify the slope β . Therefore it is necessary to make some assumption on the ratio of the error variances. In the case that both the observed variables are normally distributed and the ratio of the error variances is known, the maximum likelihood estimates of the slope and intercept are given by

$$\hat{\beta} = \frac{s_{yy} - \lambda s_{xx} + \sqrt{(s_{yy} - \lambda s_{xx})^2 + 4\lambda s_{xy}^2}}{2s_{xy}} \quad [\text{C.14}]$$

$$\hat{\alpha} = \bar{y} - \hat{\beta}\bar{x} \quad [\text{C.15}]$$

If $\lambda = 1$ then this is known as orthogonal regression or total least squares regression and the slope is equal to the first principal component of x and y . If $\lambda \neq 1$ it is known as weighted distance regression. If $\lambda = 0$ then [C.14] reduces to the ordinary least squares regression of x -on- y .

Often we do not have any information on the ratio of the error variances and it is assumed that $\lambda = 1$. If the difference in the ratio of variances of the two variables is large, i.e. $s_{xx} \gg s_{yy}$, it may not be safe to assume that $\lambda = 1$, since the scale of the errors may be related to the scale of the variable. Instead it may be safer to assume that $\lambda = 1$ for normalised data

$$z_x = \frac{(x - \bar{x})}{\sqrt{s_{xx}}}, \quad z_y = \frac{(y - \bar{y})}{\sqrt{s_{yy}}} \quad [\text{C.16}]$$

In this case the normalised variables have zero mean and unit variance, so from [C.14] we have $\hat{\beta}_z = \pm 1$ for the normalised data. Transforming back to the original data

$$\hat{\beta} = \text{sign}(s_{xy}) \sqrt{\frac{s_{yy}}{s_{xx}}} \quad [\text{C.17}]$$

The formula for the intercept for the original data remains unchanged as $\hat{\alpha} = \bar{y} - \hat{\beta}\bar{x}$. The ratio of error variances for the original data becomes

$$\lambda = s_{yy} / s_{xx} \quad [\text{C.18}]$$

This type of regression is called the geometric mean regression and is the geometric mean of the ordinary least squares line of y -on- x and x -on- y :

$$\hat{\beta}_{GMR} = \text{sign}(s_{xy}) \sqrt{\frac{\hat{\beta}_{y \text{ on } x}}{\hat{\beta}_{x \text{ on } y}}} = \text{sign}(s_{xy}) \sqrt{\frac{s_{xy}}{s_{xx}} \cdot \frac{s_{yy}}{s_{xy}}} = \text{sign}(s_{xy}) \sqrt{\frac{s_{yy}}{s_{xx}}} \quad [\text{C.19}]$$

Robustness of the estimators:

This refers to the quality of the estimates when there is contamination in the data ('bad' data points) or the assumptions of the model are not satisfied by the data. The estimate of the slope given by [C.14] is known to be highly non-robust, even more so than the ordinary least-squares estimate [C.9]. Thus it is important that before using [C.14], that

one has reason to believe that it is a valid model for the data and that the dataset has been checked for outliers. If the fitted regression line does not look plausible, then it is possible that the model is not applicable in that situation or that outliers are corrupting the model parameter estimates. Common reasons for violation of model assumptions include:

- x and y are not linearly related
- x and y are not normally distributed – in this case a transformation may fix this.
- Error variances are dependent on x or y , i.e. $\sigma_\delta = f(x)$ or $\sigma_\epsilon = f(y)$
- Errors are not independent, e.g. subsequent observations have correlated errors.

Confidence intervals:

It is possible to derive analytic expressions for confidence interval for the regression parameters based on the standard properties of maximum likelihood estimators. However, since the assumptions of the model are often violated by the data, these analytic expressions are often not valid and can give a false estimate of confidence. In many cases a bootstrap technique may be more appropriate.

Appendix D

JOURNAL OF GEOPHYSICAL RESEARCH, VOL. 113, C03029, doi:10.1029/2007JC004438, 2008



A parametric model for ocean wave period from K_u band altimeter data

E. B. L. Mackay,¹ C. H. Retzler,² P. G. Challenor,³ and C. P. Gommenginger³

Received 6 July 2007; revised 5 December 2007; accepted 11 December 2007; published 28 March 2008.

[1] Using a large collocated data set of altimeter and buoy measurements, we examine the relationship between the altimeter K_u -band measurements of significant wave height, H_s , backscatter coefficient, σ_0 , and the buoy wave period. This is used to derive an empirical altimeter wave period model for TOPEX, Poseidon, Jason-1, ERS-2, Envisat, and GEOSAT follow-on. We show that there is a step change in the response of σ_0 at around 13 dB and above this value σ_0 is not related to wave period. The results are compared to algorithms proposed by two previous authors (Gommenginger et al., 2003; Quilfen et al., 2004) and examined in terms of absolute accuracy (RMS error), ability to replicate the joint distribution of wave height and period, and residual trends with various parameters. The new algorithm is shown to perform better than the previous algorithms in all metrics considered. Finally, we demonstrate that there is a limiting accuracy achievable for a function of the form $f(H_s, \sigma_0)$ and that our model comes close to this.

Citation: Mackay, E. B. L., C. H. Retzler, P. G. Challenor, and C. P. Gommenginger (2008), A parametric model for ocean wave period from K_u band altimeter data, *J. Geophys. Res.*, 113, C03029, doi:10.1029/2007JC004438.

1. Introduction

[2] Global measurements of wave period are important for many applications such as ocean engineering and climatological studies. At present, numerical wave model and satellite remote sensing data are the only sources of wave period information available globally. Both wave model and satellite remote sensing data have their limitations.

[3] Of the two types of remote sensing data, synthetic aperture radar (SAR) provides the only direct source of spectral information, important for assimilation into wave models [Abdalla et al., 2006]. However, SAR data are sparse both temporally and spatially (ERS SAR images are acquired at intervals of 200 km along track). Moreover, SAR spectra can only capture the long-wave part of ocean wavefields. Violante-Carvalho et al. [2005] note that the high-frequency cutoff is sea state dependent, but in general, waves shorter than 150–200 m (around 0.1 Hz for deep water linear waves) propagating parallel to the satellite track are not mapped directly by SAR. Several inversion schemes exist to extract wave spectra from SAR [e.g., Collard et al., 2005; Schulz-Stellenfleth et al., 2005]. Recently, Schulz-Stellenfleth et al. [2007] proposed an empirical approach for the retrieval of integral ocean wave parameters from SAR data. They compare SAR derived estimates of H_s , T_z , T_m , and T_e to collocated WAM spectra. The RMS difference

compared to the WAM spectra is 0.45 m for H_s , 0.80 s for T_z and T_m , and 0.77 s for T_e . They note that the lowest correlation is observed for T_z because it has the strongest dependence on the high-frequency tail of the spectrum, which is not seen by SAR.

[4] The measurement of significant wave height by satellite altimeters is well established and altimeter measurements of significant wave height are widely accepted to be of comparable accuracy to that of in situ measurements [e.g., Krogstad and Barstow, 1999; Challenor and Cotton, 2002]. In addition to significant wave height (and range), altimeters measure the backscattered power σ_0 , returned from the sea surface. The backscatter coefficient is routinely used to estimate near-surface wind speed (U_{10}), but there is evidence that altimeter wind speed are affected by the degree of sea state development, and can be biased low by as much as 1.5 m/s in developing wind sea conditions [Gommenginger et al., 2002].

[5] Several models have been proposed relating altimeter H_s and σ_0 to wave period [Davies et al., 1997; Hwang et al., 1998; Sarkar et al., 1998; Gommenginger et al., 2003; Quilfen et al., 2004; Kshatriya et al., 2005]. To date the most accurate model proposed is that of Quilfen et al. [2004, hereafter referred to as Q04]. They use a neural network to establish a relationship between altimeter H_s and σ_0 with buoy T_z , based on a collocated data set of TOPEX/Poseidon and National Data Buoy Center (NDBC) buoy measurements. They exclude data where $\sigma_0 > 16$ dB from their analysis, suggesting that these are due to surface slicks for which there are no waves. Their algorithm is

$$T_z = \exp(-17.1642a + 13.5844) \quad (1)$$

¹School of Civil Engineering and the Environment, University of Southampton, Southampton, UK.

²Pelamis Wave Power Ltd., Edinburgh, UK.

³National Oceanography Centre, Southampton, UK.

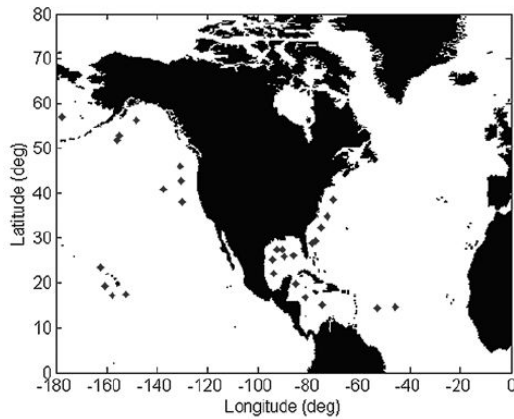


Figure 1. Locations of the 28 deep-water NDBC buoys used in the collocated data set.

where

$$a = \frac{1}{1 + \exp(0.6573H_s^{0.1084}\sigma_0^{0.2962} - 2.2377)} \quad (2)$$

[6] Although the Q04 algorithm is quite accurate, there are some disadvantages with this approach. First, the accuracy of the algorithm attainable from a neural network is limited by the architecture of the network. Second, the underlying relationship between the variables is often not clear from the output of a neural network. So, in order to apply the Q04 algorithm to data from other altimeters, the measurements must be cross-calibrated to the same levels. *Quilfen et al.* [2004] also create a second algorithm, which makes use of C-band data as well. We will only consider their Ku-band algorithm in this paper. A brief discussion of dual-frequency period algorithms is given in section 5.

[7] An earlier semiempirical model was proposed by *Gommenginger et al.* [2003, hereafter referred to as G03]. They use heuristic arguments to show that $T \sim \sigma_0^{0.25} H_s^{0.5}$, where σ_0 denotes the backscatter in its linear, non-dB form, (elsewhere in the paper the symbol σ_0 without the subscript L denotes the backscatter coefficient in decibels). Empirical models for T_z , T_m , and T_p (the inverse of the peak spectral frequency) are created using linear regressions of wave period against $X = \sigma_0^{0.25} H_s^{0.5}$ in both linear and log-log space, using collocated NDBC buoy and TOPEX Ku-band measurements. The models created by performing the log-log regression proved to be more accurate and we will only consider these from now on. Although not as accurate as the Q04 algorithm, the G03 algorithm is still widely used, so it is included here for comparison.

[8] Numerical wave models such as WAM [*WAMDI Group*, 1988] and WaveWatch III [*Tolman et al.*, 2002] provide directional spectra at high spatial and temporal resolutions, but their performance is limited by the accuracy of the input data, the model physics and numerical scheme. Details of the performance of the WAM model run at the European Centre for Medium Range Weather Forecasting

(ECMWF) can be found in the work of *Janssen et al.* [1997, 2005] and *Bidlot et al.* [2002]; a validation of WaveWatch III run at the U.S. National Centers for Environmental Prediction (NCEP) is given by *Tolman* [2002]. A review of the current state of the art in wind-wave modeling is given by *Cavaleri et al.* [2007].

[9] Previous comparisons of buoy, altimeter, and model period data showed that the models in question performed worse than the existing altimeter wave period algorithms. *Caires et al.* [2005] perform a triple collocation of T_z measurements from NDBC buoys, TOPEX G03 algorithm, and the ECMWF ERA-40 wave reanalysis. They show that the standard deviation in the ERA-40 T_z data is higher than both the buoy data and TOPEX G03 estimate. *Quilfen et al.* [2004] compared one month of global data from WaveWatch III to NDBC data and T_z estimates from TOPEX using the Q04 algorithm. They showed that in all locations the WaveWatch III data had a larger bias than the altimeter data when compared to the buoy measurements. However, since these comparisons were performed improvements have been made in numerical wave modeling. For example, *Bidlot et al.* [2007] show that using a reformulated dissipation source term reduces the RMS error in T_z for the ECMWF WAM model, compared to the version of WAM used for the ERA-40 reanalysis.

[10] In this paper we use a large collocated data set of NDBC buoy measurements and Ku-band altimeter (from several missions) to examine the relationship between the altimeter H_s and σ_0 , and buoy wave period and derive a new altimeter wave period model. The new model is fitted for TOPEX, Poseidon, Jason-1, ERS-2, Envisat, and GEOSAT Follow-on (GFO) and the results for TOPEX are compared to the results using the G03 and Q04 algorithms. We finish by discussing the limitations of an altimeter wave period function of the form $T = f(H_s, \sigma_0)$.

2. Collocated Data Set

[11] The collocated data used in this paper and the quality control checks applied are described in detail in Appendix A. Only NDBC buoys located in deep water in open ocean, at least 200 km from land, have been chosen, so that there are no shallow water effects and spatial variability is low. The locations of the buoys are shown in Figure 1.

[12] Spectral moments are usually defined as integrals over frequencies from zero to infinity. In practice no instrument can measure infinitely high frequencies so either a theoretical high frequency tail must be added to the spectrum or an appropriate cutoff frequency chosen. In this paper, moments are calculated as the integral over the frequency range reported by the buoys, detailed in Table A2 in Appendix A.

3. Development of the New Period Algorithm

[13] To develop a new algorithm we start by observing trends using the combined collocated data from the six altimeters, a total of 30,733 data points. Differences in calibration between altimeters are small, of the order of tenths of meters for H_s and tenths of decibels for σ_0 , and the greater number of data points makes trends in the data easier to observe (absolute calibrations of H_s against buoy data are

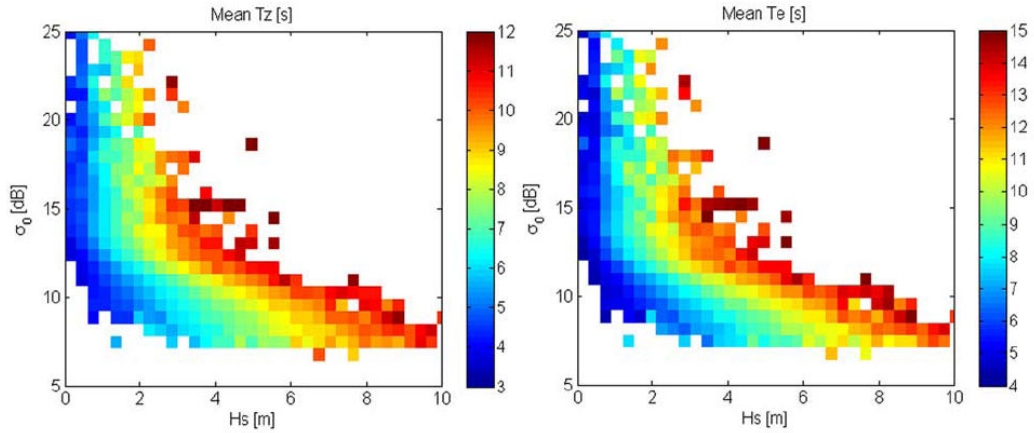


Figure 2. Mean T_z and T_e against H_s and σ_0 for combined collocated data.

given in Appendix A, and relative calibrations of σ_0 can be found in the work of, e.g., Callahan et al. [1994] and Tran et al. [2005]). Since different period parameters are useful for different applications (T_z is often used for ocean engineering, while T_e is used for wave energy applications), we will consider how altimeter measurements relate to both T_z and T_e .

[14] Figures 2a and 2b show the mean T_z and T_e for bins of H_s and σ_0 . It is apparent that there is a threshold level around 13 dB above which σ_0 is no longer related to the wave period. Figure 3a shows a similar plot of mean significant steepness (defined as $2\pi H_s/gT_z^2$) for bins of H_s and σ_0 . It can be seen that times when σ_0 is above the threshold level correspond to times of low significant steepness. Figure 3b shows a density plot of σ_0 against significant steepness. The step-change in the response of σ_0 to significant steepness at around 13 dB is clearly visible.

[15] From Figure 2, it appears that when σ_0 is below the threshold level, for constant T_e or T_z the relationship between H_s and σ_0 is linear. To test this hypothesis, we

use data from individual altimeters, so as not to introduce any bias from calibration differences. The data is binned by buoy T_z or T_e in bins of size 1 s and we use orthogonal regression [Cheng and Van Ness, 1999] to fit lines of the form $\sigma_0 = A + BH_s$. Figure 4 shows the results for TOPEX and T_z , but the same trends were observed for all the altimeters. A strong correlation is observed for all values of T_z , with no evidence of non-linearity. The same relationship was also observed for T_e .

[16] Lines of the form $\sigma_0 = A \exp(BH_s)$ and $\sigma_0 = AH_s^\beta$ were also tried, but the best fit was obtained for the linear relationship. The G03 algorithm makes the implicit assumption that for constant T_z the relationship between H_s and σ_0 is of the form $\sigma_0 = AH_s^\beta$, since

$$T_z = 10^\alpha (\sigma_0^{0.25} H_s^{0.5})^\beta \Rightarrow \sigma_0 = \left(\frac{T_z}{10^\alpha}\right)^{4/\beta} H_s^{-2} \quad (3)$$

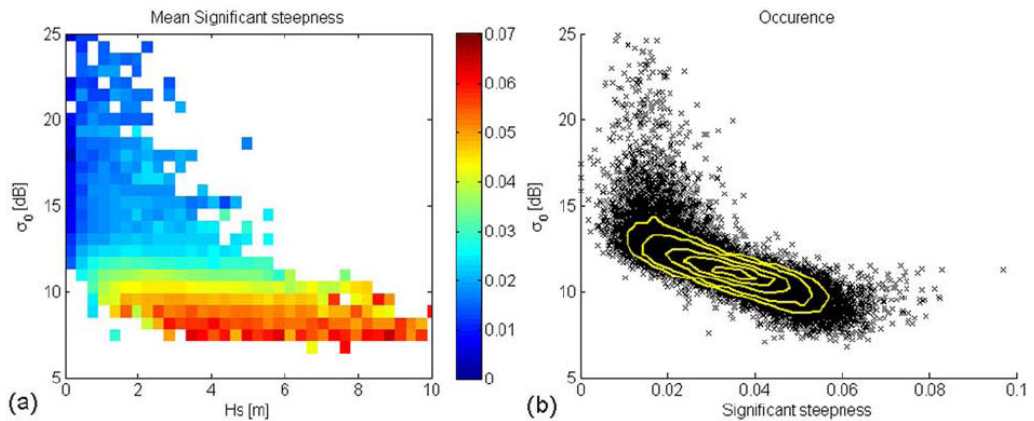


Figure 3. (a) Mean significant steepness against H_s and σ_0 for combined collocated data. (b) Scatterplot of significant steepness against σ_0 , with contours showing distribution of data.

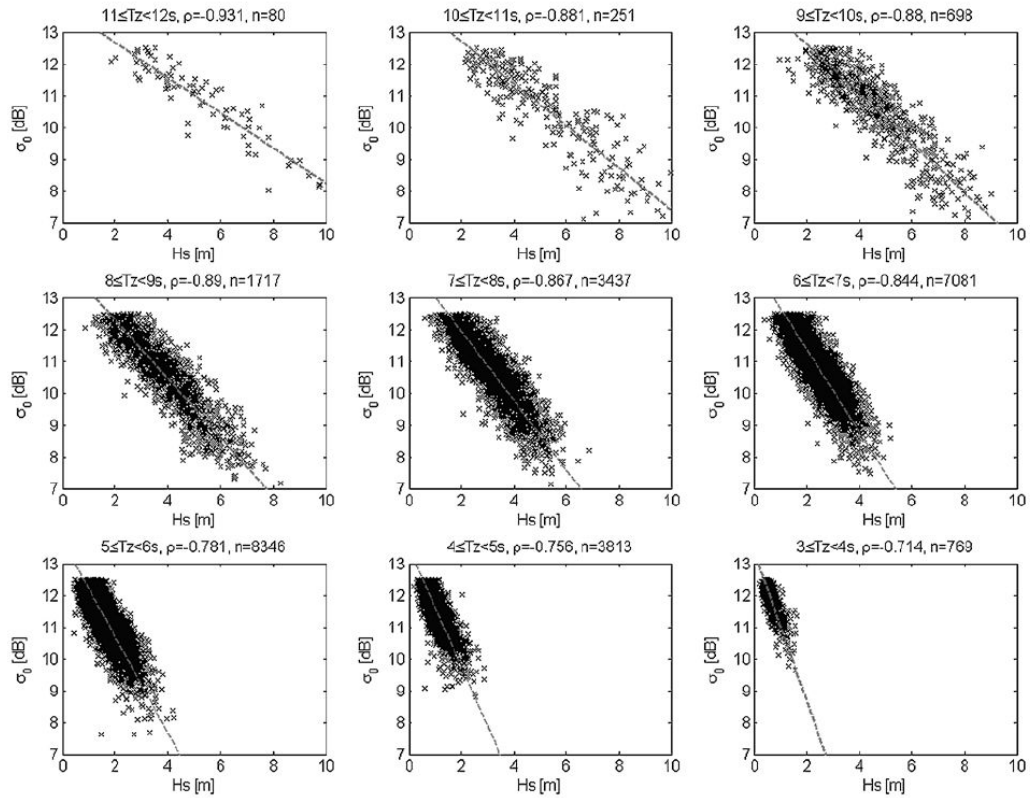


Figure 4. Linear fits to TOPEX data for T_z between 3 and 12 s. The correlation, ρ , and number of points, n , are given at the top of each plot.

[17] The slopes and intercepts of the fitted lines are shown in Figure 5 and Table 1. The slope of the line, B , varies smoothly with T_z . Lines of the following forms were fitted: (1) $B = \alpha T^2 + \beta T + \gamma$, (2) $B = \alpha T^\beta$, (3) $B = \alpha \exp(\beta T)$,

and (4) $B = \alpha + \beta \ln(T)$. The best results were obtained for $B = \alpha \exp(\beta T)$.

[18] For the intercept A , it was found that if the values of H_s were offset by a constant γ , then A remains roughly constant with T . For σ_0 above the threshold we find no dependence of T on σ_0 . It is therefore impossible to define an altimeter wave period model of the form $T = f(H_s, \sigma_0)$. So our model for T is

$$T = \begin{cases} \frac{1}{\beta} \ln \left[\frac{1}{\alpha} \left(\frac{\sigma_0 - A}{H_s + \gamma} \right) \right] & \text{if } \sigma_0 \leq \delta \\ \frac{1}{\beta} \ln \left[\frac{1}{\alpha} \left(\frac{\delta - A}{H_s + \gamma} \right) \right] & \text{if } \sigma_0 > \delta \end{cases} \quad (4)$$

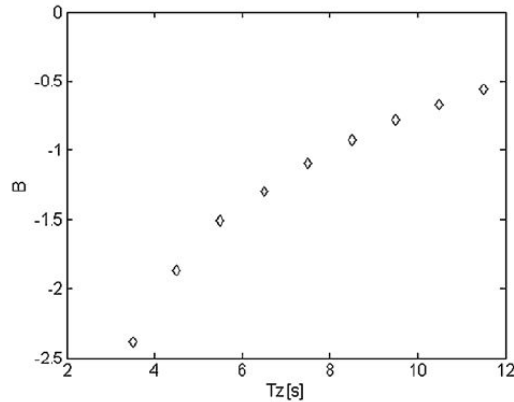


Figure 5. Scatterplot of slope of fitted line against T_z .

Table 1. Slope and Intercept of Fitted Line for Various T_z

T_z [s]	A	B
$3 \leq T_z < 4$	13.61	-2.103
$4 \leq T_z < 5$	13.48	-1.593
$5 \leq T_z < 6$	13.81	-1.409
$6 \leq T_z < 7$	13.97	-1.195
$7 \leq T_z < 8$	14.15	-1.028
$8 \leq T_z < 9$	14.24	-0.887
$9 \leq T_z < 10$	14.17	-0.725
$10 \leq T_z < 11$	14.25	-0.652
$11 \leq T_z < 12$	13.94	-0.563

Table 2. Results for the Two-Piece T_z Model, With 95% Confidence Intervals Given in Brackets

	N	A	α	β	γ	δ	$\sigma_0 \leq \delta$ dB		$\sigma_0 > \delta$ dB		Overall	
							Bias	rmse	Bias	rmse	Bias	rmse
TOPEX	8983	17.11 (± 0.27)	-4.054 (± 0.21)	-0.1558 (± 0.01)	1.658 (± 0.17)	12.87 (± 0.07)	0.0009 (± 0.0238)	0.54 (± 0.02)	0.0002 (± 0.1083)	0.87 (± 0.05)	0.0007 (± 0.0243)	0.59 (± 0.02)
POSEIDON	500	19.40 (± 2.08)	-2.831 (± 0.60)	-0.1090 (± 0.03)	3.496 (± 1.42)	12.811 (± 0.31)	0.00003 (± 0.1005)	0.55 (± 0.09)	0.0358 (± 0.4523)	0.88 (± 0.19)	0.0015 (± 0.1019)	0.60 (± 0.08)
JASON	3980	17.68 (± 0.50)	-4.094 (± 0.42)	-0.1488 (± 0.01)	1.851 (± 0.30)	12.950 (± 0.17)	0.0001 (± 0.0341)	0.53 (± 0.03)	0.0028 (± 0.1599)	0.90 (± 0.06)	-0.0001 (± 0.0348)	0.59 (± 0.02)
ERS-2	8283	17.42 (± 0.38)	-3.906 (± 0.23)	-0.1422 (± 0.01)	2.072 (± 0.22)	12.39 (± 0.08)	-0.0007 (± 0.0248)	0.54 (± 0.02)	0.0004 (± 0.0933)	0.83 (± 0.04)	-0.0008 (± 0.0241)	0.59 (± 0.02)
ENVISAT	2918	16.28 (± 0.45)	-4.248 (± 0.42)	-0.1630 (± 0.01)	1.314 (± 0.27)	12.29 (± 0.11)	0.0000 (± 0.0395)	0.50 (± 0.02)	0.0048 (± 0.1612)	0.85 (± 0.11)	0.0002 (± 0.0408)	0.56 (± 0.03)
GFO	6069	17.16 (± 0.31)	-4.550 (± 0.301)	-0.1648 (± 0.01)	1.669 (± 0.18)	12.88 (± 0.09)	0.0008 (± 0.0277)	0.51 (± 0.01)	0.0014 (± 0.1186)	0.83 (± 0.04)	0.0006 (± 0.0283)	0.56 (± 0.01)
						Mean	0.0003	0.53	0.0068	0.86	0.0004	0.58

[19] To fit the model described by equation (4) we divide the collocated data set into a development data set (50%) for the determination of the fitted coefficients, and a validation data set (50%) for the calculation of bias and RMS error. The data forming the development and validation data sets are sampled at random without replacement from the original data set. The model is fitted using a simplex search method [Lagarias *et al.*, 1998] to find the five parameters A , α , β , γ , and δ , which minimize the sum of squared residuals $(T(alt) - T(buoy))^2$.

[20] It was found that if the fitting process was repeated, there were small variations in the fitted parameters and also in the bias and RMS error in the validation data set. This is due to the random nature of separating the collocated data into development and validation data sets. To account for this the fitting process was carried out 1000 times to establish confidence bounds on all the parameters. All parameters were observed to vary normally about their mean values, and the 95% confidence intervals quoted have been calculated as 1.96 times the standard deviation of the parameter.

4. Results

[21] The model was fitted for both T_z and T_e . The fitted parameters and confidence intervals are shown in Tables 2 and 3. The bias is calculated as the mean of $T(alt) - T(buoy)$ and the RMS error is calculated as the square root of the mean of $(T(alt) - T(buoy))^2$. Values of bias and RMS error are given for each section of the two-piece model, and

an overall value. The differences in the fitted model parameters between altimeters are most likely due to calibration differences in both H_z and σ_0 .

[22] For comparison the G03 and Q04 models were also fitted. The Q04 model is defined only for using TOPEX data for $\sigma_0 \leq 16$ dB, comprising 8866 data points. The bias in T_z is -0.067 s, with an RMS error of 0.69s.

[23] The G03 model was fitted for each altimeter, following the authors' method. That is, σ_0 was kept in its linear, nondecibel form and orthogonal regression was used to find A and B such that $\log_{10}(T_z) = A + B \log_{10}(X)$ where $X = \sigma_0^{0.25} H_s^{0.5}$. Again, the collocated data set was divided into development and validation data sets and the fit was repeated 1000 times to establish confidence bounds for the parameters. The results are given in Table 4. It can be seen that, the two-piece algorithm has negligible bias and performs better than both the Q04 and G03 algorithms in terms of RMS error, with 15% reduction in RMS error from Q04 and 25% reduction from G03.

[24] Figure 6 shows scatterplots of the three algorithms against the buoy measurements for TOPEX data, with the contours showing the distribution of the data (contours are omitted from the top right plot as there are an insufficient number of data points). Similar trends were observed for other altimeters. Below 12.5dB the plot for the two-piece algorithm shows a tighter distribution about the line T_z (altimeter) = T_z (buoy) than both the Q04 and G03 algorithms. The same plot for T_e (Figure 7) has considerably more scatter. The slight discretization of the two-piece T_z and T_e values, for $\sigma_0 > \delta$, visible in Figures 6 and 7 is due to

Table 3. Results for the Two-Piece T_e Model, With 95% Confidence Intervals Given in Brackets

	N	A	α	β	γ	δ	$\sigma_0 \leq \delta$ dB		$\sigma_0 > \delta$ dB		Overall	
							Bias	rmse	Bias	rmse	Bias	rmse
TOPEX	8983	15.80 (± 0.25)	-3.373 (± 0.277)	-0.1232 (± 0.0078)	1.384 (± 0.205)	12.48 (± 0.09)	0.0003 (± 0.0431)	0.97 (± 0.03)	0.0049 (± 0.1424)	1.40 (± 0.07)	0.0005 (± 0.0423)	1.05 (± 0.03)
POSEIDON	500	18.22 (± 1.96)	-2.380 (± 0.478)	-0.0802 (± 0.0213)	3.309 (± 1.495)	12.58 (± 0.19)	-0.0001 (± 0.2043)	1.05 (± 0.12)	0.0377 (± 0.6119)	1.36 (± 0.22)	0.0021 (± 0.2000)	1.10 (± 0.10)
JASON	3980	16.34 (± 0.44)	-3.191 (± 0.355)	-0.1126 (± 0.0111)	1.701 (± 0.344)	12.50 (± 0.12)	-0.0021 (± 0.0645)	0.95 (± 0.05)	0.0022 (± 0.2122)	1.45 (± 0.10)	-0.0024 (± 0.0640)	1.06 (± 0.04)
ERS-2	8283	16.05 (± 0.48)	-3.225 (± 0.265)	-0.1098 (± 0.0099)	1.784 (± 0.339)	12.08 (± 0.06)	0.0004 (± 0.0455)	0.97 (± 0.03)	0.0037 (± 0.1366)	1.31 (± 0.06)	0.0007 (± 0.0435)	1.04 (± 0.03)
ENVISAT	2918	15.37 (± 0.46)	-3.253 (± 0.379)	-0.1181 (± 0.0126)	1.251 (± 0.359)	11.98 (± 0.10)	-0.0008 (± 0.0707)	0.88 (± 0.05)	-0.0024 (± 0.2023)	1.27 (± 0.12)	-0.0019 (± 0.0701)	0.96 (± 0.05)
GFO	6069	15.87 (± 0.27)	-3.940 (± 0.327)	-0.1332 (± 0.0080)	1.338 (± 0.177)	12.54 (± 0.11)	0.0010 (± 0.0525)	0.92 (± 0.03)	0.0020 (± 0.1664)	1.33 (± 0.07)	0.0006 (± 0.0521)	1.00 (± 0.03)
						Mean	-0.0002	0.96	0.0080	1.35	-0.0001	1.03

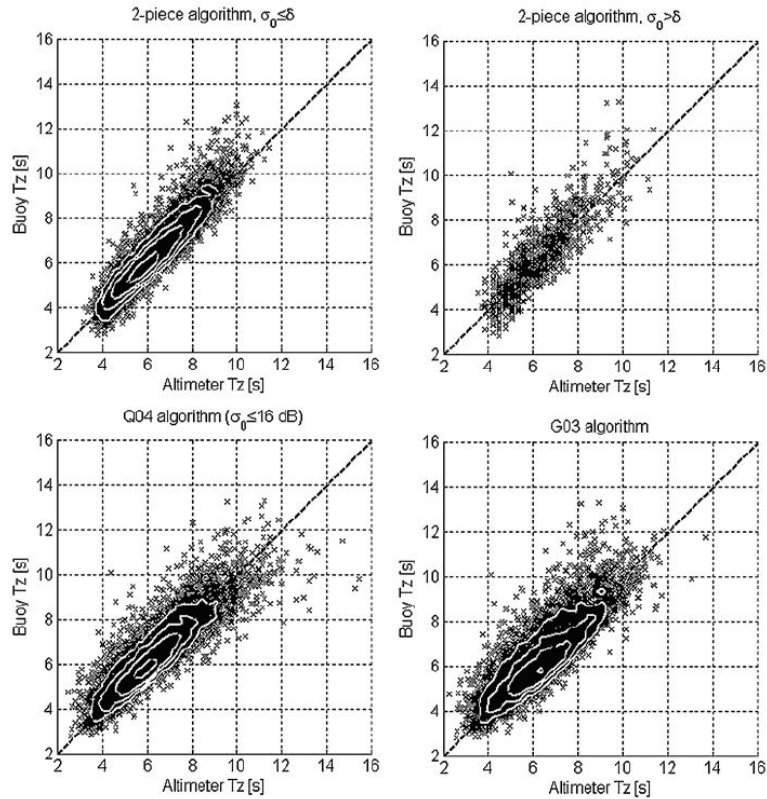
Table 4. Results for the G03 T_z Model, With 95% Confidence Intervals Given in Brackets

	N	A	B	Bias	rmse
TOPEX	8983	0.382 (± 0.007)	0.941 (± 0.015)	-0.007 (± 0.033)	0.794 (± 0.017)
POSEIDON	500	0.435 (± 0.029)	0.819 (± 0.062)	-0.014 (± 0.134)	0.788 (± 0.093)
JASON	3980	0.410 (± 0.017)	0.883 (± 0.039)	-0.014 (± 0.046)	0.774 (± 0.029)
ERS-2	8283	0.452 (± 0.006)	0.839 (± 0.014)	-0.015 (± 0.034)	0.782 (± 0.018)
ENVISAT	2918	0.323 (± 0.010)	1.067 (± 0.023)	0.001 (± 0.057)	0.766 (± 0.030)
GFO	6069	0.463 (± 0.006)	0.796 (± 0.014)	-0.015 (± 0.038)	0.746 (± 0.019)
			Mean	-0.011	0.775

the fact that the period algorithm only depends on H_s in this region and TOPEX H_s measurements were reported to the nearest 0.1 m (the small number of intermediate values are due to the drift correction at the end of the side A circuit). The effect on the derived values of T_z is small, for $H_s = 1.0$ m, the discretization is 0.3 s and at $H_s = 3.0$ m the discretization is 0.14 s.

[25] Figure 8 shows the fit of the three models to the collocated TOPEX data. It is clear that the G03 model does not follow the contours of the data. This is a result of the a priori definition of the exponents in their expression for X . The Q04 model follows the contours of the data reasonably well, but has the clear disadvantage that the range of applicability is limited to $\sigma_0 < 16$ dB. The two-piece model follows the contours well over the entire range of the data; however, the sharp corner at $\sigma_0 = \delta$ is likely to be an oversimplification. It should be noted that the two-piece algorithm will give negative values of period if H_s and σ_0 are both low, but these are far outside the normal range of H_s and σ_0 and a negative value of period will probably indicate a bad measurement of either H_s or σ_0 .

[26] The new algorithm displays a marked improvement in the residual errors (see Figure 9) with a reduced scatter and less residual trend than the G03 and Q04 algorithms, particularly with the buoy significant steepness and altimeter backscatter. For the two-piece algorithm there is a noticeable residual trend with the buoy T_z . However, there is no residual trend with altimeter T_z (not shown here) so it is not possible to apply a simple correction for this. The

**Figure 6.** Scatterplots of altimeter T_z against buoy T_z for the Q04, G03, and two-piece algorithms using TOPEX data, with contours showing distribution of data.

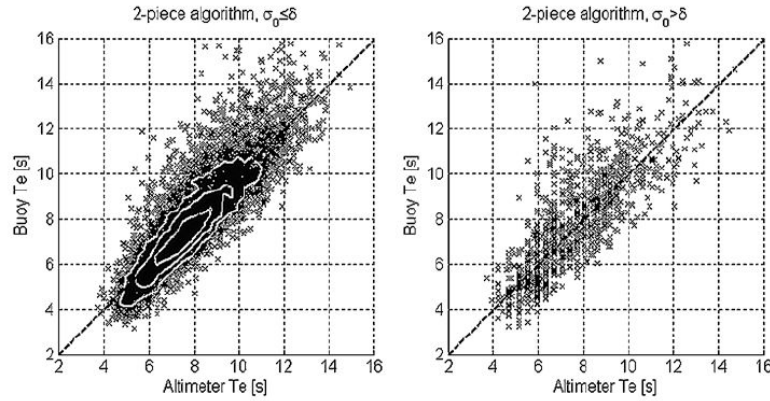


Figure 7. Scatterplot of altimeter T_e (two-piece algorithm) against T_e (buoy) for TOPEX data, with contours showing distribution of data.

reason for the residual trend with buoy T_z is discussed in section 5.

[27] In Figure 10 the distributions of T_z and significant steepness from buoy data are compared with those derived from altimeters via the three models. The two-piece algorithm shows the best fit to the buoy data, particularly for steepness.

[28] Though much improved, the two-piece algorithm still over-predicts steepness occurrence around the mode at 0.04. The reason why steepness distribution is too peaked is that the mean steepness for σ_0 below ~ 13 dB is always greater than about 0.02 (see Figure 3) and the lower part of the two-piece model emulates this mean trend. This also explains the residual trend of underestimation for low steepness in Figure 9. Note also that while the altimeter distribution declines smoothly to the right of the peak, to the left it features a small hump at around 0.02. This is due to the form of the upper part of the algorithm which is solely dependent on H_s and therefore has no variation in steepness for a given H_s .

[29] The T_z distribution produced by the two-piece algorithm is very close to that of the Q04 algorithm (see Figure 10). Both are a slight improvement on the G03 algorithm in terms of the location of the peak.

[30] The joint distribution of H_s with T_z for the buoy data and the three models is shown in Figure 11. The new algorithm is clearly better than the G03 algorithm in its ability to reproduce the joint distribution and is a better match to the peak of the distribution than the Q04 algorithm. The G03 algorithm's poor reproduction of the joint distribution of H_s and T_z is a result of its strong dependence on H_s . For $\sigma_0 > \delta$ the two-piece algorithm has no dependence on σ_0 , therefore it is not possible to reproduce the joint distribution of wave height and period in this range. However, the algorithm is able to follow the mean value of T_z , as shown in Figure 12.

5. Discussion

[31] An altimeter wave period model of the form $T = f(H_s, \sigma_0)$ can only give one value of period for a given H_s and σ_0 . However, from the collocated data set it is clear that

for a given H_s and σ_0 there are a range of values of T_e and T_z . In this section we discuss how this will affect the performance of an altimeter wave period model.

[32] Figure 13 shows the standard deviation and skewness in the distribution of T_z for the combined collocated data, binned by H_s and σ_0 . It is clear that there is considerable variation of the measured buoy period for a given value of H_s and σ_0 . Because the two-piece algorithm is matched to the mean value of period in each bin, it cannot reproduce the full range of periods observed and will miss low and high values. The positive skewness in the distribution means that period values higher than the mean are more frequent or lie further from the mean than lower values. These two characteristics of the data imply that the residual trend with buoy T_z , for the two-piece model (Figure 9) is a result of the physical relationship between H_s , σ_0 and T_z rather than the fit of the model.

[33] Measurements with high σ_0 correspond to times of low wind speed ($\sigma_0 = 13$ dB $\Leftrightarrow U_{10} \approx 4$ ms $^{-1}$) or, equivalently, swell conditions. Since we can only create a period algorithm based on H_s when $\sigma_0 > \delta$, we are forced to create a model in which all swell has same steepness for a given H_s . The limitation posed by the step change in the response of σ_0 around 13 dB does not seem too severe. The range of steepness is in fact quite small for $\sigma_0 > \delta$ (see Figure 3b) and from Figure 6 we can see that the performance of the model is reasonable for $\sigma_0 > \delta$ with fairly low levels of scatter and an RMS error of less than 0.9 s for T_z . The information that σ_0 is above the threshold is sufficient to infer that the wave conditions are swell dominated and period can be reasonably well estimated from H_s alone.

[34] The higher RMS error of the model when $\sigma_0 > \delta$ is partly a result of the greater variation in T_z for higher σ_0 values, displayed in Figure 13. In swell conditions integral period parameters are only weakly related to the high-frequency part of the spectrum on which backscatter is strongly dependent, so it is not surprising that the backscatter is not correlated to wave period in low wind conditions. Conversely, above a certain wind speed, from the good performance of our period model we can infer that integral wave period parameters are strongly correlated to some

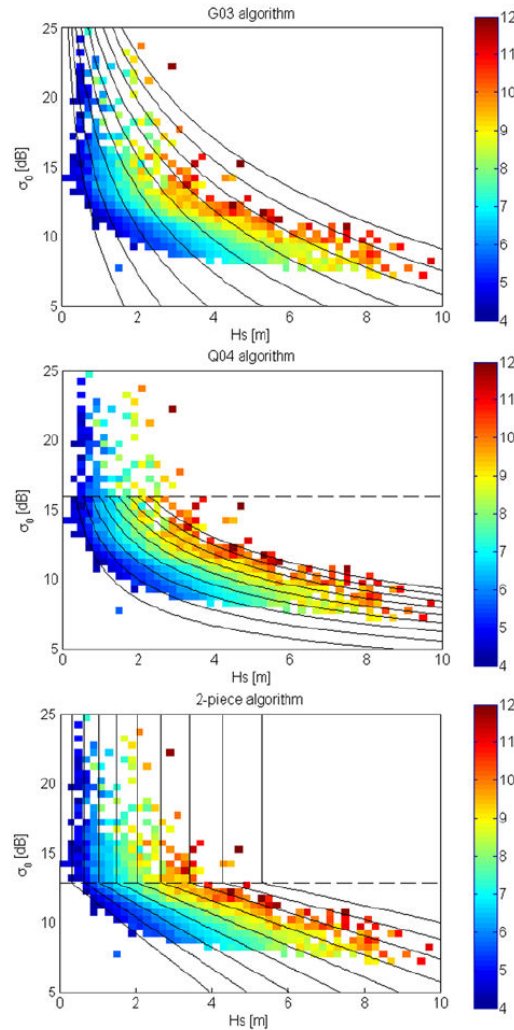


Figure 8. Mean T_z binned by H_s and σ_0 for TOPEX data with contours of T_z for the two-piece, Q04 and G03 models overlaid. Contours are at 1 s intervals, from 4 to 12 s.

function of H_s and the shape of the high-frequency tail of the spectrum. The precise determination of how σ_0 is related to the shape and energy of the wave spectrum is beyond the scope of this paper.

[35] *Caires et al.* [2005] noted that the G03 algorithm performs worse in times of high swell component or low wind speed. They suggest this is due to one of the physical assumptions used to derive the model breaking down for swell conditions. However, from Figure 8 we can see that the model contours do not follow the data very well over the rest of the range either, so we suggest that this is not related to the change in response of σ_0 but a mismatch between the model and the physics.

[36] The strong dependence of backscatter on the high-frequency components of the spectrum is consistent with the fact that we observe more variability in T_e than T_z for a given value of H_s and σ_0 (see Figure 14). T_z is more dependent on the higher-frequency components of the spectrum as it varies with m_2 , while T_e depends more on the lower-frequency components, since it varies with m_{-1} . The higher variability for T_e was also evident in the higher RMS error for the T_e model compared to the T_z model. Indeed, when we fit the model for T_m we find that $rmse(T_e) > rmse(T_m) > rmse(T_z)$.

[37] Figure 15 shows scatterplots of T_z against T_e for buoy measurements and the two-piece altimeter model. From the buoy measurements it can be seen that there is not a fixed relationship between T_e and T_z since the ratio of T_e/T_z depends on the spectral shape. For the altimeter model we see a near-constant relationship between T_e and T_z , implying that the two-piece model is not able to discern changes in spectral shape. This is probably a result of the strong dependence of σ_0 on the high-frequency components of the spectrum.

[38] Part of the discrepancy between the buoy and altimeter estimates of wave period is due to the fact that buoys and altimeters are sensitive to different sea surface length scales. Altimeter backscatter measurements are dependent on centimetric scale waves, whereas the buoys used in this study have a high-frequency limits of either 0.4 Hz or 0.485 Hz (see Table A2) corresponding to wavelengths of 6.6 m and 9.8 m. Buoy measurements of period are subject to systematic errors as a result of their inability to measure the high-frequency part of the spectrum. *Caires et al.* [2005] note that T_z is sensitive to the value of the high-frequency cutoff used to calculate the spectral moments. If the moments of the spectrum are calculated as the integral over frequencies from 0 to a finite frequency rather than to infinity, then T_z will be overestimated. For example, in the case of a Pierson-Moskowitz spectrum with a cutoff of 0.4 Hz, typical of buoys, T_z will be overestimated 16% for a peak frequency of 0.2 Hz, 4% for a peak frequency of 0.1 Hz, and 1% for a peak frequency of 0.05 Hz. The cut off is less important for T_e , with a 4% overestimate for a peak frequency of 0.2 Hz and 0.3% overestimate for a peak frequency of 0.1 Hz.

[39] *Quilfen et al.* [2004] show that using backscatter measurements at C-band and Ku-band frequencies enables a more accurate algorithm to be developed. Since C-band (4.20–5.75 GHz) measurements are at a lower frequency than Ku-band (10.9–22.0 GHz), they are dependent on slightly longer waves. Thus by using the measurements at both frequencies, it is possible to extract more information on the shape of the entire spectrum and hence integral period parameters. It is likely that using the S-band (1.55–4.20 GHz) measurements of Envisat it will be possible to create a more accurate algorithm still, as the backscatter will depend on even lower frequencies.

[40] From the above discussion it is clear that there is a limit to how accurate a period function of the $T = f(H_s, \sigma_0)$ can be. To benchmark the performance of our parametric two-piece model, we can use a basic nonparametric model such as a look-up table of values. That is, the altimeter period is defined to be the mean buoy period from the collocated data for a given bin of H_s and σ_0 . The choice of

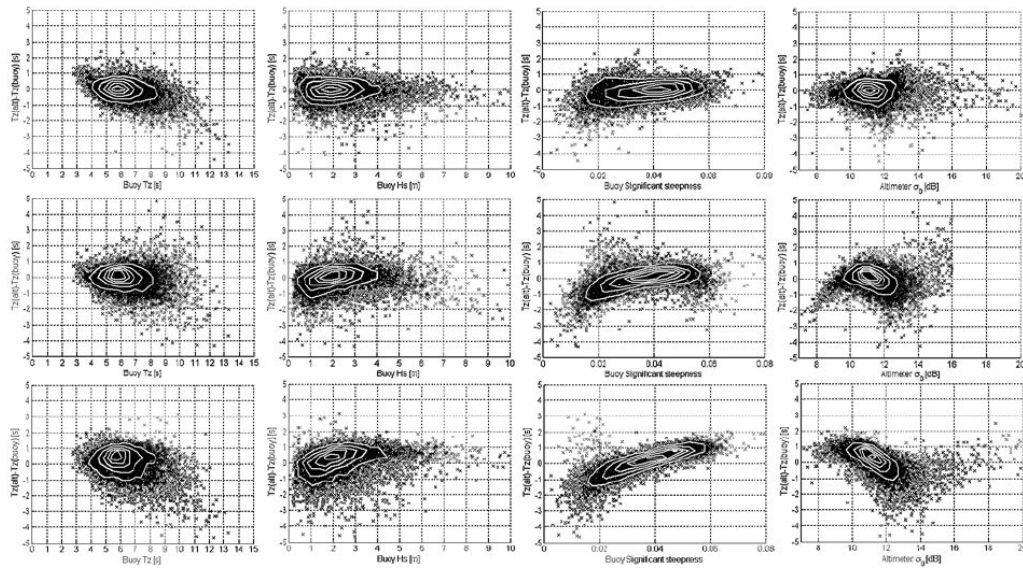


Figure 9. Residual errors for the (top) two-piece model, (middle) Q04 model, and (bottom) G03 model for TOPEX data, with contours showing distribution of data.

bin size is a compromise between having sufficient data in each bin to give a smooth distribution of period across the look-up table and increasing the retrieval error from having too coarse a resolution. From limited experimentation it was found that bins of size 0.1 m by 0.2 dB, gave adequate results.

[41] Splitting the data into development and validation data sets and using the development data set to form the look-up table for the validation data set proved always to give a higher RMS error than the two-piece function. This was due to not having sufficient data to both have a good resolution and smooth distribution, even when the development data set is defined to be 80% of the entire collocated data set.

[42] When the data set is not split, the RMS retrieval error gives an idea of the limit of the accuracy of a function of the form $T = f(H_s, \sigma_0)$. The results are given below in Table 5. When looking at these results, it is important to remember that this method of defining the altimeter period is circular (i.e., the same data is used for development and validation) and, as stated above, when the data is split in two this method does not perform as well as our model. We also note that the results for Poseidon are spuriously low. This is because a large number of bins in the look-up table contain only one data point, so the retrieved value for that bin will have zero error.

[43] The lowest possible RMS error will lie somewhere between the values in Table 5 and the values for our function. It

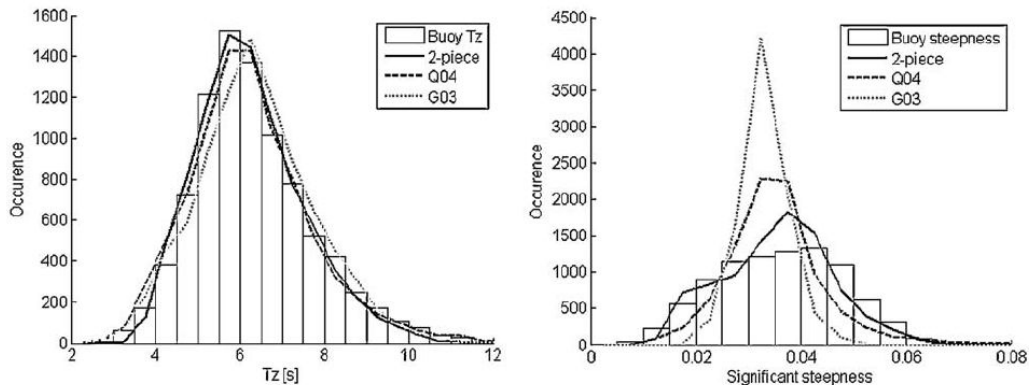


Figure 10. Histograms of buoy and altimeter T_z and significant steepness for TOPEX (data is $\sigma_0 < 16$ dB for comparison with Q04).

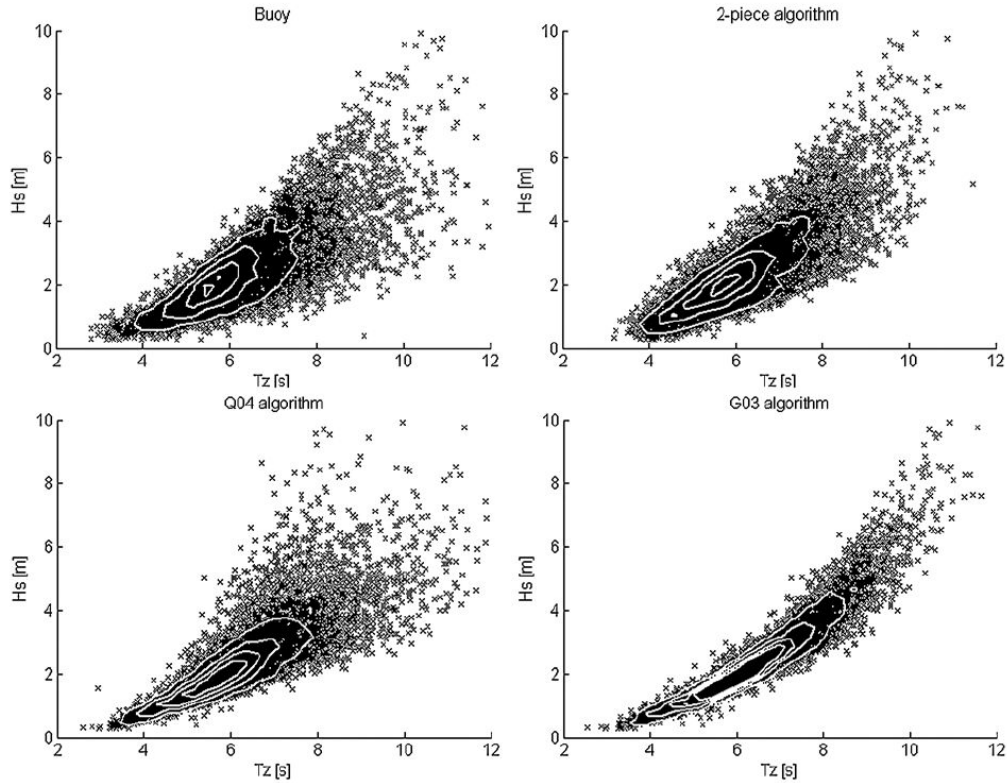


Figure 11. Buoy and altimeter joint distribution of H_s and T_z from buoy and altimeter data (TOPEX, $\sigma_0 \leq \delta$), with contours showing distribution of data.

is reassuring to see that these values are close: a difference of 0.11 s on average for T_z and 0.14 s for T_s (both ignoring Poseidon). The plots of residual errors for the look-up table method (not shown here) display the same trends as for the two-piece model (see Figure 9). This implies that these trends are a result of the relationship between the backscatter and wave period, rather than the fit of the model.

[44] If we had sufficient data then a look-up table method could possibly give a lower RMS error than our function, but in the present case we would need to smooth and interpolate the look-up table. The two-piece model has the advantage that it effectively does this by assuming a model function of the form of equation (4).

[45] From the above discussion we may draw the conclusion that it is not possible to create an altimeter wave period function of comparable accuracy to in situ measurements, from Ku-band H_s and σ_0 alone. However, we must also bear in mind that we are comparing two measurements of a random process, subject to instrumental error, that are separated by both time and space. *Monaldo* [1988] considers all these factors in detail for the case of significant wave height. A full discussion of all of these factors is beyond the scope of this paper, but we note that period parameters are subject to higher sampling variabilities than H_s , so we

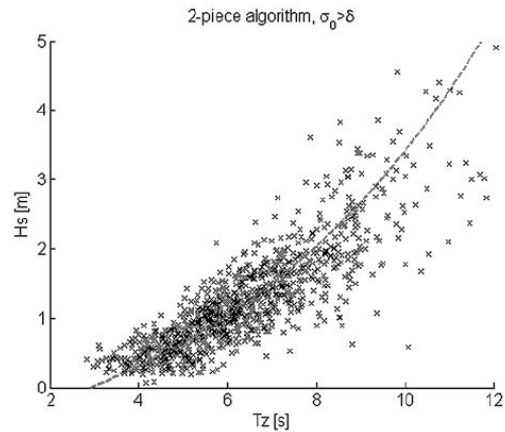


Figure 12. Joint distribution of H_s and T_z from buoy data when TOPEX $\sigma_0 > \delta$. The dashed line shows the value of T_z for two-piece algorithm.

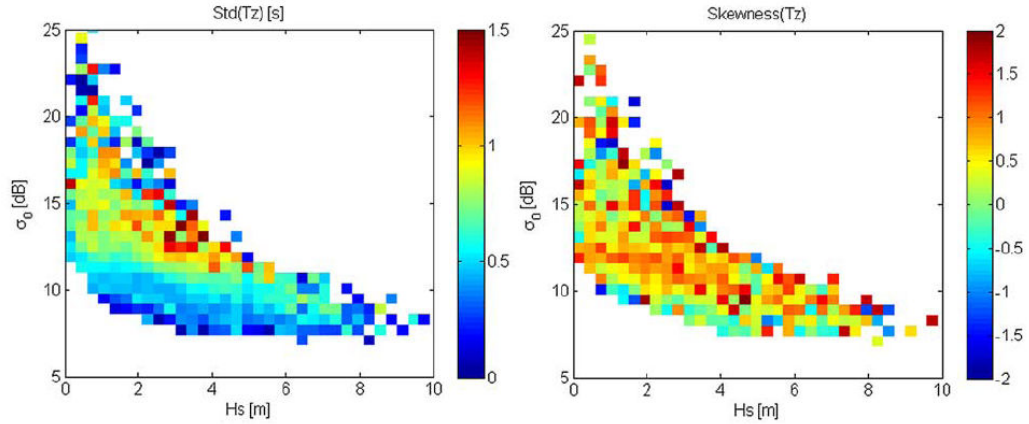


Figure 13. Standard deviation and skewness of T_z for data binned by H_s and σ_0 , for combined collocated data.

should expect a certain amount of variability from this alone. Since our model is fitted by finding parameters A , α , β , γ , and δ , which minimize the sum of squared residuals, we are implicitly assuming that there is no error in the buoy measurement of period. This is clearly not true, but is a fair approximation given that the error in the altimeter period measurement is likely to be much higher.

6. Conclusions

[46] It has been demonstrated that the two-piece altimeter wave period model we have developed performs better than the Q04 and G03 models in all metrics which we have considered. The relationship between H_s , σ_0 and wave period has been discussed. We can conclude that there is no fixed relationship between these three variables, however

there is a strong correlation, which allows a reasonable estimate of period to be calculated.

[47] It has been shown that there is a limit to the accuracy it is possible to achieve from an altimeter period function of Ku-band H_s and σ_0 alone and we showed that our model comes close to this. It may be possible to achieve a more accurate function if the user is only concerned with data for certain ranges of H_s and period, but the improvement which is possible is likely to be small. In particular the sharp corner in our two-piece function is likely to introduce some error in this range.

[48] The altimeter two-piece algorithm for T_z performs better than SAR T_z algorithm of *Schulz-Stellenfleth et al.* [2007], but the SAR algorithm performs better for T_e than the altimeter algorithm. This is because of the different wavelength scales that each instrument is sensitive to.

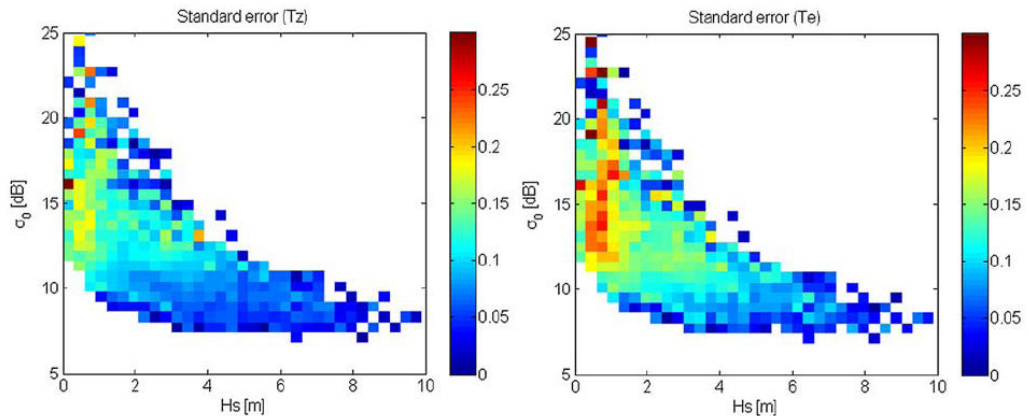


Figure 14. Standard error of T_z and T_e (defined as the standard deviation divided by the mean) for data binned by H_s and σ_0 , for combined collocated data.

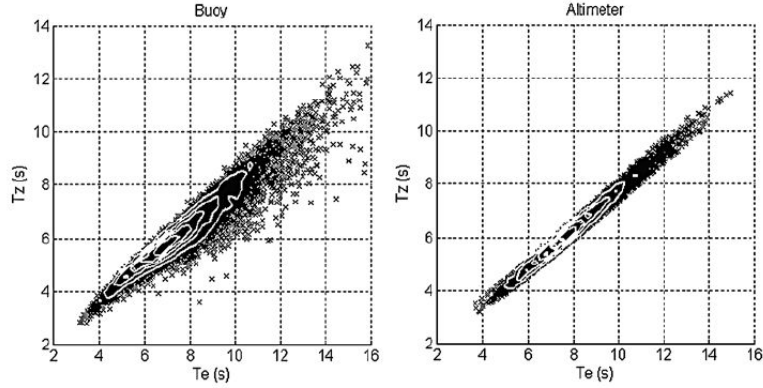


Figure 15. Scatterplots of T_z against T_e for buoy measurements and the two-piece altimeter model (TOPEX data).

[49] For a given value of H_s and σ_0 there is considerable variation in the period measured by the buoy. This is likely to be due to the dependence of σ_0 on the shape of the whole spectrum rather than a single integral parameter. Validation of the model is therefore required in other areas, particularly in the southern ocean, since the fit of our model may depend on the range of spectral shapes at the buoys used in the collocation.

Appendix A: Construction of the Collocated Data Set

A1. Altimeter Data

[50] Altimeter data has been retrieved from the RADS database [Scharroo, 2005] held at the National Oceanography Centre (Southampton, UK) for TOPEX, Poseidon, Jason, ERS-2, Envisat, and Geosat Follow-On (GFO). TOPEX values of H_s have been corrected for the drift at end of the life of the TOPEX Side A circuitry using a quadratic function based on ERS2-TOPEX crossovers. TOPEX Side B values have been offset slightly to conform to side A levels. We therefore consider data from the TOPEX A and B-side circuits as one data set. Other than this, no calibrations have been applied to the data.

[51] A series of quality checks has been developed for each altimeter based on various methods published to date [e.g., Carter et al., 1992; Cotton and Carter, 1996]. The tests for each altimeter depend on the parameters provided by the space agencies, for example no information on the standard deviation of the 20 Hz values of H_s is available for

Poseidon. The tests have been developed through examination of cumulative probability plots of various parameters (e.g., standard deviation of 10 or 20 Hz values of H_s) and histograms of percentage of data failing each test against H_s

Table A1. Details on the Series of Quality Checks Developed for Each Altimeter Based on Various Methods Published to Date

Altimeter	Criteria
ERS-2	$N \geq 15$ $0 < s.d.(h) < 0.06 + 0.1H_s$ $0 < s.d.(H_s) < 0.35 + 0.03H_s$ $0 < s.d.(\sigma_0) < 0.03\sigma_0$ H_s quality flag σ_0 quality flag
Poseidon	$N \geq 18$ $0 < s.d.(h) < 0.1 + 0.02H_s$ $\theta < 0.2$ θ quality flag Ice flag
GFO	$N \geq 9$ $0 < s.d.(h) < 0.1 + 0.01H_s$ $s.d.(H_s) < 0.15 + 0.033H_s$ $0 < \theta < 0.625$ H_s quality flag σ_0 quality flag θ quality flag
JASON	$N \geq 18$ $0 < s.d.(h) < 0.08 + 0.014H_s$ $0 < s.d.(H_s) < 0.65 + 0.05H_s$ $0 < \theta < 0.3$ $ H_s(Ku) - H_s(C) < 1$ H_s quality flag σ_0 quality flag θ quality flag Ice flag
ENVISAT	$N \geq 18$ $0 < s.d.(h) < 0.10 + 0.018H_s$ $0 < s.d.(H_s) < 0.067 + 0.086H_s$ $0 < s.d.(\sigma_0) < 0.03\sigma_0$ $0 < \theta < 0.3$ $ H_s(Ku) - H_s(S) < 3$
TOPEX	$N \geq 8$ $0 < s.d.(h) < 0.07 + 0.007H_s$ $0 < s.d.(H_s) < 0.1$ or $0.1H_s$ $0 < s.d.(\sigma_0) < 0.2$ $ H_s(Ku) - H_s(C) < 0.5$ θ quality flag

Table 5. Rms Errors for the Look-Up Table Method

	T_z rmse (s)	T_e rmse (s)
TOPEX	0.51	0.94
POSEIDON	0.26	0.53
JASON	0.44	0.86
ERS-2	0.50	0.93
ENVISAT	0.44	0.78
GFO	0.46	0.87

Table A2. Details of the NDBC Moored Buoys Used in the Collocated Data Set

Buoy Number	Latitude (deg)	Longitude (deg)	Depth (m)	Frequency Range (Hz)	Buoy Size (m)	Buoy Type	Data Period
41001	34.7	-72.7	4426.8	0.030-0.400	6	nomad	1996-2005
41002	32.3	-75.4	3785.6	0.030-0.400	6	nomad	1996-2005
41006	29.3	-77.4	~1000	0.030-0.400	6	nomad	1996
41010	29.0	-78.5	872.6	0.030-0.400	6	nomad	1996-2004
				0.020-0.485			2004-2005
41040	14.5	-53.0	4572.0	0.020-0.485	6	nomad	2005
41041	14.5	-46.0	3352.8	0.020-0.485	6	nomad	2005
42001	25.9	-89.7	3246.0	0.020-0.485	12	discus	1996-2005
42002	25.2	-94.4	3200.0	0.020-0.485	10	discus	1996-2005
42003	26.1	-85.9	3233.0	0.020-0.485	10	discus	1996-2005
42038	27.4	-92.6	1152.0	0.020-0.485	3	discus	2004-2005
42041	27.5	-90.5	1435.6	0.020-0.485	3	discus	2000-2005
42055	22.0	-94.0	3380.5	0.020-0.485	12	discus	2005
42056	19.9	-85.1	4446.0	0.020-0.485	12	discus	2005
42057	16.8	-81.5	293.0	0.020-0.485	10	discus	2005
42058	15.1	-75.1	4042.0	0.020-0.485	10	discus	2005
44004	38.5	-70.4	3182.1	0.030-0.400	6	nomad	1996-2004
				0.020-0.485			2004-2005
46001	56.3	-148.2	4206.0	0.030-0.400	6	nomad	1996-2005
46002	42.6	-130.3	3374.0	0.030-0.400	6	nomad	1996-2003
46003	51.8	-155.9	~3000	0.030-0.400	6	nomad	1996-1999
46005	46.1	-131.0	2779.8	0.030-0.400	6	nomad	1996-2004
				0.020-0.485			2004-2005
46006	40.8	-137.5	4023.4	0.030-0.400	6	nomad	1996-2005
46035	57.1	-177.6	3662.3	0.030-0.400	6	nomad	1996-2002
				0.020-0.485			2002-2005
46059	38.0	-130.0	4599.4	0.030-0.400	6	nomad	1996-2005
46066	52.7	-155.0	4999.9	0.030-0.400	6	nomad	1996-2004
				0.020-0.485			2004-2005
51001	23.4	-162.2	3252.0	0.030-0.400	6	nomad	1996-2005
				0.020-0.485			2005
51002	17.2	-157.8	5002.0	0.030-0.400	6	nomad	1996-2004
				0.020-0.485			2004-2005
51003	19.2	-160.8	4943.2	0.030-0.400	6	nomad	1996-2005
51004	17.5	-152.5	5303.5	0.030-0.400	6	nomad	1996-2003
				0.020-0.485			2003-2005

(or σ_0). The performance of the tests has been verified by examination of plots of H_s (or σ_0) for individual tracks and found to remove the vast majority of spurious data spikes while removing only a very small quantity of apparently good data.

[52] Details of the quality checks are given in Table A1. The following notation is used to describe the quality checks: N is the number of averaged 10 Hz or 20 Hz values, h is the range, and θ is the off-nadir angle.

[53] To avoid confusion with the backscatter coefficient σ_0 , the notation *s.d.* (x) is used to denote the standard deviation of variable x . Unless otherwise indicated, the notations refer to the Ku-band values.

A2. Buoy Data

[54] One-dimensional spectra have been retrieved from 28 moored buoys operated by the U.S. National Data Buoy Center (NDBC). Details of the buoys used are given in Table A2. The NDBC buoy network is the largest source of open ocean buoy data with calibrated to a consistent standard. It has been noted by previous authors [e.g., *Challenor and Cotton*, 2002] that buoy networks operated by other agencies (e.g., UK Met Office, Meteorological Services of Canada, Japan Meteorological Agency) have different calibrations relative to the altimeter H_s . Therefore only NDBC buoy data has been used in this analysis. For details of the estimation of omnidirectional wave spectra and quality control procedures for the buoy data, see *National Data Buoy Center* [1996, 2003].

[55] It was noticed that some of the spectra files downloaded from the NDBC website have incorrect frequency headers. If not corrected, this will obviously bias the spectral moments. The affected files are all for 2005, for buoys 41001, 41002, 42019, 42020, 44005, 44014, 46001, 46006, and 46059. However, the files archived in the National Oceanographic Data Center (NODC) have the correct frequency headers. The NDBC have confirmed this error, but at the time of writing the files on the NDBC Web site have not been corrected. Data from these files has not been used in this study, but this note is included for the information of other users of NDBC data.

A3. Collocation Criteria

[56] Time and space separation criteria of 100 km and 30 min have been used to define a coincident measurement. The median of the altimeter measurement within 100 km of the buoy is used in preference to the nearest 1 Hz value as it was found to reduce the random sampling variability and remove some outliers. The use of the median value for estimating H_s over a $2^\circ \times 2^\circ$ is recommended by *Carter* [1990]. He finds no evidence of skewness in the distribution of H_s across the square, with an average difference between the median and the mean which is not significantly different from zero.

A4. Further Quality Checks

[57] To further remove any bad points from the collocated data set, we can choose to only keep points where the buoy

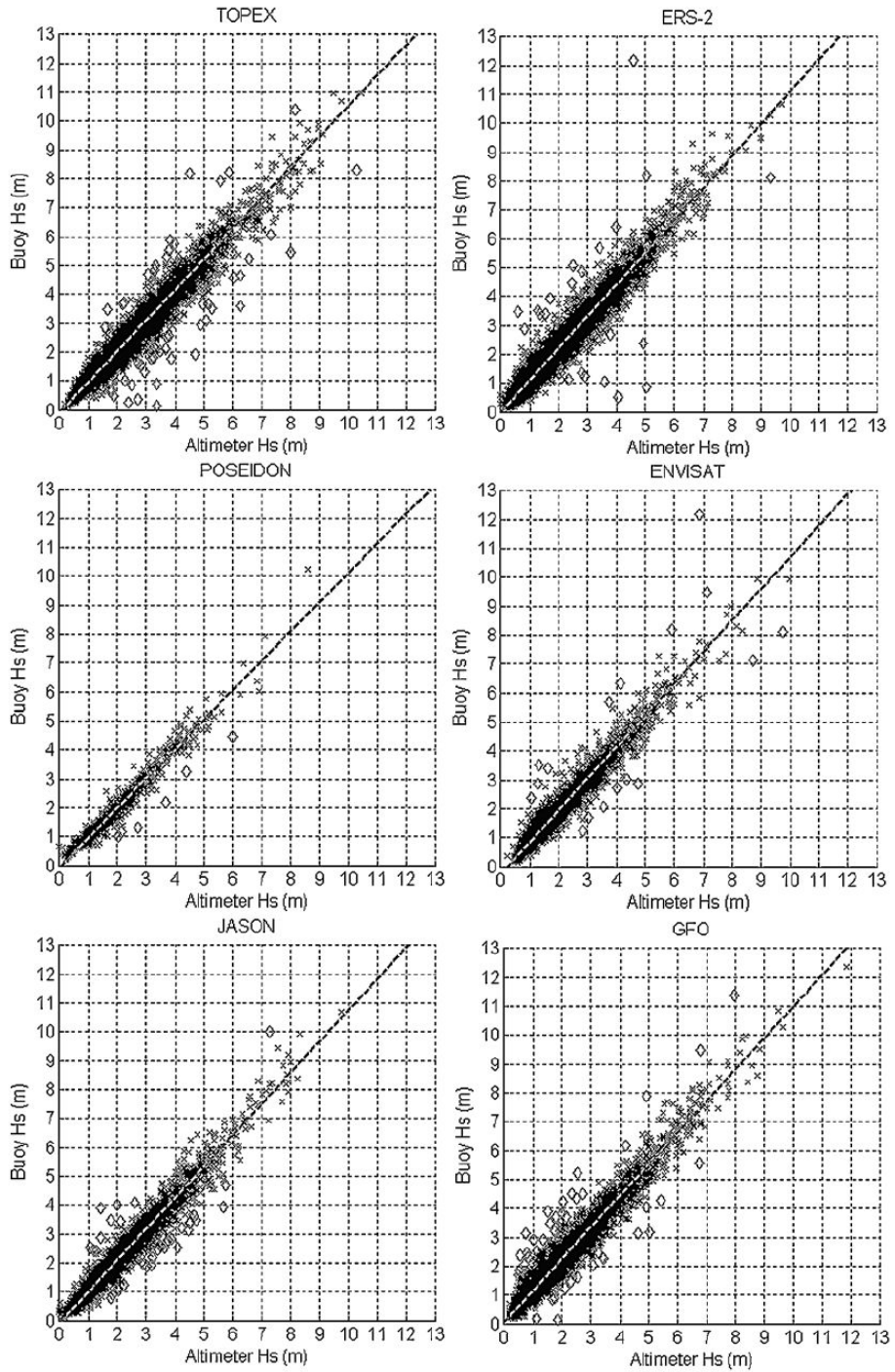


Figure A1. Orthogonal regression of buoy against altimeter H_s . Points further than $3s + 0.1H_s$ (where s is the standard deviation from the regression line) are plotted as diamonds.

Table A3. H_s Calibrations With Rogue Buoy Data and Outliers Removed^a

	A ($\pm 95\%$)	B ($\pm 95\%$)	Correlation	Residual rms	N
TOPEX	-0.071 (± 0.06)	1.062 (± 0.0009)	0.982	0.169	9008
POSEIDON	-0.060 (± 0.23)	1.032 (± 0.0034)	0.982	0.167	500
JASON	-0.080 (± 0.07)	1.095 (± 0.0013)	0.983	0.155	3981
ERS-2	-0.018 (± 0.05)	1.113 (± 0.0010)	0.982	0.165	8304
ENVISAT	-0.232 (± 0.09)	1.091 (± 0.0015)	0.983	0.157	2939
GFO	0.063 (± 0.05)	1.095 (± 0.0010)	0.984	0.157	6069

^a N is the number of points used to calculate the regression line.

and altimeter H_s are in good agreement. Orthogonal regression was used to establish best-fit lines through the data. Points further than $3s + 0.1H_s$, where s is the standard deviation from the regression line, were defined to be outliers and removed from the data set (see Figure A1). A further orthogonal regression was performed to establish the calibrations in the form H_s (buoy) = $A + BH_s$ (altimeter), together with 95% confidence intervals. The results are shown in Table A3. Note that these calibrations have not been applied to the data used for the development of the period algorithm. They are noted here for general interest.

Notation

$H_s = 4\sqrt{m_0}$	significant wave height.
$T_e = m_{-1}/m_0$	energy period.
$T_m = m_0/m_1$	mean period.
$T_z = \sqrt{m_0/m_2}$	zero upcrossing period.
$m_n = \int_0^{f_{lim}} f^n S(f) df$	n th moment of the wave power spectral density function $S(f)$.
f_{lim}	high-frequency cutoff of the measuring device.

[58] **Acknowledgments.** The authors would like to thank the reviewers for their helpful comments and careful reading of the manuscript and in particular for identifying the erroneous headers for the NDBC buoy data. We would also like to thank the U.S. National Oceanic and Atmospheric Administration for making the NDBC buoy data freely available.

References

- Abdalla, S., J.-R. Bidlot, and P. Janssen (2006), Global validation and assimilation of Envisat ASAR wave mode spectra, paper presented at Advances in SAR Oceanography from Envisat and ERS Missions (SEASAR 2006), Eur. Space Agency, Frascati, Italy.
- Bidlot, J.-R., D. Holmes, P. Wittmann, R. Lalbeharry, and H. Chen (2002), Intercomparison of the performance of operational wave forecasting systems with buoy data, *Weather Forecasting*, *17*, 287–310.
- Bidlot, J.-R., P. A. E. M. Janssen, S. Abdalla, and H. Hersbach (2007), A revised formulation of ocean wave dissipation and its model impact, *ECMWF Tech. Memo. 509*, Eur. Cent. for Medium-Range Weather Forecasting, Reading, UK.
- Caires, S., A. Sterl, and C. Gommenginger (2005), Global ocean mean wave period data: Validation and description, *J. Geophys. Res.*, *110*, C02003, doi:10.1029/2004JC002631.
- Callahan, P. S., C. S. Morris, and S. V. Hsiao (1994), Comparison of TOPEX/POSEIDON sigma0 and significant wave height distributions to Geosat, *J. Geophys. Res.*, *99*(C12), 25,015–25,024.
- Carter, D. J. T. (1990), Development of procedures for the analysis of ERS-1 radar altimeter wind and wave data, using GEOSAT data, *Study Rep. 8315/89/HGE-I*, 77 pp., Eur. Space Agency, Paris.
- Carter, D. J. T., P. G. Challenor, and M. A. Srokosz (1992), An assessment of Geosat wave height and wind speed measurements, *J. Geophys. Res.*, *97*(C7), 11,383–11,392.
- Cavaleri, L., et al. (2007), Wave modelling—The state of the art, *Progr. Oceanogr.*, *75*(4), 603–674, doi:10.1016/j.pocean.2007.05.005.
- Challenor, P. G., and P. D. Cotton (2002), The joint calibration of altimeter and in situ wave heights, *Doc. WMO/TD-1081, JCOMM Tech. Rep. 13*, World Meteorol. Org., Geneva.

Cheng, C. L., and Van J. W. Ness (1999), *Statistical Regression with Measurement Error*, Arnold, London.

Collard, F., F. Ardhuin, and B. Chapron (2005), Extraction of coastal ocean wave fields from SAR images, *IEEE J. Ocean. Eng.*, *30*(3), 526–533.

Cotton, P. D., and D. J. T. Carter (1996), Calibration and validation of ERS-2 altimeter wind/wave measurements, *Intern. Doc. 12, DRA ITT CSM/078*, 119 pp., Southampton Oceanogr. Cent., Southampton, UK.

Davies, C. G., P. G. Challenor, and P. D. Cotton (1997), Measurement of wave period from radar altimeters, in *Ocean Wave Measurement and Analysis*, edited by B. L. Edge and J. M. Hemsley, pp. 819–826, Am. Soc. Civil Eng., Reston, Va.

Gommenginger, C. P., M. A. Srokosz, P. G. Challenor, and P. D. Cotton (2002), Development and validation of altimeter wind speed algorithms using an extended collocated buoy/Topex dataset, *IEEE Trans. Geosci. Remote Sens.*, *40*, 251–260.

Gommenginger, C. P., M. A. Srokosz, P. G. Challenor, and P. D. Cotton (2003), Measuring ocean wave period with satellite altimeters: A simple empirical model, *Geophys. Res. Lett.*, *30*(22), 2150, doi:10.1029/2003GL017743.

Hwang, P. A., W. J. Teague, G. A. Jacobs, and D. W. Wang (1998), A statistical comparison of wind speed, wave height and wave period derived from satellite altimeters and ocean buoys in the Gulf of Mexico region, *J. Geophys. Res.*, *103*, 10,451–10,468.

Janssen, P., B. Hansen, and J.-R. Bidlot (1997), Verification of the ECMWF wave forecasting system against buoy and altimeter data, *Weather Forecasting*, *12*, 763–784.

Janssen, P., J.-R. Bidlot, S. Abdalla, and H. Hersbach (2005), Progress in ocean wave forecasting at ECMWF, *Tech. Memo. 478*, Eur. Cent. for Medium-Range Weather Forecasting, Reading, UK.

Krogstad, H. E., and S. F. Barstow (1999), Satellite wave measurements for coastal engineering applications, *Coastal Eng.*, *37*, 283–307.

Kshatriya, J., A. Sarkar, and R. Kumar (2005), Determination of ocean wave period from altimeter data using wave-age concept, *Mar. Geod.*, *28*(1), 71–79.

Lagaras, J. C., J. A. Reeds, M. H. Wright, and P. E. Wright (1998), Convergence properties of the Nelder-Mead simplex method in low dimensions, *SIAM J. Opt.*, *9*(1), 112–147.

Monaldo, F. (1988), Expected differences between buoy and radar altimeter estimates of wind speed and wave height and their implications on buoy-altimeter comparisons, *J. Geophys. Res.*, *93*, 2285–2302.

National Data Buoy Center (NDBC) (1996), Nondirectional and directional wave data analysis procedures, *Tech. Doc. 96-01*, Stennis Space Center, Miss.

NDBC (2003), Handbook of automated data quality control checks and procedures of the National Data Buoy Center, *Tech. Doc. 03-02*, Stennis Space Center, Miss.

Quilfen, Y., B. Chapron, and M. Serre (2004), Calibration/validation of an altimeter wave period model and application to TOPEX/Poseidon and Jason-1 altimeters, *Mar. Geod.*, *27*, 535–549.

Sarkar, A., R. Kumar, and M. Mohan (1998), Estimation of ocean wave periods by space-borne altimeters, *Ind. J. Mar. Sci.*, *27*(1), 43–45.

Scharroo, R. (2005), RADS version 2.2 user manual and format specification, Delft Inst. for Earth-Oriented Space Res., Delft Univ. of Technol., Delft, Netherlands.

Schulz-Stellenfleth, J., S. Lehner, and D. Hoja (2005), A parametric scheme for the retrieval of two-dimensional ocean wave spectra from synthetic aperture radar look cross spectra, *J. Geophys. Res.*, *110*, C05004, doi:10.1029/2004JC002822.

Schulz-Stellenfleth, J., T. König, and S. Lehner (2007), An empirical approach for the retrieval of integral ocean wave parameters from synthetic aperture radar data, *J. Geophys. Res.*, *112*, C03019, doi:10.1029/2006JC003970.

Tolman, H. L. (2002), Validation of WaveWatch III version 1.15 for a global domain, *Tech. Rep. 213*, NOAA Natl. Cent. for Environ. Predict., Camp Springs, Md.

Tolman, H. L., B. Balasubramanian, L. D. Burroughs, D. V. Chalikov, Y. Y. Chao, H. S. Chen, and V. M. Gerald (2002), Development and imple-

- mentation of wind generated ocean surface wave models at NCEP, *Weather Forecasting*, *17*, 311–333.
- Tran, N., O. Z. Zanife, B. Chapron, D. Vandemark, and P. Vincent (2005), Absolute calibration of Jason-1 and Envisat altimeter Ku-band radar cross sections from cross comparison with TRMM precipitation radar measurements, *J. Atmos. Oceanic Technol.*, *22*(9), 1389–1402.
- Violante-Carvalho, N., I. S. Robinson, and J. Schulz-Stellenfleth (2005), Assessment of ERS synthetic aperture radar wave spectra retrieved from the Max-Planck-Institut (MPI) scheme through intercomparisons of 1 year of directional buoy measurements, *J. Geophys. Res.*, *110*, C07019, doi:10.1029/2004JC002382.
- WAMDI Group (1988), The WAM model—A third generation ocean wave prediction model, *J. Phys. Oceanogr.*, *18*(12), 1775–1810.
-
- P. G. Challenor and C. P. Gommenginger, National Oceanography Centre, Southampton SO14 3ZH, UK.
- E. B. L. Mackay, School of Civil Engineering and the Environment, University of Southampton, Southampton S09 5NH, UK. (e.mackay@pelamiswave.com)
- C. H. Retzler, Pelamis Wave Power Ltd., Edinburgh EH6 6NF, UK.

Appendix E

Proceedings of the ASME 27th International Conference on Offshore Mechanics and Arctic Engineering
OMAE2008
June 15-20, 2008, Estoril, Portugal

OMAE2008-57976

WAVE ENERGY RESOURCE ASSESSMENT USING SATELLITE ALTIMETER DATA

Ed Mackay & AbuBakr Bahaj
Sustainable Energy Research Group
University of Southampton, UK

Chris Retzler
Pelamis Wave Power Ltd
Edinburgh, UK

Peter Challenor
National Oceanography Centre
Southampton, UK

ABSTRACT

The use of altimeter measurements of significant wave height and energy period for quantifying wave energy resource is investigated. A new algorithm for calculating wave period from altimeter data, developed by the authors in previous work, is used to estimate the power generated by the Pelamis wave energy converter and compared to estimates from collocated buoy data. In offshore locations accurate estimates of monthly and annual mean power can be achieved by combining measurements from six altimeter missions. Furthermore, by averaging along sections of the altimeter ground track, we demonstrate that it is possible to gauge the spatial variability in nearshore areas, with a resolution of the order of 10 km. Although measurements along individual tracks are temporally sparse, with TOPEX/Poseidon and Jason on a 10 day repeat orbit, GFO 17 days, and ERS-2 and ENVISAT 35 days, the long record of altimeter measurements means that multi-year mean power from single tracks are of a useful accuracy.

1. INTRODUCTION

Rapid expansion in the wave energy industry is foreseen over the next few years and many countries around the world are investigating the potential of wave energy developments off their shores. The ability for a wave energy developer to be able to provide spatial maps of wave energy converter (WEC) output at any location in the world, with a quantified accuracy and at a low cost will help facilitate the implementation of their devices.

Wave measurements from in-situ instrumentation are relatively sparse around the world's oceans. Wave energy developers wanting to know the resource in locations without nearby in-situ measurements are left to choose from numerical wave model data or satellite remote sensing measurements. Wave model data is normally purchased on a point-by-point basis and

spatial mapping of the wave resource can be a large cost for a feasibility study. The global coverage of satellite altimeter data provides an alternative to the use of model data, albeit with spatial and temporal limitations as the satellites have orbital periods of 10 to 35 days and widely-separated ground tracks – over 300 km for TOPEX/Poseidon and Jason.

Current industry practice is for WEC manufacturers to specify the response of a WEC in terms of two parameters: significant wave height, H_s (defined as $4\sqrt{m_0}$ where m_n is the n^{th} moment of the wave spectrum) and energy period, $T_e = m_1/m_0$ (see Table 1). With the application of linear calibrations, altimeter measurements of H_s are of comparable accuracy to that of in-situ measurements (e.g. [1], [2]). It is also possible to estimate T_e from altimeter data: an algorithm due to Mackay *et al* (2008) [3] has a root-mean-square error (RMSE) of around 1s and accurately reproduces the joint distribution of wave height and period, a necessity when calculating a WEC response.

In this paper we investigate the use of satellite altimeter data for assessing sites for potential wave energy development and the limitations imposed by the temporal sampling. The Pelamis WEC manufactured by Pelamis Wave Power Ltd is used as an example. To assess the accuracy of the altimeter power estimates we use a collocated dataset of altimeter and NDBC buoy measurements. The paper is arranged as follows: Section 2 describes the collocated dataset; in Section 3 the accuracy of individual measurements of instantaneous power produced by the Pelamis is assessed; in Section 4 measurement of monthly and annual means in offshore locations is discussed and in Section 5 we investigate the variation in power along individual altimeter tracks in order to gauge spatial variability close to shore due to topographic sheltering and shallow water effects. We finish by giving an example of the use of altimeter data for resource assessment around New Caledonia.

Table 1. Power matrix for the Pelamis, values in kW.

		T_e (s)																
		5.0	5.5	6.0	6.5	7.0	7.5	8.0	8.5	9.0	9.5	10.0	10.5	11.0	11.5	12.0	12.5	13.0
H_z (m)	0.5	Idle	Idle	Idle	Idle	Idle	Idle	Idle	Idle	Idle	Idle	Idle	Idle	Idle	Idle	Idle	Idle	Idle
	1.0	Idle	22	29	34	37	38	38	37	35	32	29	26	23	21	Idle	Idle	Idle
	1.5	32	50	65	76	83	86	86	83	78	72	65	59	53	47	42	37	33
	2.0	57	88	115	136	148	153	152	147	138	127	116	104	93	83	74	66	59
	2.5	89	138	180	212	231	238	238	230	216	199	181	163	146	130	116	103	92
	3.0	129	198	260	305	332	340	332	315	292	266	240	219	210	188	167	149	132
	3.5		270	354	415	438	440	424	404	377	362	326	292	260	230	215	202	180
	4.0			462	502	540	546	530	499	475	429	384	366	339	301	267	237	213
	4.5				554	635	642	648	628	590	562	528	473	432	382	356	338	300
	5.0					739	726	731	707	687	670	607	557	521	472	417	369	348
	5.5						750	750	750	750	737	667	658	586	520	496	446	395
	6.0							750	750	750	750	750	711	633	619	558	512	470
	6.5								750	750	750	750	750	743	658	621	579	512
	7.0									750	750	750	750	750	750	676	613	584
	7.5										750	750	750	750	750	750	686	622
	8.0											750	750	750	750	750	690	625

2. COLLOCATED ALTIMETER-BUOY DATASET

The dataset used in this paper consists of NDBC buoy measurements for the period 1996-2005 collocated with altimeter measurements from TOPEX, Poseidon, Jason, ERS-2, ENVISAT and GFO. The criteria of collocation were a spatial separation of less than 100km and a temporal separation of less than 30 minutes. To reduce the sampling variability the median of the altimeter measurements within 100 km of the buoy is used in preference to the 1Hz sample that is nearest to the buoy. Details of the quality controls applied to the data and the calibration of the altimeter H_z and T_e are given in [3]. The dataset described in [3] uses only deep water (>100 m) buoys in open ocean, at least 200 km from land. In contrast, the first generation of wave energy farms will be located within a few kilometres of the coast, in a water depth generally less than 100 m. Therefore, in addition to the 28 deep water buoys used in [3], we use data from 11 buoys in shallow water (<100 m), located closer to land. The locations of the buoys are shown in Figure 1.

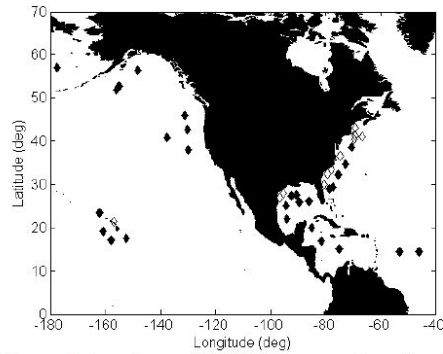


Figure 1. Locations of NDBC buoys used in collocated dataset. Solid diamonds denote buoys in depths >100m, hollow diamonds denote depths <100m.

3. COMPARISON OF INDIVIDUAL MEASUREMENTS

The algorithm used to derive T_e from the altimeter backscatter coefficient σ_0 is:

$$T_e = \begin{cases} \frac{1}{\beta} \ln \left[\frac{1}{\alpha} \left(\frac{\sigma_0 - A}{H_z + \gamma} \right) \right] & \text{if } \sigma_0 \leq \delta \\ \frac{1}{\beta} \ln \left[\frac{1}{\alpha} \left(\frac{\delta - A}{H_z + \gamma} \right) \right] & \text{if } \sigma_0 > \delta \end{cases} \quad (1)$$

where A , α , β , γ and δ are constants fitted for each altimeter, values for which are given in [3]. Note that when σ_0 exceeds the threshold δ , T_e is no longer related to σ_0 and depends on H_z only. This condition accounts for 17% of our dataset and corresponds to sea states with in low wind conditions, which nonetheless may contain significant swell.

For each pair of collocated altimeter and buoy measurements of H_z and T_e , the power produced by the Pelamis has been calculated from the values given in Table 1, interpolated to a resolution of 0.1m H_z and 0.1s T_e . The accuracy of the altimeter estimates of Pelamis power in terms of bias and RMSE is compared to the collocated buoy measurements. Differences in accuracy between different altimeters were found not to be significant at the 95% level (using a bootstrap method to estimate confidence) therefore we treat measurements from all six altimeters as one dataset. Scatter plots of altimeter against buoy estimates of Pelamis power are shown in Figure 2. The bias and RMSE in the altimeter measurements compared to the buoys are shown in Table 2.

Table 2. Bias and RMSE in altimeter Pelamis power. 95% confidence limits in brackets. Values in kW.

	Deep		Shallow	
	Bias	RMSE	Bias	RMSE
$\sigma_0 \leq \delta$	6.4 (±0.7)	55.7 (±0.8)	6.5 (±1.4)	63.8 (±1.4)
$\sigma_0 > \delta$	0.1 (±0.8)	29.1 (±1.3)	0.4 (±0.8)	22.5 (±2.3)
Overall	5.3 (±0.6)	52.2 (±0.8)	4.8 (±1.0)	55.3 (±1.8)

For $\sigma_0 \leq \delta$ the level of scatter is fairly high, but the relationship appears to be linear and the bias is small. When $\sigma_0 > \delta$ the altimeter underestimates the highest values of Pelamis power. However the bias is not significantly different from zero and these high energy swell conditions represent only a very small percentage of the data. It is interesting to note that there is a lower RMSE in Pelamis power when $\sigma_0 > \delta$, despite the fact that the period algorithm performs worse here (see [3]). This is most likely because this corresponds to times when there is low H_z and therefore low power. Figure 3 shows a quantile-quantile plot of altimeter against buoy Pelamis power, for the entire dataset. It is clear that the altimeter is capable of properly

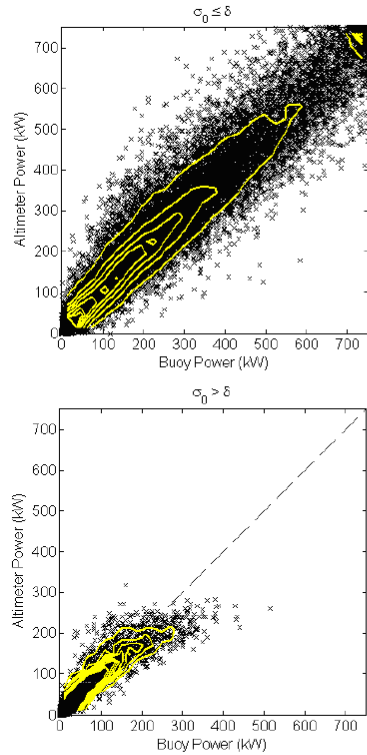


Figure 2. Scatter plots of altimeter Pelamis power against buoy Pelamis power, with contours showing density of occurrence. Top: $\sigma_0 \leq \delta$, bottom $\sigma_0 > \delta$.

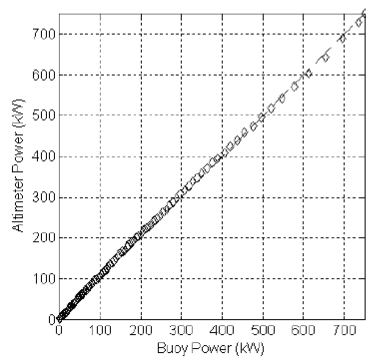


Figure 3. Quantile-quantile plot of Pelamis power measured by altimeter and buoys.

reproducing the distribution of Pelamis power measured by the NDBC buoys.

The shallow water buoys provide an independent validation of the period algorithm, as they were not used in its development. It is reassuring to see that the algorithm's performance is similar in shallow water to deep water. The same collocation criteria of 100km and 30 minutes were used for the shallow water buoys as for the deep water ones, so the higher RMSE in power for the shallow water buoys is probably due to the higher spatial variability in these areas.

In Figure 4 the mean difference in power calculated from the altimeter or buoy is binned by the differences in H_s and T_e between the altimeter and buoy. It can be seen that the difference in power is more sensitive to differences in H_s than differences in T_e , as one might expect since Pelamis power increases approximately linearly with H_s while above a T_e of 7.5 s it decreases approximately linearly with T_e .

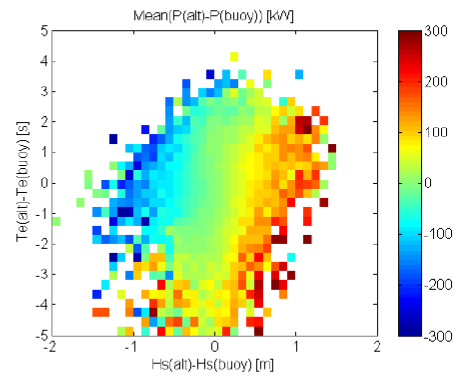


Figure 4. Mean difference in power against difference in H_s and T_e .

When considering the differences between buoy and altimeter measurements of the sea surface, we must take into account that we are comparing measurements of a random process, separated by both space and time. The ocean surface wave field is usually assumed to be ergodic. That is, under statistically stationary conditions, temporal averages and spatial averages are equivalent. Estimates of sampling variability from area averages and time averages are given in [4]. The effects of spatial and temporal separation on measurements of H_s are considered in detail in [5] and [6]. Here we make some observations of the effects of spatial and temporal separation, by considering measurements made by altimeters flying in tandem orbits.

From its launch, ENVISAT has been flying along the same ground tracks as ERS-2, leading by about 30 minutes.

Similarly, Jason flew in the same orbit as TOPEX/Poseidon, leading by 1 minute. After 6 months, TOPEX was manoeuvred into a parallel orbit half way between the original ground tracks, separated by about 150 km at the equator and about 100 km at 50° latitude. Scatter plots of the data from these tandem orbits are shown in Figure 5. Since the collocated dataset uses the median values of the altimeter measurements within 100 km of the buoy, the effects of sampling variability will be reduced.

The plot of T/P phase A orbit against Jason (both along the same ground tracks) shows low scatter indicating good precision of both altimeters. The scatter increases considerably when T/P is moved into the phase B orbit, showing the effect of spatial separation. From comparisons of the ERS-2 and ENVISAT data we can see that the effect of a temporal separation of 30 minutes is less than that of a spatial separation of 100-150 km.

4. MEANS OVER 2°×2° SQUARES

To provide a large-scale tool for identifying areas of interest for wave energy development, we can bin the altimeter data in 2°×2° squares and produce global maps of mean power. It has been demonstrated by numerous authors that satellite altimeter data can be used to obtain accurate estimates of monthly and annual mean H_z in offshore locations (e.g. [7], [8], [9]). In [10] it is shown that the monthly mean H_z calculated from 5 or more altimeter transects of a 2°×2° square surrounding a buoy compares well to the continuous measurements made by the buoy, with an RMSE of around 0.2m. Moreover, from 1992 onwards there have been at least 2 altimeters flying at all times. This means that using the combined data from TOPEX, Poseidon, Jason, ERS-2, ENVISAT and GFO, there are a minimum of 7 transects per month through each 2°×2° square surrounding the NDBC buoys. The mean number of transects per month is 21, with only 1.5% of squares having less than 10 passes per month. However, the sampling rate of a given geographical area depends on the latitude, on the number of satellites operating at that time and on the relative phasing of the various satellite orbits. See [11] for a discussion of these effects.

We follow the method described in [10] and compare the monthly mean Pelamis power from buoy data to the monthly mean from the altimeter measurements in the surrounding 2°×2° square. Only the deep water buoys have been considered in this comparison, since the assumption of stationarity on this scale is not valid in shallow water. Again, we have used the median value of the altimeter transect through the square to reduce sampling variability. Since the data from the tandem missions is so strongly correlated, these effectively represent duplicate measurements. Therefore the average of the data from the tandem missions has been used so as not to bias the estimate of monthly mean. In the case of the TOPEX phase B orbit, some additional information is gained where the new ground track falls within the square and the phase A track does not. For our

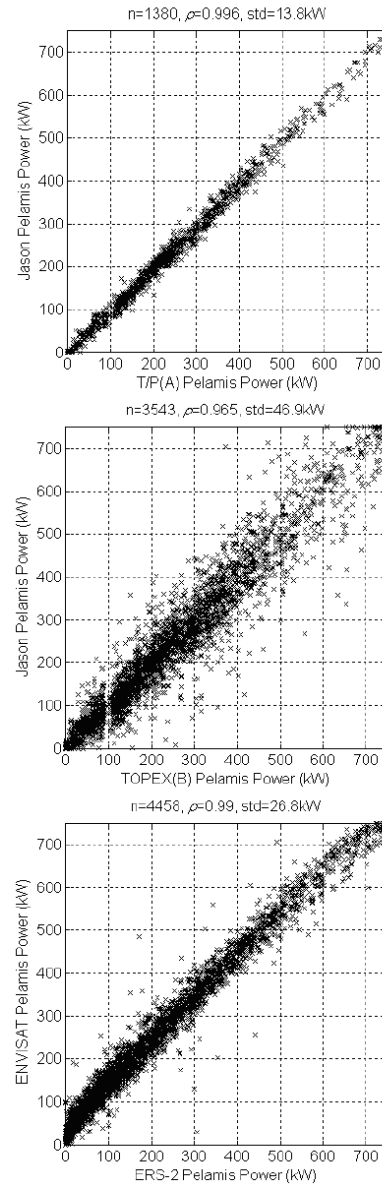


Figure 5. Scatter plots of altimeter estimates of Pelamis power for tandem orbits.

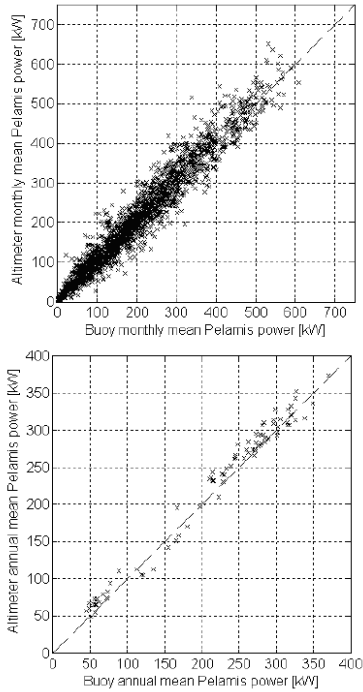


Figure 6. Scatter plot of altimeter versus buoy monthly and annual mean Pelamis power.

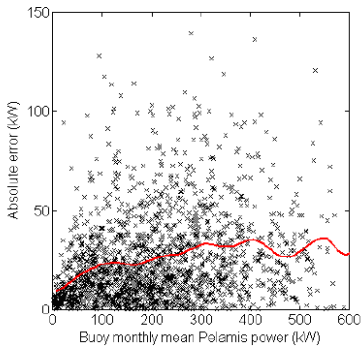


Figure 7. Absolute difference in altimeter monthly mean Pelamis power against value from buoy. Black crosses are values for individual months and red line is moving average.

analysis we have discarded months where the buoy is recording for less than 90% of the time.

Figure 6 shows scatter plots of altimeter monthly and annual mean Pelamis power against the values from the NDBC buoys. There is evidence that the variance of the error in monthly mean power increases with the mean power (see Figure 7), however this is not observed so strongly for the annual mean power. The error in monthly mean is a function of the error in individual measurements, the number of measurements and the autocorrelation structure of the monthly time series. Typically, as the monthly mean power increases, the monthly variability also increases, meaning that more samples are required for a given accuracy. The relationship between sampling frequency, autocorrelation in the data and accuracy of monthly means is discussed in detail in [12] for stationary distributions sampled at regular intervals. Their analytic method is not appropriate here, since time series of wave parameters are non-stationary due to seasonal variation. Also, using altimeter data from multiple missions produces irregular sampling intervals. However it is still useful to examine the effect of sampling rate empirically: Figure 8 shows the correlation of the altimeter monthly mean with the buoy monthly mean against number of altimeter transects. There is a slight increase in correlation from $20 < n \leq 30$ to $n > 30$ transects, but it is not significant at the 95% level. We can infer that, due to the autocorrelation in the data, sampling at a greater rate than once daily brings only marginal improvement.

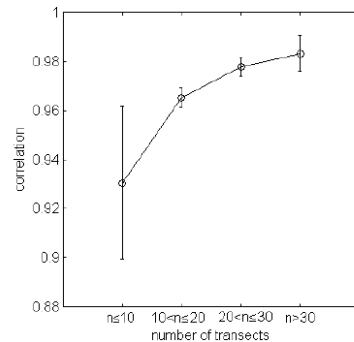


Figure 8. Correlation of altimeter monthly means with buoy monthly means against number of transects, with 95% confidence limits.

The reason that the error in annual mean is not as strongly dependent on the annual mean value as was observed for the monthly means is probably a result of the seasonal variability. In our dataset, there is large seasonal variability at the higher power locations. Over the entire dataset the altimeter monthly mean was found to have a bias of 8.2 ± 1.5 kW and RMSE of 32.6 ± 1.4 kW. The annual mean was found to have a bias of 7.1

± 2.8 kW and RMSE of 12.9 ± 1.6 kW. Since using altimeter data in $2^\circ \times 2^\circ$ squares is only indicative of the resource in that area, there is little use in being more precise about the uncertainty in relation to sampling and variability of the resource.

We do not have enough buoy data to test the accuracy of the long term, multi-year averages in 2° squares. However, we observe from the data that the errors in annual mean are approximately normally distributed and we assume that the error each year is independent of the previous year. Then by standard theory the standard deviation in error will decrease as $1/\sqrt{n}$, where n is the number of years the data is averaged over. Figure 9 shows the mean Pelamis power in $2^\circ \times 2^\circ$ squares over North Atlantic, Mediterranean, and Baltic Sea for the period 1996-2005. Since this average is taken over ten years, from the reasoning above the expected standard deviation of the error is $12.9/\sqrt{10} = 4.1$ kW. From the discussion above, this value is only indicative and dependent on the level of variability in the resource; this point is discussed further in Section 5.

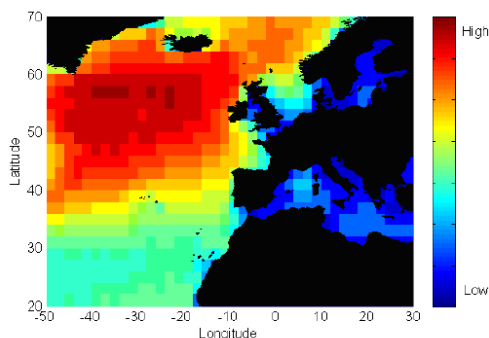


Figure 9. Mean Pelamis power over the North Atlantic for the period 1996-2005 from the combined altimeter dataset.

5. ALONG-TRACK AVERAGES

Maps of the wave climate in $2^\circ \times 2^\circ$ squares are useful for locating areas of interest for wave energy development. However, in coastal areas there is considerable spatial variability at smaller scale, so it is of benefit to analyse data along individual satellite passes to give finer resolution nearer shore. Even though measurements along individual tracks are sparse, with TOPEX/Poseidon and Jason on a 10 day repeat orbit, GFO 17 days, and ERS-2 and ENVISAT 35 days, there are many years of data for each satellite so we would expect the long-term along track averages to be of a reasonable accuracy. Indeed, when the mean power along a section of track is plotted a smooth along-track variation is observed, with values at cross over points agreeing well (see Figure 10). Again, data from the

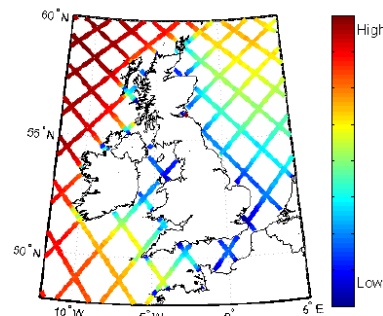


Figure 10. Mean along-track Pelamis power for T/P and Jason data for the period Jan 1992 – Dec 2007

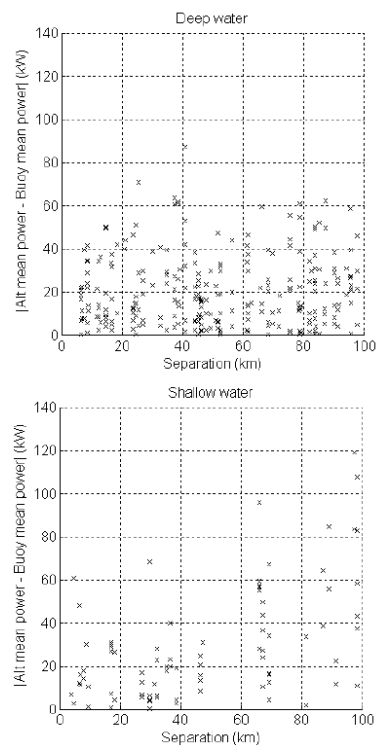


Figure 11. Difference in annual mean against separation between ground tracks and buoys.

tandem period of the missions has been averaged so as not to bias the mean.

The use of along-track averages of TOPEX/Poseidon data to estimate monthly and seasonal mean H_s is discussed in [13]. They show that even using an average over 13 years, there is still significant scatter in estimates of climatological monthly mean in track cross-over points. We examine the accuracy of along-track annual mean values. Figure 11 shows the difference in annual mean power measured by the buoy and TOPEX/Poseidon (phase A) and Jason passes against the separation between the ground tracks and the buoys. We see that for the deep water buoys there is no significant change up to 100 km, but for the shallow water buoys the difference increases at distances greater than 50 km. Therefore, for the shallow water buoys we tighten the collocation spatial criterion, now only allowing separations of less than 50km so as not to introduce differences from spatial variability in wave conditions. Figure 12 shows scatter plots of the along-track annual mean Pelamis power measured by the altimeters against buoy measurements. The bias and RMSE for each set of tracks are given in Table 3. As would be expected from the sampling frequency, the TOPEX/Poseidon and Jason tracks have the lowest errors. It is surprising to see that although the RMSE for the GFO tracks is lower than for the ERS-2 / ENVISAT tracks, this is not significant at the 95% level, despite GFO having double the sampling frequency. This is probably a consequence of both the limited size of our dataset and the fact that power levels are strongly seasonal, so one sample every 35 days still gives a reasonable estimate of the annual mean.

Table 3. Bias and RMSE in along-track annual mean Pelamis power compared to buoy measurements, 95% confidence limits given in brackets.

	Bias (kW)	RMSE (kW)
T/P & Jason	-4.7 (± 2.8)	25.2 (± 2.1)
GFO	-4.2 (± 4.2)	34.1 (± 3.1)
ERS-2 & ENVISAT	-1.5 (± 5.1)	38.6 (± 4.5)

The effect of limited temporal sampling can be examined by simulation, using hindcast data. As discussed in section 4, the uncertainty due to limited sampling is dependent on the level of variability at the site, which will vary around the world. Therefore hindcasts for several locations are used: Orkney - 14 year hindcast; Cornwall - 15 years; Aguçadoura (Portugal) - 10 years; and New Caledonia - 10 years. The two scales of variability relevant here are: synoptic (from passing weather systems, on the scale of a few days) and seasonal. As a metric for synoptic variability we use the average value of the monthly standard deviation divided by the monthly mean. The ratio between monthly standard deviation and monthly mean is not absolutely linear (see Figure 13), but this figure serves to discriminate between sites. Two metrics for seasonal variability are defined: the first is the standard deviation of individual

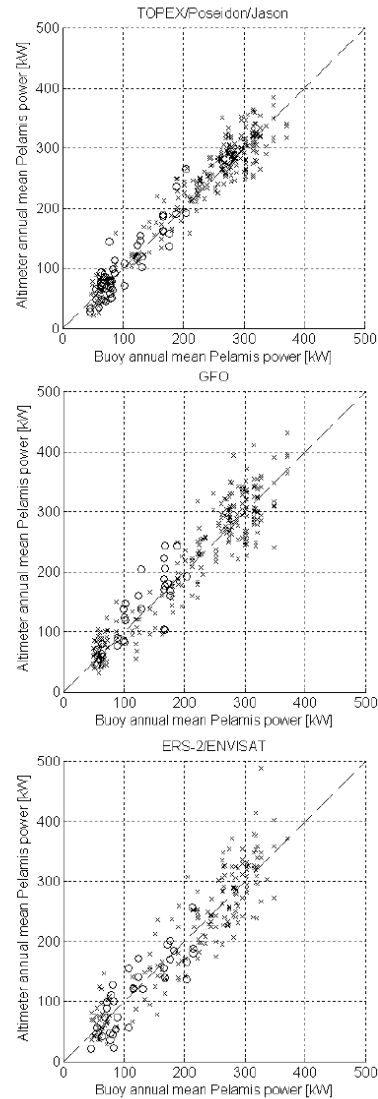


Figure 12. Scatter plots of annual mean Pelamis power measured by altimeters against buoy measurements. Values for the shallow water buoys are marked with circles.

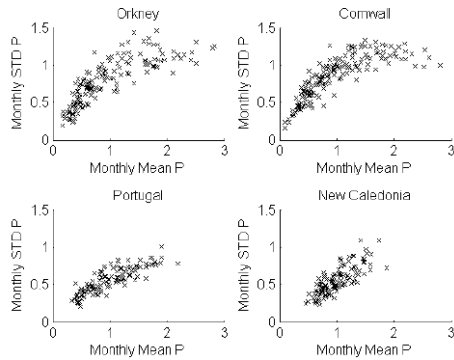


Figure 13. Scatter plots of monthly standard deviation against monthly mean power. Values have been normalised by the annual average power.

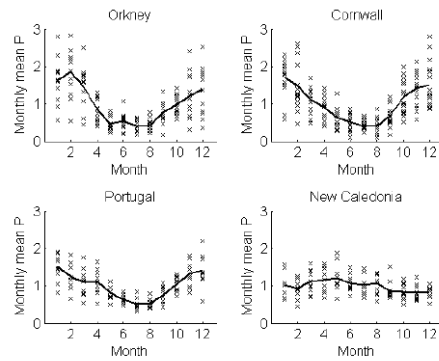


Figure 14. Variation in monthly mean power: crosses are individual months, line is climatological monthly mean. Values have been normalised by the annual average power.

monthly means, and the second is the standard deviation of the climatological monthly means. This second figure gives a measure of the seasonal cycle. Plots of the monthly mean power throughout the year are shown in Figure 14 and the metrics of variability we have defined for each site are given in Table 4. Orkney and Cornwall have very similar levels of both synoptic and seasonal variability. Portugal and New Caledonia have similar levels of synoptic variability, but whilst the standard deviation of monthly means is roughly equal, Portugal has a stronger seasonal cycle.

Table 4. Variability in power on different scales

	Orkney	Cornwall	Portugal	New Caledonia
Synoptic variability	0.96	1.03	0.60	0.55
STD of monthly means	0.38	0.37	0.27	0.27
Seasonal cycle	0.51	0.47	0.35	0.13

The effect of limited temporal sampling on the error in annual mean is tested by sampling one value every 1, 2, 3, etc. days, starting from the 1st, 2nd, 3rd, etc. sample. The results are shown in Figure 15. Since these results are based on sampling from a limited number of years, the results have some scatter, so a line of the form $y = ax^b$ has been fitted to each dataset. As would be expected from the similar levels of variability, the uncertainty from limited sampling is comparable for Orkney and Cornwall. The effects are weaker for Portugal and New Caledonia, consistent with the lower levels of synoptic and seasonal variability. From Figure 15 it is clear that the difference in the strength of the seasonal cycles between Portugal and New Caledonia has little effect. It is not clear which scale of variability is most important, but it is evident that the uncertainty from limited sampling is site dependent.

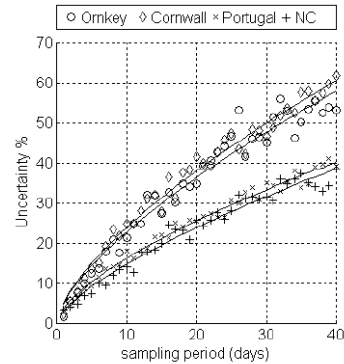


Figure 15. Percentage uncertainty (defined as $100 \cdot \text{RMSE}/\text{mean}$) from limited sampling for various sites

Despite this site dependency, we estimate the expected RMSE in the multi-year along-track mean for the entire dataset. Again, we observe the error in annual means to be approximately normally distributed and assume the error each year is independent of the previous. Hence we expect the standard deviation of the errors to decrease with $1/\sqrt{n}$, where n is the number of years of data. The attainable accuracies in mean Pelamis power (defined as half the width of the 95% confidence interval), given the length of data available for the four sets of ground tracks, are shown in Table 5.

Table 5. Attainable accuracy, given the length of data available, for along-track averages of Pelamis power.

	Years of data available	Accuracy (kW)
T/P & Jason (phase A)	15	13.0
TOPEX (phase B)	3	29.1
GFO	8	24.1
ERS-2 & ENVISAT	13	21.4

6. EXAMPLE AND DISCUSSION

In this section we give an example of the use of altimeter data for wave energy resource assessment around New Caledonia. Along-track mean values of Pelamis power are shown in Figure 16 for TOPEX / Poseidon / Jason (phase A), GFO and ERS-2 / ENVISAT. The spatial variability within each $2^\circ \times 2^\circ$ square is evident and especially strong close to the coast and much useful information can be discerned. For example, the sheltering effect in the lee of the island is clearly visible, as are the dissipative effects of the shallow reefs around the south-east and north-west corners of the main island.

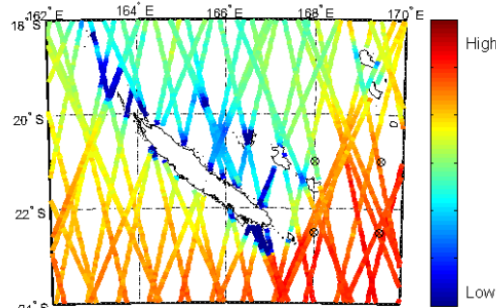


Figure 16. Mean along-track Pelamis power for combined altimeter tracks. Locations of hindcast grid points are marked with black crosses

The uncertainty in the along-track averages is visible, as are the differences between nearby tracks. The combination of the three sets of tracks illustrates the variability of the data: the along-track mean values are based on different, but overlapping periods, dependent on the length of data available for each altimeter, and certain tracks may be too high (low) from randomly picking up a greater (lesser) proportion of storms.

It would be possible to create a more consistent map from the combined tracks by using a spatio-temporal interpolation scheme based on information from track cross-over points. However, the scheme would be computationally intensive and require a careful analysis of the spatial and temporal correlation in the wave field. Moreover, the scheme would not be able to

interpolate accurately between tracks in nearshore areas where there is high spatial variability due to bathymetry or sheltering.

Individual tracks are limited by altimeter measurement problems close to shore. The waveform is distorted if there is land within the radar footprint (around 5 km in diameter) and when the satellite is tracking from land to sea it can travel up to 30 km before regaining lock on the sea surface. Often no data are obtained, but sometimes spurious measurements are recorded so robust quality checking is required.

Despite the nearshore limitations, the track maps provide attractive resolution. Figure 16 shows locations of 4 model hindcast grid points around the south-east corner at a resolution of $1.5^\circ \times 1.5^\circ$. It can be seen that to provide measurements of the spatial variability around the islands that were comparable with the altimeter tracks would require nearshore modelling at much higher resolution and concomitant cost.

7. CONCLUSIONS

Satellite altimetry measurements can be used to provide a robust estimate of the wave energy resource. Although individual altimeter measurements show a large scatter compared to buoy measurements, the large volume of altimeter data available allows the monthly and annual means to be calculated accurately for offshore locations. The global availability of altimeter data means it can be used to produce spatial maps of the mean power produced by a WEC. These maps are of two types: power maps that represent mean power over a large area, showing the spatial variation in wave power around a country or continent; and track maps whose spatial resolution is sufficient to identify, on a smaller scale, promising wave energy locations along particular stretches of coastline.

ACKNOWLEDGEMENTS

The authors would like to thank Robin Hankin of the National Oceanography Centre, Southampton, for valuable discussions and comments on this paper. We would also like to thank Société de Recherche du Pacifique (SRP) for the provision of the hindcast data for New Caledonia.

REFERENCES

- [1] Krogstad HE and Barstow SF, 1999, "Satellite Wave Measurements for Coastal Engineering Applications", *Coastal Eng.*, 37, 283-307
- [2] Challenor PG and Cotton PD, 2002, "The joint calibration of altimeter and in situ wave heights", World Meteorological Organization document number WMO/TD-No.1081.

- [3] Mackay EBL, Retzler CH, Challenor PG, Gommenginger C, 2008, "A Parametric Model for Ocean Wave Period from Ku-band Altimeter Data", *J. Geophys. Res. C* in press
- [4] Krogstad HE, Wolf J, Thompson SP, Wyatt LR, 1999, "Methods for Intercomparison of wave data" *Coastal Eng.*, 37, 235-257
- [5] Monaldo F, 1988, "Expected differences between buoy and radar altimeter estimates of wind speed and wave height and their implications on buoy-altimeter comparisons", *J. Geophys. Res.*, 93, 2285-2302
- [6] Toumadre J, 1993, "Time and space scales of significant wave heights", *J. Geophys. Res.*, 98(C3), 4727-4738.
- [7] Carter DJT, Foale S, Webb DJ, 1991, "Variations in global wave climate throughout the year", *Int. J. Remote Sensing*, 12, 1687-1697
- [8] Young IR, 1994, "Global ocean wave statistics obtained from satellite observations", *Appl. Ocean Res.* 16, 235-248.
- [9] Woolf DK, Cotton PD, Challenor PG, 2003, "Measurement of the offshore wave climate around the British Isles by Satellite Altimeter", *Phil. Trans. R. Soc. A*, 361(1802) 27-31
- [10] Cotton PD and Carter DJT, 1994, "Cross calibration of TOPEX, ERS-1, and Geosat wave heights", *J. Geophys. Res.*, 99, 25,025-25,033. Correction: *J. Geophys. Res.*, 100, 7095,
- [11] Queffelec P and Croizé-Fillon D, 2007, "Investigation of large scale and regional features of wave height using multi-satellite altimeter measurements", Proc. ENVISAT Symposium, Montreux, Switzerland, 23-27 April 2007, ESA SP-636.
- [12] Challenor PG and Carter DJT, 1994, "On the accuracy of monthly means", *J. Atmos. Oce. Tech.*, 11(5), 1425-1430
- [13] Queffelec P and Bentamy A, 2007, "Analysis of wave height variability using altimeter measurements. Application to the Mediterranean Sea", *J. Atmos. Oceanic Tech.*, 24, 2078-2092.

Appendix F: Notes on time series models

This appendix provides some notes on the basics of ARMA and ARIMA time series models, referred to in the Chapters 5 and 6. The notes in this appendix are based on Priestly (1981) and Hosking (1981) and the reader is referred there for further details.

F.1 Basic definitions

A time-varying or space-varying quantity $X(t)$ is called a “random process” if for each value of t we cannot determine theoretically a precise value for $X(t)$, but instead we have a range of possible values, with an associated probability distribution describing the relative likeliness of each value. For each individual value of t , $X(t)$ is a random variable. To distinguish between individual values and the process as a whole, curly brackets are used when discussing the process as a whole: $\{X(t)\}$.

The process is said to be “stationary” if the statistical properties of the process do not change with time or space. Formally, the process $\{X(t)\}$ is said to be “completely stationary” if for any t_1, t_2, \dots, t_n and k the joint distribution of $\{X(t_1), X(t_2), \dots, X(t_n)\}$ is identical with $\{X(t_1 + k), X(t_2 + k), \dots, X(t_n + k)\}$.

Complete stationarity is quite a severe requirement, so it is often relaxed to “stationary up to order m ” which describes roughly the same physical behaviour. Formally, the process $\{X(t)\}$ is said to be stationary up to order m if for any t_1, t_2, \dots, t_n and k , all the joint moments up to order m of $\{X(t_1), X(t_2), \dots, X(t_n)\}$ exist and equal the corresponding joint moments of $\{X(t_1 + k), X(t_2 + k), \dots, X(t_n + k)\}$.

In particular, if we say that a process is second order stationary then

- (i) It has the same mean value at all time points
- (ii) It has the same variance at all time points

- (iii) The covariance between the values at any two time points, s, t , depends only on $(s - t)$, the interval between the time points and not the location of the points along the time axis.

F.2 ARMA models

Auto-regressive moving-average (ARMA) models are a class of time series models used to describe stationary, zero-mean processes. Each term in the series X_t is described by a linear combination of the preceding terms and a (unobservable) purely random process ε_t . The model is given by the recurrence relation

$$X_t + a_1 X_{t-1} + \dots + a_p X_{t-p} = \varepsilon_t + b_1 \varepsilon_{t-1} + \dots + b_q \varepsilon_{t-q} \quad [\text{F.1}]$$

where a_1, a_2, \dots, a_p and b_1, b_2, \dots, b_q are constants and the terms ε_t are a series of independent random variables distributed $N(0, \sigma_\varepsilon^2)$, sometimes referred to as the error terms or as innovation terms. In this case the model is referred to as an ARMA(p, q) model, where p is the order of the auto-regressive part of the model and q is the order of the moving-average part of the model.

Time series models are often written in terms of the backward shift operator B , where $BX_t = X_{t-1}$. If we define

$$\alpha(B) = 1 + a_1 B + \dots + a_p B^p \quad [\text{F.2}]$$

$$\beta(B) = 1 + b_1 B + \dots + b_q B^q \quad [\text{F.3}]$$

then the ARMA(p, q) model can be more succinctly written as

$$\alpha(B)X_t = \beta(B)\varepsilon_t \quad [\text{F.4}]$$

For an ARMA model to be stationary, a necessary and sufficient condition is that all the roots of $0 = \alpha(z) = 1 + a_1 z + \dots + a_p z^p$ lie outside the unit circle, i.e. $|z| > 1$. For the model to be identifiable (that there is a unique set of coefficients which correspond to any given form of the spectral density function) we also require that the roots of

$0 = \beta(z) = 1 + b_1 z + \dots + b_q z^q$ lie outside the unit circle and that $\alpha(z)$ and $\beta(z)$ have no common roots.

The power spectral density function for an ARMA(p, q) model is given by

$$h(\omega) = \frac{\sigma_\varepsilon^2 |1 + b_1 \exp(-i\omega) + \dots + b_q \exp(-iq\omega)|^2}{\pi |1 + a_1 \exp(-i\omega) + \dots + a_p \exp(-ip\omega)|^2} \quad [\text{F.5}]$$

where ω is the angular frequency in radians/sample. Note that here we have removed a factor of 2 from the denominator compared to Priestly (1981) eq. 5.4.48, since we are only interested in positive frequencies.

Note that AR(1) processes are also known as linear Markov processes or as “red noise”, due to the shape of their spectral density functions.

Estimation of model parameters

To fit an ARMA model to the data we need to determine the order of the model and estimate the parameters. The logical sequence to proceed would be to first determine the order and then estimate the parameters. However, the methods which have been developed for order determination require parameter estimation as a preliminary stage. It is therefore necessary to estimate the parameters for a range of model orders, and then compare the fit.

Two methods have been implemented in MATLAB for estimation of ARMA parameters, one in the time domain and one in the frequency domain. The time domain method finds the maximum likelihood estimates of the parameters, but can be slow to run if the length of the observed series is long. The frequency domain method is much faster to run and can be used to find initial estimates of the parameters for the time domain method. Note that both methods may fail to converge to the optimal solution, depending on starting values for the optimisation.

The method for parameter estimation in the time domain is given by Priestly (1981) p360. We rewrite equation F.1 as

$$\varepsilon_t = (X_t + a_1 X_{t-1} + \dots + a_p X_{t-p}) - (b_1 \varepsilon_{t-1} + \dots + b_q \varepsilon_{t-q}) \quad [\text{F.6}]$$

and set as starting values $\varepsilon_1 = \varepsilon_2 = \dots = \varepsilon_p = 0$. Then

$$\begin{aligned} \varepsilon_{p+1} &= (X_{p+1} + a_1 X_p + \dots + a_p X_1) \\ \varepsilon_{p+2} &= (X_{p+2} + a_1 X_{p+1} + \dots + a_p X_2) - b_1 \varepsilon_{p+1} \\ &\vdots \\ \varepsilon_{p+q} &= (X_{p+q} + a_1 X_{p+q-1} + \dots + a_p X_q) - (b_1 \varepsilon_{p+q-1} + \dots + b_q \varepsilon_{p+1}) \\ &\vdots \end{aligned} \quad [\text{F.7}]$$

Given the order of the model (p, q) , we can evaluate the sum of squares

$$Q(a_1, \dots, a_p, b_1, \dots, b_q) = \sum_{t=p+1}^N \varepsilon_t^2 \quad [\text{F.8}]$$

The MATLAB function `fminsearch` is used to minimise Q and find the maximum likelihood estimates of $a_1, \dots, a_p, b_1, \dots, b_q$. This involves calculating $N-p$ error terms at each iteration. The error variance is estimated by

$$\hat{\sigma}_\varepsilon^2 = \frac{Q(\hat{a}_1, \dots, \hat{a}_p, \hat{b}_1, \dots, \hat{b}_q)}{N - 2p - q - 1} \quad [\text{F.9}]$$

The frequency domain approach estimates the parameters of the model by fitting the spectrum given by [F.5] to the observed spectrum. The observed spectrum, $s(\omega)$, is calculated and averaged to 100 frequency bins between 0 and π . Note that the choice of 100 frequency bins has been chosen arbitrarily, and sensitivity to the number or range of frequencies has not been tested. The fit is performed on the logged spectra, since these have lower sampling uncertainty. Again the function `fminsearch` is used to minimise

$$\sum_{i=1}^{100} [\log(s(\omega_i)) - \log(h(\omega_i))]^2 \quad [\text{F.10}]$$

To determine the order of the model, we use Akaike's information criterion (AIC), described by Priestly (1981), p373. This is a very general criterion, based on information theoretic concepts, which can be used to identify statistical models in a wide range of situations. When a model involving k independently adjusted parameters is fitted to data, the AIC is defined as

$$AIC(k) = -2\ln[\text{maximised likelihood}] + 2k \quad [\text{F.11}]$$

For an ARMA(p, q) model the AIC is given by

$$AIC(p, q) = N\ln\hat{\sigma}_\varepsilon^2 + 2(p + q) \quad [\text{F.12}]$$

where $\hat{\sigma}_\varepsilon^2$ is given by equation 9. The order of the model is determined by the values of p and q at which $AIC(p, q)$ takes its minimum value.

F.3 Fractional difference models

The ARMA models described in the previous section provide a very general class of models for short-term correlated processes. Fractionally differenced models provide an extension of ARMA models, capable of modelling long-range dependence as well. They arise as a generalisation of the autoregressive integrated moving average (ARIMA) process. An ARIMA(p, d, q) process is obtained by integrating an ARMA(p, q) process and is given by

$$\alpha(B)\Delta^d X_t = \beta(B)\varepsilon_t \quad [\text{F.13}]$$

where Δ is the difference operator defined by $\Delta X_t = X_t - X_{t-1} = (1 - B)X_t$. Conversely, applying term-by-term differencing d times to an ARMA(p, q) process gives an ARIMA(p, d, q) process.

A special case is the ARIMA(0,1,0) process or random walk, the discrete time analogue of Brownian motion, defined by

$$\Delta X_t = X_t - X_{t-1} = \varepsilon_t \quad [\text{F.14}]$$

The first difference of $\{X_t\}$ is the discrete time white noise process $\{\varepsilon_t\}$.

The fractional difference operator Δ^d is defined in the natural way, by a binomial series:

$$\Delta^d = (1 - B)^d = \sum_{k=0}^{\infty} \binom{d}{k} (-B)^k = 1 - dB + \frac{d(d-1)}{2!} B^2 - \frac{d(d-1)(d-2)}{3!} B^3 + \dots \quad [\text{F.15}]$$

The ARIMA(p, d, q) process is stationary and invertible if $|d| < \frac{1}{2}$ and all the roots of $\alpha(z)$ and $\beta(z)$ lie outside the unit circle. For $0 < d < \frac{1}{2}$ these processes are capable of modelling long-term persistence.

The ARIMA($p, d, 0$) is also sometimes denoted as FAR(p), short for fractionally differenced autoregressive process of order p .

Estimation of model parameters

Hosking (1981) recommends the following procedure for fitting an ARIMA(p, d, q) model:

1. Estimate d in the ARIMA($0, d, 0$) model $\Delta^d X_t = \varepsilon_t$
2. Define $u_t = \Delta^d X_t$
3. Identify and estimate α and β in the ARIMA($p, 0, q$) model $\alpha(B)u_t = \beta(B)\varepsilon_t$
4. Define $Y_t = \{\beta(B)\}^{-1}\alpha(B)X_t$
5. Estimate d in the ARIMA ($0, d, 0$) model $\Delta^d Y_t = \varepsilon_t$
6. Check for convergence of the d, α and β parameters; if not converged then go to step 2.

Appendix G: Results of extreme value analysis of NDBC buoy data

The following notation is used:

N	number of hourly samples after interpolation
n	number of declustered peaks used to fit model
u	threshold
σ	estimated GPD scale parameter
ζ	estimated GPD shape parameter
$H_{s,50}$	estimated 50 year return value of H_s
$H_{s,100}$	estimated 100 year return value of H_s
max. ob.	maximum observed H_s

95% confidence intervals for estimates are given in brackets.

Aggregate values refer to annual return values derived from the seasonal models.

Buoy 46002:

Period	N	n	u [m]	σ	ζ	$H_{s,50}$ [m]	$H_{s,100}$ [m]	Max. ob. [m]
Jan-Feb	33589	140	5.5	1.66 (1.41, 2.04)	-0.06 (-0.27, 0.05)	13.5 (11.0, 15.6)	14.3 (11.2, 17.1)	14.3
Mar-Apr	33947	125	4.8	1.68 (1.37, 2.06)	-0.20 (-0.35, -0.08)	10.4 (9.5, 11.4)	10.8 (9.7, 11.9)	10.4
May-Jun	32943	56	3.9	0.98 (0.72, 1.36)	-0.06 (-0.28, 0.08)	8.0 (6.9, 8.9)	8.5 (7.1, 9.7)	7.6
Jul-Aug	36099	60	2.9	0.57 (0.44, 0.77)	-0.08 (-0.42, 0.10)	5.2 (4.3, 6.1)	5.5 (4.4, 6.6)	5.7
Sep-Oct	35076	23	6.1	1.98 (1.25, 3.62)	-0.26 (-0.77, -0.03)	10.9 (9.8, 11.3)	11.4 (10.2, 12.0)	10.1
Nov-Dec	34048	52	7.6	2.35 (1.74, 3.34)	-0.43 (-0.72, -0.23)	12.3 (11.7, 12.9)	12.5 (11.9, 13.2)	11.9
Aggregate:						13.5 (12.2, 15.6)	14.3 (12.4, 17.1)	
Annual	205702	271	6.2	1.80 (1.59, 2.05)	-0.14 (-0.25, -0.05)	13.8 (12.5, 15.2)	14.3 (12.7, 16.0)	14.3

Buoy 46005:

Period	N	n	u [m]	σ	ζ	$H_{s,50}$ [m]	$H_{s,100}$ [m]	Max. ob. [m]
Jan-Feb	37994	84	7.0	1.38 (1.09, 1.78)	-0.12 (-0.29, 0.01)	12.3 (11.2, 13.3)	12.8 (11.5, 14.1)	12.0
Mar-Apr	39159	158	4.8	1.80 (1.54, 2.17)	-0.19 (-0.31, -0.11)	11.0 (10.2, 11.8)	11.4 (10.4, 12.3)	10.4
May-Jun	39839	40	4.2	1.20 (0.88, 1.70)	-0.09 (-0.35, 0.06)	8.5 (7.2, 9.4)	9.0 (7.5, 10.2)	8.4
Jul-Aug	42720	203	2.1	0.80 (0.69, 0.95)	-0.14 (-0.26, -0.05)	5.3 (4.8, 5.8)	5.5 (4.9, 6.1)	5.2
Sep-Oct	39603	127	4.5	1.47 (1.19, 1.82)	0.04 (-0.09, 0.14)	13.2 (11.3, 14.9)	14.5 (12.0, 16.8)	11.7
Nov-Dec	36406	174	6.0	1.80 (1.51, 2.17)	-0.17 (-0.30, -0.06)	12.7 (11.7, 13.8)	13.2 (12.0, 14.5)	12.5
Aggregate:						13.8 (12.8, 15.2)	14.7 (13.4, 16.9)	
Annual	235721	619	5.3	2.01 (1.85, 2.19)	-0.20 (-0.25, -0.14)	12.8 (12.1, 13.6)	13.2 (12.4, 14.0)	12.5

Buoy 46011:

Period	<i>N</i>	<i>n</i>	<i>u</i> [m]	σ	ζ	<i>H</i> _{5,50} [m]	<i>H</i> _{5,100} [m]	Max. ob. [m]
Jan-Feb	25698	64	4.5	1.62 (1.30, 2.16)	-0.30 (-0.61, -0.16)	8.8 (7.6, 9.5)	9.0 (7.6, 9.9)	9.1
Mar-Apr	32092	95	4.1	0.65 (0.51, 0.84)	0.04 (-0.14, 0.17)	8.1 (6.9, 9.2)	8.6 (7.2, 10.1)	8.0
May-Jun	35853	119	3.0	0.66 (0.54, 0.82)	-0.09 (-0.27, 0.02)	5.8 (5.0, 6.5)	6.1 (5.2, 7.0)	5.9
Jul-Aug	36783	59	2.6	0.34 (0.25, 0.48)	-0.29 (-0.54, -0.12)	3.5 (3.3, 3.6)	3.5 (3.4, 3.7)	3.4
Sep-Oct	36290	29	3.8	0.97 (0.70, 1.55)	-0.59 (-1.20, -0.34)	5.3 (5.0, 5.4)	5.3 (5.0, 5.5)	5.4
Nov-Dec	29990	99	4.0	1.66 (1.39, 1.97)	-0.41 (-0.55, -0.30)	7.6 (7.1, 8.0)	7.7 (7.2, 8.2)	7.8
Aggregate:						8.9 (7.9, 9.7)	9.2 (8.1, 10.4)	
Annual	196706	126	5.0	1.05 (0.89, 1.29)	-0.17 (-0.34, -0.07)	8.8 (7.9, 9.5)	9.1 (8.0, 10.0)	9.1

Buoy 46012:

Period	<i>N</i>	<i>n</i>	<i>u</i> [m]	σ	ζ	<i>H</i> _{5,50} [m]	<i>H</i> _{5,100} [m]	Max. ob. [m]
Jan-Feb	31596	122	4.0	1.10 (0.91, 1.35)	-0.12 (-0.29, 0.00)	8.5 (7.4, 9.5)	8.9 (7.6, 10.1)	8.7
Mar-Apr	28511	119	3.8	0.92 (0.77, 1.11)	-0.15 (-0.30, -0.04)	7.3 (6.6, 8.0)	7.6 (6.7, 8.5)	7.4
May-Jun	29316	107	3.1	0.88 (0.73, 1.07)	-0.25 (-0.41, -0.12)	5.8 (5.2, 6.3)	5.9 (5.3, 6.5)	5.9
Jul-Aug	33941	100	2.4	0.46 (0.38, 0.58)	-0.15 (-0.35, -0.03)	4.1 (3.7, 4.4)	4.2 (3.8, 4.7)	4.2
Sep-Oct	37244	76	3.3	1.02 (0.82, 1.32)	-0.34 (-0.60, -0.20)	5.8 (5.2, 6.1)	5.9 (5.3, 6.3)	6.0
Nov-Dec	37691	143	3.9	1.34 (1.13, 1.61)	-0.18 (-0.33, -0.08)	8.6 (7.6, 9.4)	8.9 (7.8, 9.9)	8.6
Aggregate:						8.9 (8.2, 9.8)	9.2 (8.4, 10.4)	
Annual	198299	106	5.2	0.99 (0.81, 1.24)	-0.14 (-0.30, -0.02)	8.9 (8.2, 9.6)	9.2 (8.3, 10.1)	8.7

Buoy 46013:

Period	<i>N</i>	<i>n</i>	<i>u</i> [m]	σ	ζ	<i>H</i> _{5,50} [m]	<i>H</i> _{5,100} [m]	Max. ob. [m]
Jan-Feb	32328	72	4.8	0.96 (0.76, 1.31)	-0.03 (-0.26, 0.12)	9.4 (8.0, 10.6)	10.0 (8.2, 11.7)	9.6
Mar-Apr	34831	39	5.1	1.10 (0.78, 1.57)	-0.63 (-0.98, -0.38)	6.7 (6.6, 6.9)	6.8 (6.6, 6.9)	6.7
May-Jun	36151	154	3.2	0.81 (0.71, 1.07)	-0.18 (-0.51, -0.08)	6.1 (5.1, 6.7)	6.3 (5.2, 7.0)	7.1
Jul-Aug	36233	56	3.1	0.42 (0.33, 0.57)	-0.02 (-0.21, 0.10)	5.0 (4.4, 5.4)	5.2 (4.6, 5.8)	4.8
Sep-Oct	36146	133	3.0	0.78 (0.65, 0.97)	-0.08 (-0.34, 0.04)	6.5 (5.3, 7.5)	6.9 (5.4, 8.1)	7.4
Nov-Dec	35768	72	5.0	1.61 (1.24, 2.03)	-0.36 (-0.53, -0.22)	8.7 (8.2, 9.2)	8.9 (8.3, 9.4)	8.6
Aggregate:						9.4 (8.6, 10.7)	10.0 (8.7, 11.7)	
Annual	211457	169	5.1	1.07 (0.92, 1.27)	-0.14 (-0.28, -0.04)	9.4 (8.5, 10.2)	9.7 (8.7, 10.8)	9.6

Buoy 46014:

Period	<i>N</i>	<i>n</i>	<i>u</i> [m]	σ	ζ	<i>H</i> _{5,50} [m]	<i>H</i> _{5,100} [m]	Max. ob. [m]
Jan-Feb	33897	108	4.9	1.35 (1.11, 1.65)	-0.18 (-0.33, -0.05)	9.6 (8.7, 10.7)	10.0 (8.9, 11.3)	9.8
Mar-Apr	34600	103	4.5	0.86 (0.68, 1.08)	-0.14 (-0.30, -0.02)	7.7 (7.1, 8.3)	8.0 (7.2, 8.7)	7.5
May-Jun	34491	57	4.0	0.49 (0.38, 0.65)	-0.16 (-0.46, -0.01)	5.6 (5.1, 6.0)	5.8 (5.1, 6.3)	5.8
Jul-Aug	37490	83	3.2	0.47 (0.37, 0.62)	-0.20 (-0.38, -0.07)	4.7 (4.4, 4.9)	4.8 (4.5, 5.1)	4.6
Sep-Oct	38436	110	3.6	0.80 (0.65, 1.02)	0.05 (-0.15, 0.17)	8.5 (6.9, 9.9)	9.2 (7.1, 11.2)	8.5
Nov-Dec	38132	123	4.9	1.48 (1.22, 1.82)	-0.19 (-0.34, -0.09)	9.9 (9.0, 10.7)	10.3 (9.2, 11.2)	9.8
Aggregate:						10.2 (9.6, 11.1)	10.6 (9.8, 11.9)	
Annual	217046	266	5.1	1.23 (1.08, 1.42)	-0.14 (-0.24, -0.07)	10.2 (9.4, 11.0)	10.6 (9.7, 11.5)	9.8

Buoy 46022:

Period	<i>N</i>	<i>n</i>	<i>u</i> [m]	σ	ζ	<i>H</i> _{5,50} [m]	<i>H</i> _{5,100} [m]	Max. ob. [m]
Jan-Feb	32802	116	5.0	1.22 (1.01, 1.49)	-0.05 (-0.24, 0.08)	11.0 (9.3, 12.7)	11.6 (9.6, 14.0)	11.5
Mar-Apr	34807	76	5.0	0.98 (0.75, 1.34)	-0.18 (-0.39, -0.04)	8.3 (7.7, 8.7)	8.5 (7.9, 9.1)	7.8
May-Jun	34741	98	3.5	0.90 (0.74, 1.11)	-0.23 (-0.37, -0.11)	6.3 (5.8, 6.7)	6.4 (5.9, 7.0)	6.1
Jul-Aug	36545	152	2.6	1.11 (0.94, 1.31)	-0.42 (-0.55, -0.31)	5.0 (4.8, 5.2)	5.1 (4.8, 5.3)	5.1
Sep-Oct	33092	99	3.8	0.83 (0.66, 1.07)	0.08 (-0.15, 0.20)	9.4 (7.3, 11.5)	10.4 (7.6, 13.2)	10.2
Nov-Dec	32118	58	6.0	2.06 (1.51, 2.80)	-0.53 (-0.82, -0.33)	9.6 (9.1, 9.9)	9.7 (9.2, 10.1)	9.6
Aggregate:						11.3 (9.8, 13.2)	12.0 (10.2, 14.6)	
Annual	204105	158	5.9	1.26 (1.06, 1.49)	-0.12 (-0.26, -0.01)	11.2 (10.0, 12.3)	11.6 (10.2, 13.0)	11.5

Buoy 46023:

Period	<i>N</i>	<i>n</i>	<i>u</i> [m]	σ	ζ	<i>H</i> _{5,50} [m]	<i>H</i> _{5,100} [m]	Max. ob. [m]
Jan-Feb	31447	175	3.6	1.42 (1.18, 1.71)	-0.24 (-0.36, -0.13)	8.1 (7.6, 8.7)	8.4 (7.7, 9.0)	7.5
Mar-Apr	33071	93	4.4	0.69 (0.55, 0.88)	-0.01 (-0.20, 0.11)	8.0 (6.9, 9.0)	8.4 (7.1, 9.8)	8.0
May-Jun	34504	95	3.3	0.80 (0.65, 0.99)	-0.22 (-0.40, -0.09)	5.8 (5.2, 6.3)	6.0 (5.3, 6.5)	5.9
Jul-Aug	38530	108	2.5	0.43 (0.36, 0.52)	-0.19 (-0.35, -0.08)	3.9 (3.6, 4.2)	4.0 (3.7, 4.4)	4.0
Sep-Oct	36684	65	3.5	0.67 (0.48, 0.92)	0.01 (-0.22, 0.17)	6.9 (5.8, 7.7)	7.3 (6.0, 8.5)	6.8
Nov-Dec	28868	147	3.7	1.33 (1.11, 1.59)	-0.24 (-0.38, -0.13)	7.9 (7.1, 8.6)	8.1 (7.3, 8.9)	8.0
Aggregate:						8.5 (8.0, 9.3)	8.7 (8.2, 10.0)	
Annual	203104	99	5.4	0.97 (0.78, 1.20)	-0.28 (-0.45, -0.15)	8.1 (7.7, 8.5)	8.2 (7.7, 8.7)	8.0

Buoy 46026:

Period	<i>N</i>	<i>n</i>	<i>u</i> [m]	σ	ζ	<i>H</i> _{5,50} [m]	<i>H</i> _{5,100} [m]	Max. ob. [m]
Jan-Feb	32334	179	3.1	1.29 (1.11, 1.53)	-0.17 (-0.31, -0.07)	8.0 (7.1, 8.7)	8.3 (7.2, 9.2)	8.0
Mar-Apr	34933	123	3.3	0.74 (0.61, 0.92)	-0.07 (-0.21, 0.04)	6.7 (6.0, 7.5)	7.1 (6.2, 8.0)	6.7
May-Jun	36040	63	3.2	0.48 (0.37, 0.64)	-0.09 (-0.30, 0.06)	5.1 (4.6, 5.5)	5.3 (4.7, 5.9)	5.1
Jul-Aug	34675	33	2.7	0.29 (0.19, 0.47)	0.05 (-0.29, 0.24)	4.1 (3.5, 4.4)	4.3 (3.6, 4.8)	4.0
Sep-Oct	34717	75	2.7	0.89 (0.74, 1.33)	-0.17 (-0.72, -0.02)	5.7 (4.4, 6.6)	6.0 (4.5, 7.1)	6.6
Nov-Dec	36000	83	3.9	0.97 (0.76, 1.26)	-0.08 (-0.25, 0.05)	8.0 (7.1, 8.7)	8.4 (7.3, 9.4)	7.5
Aggregate:						8.3 (7.7, 9.1)	8.7 (7.9, 9.7)	
Annual	208699	100	4.7	0.98 (0.80, 1.24)	-0.18 (-0.34, -0.06)	8.1 (7.4, 8.7)	8.3 (7.5, 9.1)	8.0

Buoy 46027:

Period	<i>N</i>	<i>n</i>	<i>u</i> [m]	σ	ζ	<i>H</i> _{5,50} [m]	<i>H</i> _{5,100} [m]	Max. ob. [m]
Jan-Feb	23887	80	4.7	1.08 (0.83, 1.39)	-0.17 (-0.38, -0.03)	8.5 (7.5, 9.4)	8.8 (7.6, 9.8)	8.5
Mar-Apr	27852	124	3.7	1.13 (0.93, 1.41)	-0.19 (-0.35, -0.07)	7.7 (6.9, 8.5)	8.0 (7.0, 8.9)	7.7
May-Jun	27875	136	2.8	0.81 (0.67, 0.97)	-0.29 (-0.43, -0.17)	5.1 (4.7, 5.4)	5.2 (4.8, 5.6)	5.1
Jul-Aug	27901	44	3.4	0.33 (0.23, 0.50)	-0.04 (-0.31, 0.14)	4.9 (4.4, 5.2)	5.0 (4.5, 5.5)	4.7
Sep-Oct	27334	103	3.3	0.67 (0.53, 0.87)	0.19 (0.00, 0.30)	10.0 (7.4, 12.3)	11.4 (7.9, 14.8)	9.6
Nov-Dec	26963	38	6.0	1.07 (0.68, 1.75)	-0.07 (-0.37, 0.13)	10.3 (9.3, 11.0)	10.8 (9.6, 11.9)	9.4
Aggregate:						11.0 (9.8, 12.6)	11.9 (10.2, 15.0)	
Annual	161812	561	3.7	1.22 (1.12, 1.34)	-0.09 (-0.15, -0.03)	10.3 (9.4, 11.3)	10.7 (9.7, 11.9)	9.6

Buoy 46028:

Period	<i>N</i>	<i>n</i>	<i>u</i> [m]	σ	ζ	<i>H</i> _{5,50} [m]	<i>H</i> _{5,100} [m]	Max. ob. [m]
Jan-Feb	26975	60	5.0	0.85 (0.60, 1.21)	0.03 (-0.17, 0.18)	9.7 (8.4, 10.6)	10.4 (8.8, 11.7)	8.8
Mar-Apr	27967	99	4.2	0.80 (0.62, 1.03)	-0.09 (-0.27, 0.04)	7.7 (6.9, 8.4)	8.0 (7.0, 9.0)	7.5
May-Jun	31486	90	3.5	0.44 (0.35, 0.59)	0.18 (-0.03, 0.29)	7.5 (6.0, 8.9)	8.4 (6.3, 10.3)	6.9
Jul-Aug	33797	46	3.1	0.28 (0.20, 0.42)	-0.02 (-0.26, 0.13)	4.4 (4.0, 4.6)	4.5 (4.1, 4.9)	4.3
Sep-Oct	32291	80	3.3	1.14 (0.91, 1.49)	-0.33 (-0.58, -0.18)	6.1 (5.6, 6.6)	6.3 (5.6, 6.8)	6.3
Nov-Dec	31058	71	5.0	0.88 (0.65, 1.17)	0.03 (-0.14, 0.15)	9.8 (8.5, 10.8)	10.5 (8.9, 11.8)	9.0
Aggregate:						10.6 (9.5, 11.6)	11.4 (10.1, 12.8)	
Annual	183574	389	4.2	0.99 (0.89, 1.11)	-0.06 (-0.14, 0.01)	9.8 (8.9, 10.7)	10.2 (9.2, 11.4)	9.0

Buoy 46029:

Period	<i>N</i>	<i>n</i>	<i>u</i> [m]	σ	ζ	<i>H</i> _{5,50} [m]	<i>H</i> _{5,100} [m]	Max. ob. [m]
Jan-Feb	18666	75	5.1	1.56 (1.24, 2.10)	-0.09 (-0.45, 0.06)	12.0 (9.0, 14.6)	12.6 (9.1, 15.9)	12.8
Mar-Apr	17598	60	4.3	1.59 (1.25, 2.24)	-0.10 (-0.49, 0.05)	11.0 (8.3, 13.3)	11.5 (8.4, 14.6)	11.5
May-Jun	24473	106	2.6	0.82 (0.67, 1.04)	-0.05 (-0.23, 0.07)	6.7 (5.6, 7.8)	7.1 (5.8, 8.5)	6.7
Jul-Aug	26006	37	2.5	0.52 (0.36, 0.80)	-0.05 (-0.32, 0.12)	4.7 (4.0, 5.1)	5.0 (4.1, 5.6)	4.5
Sep-Oct	25564	64	4.0	1.36 (1.00, 1.86)	-0.01 (-0.20, 0.12)	10.9 (9.2, 12.2)	11.8 (9.6, 13.6)	9.3
Nov-Dec	24164	94	5.6	1.51 (1.20, 1.98)	-0.11 (-0.38, 0.03)	12.0 (9.9, 13.7)	12.5 (10.0, 14.7)	12.8
Aggregate:						12.8 (11.4, 15.3)	13.4 (11.9, 16.8)	
Annual	136471	250	5.2	1.58 (1.39, 1.81)	-0.12 (-0.24, -0.03)	12.5 (10.9, 14.0)	13.0 (11.1, 14.8)	12.8

Buoy 46041:

Period	<i>N</i>	<i>n</i>	<i>u</i> [m]	σ	ζ	<i>H</i> _{5,50} [m]	<i>H</i> _{5,100} [m]	Max. ob. [m]
Jan-Feb	19490	33	5.8	1.25 (0.90, 1.82)	-0.16 (-0.44, 0.00)	10.0 (8.6, 11.0)	10.4 (8.8, 11.6)	9.7
Mar-Apr	22688	25	5.4	1.57 (1.04, 2.42)	-0.47 (-0.86, -0.22)	8.3 (7.5, 8.7)	8.4 (7.6, 8.9)	8.2
May-Jun	24117	61	3.0	0.55 (0.40, 0.76)	0.20 (-0.01, 0.32)	8.1 (6.0, 9.7)	9.2 (6.5, 11.6)	7.0
Jul-Aug	29093	49	2.4	0.63 (0.47, 0.87)	-0.09 (-0.33, 0.05)	4.9 (4.1, 5.4)	5.1 (4.2, 5.9)	4.7
Sep-Oct	26519	50	4.3	1.04 (0.73, 1.50)	0.09 (-0.14, 0.23)	10.7 (8.6, 12.2)	11.8 (9.1, 14.1)	9.8
Nov-Dec	26228	49	6.3	1.14 (0.82, 1.62)	-0.06 (-0.39, 0.10)	11.1 (9.3, 12.5)	11.6 (9.5, 13.5)	11.4
Aggregate:						11.9 (10.5, 13.4)	12.8 (11.2, 15.1)	
Annual	148135	131	5.9	1.20 (1.00, 1.50)	-0.11 (-0.28, 0.00)	11.2 (9.8, 12.5)	11.6 (10.0, 13.3)	11.4

Buoy 46042:

Period	<i>N</i>	<i>n</i>	<i>u</i> [m]	σ	ζ	<i>H</i> _{5,50} [m]	<i>H</i> _{5,100} [m]	Max. ob. [m]
Jan-Feb	27269	105	4.2	1.02 (0.83, 1.29)	0.02 (-0.14, 0.12)	10.2 (8.6, 11.7)	11.0 (9.0, 12.9)	9.4
Mar-Apr	28087	109	3.9	1.01 (0.83, 1.24)	-0.26 (-0.41, -0.15)	6.9 (6.4, 7.3)	7.0 (6.5, 7.6)	6.6
May-Jun	27884	90	3.1	0.86 (0.72, 1.06)	-0.21 (-0.45, -0.08)	5.9 (5.1, 6.6)	6.1 (5.2, 6.9)	6.3
Jul-Aug	30036	32	2.8	0.63 (0.48, 0.91)	-0.41 (-0.87, -0.22)	4.1 (3.7, 4.3)	4.2 (3.7, 4.4)	4.2
Sep-Oct	30329	97	3.0	1.12 (0.91, 1.40)	-0.26 (-0.42, -0.13)	6.3 (5.7, 6.8)	6.5 (5.8, 7.1)	6.1
Nov-Dec	29765	29	5.6	1.52 (1.04, 2.31)	-0.36 (-0.75, -0.15)	8.9 (8.2, 9.3)	9.1 (8.4, 9.6)	8.6
Aggregate:						10.2 (9.0, 11.7)	11.0 (9.2, 12.9)	
Annual	173370	347	4.2	0.89 (0.78, 1.00)	0.02 (-0.06, 0.09)	10.6 (9.4, 11.9)	11.3 (9.8, 12.9)	9.4

References

- Abdalla S, Bidlot JR, Janssen P, (2006). Global validation and assimilation of Envisat ASAR wave mode spectra. Proc. Advances in SAR Oceanography from Envisat and ERS Missions (SEASAR 2006), Eur. Space Agency, Frascati, Italy.
- Alexander LV, Tett SFB, Jonsson T, (2005). Recent observed changes in severe storms over the United Kingdom and Iceland. *Geophys. Res. Lett.*, 32(13), L13704.
- Allan J and Komar P, (2000). Are ocean wave heights increasing in the Eastern North Pacific? *Eos Trans. AGU*, 81, 561–567.
- Allen MR and Stott PA, (2003). Estimating signal amplitudes in optimal fingerprinting, part I: Theory. *Clim. Dyn.*, 21, 477-491.
- Allender J, Audunson T, Barstow SF, Bjerken S, Krogstad HE, Steinbakke P, Vartdal L, Borgman LE, Graham C, (1989). The WADIC Project: A comprehensive field evaluation of directional wave instrumentation. *Oce. Eng.*, 16(5/6), 505-536.
- Ambaum MHP, Hoskins BJ, Stephenson DB, (2001). Arctic oscillation or North Atlantic oscillation? *J. Clim.* 14(16) 3495-3507.
- Anderson CW, Carter DJT, Cotton PD, (2001). Wave Climate Variability and Impact on Offshore Design Extremes. Report for Shell International and the Organization of Oil & Gas Producers, pp90. Available from http://www.ogp.org.uk/metocean/meetings_and_agendas.
- Bacon S and Carter DJT, (1991). Wave climate changes in the North Atlantic and North Sea. *Int. J. Climatol.*, 11, 545–558.
- Bacon S and Carter DJT, (1993). A connection between mean wave height and atmospheric pressure gradient in the North Atlantic. *Int. J. Climatol.*, 13, 423–426.
- Barbosa S, Silva ME, Fernandes MJ, (2006). Wavelet analysis of the Lisbon and Gibraltar North Atlantic Oscillation winter indices. *International Journal of Climatology*, 26(5) 581-593.
- Barnston AG and Livezey RE, (1987). Classification, seasonality and persistence of low-frequency atmospheric circulation patterns. *Mon. Weather Rev.*, 115, 1083–1126.
- Barrick DE, Lipa BJ, Steele KE, (1989). Comments on Theory and application of calibration techniques for an NDBC directional wave measurements buoy: nonlinear effects. *IEEE J. Oce. Eng.*, 14(3), 268-272.
- Barring L and von Storch H, (2004). Scandinavian storminess since about 1800. *Geophys Res Lett* 31: L20202, doi: 10.1029/2004GL020441, 1–4.

- Barstow S and Kollstad T, (1991). Field trials of the Directional Waverider. Proc. First Int. Offshore and Polar Eng. Conf., 1991, Heriot-Watt University, Edinburgh.
- Barstow S and Krogstad HE, (1995). Wave Climate Assessment by Satellite Remote Sensing. Proc. Fifth Int. Offshore and Polar Eng. Conf. (ISOPE 95), The Hague, Netherlands.
- Barstow S, Haug O, Krogstad HE, (1998). Satellite altimeter data in wave energy studies. Ocean wave measurement and analysis, Vol. 1. (Proc.3rd Int. Symp.: Waves 97, 3-7 Nov 1997, Virginia Beach, USA), p339-354.
- Beirlant J, Joossens E, Segers J, (2009). Second-order refined peaks-over-threshold modelling for heavy-tailed distributions. J. Statistical Planning and Inference, 139(8) 2800-2815.
- Bengtsson L, Hagemann S, Hodges KI, (2004). Can climate trends be calculated from re-analysis data? J Geophys Res 109, doi: 10.1029/2004JD004536.
- Bengtsson L, Hodges KI, Roeckner E, (2006). Storm tracks and climate change. J. Clim., 19, 3518–3543.
- Benoit M, Frigaard P, Schaffer HA, (1997). Analysing multidirectional wave spectra: A tentative classification of available methods. Proc. IAHR Seminar: Multidirectional Waves and their Interaction with Structures, 27th IAHR Congress, San Francisco, August 1997.
- Bernardino M, Boukhanovsky A, Guedes Soares C, (2008). Alternative approaches to storm statistics in the ocean. Proc. 27th Int. Conf. Offshore Mech. and Arctic Eng. OMAE2008, June 15-20, 2008, Estoril, Portugal, OMAE2008-58053.
- Bidlot JR, Holmes DJ, Wittmann PA, Lalbeharry R, Chen HS, (2002). Intercomparison of the Performance of Operational Ocean Wave Forecasting Systems with Buoy Data. Weather and Forecasting 17, 287-310.
- Bidlot JR, Janssen PAEM, Abdalla S, Hersbach H, (2007). A revised formulation of ocean wave dissipation and its model impact. ECMWF Tech. Memo. 509, Eur. Cent. for Medium-Range Weather Forecasting, Reading, UK.
- Booij N, Ris RC, Holthuijsen LH, (1999). A third-generation wave model for coastal regions. 1: Model description and validation. J. Geophys. Res. 104(C4) 7649 (98JC02622)
- Bromirski PD, Cayan DR, Flick RE, (2005). Wave spectral energy variability in the northeast Pacific . J. Geophys. Res. C, 110(C3), DOI: 10.1029/2004JC002398,
- Brown GS, (1977). The average impulse response of a rough surface and its applications. IEEE Trans Antennas Propag. AP-25, 67-74.
- Cailliau D and Zlotnicki V, (2000). Precipitation detection by the TOPEX/POSEIDON dual-frequency radar altimeter, special sensor microwave/imager and climatological average shipboard reports. IEEE Trans Geosci. Rem. Sens. 38. 205-213.

- Caires S and Sterl A, (2003). Validation of ocean wind and wave data using triple collocation. *J. Geophys. Res.*, 108(C3), 3098
- Caires S and Sterl A, (2005a). A New Nonparametric Method to Correct Model Data: Application to Significant Wave Height from the ERA-40 Re-Analysis. *J. Atmos. Oce. Tech.*, 22(4) 443-459.
- Caires S and Sterl A, (2005b). 100-Year Return Value Estimates for Ocean Wind Speed and Significant Wave Height from the ERA-40 Data. *J. Climate* 18(7) 1032–1048.
- Caires S and Swail V, (2004). Global wave climate trend and variability analysis. In: Preprints of the eighth international workshop on wave forecast and hindcast, 14–19 November 2004, North Shore, Hawaii.
- Caires S, Sterl A, Bidlot JR, Graham N, Swail V, (2004). Intercomparison of Different Wind–Wave Reanalyses. *J. Climate*, 17(10) 1893-1913.
- Caires S, Sterl A, Gommenginer C, (2005). Global ocean mean wave period data: Validation and description. *J. Geophys. Res.*, 110, C02003, doi:10.1029/2004JC002631, 2005.
- Callahan PS, Morris CS, Hsiao SV, (1994). Comparison of TOPEX/POSEIDON sigma0 and significant wave height distributions to Geosat. *J. Geophys. Res.*, 99(C12), 25015-25024.
- Carter DJT, (1993). Estimating extreme wave heights in the NE Atlantic from Geosat Data. HSE Offshore Technology Report OTH 93 396. HMSO London 24pp.
- Carter DJT and Challenor PG, (1981). Estimating return values of environmental parameters. *Quarterly J. R. Met. Soc.*, 107, 259-266.
- Carter DJT and Draper L, (1988). Has the North-East Atlantic become rougher? *Nature*, 332, p494.
- Carter DJT and Tucker MJ, (1986). Uncertainties in environmental design criteria. *Underwater Technology* 12, 2-8 & 33.
- Carter DJT, Challenor PG, Srokosz MA, (1992). An assessment of Geosat wave height and wind speed measurements. *J. Geophys. Res.*, 97(C7), 11383-11392.
- Carter DJT, Foale S, Webb DJ, (1991). Variations in global wave climate throughout the year. *International Journal of Remote Sensing*, 12, pp1687-1697.
- Castillo E and Hadi AS, (1997). Fitting the Generalized Pareto Distribution to Data. *J. Am. Stat. Assoc.*, 92(440), 1609-1620.
- Cavaleri L, (2006). Wave modelling – Where to go in the future. *Bull. Am. Met. Soc.*, 87(2), 207-214.
- Cavaleri L and 25 co-authors, (2007). Wave modelling – The state of the art. *Progress in Oceanography*, 75, 603–674.

- Challenor PG, (1993). Spatial scales of wave height. pp.493-498 in, Proc. First ERS-1 Symp., Space at the service of our environment, 4-6 November 1992, Cannes, France, Vol.I, (ed.B.Kaldeich).Noordwijk: European Space Agency. 930pp. (ESA SP-359).
- Challenor PG, (2006). Lectures on satellite altimetry . National Oceanography Centre, Southampton, UK.
- Challenor PG and Carter DJT, (1994). On the accuracy of monthly means. *J. Atmos. and Oceanic Tech.*, 11(5) 1425–1430.
- Challenor PG and Cotton PD, (2002). The joint calibration of altimeter and in situ wave heights. World Meteorological Organization document number WMO/TD-No.1081, JCOMM Technical Report No. 13.
- Challenor PG and Srokosz MA, (1989). The extraction of geophysical parameters from radar altimeter return from a non-linear sea surface. p257-268 in *Mathematics in Remote Sensing*, edited by SR Brooks, Clarendon, Oxford.
- Challenor PG, Foale S, Webb DJ, (1990). Seasonal changes in the global wave climate measured by the Geosat altimeter. *Int. J. Remote Sensing*, 11(12), 2205-2213.
- Chaouche A and Bacro JN, (2006). Statistical Inference for the Generalized Pareto Distribution: Maximum Likelihood Revisited. *Comm. Stat.: Theory and Methods*, 35(5), 785-802.
- Chelton D, Walsh EJ, MacArthur JL, (1989). Pulse compression and sea level tracking in satellite altimetry. *J. Atmos. Oce. Tech.*, 6, 407-438.
- Cheng CL and Van Ness JW, (1999). *Statistical Regression with Measurement Error*. Arnold, London.
- Coles S, (2001). *An Introduction to the Statistical Modelling of Extreme Values*. Springer-Verlag, London.
- Collard F, Ardhuin F, Chapron B , (2005). Extraction of coastal ocean wave fields from SAR images. *IEEE J. Oce. Eng.*, 30(3), 526–533.
- Collins M, Booth BBB, Harris GR, Murphy JM, Sexton DMH, Webb MJ, (2006). Towards quantifying uncertainty in transient climate change. *Climate Dynamics*, 27, 127-147.
- Cotton PD, (2001). Geosat follow on altimeter wind speed and significant wave height calibration. *Satellite Observing Systems*, 15 Church St, Godalming, Surrey, GU7 1EL.
- Cotton PD and Carter DJT, (1994). Cross calibration of TOPEX, ERS-1, and Geosat wave heights. *J. Geophys. Res.*, 99, 25,025– 25,033. Correction: *J. Geophys. Res.*, 100, 7095.

- Cotton PD and Carter DJT, (1996). Calibration and validation of ERS-2 altimeter wind/wave measurements. Final report. Southampton Oceanography Centre, Internal Document No. 12, (119pp.). (DRA ITT CSM/078).
- Cotton PD, Challenor PG, Carter DJT, (1997). An assessment of the accuracy and reliability of Geosat, ERS-1, ERS-2, TOPEX and Poseidon measurements of significant wave height and surface wind speed. Proc. CEOS wind and wave validation workshop. European Space Agency-ESTEC, Noordwijk, The Netherlands.
- Cotton PD, Challenor PG, Lefevre JM, (2004). Calibration of Envisat and ERS-2 wind and wave data through comparison with in situ data and wave model analysis fields. Proc. 2004 Envisat & ERS Symp., Salzburg, Austria, 6-10 September 2004 (ESA SP-572, April 2005).
- Cox AT and Swail VR, (2001). A 40-year Global Reanalysis of Ocean Waves 1958-1997 (GROW). *J. Geophys. Res.*, 106(C2) 2313-2329.
- Davies CG, Challenor PG, Cotton PD, (1997). Measurement of wave period from radar altimeters. *Ocean wave measurement and analysis*, edited by B. L. Edge and J. M. Hemsley, pp. 819– 826, Am. Soc. Civil Eng., USA, 1997.
- Davison AC and Smith RL, (1990). Models for Exceedances over High Thresholds. *J. R. Stat. Soc. B (Methodological)*, 52(3) 393-442.
- de Vries J, Waldron J, Cunningham V, (2003). Field Tests of the New Datawell DWR-G GPS Wave Buoy. *Sea Technology*, December 2003, pp. 50-55.
- Doblas-Reyes FJ, Pavan V, Stephenson DB, (2003). The skill of multi-model seasonal forecasts of the wintertime North Atlantic Oscillation. *Climate Dynamics*, 21(5-6) 501-514.
- Dobson E, Monaldo F, Goldhirsh J, Wilkerson J, (1987). Validation of GEOSAT altimeter-derived wind speeds and significant wave heights using buoy data. *John Hopkins APL Tech. Digest* 8, 222-233.
- Donelan MA and Pierson WJ, (1983). The sampling variability of estimates of spectra of wind-generated waves. *J. Geophys. Res.*, 88, 4381-4392.
- DTI, (2004). Atlas of UK Marine Renewable Energy Resources: Technical Report. DTI Report No. R.1106, produced by ABPmer, Met Office, Garrad Hassan and Proudman Oceanographic Laboratory.
- Dupuis DJ, (1996). Estimating the Probability of Obtaining Nonfeasible Parameter Estimates of the Generalized Pareto Distribution. *J. Stat. Comp. Sim.*, 54, 197–209.
- Dupuis DJ, (1998). Exceedances over High Thresholds: A Guide to Threshold Selection. *Extremes*, 1(3) 251-261, DOI 10.1023/A:1009914915709.
- Dupuis DJ and Tsao M, (1998). A Hybrid Estimator for Generalized Pareto and Extreme-Value Distributions. *Comm. Stat.: Theory and Methods*, 27, 925–941.

- Elsinghorst C, Groeneboom P, Jonathan P, Smulders L, Taylor PH, (1998). Extreme value analysis of North Sea storm severity. *J. Offshore Mech. Arctic Eng.* 120 (3), 177– 183.
- ESBI, (2005). Accessible Wave Energy Resource Atlas : Ireland. Report No. 4D404A-R2, for Marine Institute/Sustainable Energy Ireland.
- Feldstein SB, (2000). The Timescale, Power Spectra, and Climate Noise Properties of Teleconnection Patterns. *J. Clim.*, 13, 4430–4440.
- Feng H, Vandemark D, Quilfen Y, Chapron B, Beckley B, (2006). Assessment of wind-forcing impact on a global wind-wave model using the TOPEX altimeter. *Oce. Eng.*, 33, 1431–1461.
- Ferreira JA and Guedes Soares C, (1998). An application of the peaks over threshold method to predict extremes of significant wave height. *J. Offshore Mech. and Arctic Eng.*, 120 (3), 165– 176.
- Ferreira JA and Guedes Soares C, (1999). Modelling the long-term distribution of significant wave height with the beta and gamma models. *Ocean Engineering* 26, 713–725.
- Fletcher CG and Saunders MA, (2006). Winter North Atlantic Oscillation Hindcast Skill: 1900–2001. *J. Climate*, 19, 5762-5776.
- Forristall GZ, (2000). Wave Crest Distributions: Observations and Second-Order Theory. *J. Phys. Oce.*, 30(8) 1931–1943.
- Forristall GZ, (2008). How should we combine long and short term wave height distributions? *Proc. 27th Int. Conf. Offshore Mech. and Arctic Eng. OMAE2008*, June 15-20, 2008, Estoril, Portugal, OMAE2008-58012.
- Forristall GZ, Barstow SF, Krogstad HE, Marc Prevosto, Taylor PH, Tromans PS, (2004). Wave Crest Sensor Intercomparison Study: An Overview of WACSIS. *J. Offshore Mech. Arctic Eng.*, 126(1) 26-34.
- Forristall GZ, Heideman JC, Leggett IM, Roskam B, Vanderschuren L, (1996). Effect of Sampling Variability on Hindcast and Measured Wave Heights. *J. Waterway, Port, Coastal and Ocean Eng.*, 122(5) 216-225. Discussion: *Y. Goda*, 124(4) 214
- Freilich MH and Challenor PG, (1994). A new approach for determining fully empirical altimeter wind speed model functions. *J. Geophys. Res.* Vol. 99 , No. C12 , p. 25,051-25,062 (94JC01996)
- Fu LL and Cazenave A, (2001). Satellite altimetry and earth sciences: a handbook of techniques and applications. Academic Press, International Geophysics Series, Vol 69
- Geng Q and Sugi M, (2001). Variability of the North Atlantic cyclone activity in winter analysed from NCEP-NCAR reanalysis data. *J Clim* 14:3863–3873

- Gillett NP, Graf HF, Osborn TJ, (2003). Climatic change and North Atlantic Oscillation. The North Atlantic Oscillation: climate significance and environmental impact. Pages 193-209
- Glowienka-Hensa R, (1985). Studies on the variability of the Icelandic Low and Azores High between 1881 and 1983. *Contrib. Atmos. Phys.*, 58, 160–170
- Goda Y, Hawkes P, Mansard E, Martin MJ, Mathiesen M, Peltier E, Thompson E, van Vledder G. , (1993). Intercomparison of extremal wave analysis methods using numerically simulated data. pp.963-977 in, *Ocean wave measurement and analysis*, (ed.O.T.Magoon & J.M.Hemsley). New York: American Society of Civil Engineers. 1054pp.
- Gommenginger CP, Srokosz MA, Challenor PG, Cotton PD, (2002). Development and validation of altimeter wind speed algorithms using an extended collocated buoy/Topex dataset. *IEEE Trans. Geosc. Remote Sens.*, 40(2), 251– 260, 2002.
- Gommenginger CP, Srokosz MA, Challenor PG, (2003). Measuring ocean wave period with satellite altimeters: A simple empirical model. *Geophysical Research Letters*, 30 (22),
- Gower JFR, (1996). Intercalibration of wave and wind data from Topex/Poseidon and moored buoys off the west coast of Canada. *J. Geophys. Res.*, 101, 3817-3829.
- Gower JFR, (2002). Temperature, wind and wave climatologies, and trends from marine meteorological buoys in the northeast Pacific. *J. Climate*, 15, 3709–3718.
- Graham NE and Diaz HF, (2001). Evidence for intensification of north Pacific winter cyclones since 1948. *Bull. Am. Met. Soc.*, 82, 1869–1893
- Graham NE, Strange RR, Diaz HF, (2002). Intensification of North Pacific winter cyclones 1948–98: Impacts on California wave climate. *Proc. 7th Intl. Workshop Wave Hindcasting AB, Forecasting, Banff, Canada, Oct. 2002.*
- Greenslade DJM and Young IR, (2004). Background errors in a global wave model determined from altimeter data. *J. Geophys. Res.*, 109, C09007, doi:10.1029/2004JC002324
- Grevemeyer I, Herber R, Essen HH, (2000). Microseismological evidence for a changing wave climate in the northeast Atlantic Ocean. *Nature*, 408, 349–352
- Grimshaw SD, (1993). Computing maximum likelihood estimates for the generalized Pareto distribution. *Technometrics* 35, 185–191
- Guedes Soares C and Scotto MG, (2001). Modelling uncertainty of long-term predictions of significant wave height. *Ocean Engineering* 28, 329–342.
- Guedes Soares C and Scotto MG, (2004). Application of the r largest-order statistics for long-term predictions of significant wave height. *Coastal Engineering* 51(5-6) 387-394

- Guedes Soares C, Ferreira RG, Scotto MG, (2003). On the prediction of extreme values of significant wave heights. Proc. 22nd Int. Conf. Offshore Mech. and Arctic Eng. (OMAE 2003). Paper OMAE2003-37478.
- Gulev SK and Grigorieva V, (2004). Last century changes in ocean wind wave height from global visual wave data. *Geophys. Res. Lett.*, 31, L24302, doi:10.1029/2004GL021040.
- Gulev SK and Grigorieva V, (2006). Variability of the Winter Wind Waves and Swell in the North Atlantic and North Pacific as Revealed by the Voluntary Observing Ship Data. *J. Climate*, 19(21), 5667–5685
- Gulev SK and Hasse L, (1999). Changes of wind waves in the North Atlantic over the last 30 years. *Int. J. Climatol.*, 19, 1091–1117
- Gulev SK, Grigorieva V, Sterl A, Woolf D, (2003). Assessment of the reliability of wave observations from voluntary observing ships: Insights from the validation of a global wind wave climatology based on voluntary observing ship data. *J. Geophys. Res.*, 108, 3236, doi:10.1029/2002JC001437.
- Gunther H, Rosenthal W, Stawarz M, Carretero JC, Gomez M, Lozano I, Serrano O, Reistad M, (1998). The wave climate of the Northeast Atlantic over the period 1955– 1994: The WASA wave hindcast. *Global Atmos. Ocean Syst.*, 6, 121–163
- Halliday JR and Douglas NG, (2008). Baseline survey of available wave data. The Crown Estate, 126 Pages. ISBN: 978-1-906410-02-5
- Harrison GP and Wallace AR, (2005). Sensitivity of wave energy to climate change. *IEEE Trans. Energy Conversion*, 20(4), 870-877
- Haslett J and Raftery AE, (1989). Space-Time Modelling with Long-Memory Dependence: Assessing Ireland's Wind Power Resource. *Applied Statistics*, 38(1) 1-50
- Hasselmann K , (1962). On the non-linear energy transfer in a gravity wave spectrum, part 1. General theory. *J. Fluid Mech.* 12, 481-500
- Hasselmann S, Lionello P, Hasselmann K, (1997). An Optimal Interpolation Scheme for the Assimilation of Spectral Data. *J. Geophys. Res.*, 102(C7), 15823-15836
- Hastenrath S, (2002). Dipoles, temperature gradients, and tropical climate anomalies. *Bull. Am. Met. Soc.*, 83, 735–738
- Hayne GS and Hancock III DW, (1990). Corrections for the effect of significant wave height and attitude on Geosat radar altimeter measurements. *J. Geophys. Res.* 95, 2837-2842.
- Hosking JRM, (1981). Fractional differencing. *Biometrika*, 68(1), 165-176
- Hosking JRM and Wallis JR, (1987). Parameter and quantile estimation for the generalized Pareto distribution. *Technometrics*, 29, 339-349

- Hurrell JW, (1995). Decadal trends in the North Atlantic Oscillation and relationships to regional temperature and precipitation. *Science* 269, 676-679.
- Hurrell JW and van Loon H, (1997). Decadal variations in climate associated with the NAO. *Climatic Change*, 36, 301-326
- Hurrell JW, Hoerling MP, Phillips AS, Xu T, (2004). Twentieth century North Atlantic climate change. Part I: Assessing determinism. *Climate Dynamics* 23: 371-389
- Hurrell JW, Kushnir Y, Ottersen G, Visbeck M, (2003). An overview of the North Atlantic Oscillation. *The North Atlantic Oscillation: climate significance and environmental impact*. p1-35
- Hwang PA, Teague WJ, Jacobs GA, Wang DW, (1998). A statistical comparison of wind speed, wave height and wave period derived from satellite altimeters and ocean buoys in the Gulf of Mexico region. *J. Geophys. Res.*, 103, 10,451-10,468, 1998.
- James ID, (1986). A note on the theoretical comparison of wave staff and wave rider buoys in steep gravity waves. *Oce. Eng.*, 13, 209-214.
- Janssen PAEM, (1998). On error growth in wave models. ECMWF Tech. Memo. 249. ECMWF, Reading, UK, p. 12.
- Janssen PAEM, (2004). *The Interaction of Ocean Waves and Wind*. Cambridge University Press, ISBN 0-521-465-40-0, 300pp
- Janssen PAEM, (2008). Progress in ocean wave forecasting. *J. Comp. Phys.*, 227, 3572-3594
- Janssen PAEM, Abdalla S, Hersbach H, Bidlot JR, (2007). Error Estimation of Buoy, Satellite and Model Wave Height Data. *J. Atmos. Oce. Tech.*, 24, 1665-1677
- Janssen PAEM, Hansen B, Bidlot JR, (1997). Verification of the ECMWF wave forecasting system against buoy and altimeter data. *Weather and Forecasting* 12, 763-784.
- Jonathan P and Ewans KC, (2006). Uncertainties in extreme wave height estimates for hurricane dominated regions. *Proc. 25th Int. Conf. Offshore Mech. and Arctic Eng.*, June 4-8, 2006, Hamburg, Germany.
- Jonathan P and Ewans KC, (2007). The effect of directionality on extreme wave design criteria. *Ocean Engineering*, 34, 1977-1994
- Jonathan P and Ewans KC, (2008). Modelling the seasonality of extreme waves in the Gulf of Mexico. *Proc. 27th Int. Conf. Offshore Mech. and Arctic Eng. OMAE2008*, June 15-20, 2008, Estoril, Portugal, OMAE2008-57131
- Jonathan P, Ewans K, Forristall G, (2008). Statistical estimation of extreme ocean environments: The requirement for modelling directionality and other covariate effects. *Ocean Engineering*, 35, 1211- 1225

- Jones PD, Jonsson T, Wheeler D, (1997). Extension to the North Atlantic Oscillation using early instrumental pressure observations from Gibraltar and South-West Iceland. *Int. J. Climatology*, 17, 1433-1450
- Jones PD, Osborn TJ, Briffa KR, (2003). Pressure-Based Measures of the North Atlantic Oscillation (NAO): A Comparison and an Assessment of Changes in the Strength of the NAO and in Its Influence on Surface Climate Parameters. *The North Atlantic Oscillation: climate significance and environmental impact*. p51-62
- Jonsson T and Miles MW, (2001). Anomalies in the seasonal cycle of sea level pressure in Iceland and the North Atlantic Oscillation. *Geophys. Res. Lett.*, 28(22) 4231-4234
- Joosten HP, (2006a). Wave buoys and their elastic mooring. *Int. Oce. Sys.*, 10(3), 18-21
- Joosten HP, (2006b). Directional wave buoys and their elastic mooring. *Int. Oce. Sys.*, 10(4), 18-21
- Juarez SF and Schucany WR, (2004). Robust and Efficient Estimation for the Generalized Pareto Distribution. *Extremes* 7(3) 237-251, DOI 10.1007/s10687-005-6475-6
- Kahma K, Hauser D, Krogstad HE, Lehner S, Monbaliu JAJ, Wyatt LR, (2005). *Measuring and Analysing the Directional Spectra of Ocean Waves*. EU COST Action 714, EUR 21367, ISBN 92-898-0003-8
- Kerbiriou MA, Prevosto M, Maisondieu C, Clement A, Babarit A, (2007). Influence of Sea-States Description on Wave Energy Production Assessment. *Proc. 7th European Wave and Tidal Energy Conference, Porto, Portugal, 2007*
- Komen GJ, Cavaleri L, Donelan M, Hasselmann K, Hasselman S, Janssen PAEM, (1994). *Dynamics and Modelling of Ocean Waves*. Cambridge University Press
- Krogstad HE and Barstow SF, (1999). Satellite Wave Measurements for Coastal Engineering Applications. *Coastal Eng*, 37, 283-307
- Krogstad HE, Barstow SF, Aasen SE, Rodriguez I, (1999a). Some recent developments in wave buoy measurement technology. *Coastal Eng*. 37, 309-329
- Krogstad HE, Wolf J, Thompson SP, Wyatt LR, (1999b). Methods for Intercomparison of wave data. *Coastal Eng.*, 37, 235-257
- Kshatriya J, Sarkar A, Kumar R, (2005). Determination of ocean wave period from altimeter data using wave-age concept. *Marine Geodesy*, 28(1), 71-79
- Kushnir Y, Cardone VJ, Greenwood JG, Cane MA, (1997). The recent increase in North Atlantic wave heights. *J. Climate*, 10, 2107–2113
- Kuzmina SI, Bengtsson L, Johannessen OM, Drange H, Bobylev LP, Miles MW, (2005). The North Atlantic Oscillation and greenhouse-gas forcing. *Geophys. Res. Lett.*, 32, L04703

- Lagarias JC, Reeds JA, Wright MH, Wright PE, (1998). Convergence properties of the Nelder-Mead simplex method in low dimensions. *SIAM J. Opt.*, 9(1), 112– 147.
- Leckebusch GC, Koffi B, Ulbrich U, Pinto JG, Spanghel T, Zacharias S, (2006). Analysis of frequency and intensity of European winter storm events from a multi-model perspective, at synoptic and regional scales. *Climate Research*, 31, 59-74
- Lionello P, Gunther H, Janssen PAEM, (1992). Assimilation of altimeter data in a global third-generation wave model. *J. Geophys. Res.*, 97, 14453-14474.
- Liu PC, Schwab DJ, Jensen RE, (2002). Has wind–wave modelling reached its limit? *Oce. Eng.*, 29, 81–98
- Longuet-Higgins MS, (1986). Eulerian and Lagrangian aspects of surface-waves. *J. Fluid Mech.*, 173, 683–707
- Luceno A, (2006). Fitting the generalized Pareto distribution to data using maximum goodness-of-fit estimators. *Comp. Stat. & Data Analysis*, 51, 904 – 917
- Machel H, Kapala A, Flohn G, (1998). Behaviour of the centres of action above the Atlantic since 1881. Part I: characteristics of seasonal and interannual variability. *International Journal of Climatology* 18: 1–22.
- Mackay EBL, Retzler CH, Challenor PG, Gommenginger CP, (2008a). A parametric model for ocean wave period from Ku-band altimeter data. *J. Geophys. Res.*, 113, C03029, doi:10.1029/2007JC004438
- Mackay EBL, Retzler CH, Challenor PG, Bahaj AS , (2008b). Wave energy resource assessment using satellite altimeter data. *Proc. ASME 27th Int. Conf. Offshore Mech. Arctic Eng.* Paper number OMAE2008-57976
- Marshall JC, Johnson H, Goodman J, (2001). A study of the interaction of the North Atlantic Oscillation with ocean circulation. *J. Climate*. 14, 1399–1421
- Mathiesen M, Goda Y, Hawkes P, Mansard E, Martin MJ, Peltier E, Thompson E, van Vledder G., (1994). Recommended practice for extreme wave analysis. *J. Hydraulic Res*, 32(6), 803–14.
- McCabe GJ, Clark MP, Serreze MC, (2001). Trends in Northern Hemisphere surface cyclone frequency and intensity. *J Clim* 14:2763–2768
- Metoc Plc, (2004). Seapower SW Review. Metoc Report No. 1220. for South West of England Regional Development Agency
- Mills TC, (2004). Is the North Atlantic oscillation a random walk? A comment with further results. *International Journal of Climatology*, 24(3) 377 - 383
- Moharram SH, Gosain AK, Kapoor PN, (1993). A comparative study for the estimators of the generalized Pareto distribution. *J. Hydrol.*, 150, 169-185.

- Mollison D, (1994). Assessing the wave energy resource . pp.205-220 in, Statistics for the environment, 2: Water related issues. Proc. SPRUCE II, Rothamsted Experimental Station, Harpenden, UK, 13-16 Sept 1993, (ed.V.Barnett & K.F.Turkman). Chichester: John Wiley & Sons. 391pp.
- Monaldo F, (1988). Expected differences between buoy and radar altimeter estimates of wind speed and wave height and their implications on buoy-altimeter comparisons. *J. Geophys. Res.*, 93, 2285-2302
- Monaldo F, (1990). Corrected spectra of wind speed and significant wave height. *J. Geophys. Res.*, 95(C3), 3399–3402
- Monbet V, Ailliot P, Prevosto M, (2007). Survey of stochastic models for wind and sea state time series. *Probabilistic Engineering Mechanics*, 22(2) 113-126
- Morton ID and Bowers J, (1997). Extreme value analysis in a multivariate offshore environment. *Applied Ocean Research* 18 (1996) 303-317
- Morton ID, Bowers J, Mould G, (1997). Estimating return period wave heights and wind speeds using a seasonal point process model. *Coastal Eng.* 31, 305-326
- Naess A, (1998). Statistical extrapolation of extreme value data based on the Peaks Over Threshold method. *J. Offshore Mech. Arctic Eng.*, 120, 91-96
- Naess A and Clausen PH, (2001). Combination of the peaks-over-threshold and bootstrapping methods for extreme value prediction. *Structural Safety*, 23(4), 315-330
- Naess A and Haug E, (2008). Extreme value statistics of wind speed data by the POT and AER methods. Proc. 27th Int. Conf. Offshore Mech. and Arctic Eng. OMAE2008, June 15-20, 2008, Estoril, Portugal, OMAE2008-58035
- Nakamura H, (1996). Year-to-year and interdecadal variability in the activity of intraseasonal fluctuations in the Northern Hemisphere wintertime circulation. *Theor. Appl. Climatol.*, 55, 19-32.
- National Data Buoy Center (NDBC), (1996). Nondirectional and directional wave data analysis procedures. Tech. Doc. 96– 01, Stennis Space Center, Miss.
- National Data Buoy Center (NDBC), (2003). Handbook of automated data quality control checks and procedures of the National Data Buoy Center. Tech. Doc. 03– 02, Stennis Space Center, Miss.
- National Oceanic and Atmospheric Administration (NOAA), (2005). Second Workshop Report on the Quality Assurance of Real-Time Ocean Data. CCPO Technical Report Series No. 05-01, July 2005, Norfolk, VA. 48pp
- Neu HJA, (1984). Interannual variations and longer-term changes in the sea state of the North Atlantic from 1970 to 1982. *J. Geophys. Res.*, 89, 6397–6402
- Niclasen BA and Simonsen K, (2008). Note on wave parameters from moored wave buoys. *Applied Ocean Research* (2008), doi:10.1016/j.apor.2008.01.003

- O'Reilly WC, Herbers THC, Seymour RJ, Guza RT, (1996). A comparison of directional buoy and fixed platform measurements of Pacific swell. *J. Atmos. Oce. Tech.*, 13(1), 231–238.
- Osborn TJ, (2004). Simulating the winter North Atlantic Oscillation: the roles of internal variability and greenhouse gas forcing. *Climate Dynamics* 22(6-7) 605-623
- Osborn TJ, Briffa KR, Tett SFB, Jones PD, Trigo RM, (1999). Evaluation of the North Atlantic oscillation as simulated by a climate model. *Clim. Dyn.*, 15, 685–702, 1999.
- Paciorek CJ, Risbey JS, Ventura V, Rosen RD, (2002). Multiple indices of Northern Hemisphere cyclone activity, Winters 1949–99. *J. Climate*, 15(13), 1573–1590
- Paeth H, Latif M, Hense A, (2003). Global SST influence on twentieth century NAO variability. *Climate Dynamics* 21: 63–75
- Pedersen T and Siegel E, (2008). Wave Measurements from Subsurface Buoys. Proc IEEE/OES/CMTC Ninth Working Conference on Current Measurement Technology, 224-233
- Peng L and Welsh AH, (2001). Robust Estimation of the Generalized Pareto Distribution. *Extremes*, 4(1) 53-65, DOI 10.1023/A:1012233423407
- Perrie W, Jiang J, Long Z, Toulany B, Zhang W, (2004). NW Atlantic wave estimates and climate change. In: Preprints of the eighth international workshop on wave forecast and hindcast, 14–19 November 2004, North Shore, Hawaii
- Pickands III, J, (1975). Statistical inference using extreme order statistics. *Annals of Statistics*, 3, 119-131
- Pinto JG, Ulbrich U, Leckebusch GC, Spangh T, Reyers M, Zacharias S, (2007). Changes in storm track and cyclone activity in three SRES ensemble experiments with the ECHAM5/MPI-OM1 GCM. *Climate Dynamics*, 29(2-3), 195-210
- Pitt EG, (1997). Waves and Winds in the North-West Approaches to the United Kingdom. Health and Safety Executive Offshore Technology Report, OTH 500, 70pp
- Pitt EG, (2006a). The wave power climate at the Wave Hub site. *Applied Wave Research*
- Pitt EG, (2006b). Review of wave measurement technology. *Applied Wave Research*
- Pitt EG, (2008). The Assessment of the Wave Power Resource. EMEC Draft Guideline Standard. Available from http://www.emec.org.uk/national_standards.asp
- Ponce de Leon S and Guedes Soares C, (2005). On the sheltering effect of islands in ocean wave models. *J. Geophys. Res.*, 110, C09020, doi:10.1029/2004JC002682

- Pontes T, De Bettencourt L, Athanassoulis GA, Tsoulos L, Nakos B, Skarsoulis E, Stefanakos CN, Skopeliti A, Cavaleri L, Bertotti L, Mollison D, Lewis T, Olivera-Pires H, Barstow S, Christopoulos S, (1997). WERATLAS: European Wave Energy Atlas. European Commission JOULE Programme, Portugal
- Portis DH, Walsh JE, Hamly ME, Lamb PJ, (2001). Seasonality of the North Atlantic Oscillation. *J. Climate*, 14, 2069-2078
- Prevosto M, Krogstad HE, Robin A, (2000). Probability distributions for maximum wave and crest heights. *Coastal Eng.*, 40.329–360
- Priestly MB, (1981). *Spectral Analysis and Time Series*. Elsevier Academic Press, London
- Quarty GD, (1997). Achieving accurate altimetry across storms: Improved wind and wave estimates from C band. *J. Atmos. & Oceanic Tech.* 14(3), 705-715.
- Queffeuou P, (2004). Long-term validation of wave height measurements from altimeters. *Marine Geodesy*, 27, 495–510
- Queffeuou P and Bentamy A, (2007). Analysis of wave height variability using altimeter measurements. Application to the Mediterranean Sea. *J. Atmos. Oceanic Tech.*, 24, 2078-2092.
- Queffeuou P and Croizé-Fillon D, (2007). Investigation of large scale and regional features of wave height using multi-satellite altimeter measurements. *Proc. ENVISAT Symposium, Montreux, Switzerland, 23-27 April 2007, ESA SP-636.*
- Quilfen Y, Chapron B, Serre M, (2004). Calibration/Validation of an Altimeter Wave Period Model and Application to TOPEX/Poseidon and Jason-1 Altimeters. *Marine Geodesy*, 27: 535–549.
- Rademakers PJ, (1993). Waverider-wavestaff comparison. *Oce. Eng.*, 20(2) 187-193
- Rainey RCT, (2007). Pelamis P1B performance at EMEC site. Atkins Technical Note TN/5010105/003
- Repko A, Van Gelder PHAJM, Voortman HG, Vrijling JK, (2004). Bivariate description of offshore wave conditions with physics-based extreme value statistics. *Applied Ocean Research*, 26, 162–170
- Rice SO, (1944&1945). The mathematical analysis of random noise. *Bell Systems Technical Journal*, 23, 282-332 and 24, 46-156
- Rodríguez G, Soares CG, Machado U, (1999). Uncertainty of the sea state parameters resulting from the methods of spectral estimation. *Oce. Eng.*, 26, 991–1002
- Rogers JC, (1990). Patterns of low-frequency monthly sea level pressure variability (1899–1986) and associated wave cyclone frequencies. *J. Climate*, 3(12), 1364–1379

- Rogers JC, (1997). North Atlantic storm track variability and its association to the North Atlantic Oscillation and climate variability of Northern Europe. *J. Climate* 10(7), 1635-1647
- Rogers WE, Wittmann PA, Wang DWC, Clancy RMC, Hsu YL, (2005). Evaluations of Global Wave Prediction at the Fleet Numerical Meteorology and Oceanography Center. *Weather and Forecasting*, 20(5) 745–760
- Sarkar A, Kumar R, Mohan M, (1998). Estimation of ocean wave periods by spaceborne altimeters. *Indian Journal of Marine Sciences*, 27(1), 43-45
- Scaife AA, Knight JR, Vallis GK, Folland CK, (2005). A stratospheric influence on the winter NAO and North Atlantic surface climate. *Geophys. Res. Lett.*, 32, L18715
- Scharroo R, (2005). RADS version 2.2, User Manual and Format Specification. Delft Institute for Earth-Oriented Space Research, Delft University of Technology, Kluyverweg 1, 2629HS Delft, The Netherlands.
- Schulz-Stellenfleth J, Konig T, Lehner S, (2007). An empirical approach for the retrieval of integral ocean wave parameters from synthetic aperture radar data. *J. Geophys. Res.*, 112, C03019, doi:10.1029/2006JC003970
- Schulz-Stellenfleth J, Lehner S, Hoja D, (2005). A parametric scheme for the retrieval of two-dimensional ocean wave spectra from synthetic aperture radar look cross spectra. *J. Geophys. Res.*, 110, C05004, doi:10.1029/2004JC002822.
- Serreze MC, Carse F, Barry RG, Rogers JC, (1997). Icelandic low cyclone activity: climatological features, linkages with the NAO, and relationship with recent changes in the Northern Hemisphere circulation. *J. Climate*, 10, 453–464
- Singh VP and Guo H, (1995). Parameter estimation for 3-parameter generalized Pareto distribution by the principle of maximum entropy (POME). *Hydrol. Sci. J.*, 40, 165-181
- Sobey R and Orloff L, (1995). Triple annual maximum series in wave climate analyses. *Coastal Engineering*, 26, 135-151
- Soukissian TH, Kalantzi G, Karagali I, (2006). De-clustering of Hs Time Series for Applying the Peaks-Over-Threshold Method. Proc. 16th Int. Offshore and Polar Eng. Conf., San Francisco, California, USA, May 28-June 2, 2006
- Steele KE, (1996). Ocean Current Kinematic Effects on Pitch–Roll Buoy Observations of Mean Wave Direction and Nondirectional Spectra. *J. Atmos. Oce. Tech.*, 14, 278-293
- Steele KE and Earle MD, (1979). The status of data produced by NDBC wave data analyzer (WDA) systems. *Oceans '79*, 1-10, 1979
- Steele KE and Mettlach TR, (1993). NDBC wave data - current and planned. *Ocean Wave Measurement and Analysis - Proc. Second Int. Symp. ASCE*, 198-207.

- Steele KE, Lau J, Hsu YH, (1985). Theory and application of calibration techniques for an NDBC directional wave measurements buoy. *Oce. Eng.*, 10(4) 382- 396
- Stefanakos CN and Athanassoulis GA, (2006). Extreme value predictions based on nonstationary time series of wave data. *Environmetrics*, 17(1) 25 - 46
- Stefanakos CN, Athanassoulis GA, Barstow SF, (2006). Time series modelling of significant wave height in multiple scales, combining various sources of data. *J. Geophys. Res. C: Oceans*, 111(10) C10001
- Stephenson DB, Pavan V, Bojariu R, (2000). Is the North Atlantic Oscillation a Random Walk? *Int. J. Climatol.* 20: 1–18 (2000)
- Stephenson DB, Pavan V, Collins M, Junge MM, Quadrelli R, (2006). North Atlantic Oscillation response to transient greenhouse gas forcing and the impact on European winter climate: a CMIP2 multi-model assessment. *Climate Dynamics*, 27(4) 401-420
- STOWASUS Group, (1998). Regional storm, wave and surge scenarios for the 2100 century (STOWASUS-2100). Final report. Available online at <http://www.dmi.dk/pub/STOWASUS-2100/>
- Strong B, Brumley B, Terray EA, Stone GW, (2000). The performance of ADCP-derived wave directional spectra and comparison with other independent measurements. *Proc. Oceans2000*, IEEE Press, 1195-1203
- Swail VR and Cox AT, (2000). On the Use of NCEP–NCAR Reanalysis Surface Marine Wind Fields for a Long-Term North Atlantic Wave Hindcast. *J. Atmos. Oce. Tech.*, 17(4) 532–545
- Swail VR, Cardone VJ, Ferguson M, Gummer DJ, Harris EL, Orelup EA, Cox AT, (2006). The MSC50 Wind and Wave Reanalysis. *Proc. 9th Int. Workshop on Wave Hindcasting and Forecasting*. September 25-29, 2006, Victoria, B.C.
- Swail VR, Ceccacci EA, Cox AT, (2000). The AES40 North Atlantic Wave Reanalysis: Validation and Climate Assessment. *Proc. 6th Int. Workshop on Wave Hindcasting and Forecasting*, November 6-10, Monterey, CA,
- Tawn JA, (1988). An extreme-value theory model for dependent observations. *J. Hydrol.* 101, 227-250.
- Tayfun MA and Fedele F, (2007). Wave-height distributions and nonlinear effects. *Ocean Eng.*, 34, 1631-1649
- Taylor PH and Goh JYK, (2000). Extrapolation of long-term storm statistics, the POT method and data transformation. *Proc. 19th Int. Conf. on Offshore Mech. and Arctic Eng.* OMAE00-6127, ASME.
- Tebaldi C and Knutti R, (2007). The use of the multi-model ensemble in probabilistic climate projections. *Phil. Trans. R. Soc. London. A*, 365(1857) 2053-2075

- Terray L, Demory ME, Déqué M, de Coetlogon G, Maisonnave E, (2004). Simulation of late-21st-century changes in wintertime atmospheric circulation over Europe due to anthropogenic causes. *J. Climate*, 17, 4630-4635.
- Thompson DWJ, Lee S, Baldwin MP, (2003). Atmospheric Processes Governing the Northern Hemisphere Annular Mode/North Atlantic Oscillation. *The North Atlantic Oscillation: climate significance and environmental impact*. Pages 81-112
- Thorpe TW, (1992). *A Review of Wave Energy*. Department of Trade and Industry, ETSU-R-72
- Thorpe TW, (1999). *A Brief Review of Wave Energy*. Department of Trade and Industry, ETSU-R-120
- Tolman HL, (1998). Effect of observation errors in linear regression and bin-average analyses. *Quart. J. Roy. Meteor. Soc.*, 124, 897-917
- Tolman HL, (2002a). Validation of WAVEWATCH III version 1.15 for a global domain. Tech. Rep. 213, NOAA Natl. Cent. for Environ. Predict., Camp Springs, Md.
- Tolman HL, (2002b). Alleviating the Garden Sprinkler Effect in wind wave models. *Ocean Modelling*, 4, 269-289
- Tolman HL, (2003). Treatment of unresolved islands and ice in wind wave models. *Ocean Modelling*, 5, 219-231
- Tolman HL, Balasubramanian B, Burroughs LD, Chalikov DV, Chao YY, Chen HS, Gerald VM, (2002). Development and implementation of wind generated ocean surface wave models at NCEP. *Weather and Forecasting*, 17, 311-333
- Tournadre J, (1993). Time and Space Scales of Significant Wave Height. *J. Geophys. Res.*, 98, C3, 4727-4738
- Tran N and Chapron B, (2006). Combined Wind Vector and Sea State Impact on Ocean Nadir-Viewing Ku- and C-Band Radar Cross-Sections. *Sensors* 2006, 6, 193-207
- Trenberth KE, (1984). Signal versus noise in the Southern Oscillation. *Mon. Wea. Rev.*, 112, 326-332
- Trenberth KE, (1995). Atmospheric circulation climate changes. *Climatic Change*, 31, 427-453
- Trenberth KE and Paolino DA, (1980). The Northern Hemisphere sea-level pressure data set: Trends, errors and discontinuities. *Mon Wea Rev* 108:855-872
- Trenberth KE, Jones PD, Ambenje P, Bojariu R, Easterling D, Klein A, Parker D, Rahimzadeh F, Renwick JA, Rusticucci M, Soden B, Zhai P, (2007). Observations: Surface and Atmospheric Climate Change. . In: *Climate Change 2007: The Physical Science Basis. Contribution of Working Group I to the*

Fourth Assessment Report of the Intergovernmental Panel on Climate Change [Solomon, S., D. Qin, M. Manning, Z. Chen, M. Marquis, K.B. Averyt, M. Tignor and H.L. Miller (eds.)]. Cambridge University Press, Cambridge, United Kingdom and New York, NY, USA.

- Tromans PS and Vanderschuren L, (1995). Response based design conditions in the North Sea: Application of a new method. Proc. Offshore Tech. Conf., OTC 7683
- Tucker MJ and Pitt EG, (2001). Waves in Ocean Engineering. Elsevier Science Ltd, London
- Ulaby FT, Moore RK, Fung AK, (1986). Microwave Remote Sensing - Active and Passive, Vol II, Radar Remote Sensing and Surface Scattering and Emission Theory. Addison-Wesley, Reading, MA.
- Van Vledder G, Goda Y, Hawkes P, Mansard E, Martin MJ, Mathiesen M, Peltier E, Thompson E, (1994). Case studies of extreme wave analysis: a comparative analysis. pp.978-992 in, Ocean wave measurement and analysis, (ed.O.T.Magoon & J.M.Hemsley). New York: American Society of Civil Engineers. 1054pp.
- Vikebo F, Furevik T, Furnes G, Kvamst NG, Reistad M, (2003). Wave height variations in the North Sea and on the Norwegian Continental Shelf, 1881–1999. Cont. Shelf Res., 23, 251–263.
- Violante-Carvalho N, Robinson IS, Schulz-Stellenfleth J, (2005). Assessment of ERS synthetic aperture radar wave spectra retrieved from the Max-Planck-Institut (MPI) scheme through intercomparisons of 1 year of directional buoy measurements. J. Geophys. Res., 110, C07019, doi:10.1029/2004JC002382.
- Visbeck M, Chassignet EP, Curry RG, Delworth TL, Dickson RR, Krahnemann G, (2003). The Ocean's Response to North Atlantic Oscillation Variability. The North Atlantic Oscillation: climate significance and environmental impact. Pages 113-146
- Voorrips AC, (1999). Spectral wave data assimilation for the prediction of waves in the North Sea. Coastal Eng., 37, 455–469
- Walsh EJ, (1982). Pulse to pulse correlation in satellite radar altimeters. Radio Sci. 17, 786-800
- WAMDI Group, (1988). The WAM model—A third generation ocean wave prediction model. J. Phys. Oce., 18(12), 1775–1810
- Wang XL and Swail VR, (2001). Changes of extreme wave heights in Northern Hemisphere Oceans and related atmospheric circulation regimes. J. Climate, 14, 2204–2221
- Wang XL and Swail VR, (2002). Trends of Atlantic wave extremes as simulated in a 40-year wave hindcast using kinematically reanalyzed wind fields. J. Climate, 15, 1020–1035

- Wang XL and Swail VR, (2005). Historical and possible future changes of wave heights in northern hemisphere oceans. In: Perrie W (ed) Atmosphere ocean interactions, Vol 2. (Advances in Fluid Mechanics Series Vol 39) Wessex Institute of Technology Press
- Wang XL and Swail VR, (2006). Climate change signal and uncertainty in projections of ocean wave heights. *Climate Dynamics*, 26(2-3), 109-126
- Wang XL, Swail VR, Zwiers FW, (2004a). Climatology and changes of extra-tropical storm tracks and cyclone activities as derived from two global reanalyses and the Canadian CGCM2 projections of future climate. . In: Preprints of the eighth international workshop on wave forecast and hindcast, 14–19 November 2004, North Shore, Hawaii
- Wang XL, Zwiers FW, Swail VR, (2004b). North Atlantic Ocean Wave Climate Change Scenarios for the Twenty-First Century. *J. Climate*, 17, 2368-2383
- Wang XL, Swail VR, Zwiers FW, (2006a). Climatology and changes of extra-tropical cyclone activity: Comparison of ERA-40 with NCEP/NCAR Reanalysis for 1958-2001. *J. Climate*, 19, 3145-3166
- Wang XL, Swail VR, Zhang X, Zwiers FW, Allen M, (2006b). Detection of Human Influence on Trends of North Atlantic Ocean Wave Heights and Atmospheric Storminess. Proc. 9TH International Workshop on Wave Hindcasting and Forecasting, Victoria, B.C., Canada, September 24-29, 2006
- Wanner H, Brönnimann S, Casty C, Gyalistras D, Luterbacher J, Schmutz C, Stephenson DB, Xoplaki E, (2001). North Atlantic Oscillation – Concepts And Studies . *Surveys in Geophysics*, 22(4) 321-381
- WASA Group, (1998). Changing waves and storms in the Northeast Atlantic? *Bull. Am. Met. Soc.*, 79, 741–760
- Weisse R, von Storch H, Feser F, (2005). Northeast Atlantic and North Sea storminess as simulated by a regional climate model 1958–2001 and comparison with observations. *J. Climate*, 18(3), 465–479
- Wolf J and Woolf DK, (2006). Waves and climate change in the north-east Atlantic. *Geophys. Res. Lett.* 33(6) L06604, 4pp (DOI 10.1029/2005GL025113)
- Woolf DK and Coll J, (2006). Impacts of climate change on storms and waves. In, Buckley, P.J., Dye, S.R. and Baxter, J.M. (eds.) *Marine Climate Change Impacts Annual Report Card 2006*. Lowestoft, UK, MCCIP.
- Woolf DK, Challenor, PG, Cotton PD, (2002). The variability and predictability of the North Atlantic wave climate. *J. Geophys. Res.*, 107(C10), 3145
- Woolf DK, Cotton PD, Challenor, PG, (2003). Measurement of the offshore wave climate around the British Isles by Satellite Altimeter. *Philosophical Transactions of The Royal Society of London, Series A*, 361, 27-31

- Wunsch C, (1999). The Interpretation of Short Climate Records, with Comments on the North Atlantic and Southern Oscillations. *Bulletin of the American Meteorological Society* 80: 245–255
- Young IR, (1986). Probability distribution of spectral integrals. *J. Waterway, Port, Coastal and Ocean Eng.*, 112(4) 338-341
- Young IR, (1994). Global ocean wave statistics obtained from satellite observations. *Appl. Ocean Res.* 16, 235–248.
- Young IR, (1999a). *Wind generated ocean waves*. Elsevier
- Young IR, (1999b). An Intercomparison of GEOSAT, TOPEX and ERS-1 measurements of wind speed and wave height. *Oce. Eng.*, 26, 67-81
- Young IR and Holland GJ, (1996). *Atlas of the Oceans: Wind and Wave Climate*. Pergamon Press, Oxford, 241pp
- Zhang J, (2007). Likelihood Moment Estimation for the Generalised Pareto Distribution. *Aust. N. Z. J. Stat.* 49(1), 69–77
- Zveryaev II, (1999). Decadal and longer changes of the winter sea level pressure fields and related synoptic activity over the North Atlantic. *Int. J. Climatol.* 19: 1177–1185